Joel G. Carter
Editor

Solar Energy and Solar Panels

Systems, Performance and Recent Developments

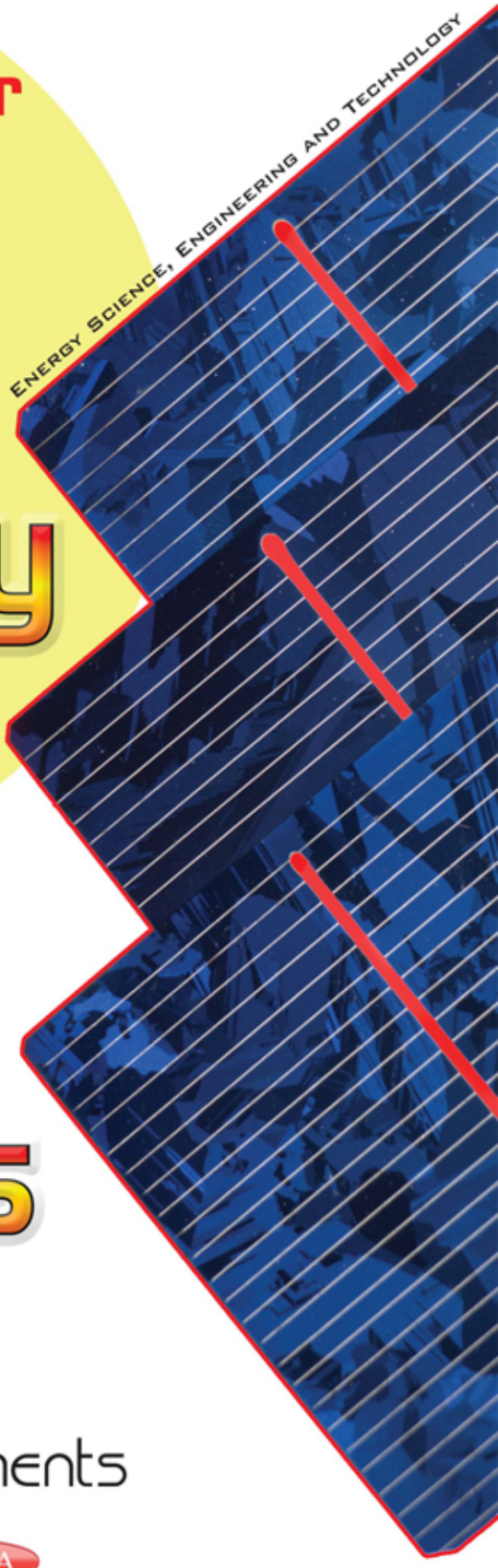

NOVA

ENERGY SCIENCE, ENGINEERING AND TECHNOLOGY

SOLAR ENERGY AND SOLAR PANELS

SYSTEMS, PERFORMANCE AND RECENT DEVELOPMENTS

ENERGY SCIENCE, ENGINEERING AND TECHNOLOGY

Additional books in this series can be found on Nova's website under the Series tab.

Additional e-books in this series can be found on Nova's website under the eBooks tab.

ENERGY SCIENCE, ENGINEERING AND TECHNOLOGY

SOLAR ENERGY AND SOLAR PANELS

SYSTEMS, PERFORMANCE AND RECENT DEVELOPMENTS

JOEL G. CARTER
EDITOR

nova publishers
New York

NOTICE TO THE READER

Library of Congress Cataloging-in-Publication Data

ISBN 978-1-53610-408-0 (e-book)

Published by Nova Science Publishers, Inc. † New York

CONTENTS

PREFACE

Indiscriminate extraction and increasing consumption of fossil fuel resources (crude oil, natural gas, and coal) are adversely affecting the major spheres of human activity. With the depletion of these fuels, efforts are being directed to the use of renewable sources such as solar, wind, and biomass. This book provides new research on the systems, performance and recent developments in solar energy.

As explained in Chapter 1, one of the best alternatives to petroleum, the production of bioethanol has increased since 1990, with a sharp increase from the year 2000 onwards. Bioethanol also offers an attractive alternative as a fuel in low-temperature fuel cells, as it can be produced in large quantities from agricultural waste and biomass. Currently, global ethanol is produced mainly from sugar and starch feedstock. Successful utilization of solar energy which is renewable, abundant, and inexpensive, for bioethanol production from biomass, has the potential to solve the fuel shortage problem. Solar energy provides an important alternative energy source, even if only a portion of this energy is harnessed for heating applications. The authors work focuses on using solar thermal energy for bioreaction leading to ethanol production. A solar reactor was developed to perform the conversion of starch (in a batch process) and glucose (in a continuous flow system) to bioethanol by heating the reactor using solar irradiation. Aqueous starch solution (5 wt%) was charged into the reactor bed loaded with baker's yeast (*Saccharomyces cerevisiae*) and enzymes, resulting in the conversion of starch into ethanol in a single-step process, yielding 0.5 M, 25 mL ethanol/day. A significant amount of ethanol corresponding to 84% of the theoretical yield was obtained after two months. The process was scaled up to 15 wt% starch, producing 1.3 M ethanol, which was demonstrated as a potential and sustainable fuel for direct ethanol fuel cells (DEFCs) (310 $mAmg_{Pt}^{-1}$, 0.75

V). Additionally, the secondary metabolite glycerol was fully reduced to 1,3-propanediol, which is the first example of a fungal strain that converts glycerol *in situ* to a value-added product. The batch process of bioethanol production was further developed to a continuous-flow process. When aqueous glucose solutions of 10, 20, 30, and 40 wt% were fed into the reactor, high ethanol yields (91, 86, 89, and 88% of the theoretical yield, respectively) were obtained, indicating the atom efficiency of the process. No loss was observed in the activity of the yeast even after two months of continuous operation of the process. The ethanol produced from 20 wt% glucose feed (2 M) was demonstrated as a potential fuel for DEFCs with current and power density values as high as 700 mA/cm^2 and 330 mW/cm^2 at a modest open circuit voltage of 1.65 V. Productive utilization of solar energy for driving the fermentation reaction as well as the special design of the reactor that facilitates *in situ* separation of ethanol from the fermentation broth, make the current process economically feasible and environmentally friendly, and therefore industrially appealing and adoptable.

In Chapter 2, the modelling techniques of PV panels from *I-V* characteristics are discussed. At the beginning, a necessary review on the various methods are presented, where difficulties in mathematics, drawbacks in accuracy, and challenges in implementation are highlighted. Next, a novel approach based on linear system identification is demonstrated in detail. Other than the prevailing methods of using approximation (analytical methods), iterative searching (classical optimization), or soft computing (artificial intelligence), the proposed method regards the PV diode model as the equivalent output of a dynamic system, so the diode model parameters can be linked to the transfer function coefficients of the same dynamic system. In this way, the problem of solving PV model parameters is equivalently converted to system identification in control theory, which can be perfectly solved by a simple integral-based linear least square method. Graphical meanings of the proposed method are illustrated to help readers understand the underlying principles. As compared to other methods, the proposed one has the following benefits: 1) unique solution; 2) no iterative or global searching; 3) easy to implement (linear least square); 4) accuracy; 5) extendable to multi-diode models. The effectiveness of the proposed method has been verified by indoor and outdoor PV module testing results. In addition, possible applications of the proposed method are discussed like online PV monitoring and diagnostics, non-contact measurement of POA irradiance and cell temperature, fast model identification for satellite PV panels, and etc.

As shown in Chapter 3, photovoltaics (PV) degradation is a key consideration during PV performance evaluation. Accurately predicting power delivery over the course of lifetime of PV is vital to manufacturers and system owners. With many systems exceeding 20 years of operation worldwide, degradation rates have been reported abundantly in the recent years. PV degradation is a complex function of a variety of factors, including but not limited to climate, manufacturer, technology and installation skill. As a result, it is difficult to determine degradation rate by analytical modeling; it has to be measured. As one set of degradation measurements based on a single sample cannot represent the population nor be used to estimate the true degradation of a particular PV technology, repeated measures through multiple samples are essential.

In Chapter 3, linear mixed effects model (LMM) is introduced to analyze longitudinal degradation data. The framework herein introduced aims to address three issues: 1) how to model the difference in degradation observed in PV modules/systems of a same technology that are installed at a shared location; 2) how to estimate the degradation rate and quantiles based on the data; and 3) how to effectively and efficiently plan degradation measurements. Solar power is always the ultimate energy source on earth. Solar energy does not drive the hydrologic cycle and wind, but also produces biomass including ancient fossil fuels and present foods. Solar energy is one of the potential renewable energy and has been actively promoted by many countries.

In Chapter 4, the policy and promotion strategy of solar energy developments between Taiwan and Japan were surveyed and compared. The results showed that the solar power increased significantly in the past ten years. The cumulative capacity of solar energy (CCSE), solar power generation (SPG), and the ratio of SPG to total power generation for Taiwan in 2014 gave on 615.2, 533.1, and 466.2 times than those in 2005. The CCSE, SPG, and the ratio of SPG to TPG for Japan in 2014 gave on 16.5, 16.4, and 17.6 times than those in 2005. Besides, an analytic hierarchy process (AHP) structure was proposed for decision makers to make decisions to prioritize and select policy and promotion strategy of solar energy developments. Taiwan and Japan have launched solar PV R&D in the 1980s and 1970s, respectively. In the early 2000s, Taiwan enacted the RED Act and rewarded the solar power generation system invested by folk investment to increase the use of renewable energy. Japan enacted the RPS Law and Feed-in Tariffs policy towards the aim of promoting the new energy electricity. Recent advances in solar harvesting technology are transforming the renewable energy landscape. Despite the plunging cost of silicon and the ground-breaking efficiencies of

new perovskite materials, research into “traditional” biomimetic, organic solar energy harvesting complexes remains important for the future success of solar energy.

In Chapter 5 the authors discuss recent findings from studies of molecular donor-acceptor complexes that show promise as the active light harvesting components in organic solar energy systems. In particular, they focus upon self-assembled and covalent complexes of porphyrins (and related molecules) and fullerenes as facile electron transfer partners, and highlight several new results. Finally, the authors discuss the role these types of “soft” organic-based materials play in the solar energy marketplace, and explore how that role is likely to change in the future.

In: Solar Energy and Solar Panels ISBN: 978-1-53610-380-9
Editor: Joel G. Carter

Chapter 1

SOLAR-ENERGY-DRIVEN BIOETHANOL PRODUCTION FROM CARBOHYDRATES FOR TRANSPORTATION APPLICATIONS

Betina Tabah[1], Indra Neel Pulidindi[1], Venkateswara Rao Chitturi[2], Leela Mohana Reddy Arava[2] and Aharon Gedanken[1,*]

[1]Department of Chemistry and Institute for Nanotechnology and Advanced Materials (BINA), Bar-Ilan University, Ramat-Gan, Israel
[2]Department of Mechanical Engineering, Wayne State University, Detroit, MI, US

ABSTRACT

As one of the best alternatives to petroleum, the production of bioethanol has increased since 1990, with a sharp increase from the year 2000 onwards. Bioethanol also offers an attractive alternative as a fuel in low-temperature fuel cells, as it can be produced in large quantities from agricultural waste and biomass. Currently, global ethanol is produced mainly from sugar and starch feedstock. Successful utilization of solar energy which is renewable,

* Corresponding author: E-mail address: gedanken@mail.biu.ac.il.

abundant, and inexpensive, for bioethanol production from biomass, has the potential to solve the fuel shortage problem. Solar energy provides an important alternative energy source, even if only a portion of this energy is harnessed for heating applications. Our work focuses on using solar thermal energy for bioreaction leading to ethanol production. A solar reactor was developed to perform the conversion of starch (in a batch process) and glucose (in a continuous flow system) to bioethanol by heating the reactor using solar irradiation. Aqueous starch solution (5 wt%) was charged into the reactor bed loaded with baker's yeast (*Saccharomyces cerevisiae*) and enzymes, resulting in the conversion of starch into ethanol in a single-step process, yielding 0.5 M, 25 mL ethanol/day. A significant amount of ethanol corresponding to 84% of the theoretical yield was obtained after two months. The process was scaled up to 15 wt% starch, producing 1.3 M ethanol, which was demonstrated as a potential and sustainable fuel for direct ethanol fuel cells (DEFCs) (310 $mAmg_{Pt}^{-1}$, 0.75 V). Additionally, the secondary metabolite glycerol was fully reduced to 1,3-propanediol, which is the first example of a fungal strain that converts glycerol *in situ* to a value-added product. The batch process of bioethanol production was further developed to a continuous-flow process. When aqueous glucose solutions of 10, 20, 30, and 40 wt% were fed into the reactor, high ethanol yields (91, 86, 89, and 88% of the theoretical yield, respectively) were obtained, indicating the atom efficiency of the process. No loss was observed in the activity of the yeast even after two months of continuous operation of the process. The ethanol produced from 20 wt% glucose feed (2 M) was demonstrated as a potential fuel for DEFCs with current and power density values as high as 700 mA/cm^2 and 330 mW/cm^2 at a modest open circuit voltage of 1.65 V. Productive utilization of solar energy for driving the fermentation reaction as well as the special design of the reactor that facilitates *in situ* separation of ethanol from the fermentation broth, make the current process economically feasible and environmentally friendly, and therefore industrially appealing and adoptable.

Keywords: Biofuels, alternate energy, bioethanol, biomass, solar energy, solar reactor, glucose, starch, *Saccharomyces cerevisiae,* fermentation, fuel cells

1. INTRODUCTION

1.1. Bioethanol – Relevance to Energy and Environment

Indiscriminate extraction and increasing consumption of fossil fuel resources (crude oil, natural gas, and coal) are adversely affecting the major spheres of human activity. With the depletion of these fuels, efforts are being directed to the use of renewable sources such as solar, wind, and biomass [1]. Problems related to environmental degradation and energy demand can be alleviated

with the use of biofuels. Bioethanol is regarded as a potential biofuel from renewable sources and widely recognized as one of the most promising transportation fuels with economic, environmental, and energy (energy density value of bioethanol: 23 MJ/L; gasoline: 35 MJ/L) benefits [2-3]. Bioethanol production is important not only for transportation applications, but also for its use as feedstock for the production of C_2 hydrocarbons. In the near future, biofuels – especially bioethanol and biobutanol – may be the vital feedstock for long chain hydrocarbons and biochemicals that are currently being produced from petroleum [4-5].

Ethanol also offers an attractive alternative as a fuel in low-temperature fuel cells because it can be produced in large quantities from agricultural wastes and biomass [6]. Therefore, current interest centers around the production of bioethanol by the fermentation of organic matter, a well-known process throughout history [7]. Brazil and the US produce first-generation bioethanol from either sugar or starch-based crops (sugarcane ethanol in Brazil and corn ethanol in the US), which is currently available at petrol stations. Second-generation bioethanol from lignocellulosic materials is still being researched [8]. Although cellulose can be effectively utilized for bioethanol production, hemicellulose conversion to bioethanol still remains a challenge. In addition, the lignin component of the biomass slows down the hydrolysis of cellulose, necessitating a pretreatment step. Extensive studies are being carried out on the pretreatment of lignocellulosic biomass for the removal of lignin and selective isolation of cellulose in a cost-effective and environmentally-friendly production system [9]. The potential global production of bioethanol from crop wastes and crop residues is estimated at 491GL a year, which can replace 32% of the total gasoline consumption [10].

Bioethanol, with advantageous gravimetric energy density (30 MJ/kg), high octane value, and combustion efficiency (the anti-knock index for gasoline: 87, for ethanol: 99), is one of the most promising alternatives to conventional transportation fuels [11-12]. In addition, the use of ethanol produced from biomass as a transport fuel can reduce CO_2 buildup [13]. Bioethanol can be blended with petrol or used as neat alcohol in dedicated engines, making it an excellent fuel for advanced future flexible-fuel hybrid vehicles [14]. In comparison to gasoline, ethanol contains only a trace of sulfur and no nitrogen; therefore, ethanol blended with gasoline helps to decrease the overall emission of sulfur oxides (SO_x) and nitrogen oxides (NO_x) [15]. In fact, NO_x are more hazardous (>200 times) than CO_x in terms of global warming potential and, together with SO_x, they are known to cause acid rain which is harmful to crops and historical monuments [16-17].

Global annual bioethanol production reached nearly 115 billion liters in 2015 [18]. Thus, breakthroughs in bioethanol production technologies are crucial for the socio-economic well-being of humankind. However, the use of bioethanol as an alternative fuel is not yet economically competitive with the petroleum-based fuel. The main strategies to increase the competitiveness of bioethanol as an alternative fuel include finding a cheap and abundant substrate as well as developing a method or technology that is more atom-efficient and productive for the production of bioethanol [19].

1.2. The Role of Fermentation in Bioethanol Production

The conversion of biomass into ethanol includes two processes: the degradation of starting plant material into fermentable sugars (hydrolysis) and the conversion of sugars into alcohol (fermentation) [20]. Fermentation is the vital stage in bioethanol production, where the selection of suitable feedstock is a challenge. Homogeneous crop materials are easily metabolized to sugars (e.g., molasses from sugar cane and starch from corn kernels), whereas bioethanol production from lignocellulosic materials is complicated due to the recalcitrant nature of the molecules (lignin) present in these materials. Therefore, pretreatment is required to render cellulose and hemicellulose more accessible to the catalytic sites [14, 20, 21]. The fermentation reaction also produces secondary metabolites, such as glycerol and acetic acid, which reduce the efficiency of alcohol production; however, anaerobic conditions can suppress the formation of these metabolites [22-23].

A common problem in bioethanol production through fermentation is the separation of microorganisms from the broth. Solid-state fermentation involves solids in the absence (or near absence) of free water. However, substrates need sufficient moisture to support growth and the metabolism of microorganisms. Solid-state fermentation, with its low energy requirements, produces less wastewater and is environment-friendly. In addition, in solid-state fermentation, microbial cultures are closer to their natural habitats and it is easy to separate them from the fermentation broth [24].Bioethanol production using various free or immobilized cells of bacteria (*Clostridium sp.*) or yeasts (*Saccharomyces sp., Zymomonas sp.*) has been intensively studied [25-29]. Fermentation using immobilized cells prevents substrate inhibition. In immobilized systems, the use of higher concentrations of carbohydrates is feasible and the recovery of the biocatalysts is simple; therefore, the biocatalysts can be reused for many fermentation cycles [25].

Immobilization of yeasts on an appropriate support is a promising strategy for the continuous flow bioethanol production [29].

Saccharomyces cerevisiae is a facultative anaerobe able to live on various fermentable and non-fermentable carbon sources. When it is grown on fermentable substrates, the metabolic energy originates from glycolysis [30]. In addition, *S. cerevisiae* is the most effective ethanol-producing microorganism for hexose sugars including glucose, mannose, and galactose. *S. cerevisiae* is a yeast with high ethanol productivity and high tolerance to the inhibitory compounds and ethanol present in the hydrolysate of lignocellulosic biomass [31].The inhibitory effect of ethanol on the growth of *S. cerevisiae* together with a kinetic model can be found elsewhere [32-33].Native strains of *S. cerevisiae* are unable to utilize xylose for the fermentation process. Some yeast strains have been reported to ferment xylose into ethanol; however, the rate and yield of the conversion are considerably lower than glucose fermentation [34-35].

1.3. Use of Solar Radiation for the Conversion of Biomass into Fuels and Chemicals

The conversion of the sun's energy into chemical energy, photosynthesis, is the basis for life on Earth. Directly or indirectly, photosynthesis fills all of our food requirements and many of our needs for fiber and building materials. The energy stored within fossil fuels, like most energy sources we use today, is also based on chemical energy that came from the sun via photosynthesis. In order to provide new and efficient ways to collect and utilize solar energy, the energy-harvesting systems of plants can be adapted to man-made systems [7, 36].

In the 21st century, it is crucial to have a successful transition to clean well-regulated independent energies (such as solar, wind, and biomass). Solar energy may be an important alternative energy source, even if only a portion of this energy is harnessed for heating applications. The solar irradiance data in Israel is analyzed by Lamedh Energy in order to roughly estimate the cumulative output of solar power facilities in Israel, considering the strong link between the two variables, as demonstrated in their comprehensive study on photovoltaic facilities [37].The solar energy cumulative flux, measured at the Israel Meteorological Service station in Bet Dagan (Israel's Central Coastal Plane) during 2015, was on average 5,269 Wh/m^2 per day, which is about 2.8% higher than the 1965-2014 multi-year average, well within the standard

annual deviation range (±4.0%). 2016 is also expected to show above average solar irradiance across Israel, continuing the trend of above-average irradiance records [37].

Solar energy is an abundant sustainable energy source, and exploiting it for biofuel production has economic and environmental advantages. The use of this alternate green renewable resource may provide a solution to meet the growing energy demands. The utilization of solar thermal energy for biofuel production has a significant impact on the overall energetics (energy return on energy invested, EROEI) of the process. To our knowledge, the exploitation of solar energy for bioethanol production has not been attempted. This study demonstrates a solar reactor that converts starch (in a batch process) and glucose (in a continuous-flow system) into bioethanol. Bioethanol was produced from starch in a single-step process by simultaneous saccharification and fermentation and from glucose through solid-state fermentation in the solar-energy-driven reactor. The special design of the reactor facilitated *in situ* separation of ethanol from the yeast bed by an evaporation-condensation process. Moreover, the bioethanol produced was demonstrated as a potential fuel for operating direct ethanol fuel cells [38-39].

1.4. Fuel Cells – A Promising Energy Conversion Device for the Future

Fuel cells attract attention from both the energy and environmental standpoints and appear to be one of the alternative energy sources capable of meeting future energy needs [40-42]. In general, fuel cells convert chemical energy stored in a fuel into electrical energy in a single step and produce electricity as long as fuel is supplied to the system. The main components of fuel cells are the anode, cathode, and an ion-conducting electrolyte. The basic principle underlying the operation of fuel cells is the catalytic splitting of the input fuel into electrons and ions as it passes over the anode. The generated electrons pass to the cathode by an external circuit and reduce the oxygen that passes over the cathode. The ions are transported to the cathode, where they combine with the oxide ions and generate the oxidized product. If the fuel is hydrogen, then water is formed [43]. Abundant organic raw materials such as alcohols (specifically methanol and ethanol), organic acids (formic acid), or glucose can also be used as fuels. Depending on the input fuel and electrolyte, different chemical reactions occur. The characteristic features of various types of fuel

cells are shown in Table 1. In the case of direct alcohol (methanol and ethanol) fuel cells, anion-exchange membranes can also be used.

Fuel cells exhibit higher efficiency than internal combustion engines. If a fuel cell's exhaust heat is exploited, the total efficiency can be even higher. The extractable power of a fuel cell (P_{cell}) is the product of the cell voltage (V_{cell}) and the cell current (I_{cell}): $P_{cell} = V_{cell} \times I_{cell}$. Although the ideal cell voltage is affected by the difference in the formal potentials of the oxidizer and fuel compounds ($E^{\circ}_{(ox)} - E^{\circ}_{(fuel)}$), irreversible losses in the voltage (or overpotential, η) as a result of kinetic limitations of the electron transfer processes at the electrode interfaces, ohmic resistances and concentration gradients, lead to decreased values. Therefore, $V_{cell} = (E^{\circ}_{(ox)} - E^{\circ}_{(fuel)}) - \eta$[40, 42]. Similarly, the cell current is controlled by the electrode size, the ion permeability, and the transport rates across the membrane separating the cathode and anode compartments of the fuel cell (specifically, the rate of electron transfer at the respective electrode surfaces). These parameters collectively influence the fuel cell power, and so V_{cell} and I_{cell} should be optimized for improved efficiency. Therefore, active electrocatalysts are needed to oxidize fuel at the anode and reduce oxygen/air at the cathode with low overpotentials to obtain high efficiency.

1.4.1. Domestic and Commercial Uses of Fuel Cells

Sir William Grove first demonstrated the conversion of hydrogen to electricity using an acid-electrolyte fuel cell in 1839 [40]. However, turning this idea into a practical means of energy conversion has taken several years. Through worldwide efforts over the last decade, the performance of fuel cells in various respects such as energy efficiency, volumetric and mass power density, and low temperature startup ability has achieved breakthrough progress, leading to the development of fuel cell technology that is beneficial to sustainable transportation and decentralized power developments [41].Direct methanol fuel cells (DMFCs) are used as a replacement for batteries in portable electronic devices including mp3 players, computers, and hearing aid devices. Substantial progress in the development of H_2-fueled proton exchange membrane fuel cells (PEMFCs) has pushed them into the market by several main vehicle companies in 2014. For example, H_2-fueled PEMFCs were used in a fuel cell engine with 3kW/L power density designed by Toyota (Japan) and in an engine module with 5kW/L power density designed by England Intelligent Energy EC200-192 [44].Electric vehicles that run on fuel cells exhibit quiet operation, a cold start at 243 K and negligible CO_x, NO_x, and SO_x

emissions [45].Another promising area where fuel cells can be used is small and large combined power and heating plants (or decentralized power sources)[41]. Both solid oxide fuel cells (SOFCs) and molten carbonate fuel cells (MCFCs) fall into this category. Small-range decentralized power plants that run on fuel cells are appropriate for household applications whereas larger decentralized power plants are utilized to supply heat and electricity to a more extensive area such as a village.

1.4.2. Bioethanol as a Promising Fuel for Fuel Cells

The term bioethanol describes the ethanol produced from biomass. At present, hydrogen is used as a promising fuel because of its high-energy density (32 kWh/kg). However, the storage and handling of hydrogen are problematic and so is the cost [45]. Several biofuels can serve as alternatives to hydrogen in the production of electricity in a fuel cell. These fuels include carbon-containing liquids such as ethanol, methanol, biodiesel, di-methyl esters (DME) and Fischer-Tropsch liquids. There are two biofuels currently used around the world for transport purposes – bioethanol and biodiesel [46]. Between them, ethanol is a good substitute for hydrogen in terms of production, cost, storage, and handling, but is lacking in terms of energy density. Most importantly, the use of bioethanol requires only negligible changes to fuel cell vehicles and minimal adjustment to the fueling infrastructure. Additionally, it is a safer fuel since it ignites at much higher temperatures, resulting in fewer car fires and explosions in impact accidents. Also, ethanol is a colorless, odorless, clean burning liquid fuel that can be produced primarily by the fermentation of renewable resources, such as sugar cane, wheat, corn, or even straw, and it is presently the most scalable and easily deployable among liquid fuels. Other advantages include less toxicity and higher energy density (8.0 kWh/kg) than methanol (6.1 kWh/kg), lower reactivity in the atmosphere, negligible NO_x, volatile organic compounds and SO_x content, and no toxic benzene, toluene, ethylbenzene, or xylene (BTEX) additives which are found in other fuels as a result of the production process [47].All these advantages demonstrate that bioethanol is a good option for fuel cells.

Table 1. Characteristic features of various fuel cells

Electrochemical device	Operating temp. (K)	Electrolyte	Fuel	Oxidant	Anode/Cathode Reactions
Alkaline fuel cell (AFC)	303-423	45% KOH	Hydrogen	O_2/air	$H_2 + 2OH^- \rightarrow 2H_2O + 2e^-$ $O_2 + 2H_2O + 4e^- \rightarrow 4OH^-$
Proton exchange membrane fuel cell (PEMFC)	303-353	H^+-ion exchange membrane (*e.g.*, Nafion)	Hydrogen	O_2/air	$H_2 \rightarrow 2H^+ + 2e^-$ $O_2 + 4H^+ + 4e^- \rightarrow 2H_2O$
Direct methanol fuel cell (DMFC)	303-353	H^+-ion exchange membrane (*e.g.*, Nafion)	Methanol	O_2/air	$CH_3OH + H_2O \rightarrow CO_2 + 6H^+ + 6e^-$ $O_2 + 4H^+ + 4e^- \rightarrow 2H_2O$
Direct ethanol fuel cell (DEFC)	303-333	H^+-ion exchange membrane (*e.g.*, Nafion)	Ethanol	O_2/air	$C_2H_5OH + 3H_2O \rightarrow 2CO_2 + 12H^+ + 12e^-$ $O_2 + 4H^+ + 4e^- \rightarrow 2H_2O$
Glucose fuel cell (GFC)	303-333	H^+-ion exchange membrane (*e.g.*, Nafion)	Glucose	O_2/air	$C_6H_{12}O_6 + 6H_2O \rightarrow 6CO_2 + 24H^+ + 24e^-$ $O_2 + 4H^+ + 4e^- \rightarrow 2H_2O$
Direct formic acid fuel cell (DFAFC)	303-363	H^+-ion exchange membrane (*e.g.*, Nafion)	Formic acid	O_2/air	$HCOOH \rightarrow CO_2 + 2H^+ + 2e^-$ $O_2 + 4H^+ + 4e^- \rightarrow 2H_2O$
Molten carbonate fuel cell (MCFC)	923-973	Alkali carbonate mixture	Hydrogen	O_2/air	$H_2 + CO_3^{2-} \rightarrow H_2O + CO_2 + 2e^-$ $O_2 + 2CO_2 + 4e^- \rightarrow 2CO_3^{2-}$
Solid oxide fuel cell (SOFC)	1073-1273	Yttria-stabilized zirconia	Hydrogen	O_2/air	$H_2 + O^{2-} \rightarrow H_2O + 2e^-$ $O_2 + 4e^- \rightarrow 2O^{2-}$

1.4.3. Direct Ethanol Fuel Cells – Status and Challenges

Direct ethanol fuel cells (DEFCs), characterized by oxidation of ethanol at the anode and reduction of oxygen at the cathode, can be most promising candidates for portable, mobile, and stationary applications [48]. In recent years, various DEFC configurations have been considered and their performance is being investigated. These include proton exchange membrane DEFCs (PEM-DEFCs), anion-exchange membrane DEFCs (AEM- DEFCs) and alkaline-acid DEFCs (AA-DEFCs) [49]. The basic principle underlying the operation of all three DEFCs is the same, and all the cell configurations are under development. A comprehensive review of past research on the development of DEFCs, including catalytic aspects, ion-exchange membranes, and single-cell design and performance has been reported in recent articles [6,49-55]. According to the reports, the AEM-DEFCs and AA-DEFCs configurations have superior advantages over the PEM-DEFCs in terms the utilization of non-Pt electrocatalysts, inexpensive anion exchange membranes, enhanced kinetics of ethanol oxidation and oxygen reduction under alkaline media, and high efficiency. For example, the highest peak power density reported so far for AEM-DEFCs with PdNi/C as the anode and FeCo/C as the cathode is 160 mW/cm^2 at 353 K, whereas for PEM-DEFCs with PtSn/C as the anode and Pt/C as the cathode it is only 79.5 mW/cm^2 at 363 K [56-57]. In the AA-DEFCs configuration, a maximum power density of 360 mW/cm^2 at 333 K using PdNi/C at the anode with a loading of 1.0 mg/cm^2 and Pt/C at the cathode with a loading of 3.9 mg/cm^2 was reported [49,58]. Although tremendous efforts have been expended on developing DEFCs, the power output of the AEM-DEFCs and AA-DEFCs must be substantially improved before widespread commercialization. This is possible through innovative cell design, three-dimensional architecture electrode configurations, and the continuous research and development of the key materials and components used. Advanced anode/cathode electrocatalysts including monolayer/single-atom catalysts, nanometer-film catalysts, controlled-crystal-shape catalysts, and non-Pt catalysts promise to meet the low-cost goal. Advanced ion-exchange membranes with desirable properties such as high ionic conductivity, high thermal and chemical stability, ethanol permeability, durability, water uptake, water diffusivity, and an electro-osmotic drag coefficient also need to be developed in order to achieve better ion-transport properties. The scale-up production techniques need to be developed simultaneously so that the gap between the current state of the art and the

targets can be bridged. Thus, the targets of cost and durability properties can be achieved.

2. SOLAR REACTOR AND SOLAR-ENERGY-DRIVEN FERMENTATION

2.1. Design and Fabrication of the Solar Reactor

The solar reactor was designed and fabricated to perform either continuous flow or batch fermentation and to continuously separate the aqueous ethanol solution from the yeast bed by an *in situ* evaporation-condensation mechanism (See Figure 1 for a detailed design and depiction of the components of the solar reactor) [38-39].

The selected geometry and the dimensions are the most crucial aspects of the operation of the reactor for the effective production and separation of ethanol. The reactor was fabricated using aluminum blocks so that it was lightweight and non-corrosive. The aluminum blocks used for fabricating the bottom (325 x 275 x 120 mm, length, width, and height, respectively) and top (325 x 275 x 6.3 mm) portions of the reactor were purchased from Jack Eini International (Metals) Trade Ltd., Israel. The reactor was fabricated in the mechanical workshop of Bar-Ilan University. A nearly right-angle triangular geometry was selected (Figure 1e) and the height of the reactor was kept much lower than the base (127 mm height and 275 mm base) to facilitate the condensation of ethanol vapor (from the first chamber, Figure 1c) onto the top glass surface (Figure 1a). Such geometry facilitated the free flow of the condensate from the top surface of the reactor to the second chamber, where ethanol was collected (Figure 1c). As depicted in Figure 1, the ethanol collection chamber (second chamber) is fully separated from the fermentation chamber (first chamber) by an aluminum wall. The inlet of the reactor is connected to the feed reservoir and the ethanol outlet valve is opened to collect the product ethanol at regular time intervals (Figure 1d). The analyte can also be collected from the yeast bed without opening the reactor lid.

2.2. Principle of Operation of the Solar Reactor

The temperature of the normal boiling point (T, °C) is related to the vapor pressure (P, mm Hg) of ethanol (the gas phase in equilibrium with the condensed phase) according to the Antoine equation [59],

$$P = 10^{8.04494 - (1554.3/222.65+T)}. \quad (1)$$

The T vs. P plot for ethanol is depicted in Figure 2. The evaporation-condensation process occurs at a reaction temperature (25-35°C) much lower than the boiling point of ethanol (78°C). Although the pressure during fermentation was not monitored using a pressure gauge, it can be concluded that the pressure in the reactor is much lower than the atmospheric pressure [38].

2.3. Solar-Energy-Driven Simultaneous Saccharification and Fermentation (SSF) of Starch to Bioethanol

Starch is an excellent carbon source and a major energy-storage molecule of many economically important crops. The local cultivation of renewable starch sources, such as potato and tapioca, makes it economically attractive; however, starch must be hydrolyzed to glucose before it is fermented to ethanol [60-61]. The chemical structure of starch is composed of 20-25% amylose (1,4-α-linked glucosyl units in linear form, water insoluble) and 75-80% amylopectin (1,6-α-linked branched, water soluble). Five groups of enzymes, which comprise 30% of the world's enzyme production, play a key role in the hydrolysis of starch [62]. Among them, α-amylase cleaves the 1,4-α-linked glucosyl units of amylose, yielding glucose. Likewise, amyloglucosidase (γ-amylase) cleaves the 1,6-α-linkages in amylopectin and the terminal 1,4-α-linked glucosyl units, producing glucose [38].α-Amylase derived from microbial sources has replaced the chemical hydrolysis of starch in starch-processing industries [63]. Thermal stability and alkaline characteristics are important features of amylase isolated from alkalophilic organisms [64]. The microbial α-amylases for industrial processes are derived mainly from *Bacillus subtilis, Bacillus amyloliquefaciens*, and *Bacillus licheniformis* [65].

Conventionally, the gelatinization and liquefaction of starch are carried out enzymatically at high temperatures of 90-130°C for 15 min followed by enzymatic saccharification to glucose [61]. The glucose so formed from starch

is subsequently converted to ethanol via alcoholic fermentation by yeast. This two-step process, which involves consecutive enzymatic hydrolysis and fungal fermentation, can be made more economical by coupling the enzymatic hydrolysis of starchy substrates and fungal fermentation of the derived glucose into a single step by a simultaneous saccharification and fermentation (SSF) process. In the SSF process, the stages are the same as in separate hydrolysis and fermentation systems, but both are performed in the same reactor [38,66-68].This causes less accumulation of sugars within the reactor, a greater yield of ethanol, and a higher saccharification rate [69]. Another advantage of this approach is that only a single fermentor is needed for the entire process, which decreases the investment costs [64]. In addition, the presence of ethanol in the culture medium causes the mixture to be less vulnerable to undesired microorganism invasion [70].

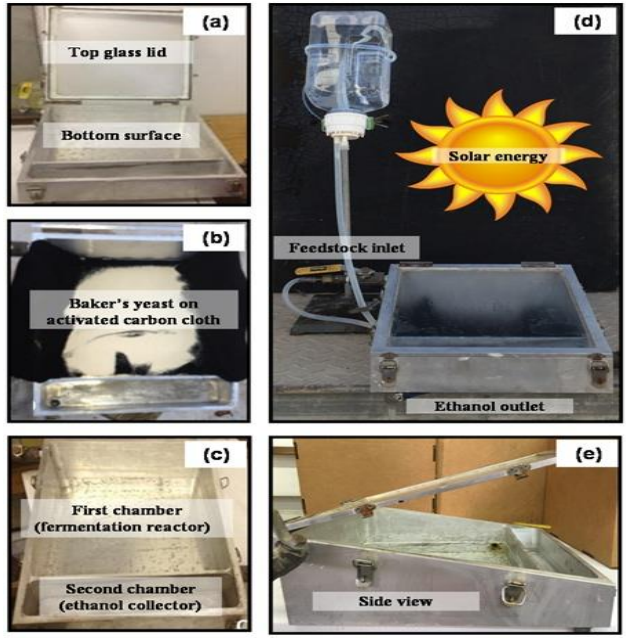

Figure 1. Open reactor (a), fermentation chamber loaded with baker's yeast on activated carbon cloth (b), the bottom surface of the reactor with two chambers (c), a complete system of the solar reactor (d), side view of the reactor (e). [Tabah, B.; Pulidindi, I. N.; Chitturi, V. R.; Arava, L. M. R.; Gedanken, A. Utilization of solar energy for continuous bioethanol production for energy applications. *RSC Adv.* [Online] 2016, *6*, 24203-24209.] Adapted by permission of The Royal Society of Chemistry.

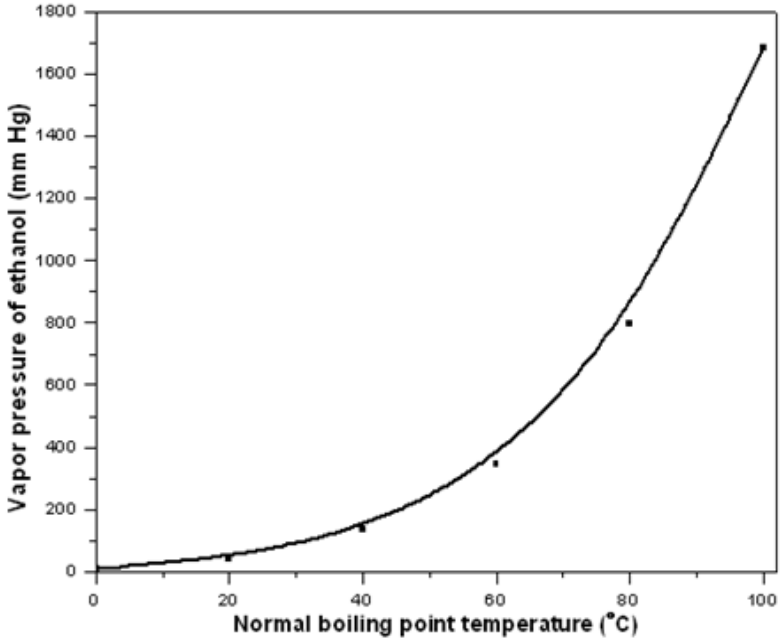

Figure 2. The vapor pressure of ethanol (mm Hg) vs. normal boiling point temperature (°C). [Tabah, B.; Pulidindi, I. N.; Chitturi, V. R.; Arava, L. M. R.; Gedanken, A. Solar-Energy Driven Simultaneous Saccharification and Fermentation of Starch to Bioethanol for Fuel-Cell Applications. *ChemSusChem* [Online] 2015, *8*, 3497-3503.] Reproduced by permission of John Wiley and Sons, Inc.

As stated before, solar energy can be an important alternative energy source if it is harnessed for heating applications. For the efficient utilization of solar energy and to make the SSF process cost-effective, our work focuses on using solar thermal energy for the conversion of potato starch into ethanol in a single-step process in the solar reactor. An aqueous starch solution (5 wt%, 1.6 L) was fed into the reactor charged with *S. cerevisiae* (75 g instant baker's yeast purchased from a local supermarket) and amylase (a mixture of 2.5 mL amyloglucosidase from *Aspergilus niger* and 2.5 mL α-amylase from *Bacillus amyloliquefaciens*) and was covered with an activated carbon cloth (Kynol®, 90 g/m^2, 0.43 mm thick, >1800 m^2/g specific surface area) (Figure 1b). The yeast was not supplemented with any additional nutrients, and no hydrothermal pretreatment was applied before the SSF process. The ethanol produced was evaporated to the top flat glass surface of the reactor which allowed the solar radiation into the bed. The ethanol droplets condensed on the

glass plate were collected in the second chamber of the reactor which has an outlet for ethanol collection (Figure 1).

The process was monitored for over two months (63 days) in the solar reactor at 30-35°C. The analytes were collected at regular time intervals and analyzed for the quantification of ethanol using proton nuclear magnetic resonance (^{1}H NMR) spectroscopy and gas chromatography (GC). The change in ethanol yield (wt%) with time (deduced from ^{1}H NMR analysis) is depicted in Figure 3.

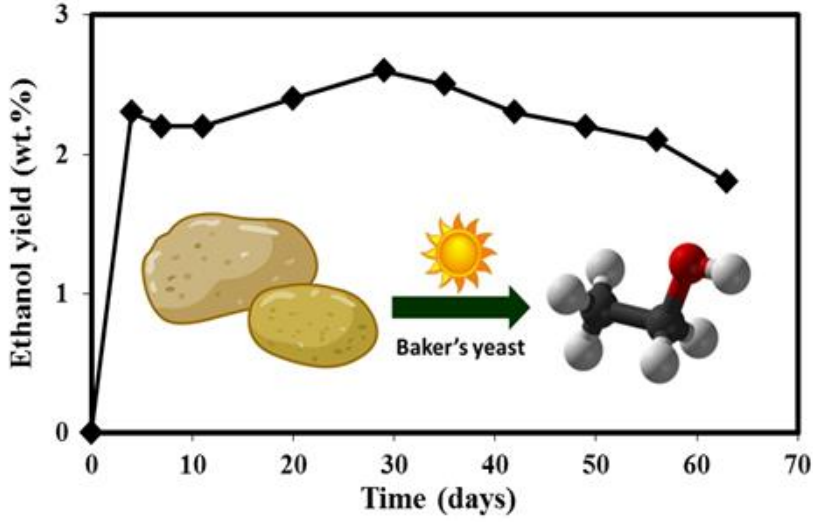

Figure 3. Solar-energy-driven bioethanol production from 5 wt% starch solution at different points in time.

The concentration of ethanol varied in the range 1.8-2.6 wt% over the course of the study. By the 63rd day, 38 g of ethanol were collected in total, which corresponds to 84% of the theoretical yield of ethanol from starch. The mass-balance calculations and detailed gas chromatograms of SSF products collected at regular time intervals were reported by Tabah *et al.*[38]. Table 2 shows the weekly ethanol concentration in the products, determined from both ^{1}H NMR and GC analysis. The concentrations of analytes calculated by the two methods matched, confirming the authenticity of the methodology used for ethanol estimation.

Table 2. Comparison of ethanol concentrations (SSF product) deduced from GC and ^{1}H NMR analysis

SSF product	Ethanol concentration (M)	
	GC	^{1}H NMR
7th day	0.54	0.48
14th day	0.50	0.49
21st day	0.60	0.55
28th day	0.53	0.56
35th day	0.57	0.54
42nd day	0.51	0.49
49th day	0.50	0.48
56th day	0.50	0.46
63rd day	0.42	0.39

For the quantification of ethanol from GC, the chromatograms were recorded and the peak responses were measured. Product identification was performed by comparing the retention time of the analyte with that of the authentic sample. The ethanol yield was calculated from the calibration plot deduced from standard ethanol [38]. The yield of ethanol ($g_{ethanol}/g_{starch}$) was calculated from the ^{1}H NMR spectra of the analytes using sodium formate (HCOONa, m = 20 mg, n = 0.294 mmol) as an internal standard in deuterium oxide (D_2O, 200 μL) [34, 71]. The formula used to calculate the amount of ethanol in a given analyte is

$$n_{EtOH} = (n_{HCOONa} \times I_{EtOH})/(3 \times I_{HCOONa}), \quad (2)$$

where n_{EtOH} is the number of moles of ethanol in the analyte, n_{HCOONa} is the number of moles of HCOONa added as an internal standard, I_{HCOONa} is the ^{1}H NMR integral of HCOONa (1H), set to 1, and I_{EtOH} is the ^{1}H NMR integral of ethanol peak centered at 1.19 ppm (-CH_3; 3H).

Using n_{EtOH}, the amount of ethanol (g) in the analyte was calculated according to the expression,

$$g_{EtOH} = \text{molecular weight of EtOH} \times n_{EtOH}. \quad (3)$$

Using the amount of ethanol in a given volume of analyte, the wt% of ethanol in the total volume of the product was calculated using

Yield of ethanol (wt%) = (g_{EtOH}/total volume of the product) x 100. (4)

^{1}H NMR spectroscopy was used for both quantitative and qualitative analyses. Representative ^{1}H NMR spectra of the analytes collected on the 7th, 14th, 21st, and 28th days of the SSF process are shown in Figure 4.

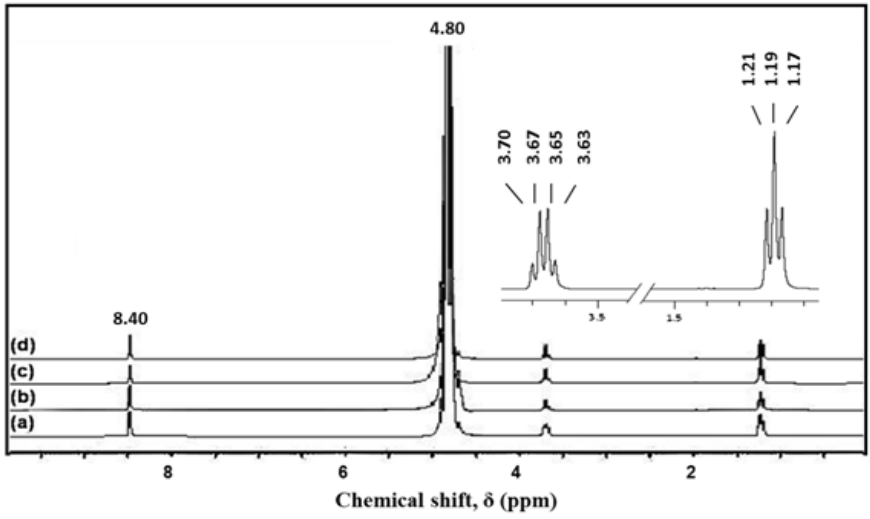

Figure 4. ^{1}H NMR spectra of the SSF product on the (a) 7th, (b) 14th, (c) 21st, and (d) 28th days (Inset shows the ethanol peaks, a 3H (t) centered at 1.19 ppm and a 2H (q) centered at 3.66 ppm). [Tabah, B.; Pulidindi, I. N.; Chitturi, V. R.; Arava, L. M. R.; Gedanken, A. Solar-Energy Driven Simultaneous Saccharification and Fermentation of Starch to Bioethanol for Fuel-Cell Applications. *ChemSusChem* [Online] 2015, *8*, 3497-3503.] Reproduced by permission of John Wiley and Sons, Inc.

Signature peaks of ethanol centered at 1.19 ppm (3H, t) and 3.66 ppm (2H, q) were observed in all the analytes (Figure 4a-4d). The singlet peak at 8.40 ppm originates from the internal standard HCOONa, and the peak at 4.80 ppm corresponds to the solvent. No reaction by-products (glycerol or acetic acid) were observed in the analytes, indicating the purity of the process (only aqueous ethanol). ^{1}H NMR spectra of authentic glycerol and acetic acid were reported by Tabah *et al.* for comparison [38].

In addition to these quantitative methods, the SSF product was also analyzed qualitatively by carbon (^{13}C) NMR spectroscopy. Figure5 shows the ^{13}C NMR spectra of the SSF products (collected biweekly) in comparison to authentic ethanol. As Figure5a indicates, the intense signals seen in all the

samples (Figure 5b-5f) at 17 and 58 ppm are the characteristic peaks of ethanol.

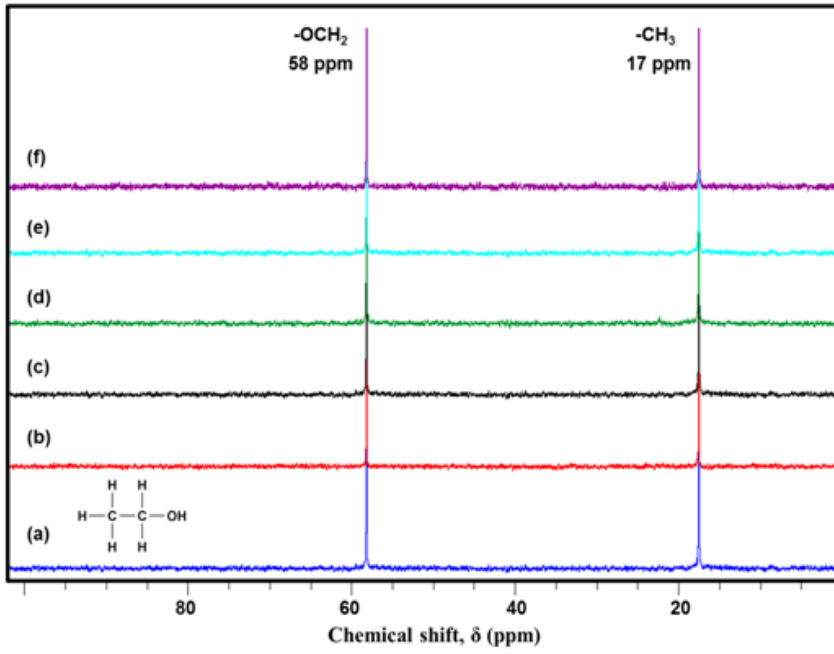

Figure 5. ^{13}C NMR spectra of (a) authentic ethanol and the SSF product collected on the (b) 7th, (c) 21st, (d) 35th, (e) 49th, and (f) 63rd days.

No peaks other than ethanol were observed in the reaction products. This indicates that the reaction product is pure aqueous ethanol and is devoid of the reactant (starch), reaction intermediate (glucose), and usual secondary metabolites of fermentation (glycerol and acetic acid). The^{13}C NMR spectra of authentic starch (peaks at 61.1, 71.6, 72.3, 73.8, 77.1, and 100 ppm), glucose (peaks at 61.5, 70.6, 72.1, 73.7, 74.9, 76.8, 92.9, and 96.7 ppm), glycerol (peaks at 62.9 and 72.3 ppm) and acetic acid (peaks at 19.6 and 175.8 ppm) are shown in Figure6 for comparison.

From the green chemistry point of view, the solar-energy-driven SSF process has numerous advantages. The reaction time is short, due to the coupling of the hydrolysis and fermentation stages into one stage. The SSF process is more economical because both the hydrolysis and fermentation stages are performed in the same reactor. The process requires no external source of heating or additional energy and produces no polluting effluent.

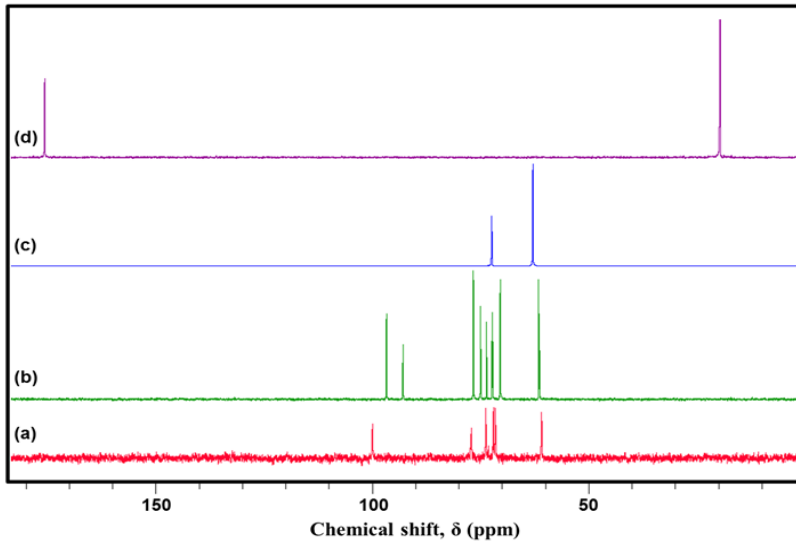

Figure 6. ^{13}C NMR spectra of authentic (a) starch, (b) glucose, (c) glycerol, and (d) acetic acid.

2.4. The Potential of Starch-Based Bioethanol for Application in Fuel Cells

The SSF process was scaled up to 15 wt% starch to produce higher concentrations of bioethanol (1.3 M, 6 wt%) to be evaluated as fuel in DEFCs [38].The experimental setup is schematically shown in Figure 7. The ethanol produced in the solar reactor was separated from the broth soon after its formation by an evaporation-condensation process in the fermentor. The potential of the as-produced bioethanol was evaluated by performing electrochemical measurements using a three-electrode one-compartment electrochemical glass cell assembled with a glassy carbon disk as the working electrode, Ag/AgCl as the reference, and Pt as the counter electrode. A cell containing 0.5 M H_2SO_4 + 1.3 M bioethanol was used as the electrolyte. The working electrode was fabricated by coating an ultrasonically dispersed suspension of Pt/C, 5 wt% Nafion, and isopropanol on the polished glassy carbon disk electrode (0.071 cm^2). The electrode contained about 14 $\mu gPt/cm^2$.

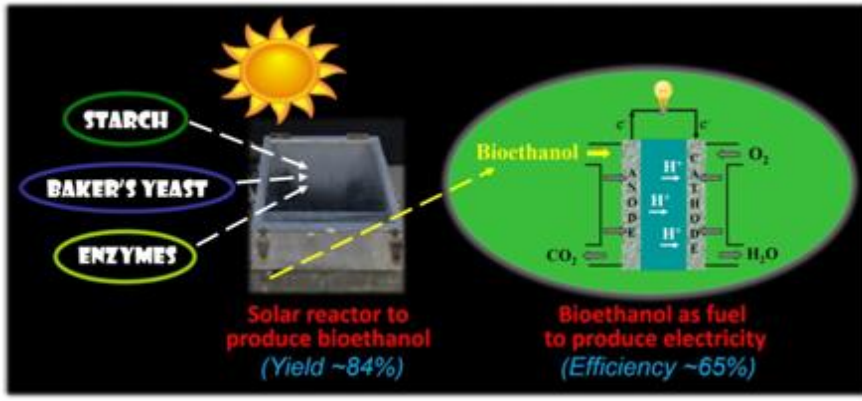

Figure 7. Schematic representation of the experimental setup (solar-energy-driven SSF of starch to produce bioethanol and its use as fuel in DEFCs to produce electricity).

The DEFC measurements were performed using an in-house-built fuel cell test station at different temperatures (303, 333, and 363 K) to evaluate the power densities. A commercial 40 wt% Pt/C (E-TEK) was used as an electrocatalyst (both anode and cathode) and gas diffusion electrodes were fabricated according to the previously reported procedure [72-73]. Linear sweep voltammograms recorded with the Pt/C catalyst in 0.5 M H_2SO_4 + 1.3 M bioethanol at a scan rate of 25 mV/s are shown in Figure8a. A well-defined ethanol oxidation peak was observed at 0.75 V with no additional impurity peaks. The voltammograms recorded with as-produced bioethanol and authentic ethanol were similar, with comparable peak currents (ca. 310 mA/mg_{Pt}). These aspects clearly indicate the high purity level of as-produced bioethanol from starch.

The single-cell DEFC performance with as-produced 1.3 M bioethanol was tested at different temperatures and the *I-V* performance curves are presented in Figure 8b. The open circuit potential (OCP) of the cell was found to be ~0.75 V (65% thermodynamic efficiency) where the effect of the temperature on the OCP was small. However, the cell performance increased with temperature due to the enhanced kinetics of ethanol oxidation at the anode and oxygen reduction at the cathode. At 303, 333, and 363 K, the cell exhibited limiting current densities of 116, 155, and 212 mA/cm^2, respectively, corresponding to the maximum power densities of 25.6, 33.3, and 47.7 mW/cm^2, respectively. In conclusion, the as-produced bioethanol from the solar-energy-driven SSF process of 15 wt% starch was successfully demonstrated as a potential fuel for DEFCs [38].

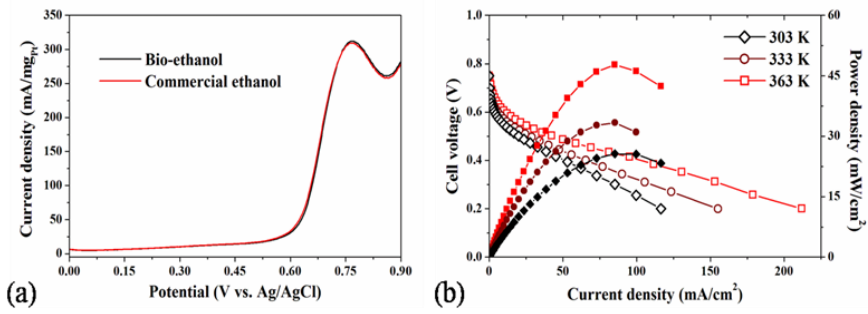

Figure 8. (a) Linear sweep voltammograms of the Pt/C catalyst for ethanol oxidation and (b) polarization and power density curves at 2 mg/cm^2 catalyst loading for Pt/C (40 wt%, E-TEK) on both an anode and cathode at different temperatures (Anode feed: 1.3 M bioethanol at 1 mL/min, cathode feed: pure humidified oxygen at 200 mL/min). [Tabah, B.; Pulidindi, I. N.; Chitturi, V. R.; Arava, L. M. R.; Gedanken, A. Solar-Energy Driven Simultaneous Saccharification and Fermentation of Starch to Bioethanol for Fuel-Cell Applications. *ChemSusChem* [Online] 2015, *8*, 3497-3503.] Reproduced by permission of John Wiley and Sons, Inc.

2.5. Continuous-Flow Bioethanol Production in the Solar Reactor Using 10-40 wt% Glucose Feed

Following the successful results with solar-energy-driven SSF of starch, the batch process of bioethanol production was further developed to a continuous-flow process [39]. Continuous-flow solid-state glucose fermentation was performed by feeding the reactor with 2 L of either 10, 20, 30 or 40 wt% aqueous glucose solutions. The reactor was charged with *S. cerevisiae* (75 g instant baker's yeast) covered with activated carbon cloth (Kynol®, 90 g/m^2, 0.43 mm thick, >1800 m^2/g specific surface area) (Figure 1b) into which the glucose solution was continuously fed (2.8 mL/h flow rate) (Figure 1d). It is important to note that the yeast was not supplemented with any additional nutrients and the pH of the glucose solutions was 7. As in the case of the solar-energy-driven SSF of starch, the fermentation took place in the first chamber (Figure 1c) and the ethanol produced evaporated to the top flat glass surface of the reactor, which allowed the solar radiation into the bed (Figure 1a). The ethanol droplets that condensed on the glass plate were collected in the second chamber of the reactor, which had an outlet for ethanol collection (Figure 1c).

For each glucose solution, the process was monitored for a month in the solar reactor at ~20°C.The fermentation was continuous, most of the

evaporation occurred during the day and only a negligible amount occurred at night. The analytes were collected at regular time intervals and analyzed for the quantification of ethanol using ^{1}H NMR spectroscopy, GC, and high performance liquid chromatography (HPLC). The concentrations of analytes determined by ^{1}H NMR, GC, and HPLC analyses matched, validating the methodology used for ethanol estimation [39].

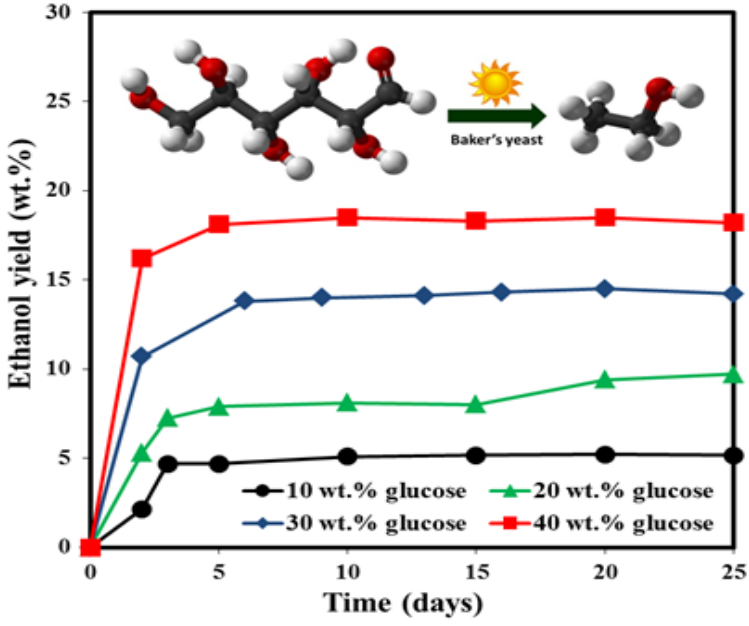

Figure 9. Time on stream studies of ethanol yield (wt%) with 10-40 wt% glucose feed solutions. [Tabah, B.; Pulidindi, I. N.; Chitturi, V. R.; Arava, L. M. R.; Gedanken, A. Utilization of solar energy for continuous bioethanol production for energy applications. *RSC Adv.* [Online] 2016, *6*, 24203-24209.] Adapted by permission of The Royal Society of Chemistry.

The maximum theoretical yield of ethanol expected from the fermentation of 1.0 g glucose is 0.51 g [74].However, due to several operative metabolic pathways in the yeast, secondary metabolites form in addition to ethanol, such as glycerol and acetic acid, reducing the efficiency of the process [39]. The concentration of aqueous ethanol (ethanol yield, wt%) collected at regular time intervals using 10-40 wt% glucose feed is depicted in Figure 9. High ethanol yields (averages of 91, 86, 89, and 88% of the theoretical yield, respectively) indicate the atom efficiency of the process.

It is noteworthy that the yeast bed was always in solid-state condition and glucose was the only nutrient supplied for the yeast. There was no effluent in the reactor, which made it very convenient to change the feed solutions between the experiments. Moreover, there was no loss in the activity of the yeast even after two months of continuous operation of the process. Figure 10 shows the HPLC chromatograms of the fermentation product (collected on the 21st day) using 10-40 wt% glucose solutions in comparison to authentic ethanol (0.5 M, retention time of ~25 min). The concentrations of the produced bioethanol were 1, 2, 3, and 4 M from 10, 20, 30, and 40 wt% glucose fermentation, respectively. These high ethanol concentrations indicate, again, the atom efficiency of the process.

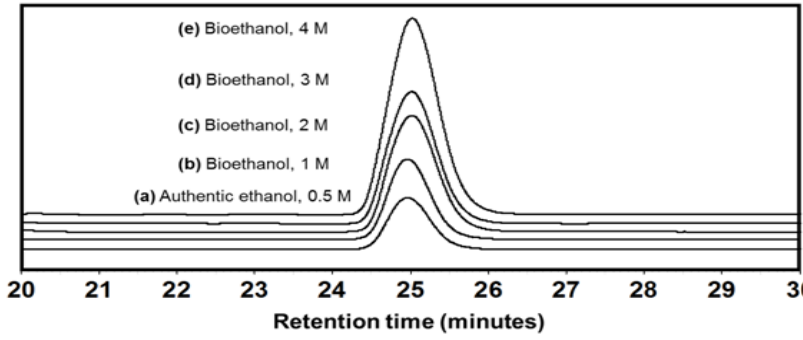

Figure 10. HPLC chromatogram of (a) authentic ethanol and fermentation product (collected on 21st day) using (b) 10 wt%, (c) 20 wt%, (d) 30 wt%, and (e) 40 wt% glucose solutions.

In addition to these quantitative methods, the fermentation product was also analyzed by ^{13}C NMR spectroscopy. Figure 11 shows the representative ^{13}C NMR spectra of the fermentation products obtained from 10-40 wt% aqueous glucose feed solutions (collected on the 10th day) in comparison to authentic ethanol. As Figure 11a indicates, the intense signals seen in all samples (Figure 11b-11e) at 17 and 58 ppm are the characteristic peaks of ethanol. No peaks other than ethanol were observed in the reaction products. The absence of the reactant (glucose, Figure 6b) or yeast in the product signifies the role of solar radiation in separating the aqueous ethanol formed in the fermentation chamber by means of evaporation and condensation. The absence of typical peaks of the usual secondary metabolites, glycerol and acetic acid (Figure 6c-6d), again indicates the product purity and its possible direct use for energy-related applications such as fuel cells.

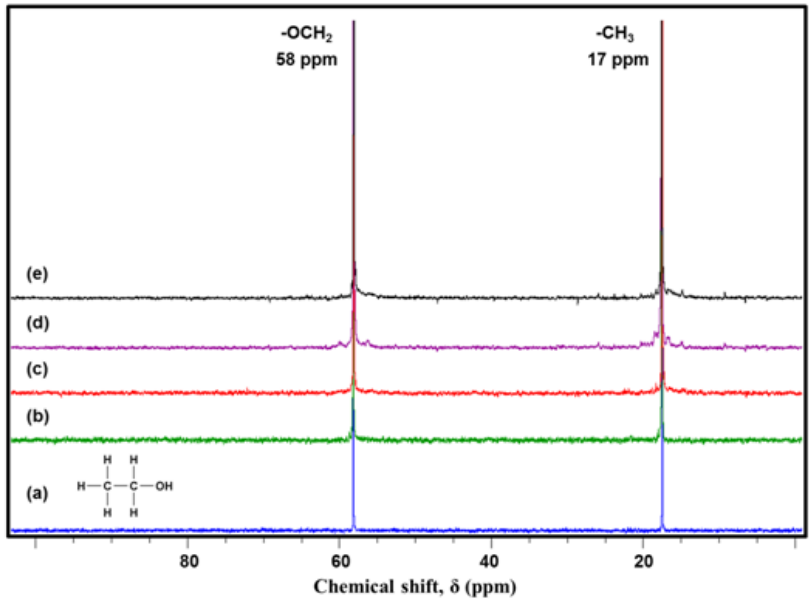

Figure 11. ^{13}C NMR spectra of (a) authentic ethanol and bioethanol collected on the 10th day of the fermentation of (b) 10 wt% glucose solution (1.1 M), (c) 20 wt% glucose solution (1.8 M), (d) 30 wt% glucose solution (3.0 M), and (e) 40 wt% glucose solution (4.0 M). [Tabah, B.; Pulidindi, I. N.; Chitturi, V. R.; Arava, L. M. R.; Gedanken, A. Utilization of solar energy for continuous bioethanol production for energy applications. *RSC Adv.* [Online] 2016, *6*, 24203-24209.] Adapted by permission of The Royal Society of Chemistry.

One of the main issues associated with bioethanol production is its purification from fermentation broth [75]. Various approaches are being studied for the extraction and distillation of ethanol (such as liquid-liquid extraction using ionic liquids, the use of microfiltration, and the substitution of membrane technology for current ethanol dewatering processes) [75-76].Although further distillation is needed to attain anhydrous ethanol, the unique advantage of the use of solar energy in the current methodology is that no additional extraction process is required to separate the aqueous ethanol from the fermentation broth. The formed ethanol in the yeast bed is simultaneously evaporated and condensed to the glass panel of the reactor, from which it flows down into a separate chamber with an outlet for ethanol collection (Figure 1). The pressure in the reactor, which is lower than atmospheric pressure, facilitates the evaporation of ethanol at a temperature much lower than its boiling point (78.5°C). The relation between the lowering

of the boiling point of ethanol and the pressure of its vapor, as well as the operation principle of the reactor, were discussed above, in section 2.2.

Albeit solar energy is unstable in terms of limited day hours and seasons, the present study demonstrates the operability and the sustainability of the process even in the winter season with its lower temperatures (~20°C). The superior features of the current approach for bioethanol production are (i) the bioethanol production process is a continuous flow which could be easily adopted for industrial applications for large scale production, (ii) high concentrations of bioethanol (4 M) are obtained by feeding 40 wt% aqueous glucose solution into the reactor, (iii) it uses solar thermal energy for fermentation and separation of the formed ethanol, (iv) it achieves high ethanol yields without electricity consumption, making the whole process green, sustainable, and most importantly cost effective, (v) it uses the same microorganism (without any additional nutrients) for a long time (two months) without loss in the activity, (vi) no polluting effluent is produced due to the solid-state fermentation, and (vii) it demonstrates the potential of the produced bioethanol as fuel in DEFCs. Thus, this process is economically feasible, having no energy requirement other than solar energy -which is free- for bioethanol production.

2.6. Application of Bioethanol Produced from Solar-Energy-Driven Glucose Fermentation for Electricity Generation Using Fuel Cells

2 M ethanol that was produced through solid-state continuous-flow fermentation of 20 wt% aqueous glucose solution was separated from the broth soon after its formation by an evaporation-condensation process and tested in alkaline-acid direct ethanol fuel cells (AA-DEFCs) for its potential as fuel [39]. AA-DEFCs have drawn much attention due to the higher power density, faster kinetics of ethanol oxidation in alkaline media, lower activation loss and faster kinetics of hydrogen peroxide reduction in acidic media due to two-electron transfer, use of non-Pt electrocatalysts, lower fuel cross-over and higher theoretical cell voltage (2.52 V) than other types of fuel cells [49,58,77]. These fuel cells are characterized by oxidation of ethanol at the anode ($CH_3CH_2OH + 12OH^- \rightarrow 2CO_2 + 9H_2O + 12e^-$; $E^o = -0.74$ V) and reduction of hydrogen peroxide at the cathode ($6H_2O_2 + 12H^+ + 12e^- \rightarrow 12H_2O$; $E^o = +1.78$ V).

Different electrocatalysts were explored to improve the kinetics of redox reactions and thereby the power density [49, 78, 79]. In the present work, PdNi/C was used for the oxidation of bioethanol at the anode and PdAu/C for the reduction of hydrogen peroxide at the cathode. The use of PdAu/C instead of Pt/C circumvents the decomposition of hydrogen peroxide into oxygen and water [80-81]. Moreover, it is less expensive than Pt [53].The current green, sustainable, and cost-effective approach is schematically summarized in Figure 12. The system is composed of alkalized bioethanol and acidified H_2SO_4 compartments separated by a cation conducting membrane. In both the anode and cathode compartments, 3D-structured electrodes were used to facilitate the diffusion of reactant species and also to improve the electrochemically active surface area for redox reactions.

Figure 12. Schematic summary of the current green, sustainable, and cost-effective approach (solar-energy-driven continuous-flow glucose fermentation to produce bioethanol and AA-DEFCs measurements using as-produced bioethanol as fuel to produce electricity). [Tabah, B.; Pulidindi, I. N.; Chitturi, V. R.; Arava, L. M. R.; Gedanken, A. Utilization of solar energy for continuous bioethanol production for energy applications. *RSC Adv.* [Online] 2016, *6*, 24203-24209.] Reproduced by permission of The Royal Society of Chemistry.

The as-synthesized bimetallic palladium electrocatalysts (30 wt% Pd_1Ni_1/C and 50 wt% Pd_1Au_1/C) were used to fabricate 3D-structured anode and cathode, where the active material loading was 1.0 and 3.5 mg/cm^2, respectively. During the operation of the fuel cells, alkalized bioethanol (2 M bioethanol + 5 M NaOH) was fed at the anode and acidified H_2O_2 (4 M H_2O_2 + 1 M H_2SO_4) was fed at the cathode. The flow rates of both bioethanol and H_2SO_4 were maintained at 2 mL/min and the performance of the fuel cells was measured at 303 and 333 K. The membrane electrode assembly (MEA) was conditioned at a constant current density until the open circuit voltage (OCV) became steady and then current-voltage (*I-V*) polarization curves were recorded by applying a potential from OCV to 0.2 V.

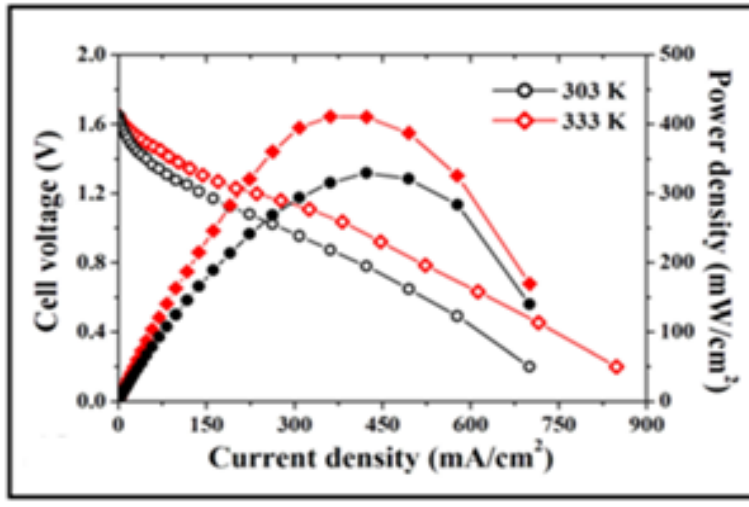

Figure 13. Current-voltage (*I-V*) polarization and power density curves recorded at 303 and 333 K. [Tabah, B.; Pulidindi, I. N.; Chitturi, V. R.; Arava, L. M. R.; Gedanken, A. Utilization of solar energy for continuous bioethanol production for energy applications. *RSC Adv.* [Online] 2016, *6*, 24203-24209.] Adapted by permission of The Royal Society of Chemistry.

I-V polarization and power density curves of AA-DEFCs operated at 303 and 333 K are shown in Figure 13. The OCV was observed to be around 1.65 V (*i.e.*,65.5% voltage efficiency) at both operating temperatures. A maximum power density of 330 mW/cm^2 was observed at 303 K. The OCV and power density observed in AA-DEFCs configuration were higher than the values reported in the literature for acid DEFCs and alkaline DEFCs [53-55]. The

improved performance can be attributed to the elimination of the mixed-potential phenomenon. When the operating temperature increased from 303 to 333 K, the power density increased from 330 to 410 mW/cm^2. The enhanced performance is attributed to the faster electrochemical kinetics of the redox (ethanol oxidation and H_2O_2 reduction) reactions at the electrode compartments, improved membrane conductivity, increased reactant delivery and product removal rates. The performance values observed in this study are higher than the literature values [39, 58, 82-84]. This is possibly due to the high catalytic activity of the bimetallic Pd electrocatalysts and the 3D-structured electrode configuration.

In conclusion, the ethanol produced from 20 wt% glucose feed (2 M) was successfully demonstrated as a potential fuel for DEFCs with current and power density values as high as 700 mA/cm^2 and 330 mW/cm^2 at a modest OCV of 1.65 V [39]. Thus, a new avenue was explored for decentralized power supply based on solar energy. Future efforts should focus on the direct conversion of marine and terrestrial biomass into ethanol using the same strategy. The utilization of solar energy -which is renewable, clean, and sustainable- for bioethanol production is surely a significant leap towards the realization of an industrially-adoptable process.

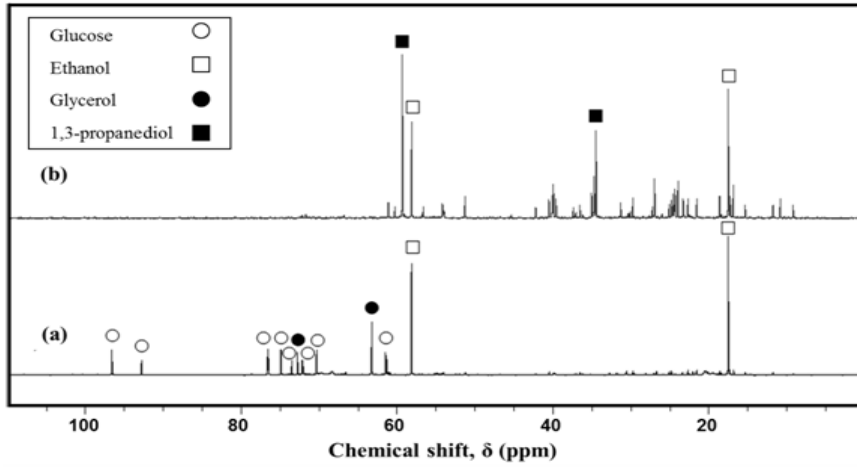

Figure 14. ^{13}C NMR spectra of the samples collected from the broth on (a) 7th day and (b) 60th day. [Tabah, B.; Pulidindi, I. N.; Chitturi, V. R.; Arava, L. M. R.; Gedanken, A. Solar-Energy Driven Simultaneous Saccharification and Fermentation of Starch to Bioethanol for Fuel-Cell Applications. *ChemSusChem* [Online] 2015, *8*, 3497-3503.] Reproduced by permission of John Wiley and Sons, Inc.

2.7. *In Situ* Bioconversion of Glycerol to 1,3-Propanediol by *S. Cerevisiae* in the Solar Reactor

In order to monitor the SSF process of starch and to determine the reaction intermediates and by-products, analytes were collected from the fermentation broth (first chamber of the solar reactor, Figure 1c) at the beginning (7^{th} day) and end(60^{th} day) of the process [38]. The ^{13}C NMR spectra of these samples are shown in Figure14. As expected, glucose, glycerol, and ethanol were present in the sample from the 7^{th} day (Figure14a). The chemical composition of the 60^{th} day analyte from the broth was quite surprising as no trace of glycerol was observed. Interestingly, instead of glycerol, its reduced product 1,3-propanediol(1,3-PDO) was observed (Figure14b). The ^{13}C NMR spectrum of the authentic 1,3-PDO was reported by Tabah*et al.* for comparison [38].

1,3-PDO is a value-added product usually produced by the reduction of glycerol [85].It has recently received attention as a high-value specialty chemical used primarily in the preparation of polyester fibers, films, and coatings [86]. In 2012, the global demand for 1,3-PDO was 60.2 kt with a market value of $2.61/kg [87]. Considering 1,3-PDO is used in the textile industry, food packaging, lubricants, and medicinal usage, demands will continue to rise [88]. By 2019, the global demand is expected to reach 150 kt and the price is estimated to increase to $3.73/kg [87]. The high price of 1,3-PDO is indicative of the economic sustainability of the glycerol conversion process (pure glycerol: $0.66/kg; crude glycerol: $0.11/kg) [87].

The selective conversion of glycerol to 1,3-PDO is still regarded as a challenging process [89].Although many microorganisms are able to metabolize glycerol in the presence of external electron acceptors (respiratory metabolism), few are able to do so fermentatively (*i.e.*, in the absence of electron acceptors). The fermentative metabolism of glycerol has been studied in great detail in several species of the *Enterobacteriaceae* family (such as *Citrobacter freundii* and *Klebsiella pneumoniae*). The dissimilation of glycerol in these organisms is strictly linked to their capacity to synthesize the highly reduced product 1,3-PDO [90].The potential for using these organisms at the industrial level is limited due to their pathogenicity, the requirement of strict anaerobic conditions, the need for rich nutrient supplementation, and the lack of availability of genetic tools and the physiological knowledge necessary for their effective manipulation [91-92].

The use of microorganisms that are amenable to industrial applications, such as *S. cerevisiae*, is highly desirable. To the best of our knowledge, this is the first report on the baker's yeast potential to metabolize glycerol to 1,3-

PDO under the anaerobic conditions in the solar reactor. Besides 1,3-PDO, the SSF reaction product ethanol was also observed in the 60th day sample (Figure 13b). It is important to note that no traces of starch or glucose were observed in the sample, indicating the complete conversion of starch (see Figure 6 for the ^{13}C NMR spectra of authentic starch and glucose).

Synthesizing 1,3-PDO by biological means is extremely important, because it is comparatively more environment-friendly than chemical conversions and, from an economical perspective, it is generally more advantageous since milder conditions are used, less energy is required, and greater yields are attainable for specific products. Furthermore, pursuing the biological route toward 1,3-PDO production is particularly appealing since it utilizes renewable feedstock and cultivation is performed at much lower temperatures and pressures, and generates no toxic by-products [86,93-94].

Following this research, which demonstrated *in situ* bioconversion of glycerol (an industrial waste) to 1,3-PDO (a value-added chemical) by *S. cerevisiae* (biocatalyst) in the solar reactor, various glycerol fermentation conditions were tested at different temperatures to optimize the process for the production of 1,3-PDO from glycerol. Accordingly, under anaerobic fermentation at 25°C, 42.3 wt% of 1,3-PDO yield was achieved with 93.6 wt% of glycerol conversion value, corresponding to 58.5% of the theoretical 1,3-PDO yield.

3. THE FUTURE OF SOLAR ENERGY UTILIZATION

3.1. Potential of Solar Energy Utilization for the Upcoming Biorefinery

Renewable biomass is an important source for alternative energy and substitute for traditional fossil resources as it is prevalent on Earth and can be readily converted into target products. Intensive research focuses on the conversion of biomass into chemicals, biofuels, and various materials and the race is on for creating new “biorefinery” processes needed for future economies. The application of process intensification techniques, such as ultrasound irradiation, in biorefineries has been proved to increase energy efficiency, shorten the reaction time, and improve product yields [95]. The development of biorefineries that utilize free, renewable, and abundant solar thermal energy will create remarkable opportunities for the forestry, biotechnology, materials, and chemical processing industries as well as

stimulating advances in agriculture. It will eventually help to create a sustainable society and industries that use renewable and carbon-neutral resources.

3.2. "Two-Stage Upscaling Method" for Bioethanol Production Using Solar Reactor

For future studies on solar energy utilization, we propose a *two-stage upscaling procedure.* In the first stage, upscaling of the current solar reactor to a size four times larger than the current apparatus (50 cm height and 110 cm base) is planned. We expect the new dimensions to enable an increase in the flow rate of the feedstock by a factor of four. In the second stage of upscaling, in addition to the dimensions (approximately ten times larger than the current reactor, 120 cm height and 200 cm base), the design of the solar reactor will be modified as well (see Figure 15, staircase design) to handle large quantities of biomass feed for demand-based supply of bioethanol for transportation and chemical industry applications.

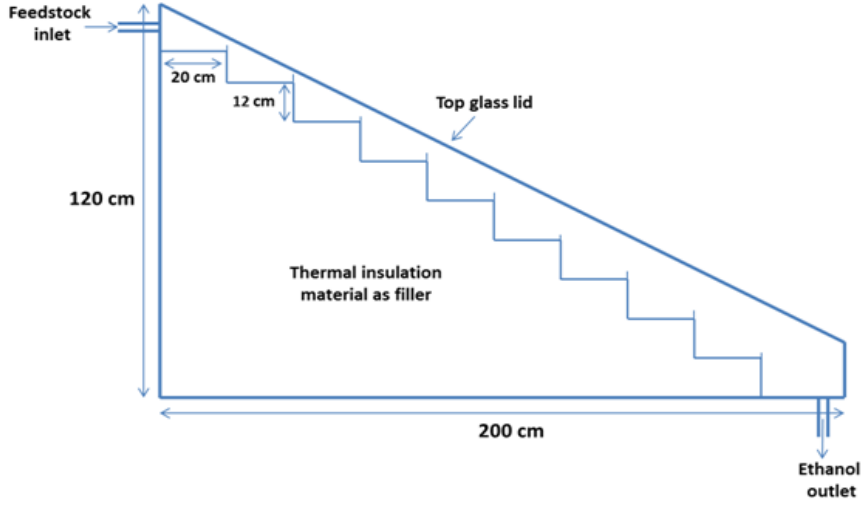

Figure 15. Staircase design of larger solar reactor for upscaling the bioethanol production process.

3.3. Exploitation of Solar-Energy Based Bioethanol for the Production of Valuable Chemicals

The bioethanol produced from solar-energy based fermentation can be used as feedstock for the production of valuable chemicals such as diethyl ether and ethylene. Dietheyl ether is an attractive motor vehicle fuel alternate and ethylene is one of the major feedstock for a variety of polymer-based materials in petrochemical industry [96-97]. Production of petrochemicals from environment-friendly non-petroleum feedstock is very important and developments of new and efficient production processes are considered as challenging research areas [96, 98-99]. Polyoxometallates such as tungstophosphoric acid, silicotungstic acid, and molybdophosphoric acid are potential catalysts which can be used for the dehydration of bioethanol under microwave irradiation conditions [96, 100-101]. Therefore, any progress in this direction will open new avenues towards sustainable biorefinery.

CONCLUSION

Currently, the only available pathway for conversion of carbohydrates into ethanol is the biological pathway, *i.e.*, fermentation, which is the most time-consuming part of the bioethanol production process. There are many reports in the literature focusing on the evaluation of different carbohydrates and fermentation conditions for accelerated bioethanol production. The current bioethanol production methods are mostly based on highly-controlled reactions and state-of-the-art instruments such as the sonicator, high-speed stirrer, and microwave, requiring a large amount of electrical energy input. In our study, solar energy was used as a heating element for the catalyst and the reaction volume, replacing an oven or a heating plate. In the same way, the distillation step was also aided by this heating element as the ethanol produced in the reactor was separated from the broth soon after its formation by an evaporation-condensation process.

High ethanol yields were obtained (84-91% of the theoretical yield) by performing various solar-energy-driven fermentation reactions indicating the atom efficiency of the process. The ethanol produced from this process was demonstrated as a potential fuel for DEFCs with current and power density values as high as 700 mA/cm^2 and 330 mW/cm^2. This economically-feasible and environment-friendly process was also demonstrated for the production of a value-added chemical 1,3-PDO. Future studies should focus on combining

the existing fermentation methods and techniques with the proposed innovative solar-energy-driven method for green, cost-effective, and industrially-appealing biomass conversion into chemicals and biofuels.

Acknowledgments

The authors acknowledge financial support from the Israel Science Foundation (ISF, Grant No. 598/12) and the Ministry of Science, Technology, and Space of Israel (Grant Nos. 3-9802 and 3-99763). The authors thank Mr. Menachem Schneeberg, head of mechanical workshop at Bar-Ilan University, for fabricating the solar reactor. The authors are also grateful to Dr. Hugo Gottlieb, head of the NMR unit at Bar-Ilan University, for fruitful discussions on NMR analysis and Dr. Alexander Varvak, head of the HPLC unit at Bar-Ilan University, for his collaboration in the calibration and operation of the HPLC.

REFERENCES

[1] Pulidindi, I. N.; Gedanken, A. Employing Novel Techniques (Microwave and Sonochemistry) in the Synthesis of Biodiesel and Bioethanol. In *Production of Biofuels and Chemicals with Ultrasound*; Fang, Z., Smith, Jr. R. L., Qi, X., Eds.; The Biofuels and Biorefineries Series Volume 4; Springer: Dordrecht, 2015; pp 159-185.

[2] Climent, M. J.; Corma, A.; Iborra, S. Conversion of biomass platform molecules into fuel additives and liquid hydrocarbon fuels. *Green Chem.* [Online] 2014, ***16***, 516-547.

[3] Zhang, W.; Lin, Y.; Zhang, Q.; Wang, X.; Wu, D.; Kong, H. Optimisation of simultaneous saccharification and fermentation of wheat straw for ethanol production. *Fuel* [Online] 2013, *112*, 331-337.

[4] Hayes, D. J.; Fitzpatrick, S.; Hayes, M. H. B.; Ross, J. R. H. The Biofine Process-Production of Levulinic Acid, Furfural, and Formic Acid from Lignocellulosic Feedstocks. In *Biorefineries-Industrial Processes and Products: Status Quo and Future Directions*; Kamm, B., Gruber, P. R., Kamm, M., Eds.; Volume 1; WILEY-VCH Verlag GmbH: Weinheim, 2005; pp 139-164.

[5] Su, H.; Xu, G.; Chen, H.; Xu, Y. Enriching duckweed as an energy crop for producing biobutanol using enzyme hydrolysis pretreatments and

strengthening fermentation process using pH-stat. *ACS Sustainable Chem. Eng.* [Online] 2015, *3*, 2002-2011.

[6] Antolini, E. Catalysts for direct ethanol fuel cells. *J. Power Sources* [Online] 2007, *170*, 1-12.

[7] Petrucci, R. H.; Herring, F. G.; Madura, J. D.; Bissonnette, C. General Chemistry: Principles and Modern Applications, 10th ed.; Pearson Canada Inc.: Toronto, Ontario, 2011, pp 275-280.

[8] Tewfik, S. R.; El Defrawy, N. M.; Sorour, M. H. Liquid fuel resources and prospects for ligno-cellulosic ethanol: An Egyptian case study. *Egypt J. Pet.* [Online] 2013, *22*, 269-276.

[9] Victor, A.; Pulidindi, I. N.; Kim, T. H.; Gedanken, A. Design of a selective solid acid catalyst for the optimization of glucose production from *Oryza sativa* straw. *RSC Adv.* [Online] 2016, *6*, 31-38.

[10] Avami, A. Assessment of optimal biofuel supply chain planning in Iran: Technical, economic, and agricultural perspectives. *Renewable Sustainable Energy Rev.* [Online] 2013, *26*, 761-768.

[11] Zhang, Y. H. P. What is vital (and not vital) to advance economically-competitive biofuels production. *Process Biochem.* [Online] 2011, *46*, 2091-2110.

[12] Anderson, J. E.; DiCicco, D. M.; Ginder, J. M.; Kramer, U.; Leone, T. G.; Raney-Pablo, H. E.; Wallington, T. J. High octane number ethanol-gasoline blends: Quantifying the potential benefits in the United States. *Fuel* [Online] 2012, *97*, 585-594.

[13] Hasunuma, T.; Kondo, A. Development of yeast cell factories for consolidated bioprocessing of lignocellulose to bioethanol through cell surface engineering. *Biotechnol. Adv.* [Online] 2012, *30*, 1207-1218.

[14] Nikolic, S.; Mojovic, L.; Rakin, M.; Pejin, D.; Pejin, J. Ultrasound-assisted production of bioethanol by simultaneous saccharification and fermentation of corn meal. *Food Chem.* [Online] 2010, *122*, 216-222.

[15] Subhedar, P.; Gogate, P. R. Intensification of Enzymatic Hydrolysis of Lignocellulose Using Ultrasound for Efficient Bioethanol Production: A review. *Ind. Eng. Chem. Res.* [Online] 2013, *52*, 11816-11828.

[16] Crews, T. E.; Peoples, M. B. Legume versus fertilizer sources of nitrogen: ecological tradeoffs and human needs. *Agric., Ecosyst. Environ.* [Online] 2004, *102*, 279-297.

[17] Mehta, P. Science behind Acid Rain: Analysis of Its Impacts and Advantages on Life and Heritage Structures. *South Asian J. Tourism Herit.* [Online] 2010, *3*, 123-132.

[18] Talebnia, F.; Karakashev, D.; Angelidaki, I. Production of bioethanol from wheat straw: An overview on pretreatment, hydrolysis and fermentation. *Bioresour. Technol.* [Online] 2010, *101*, 4744-4753.

[19] Farida, I.; Syamsu, K.; Rahayuningsih, M. Direct Ethanol Production from Breadfruit Starch (*Artocarpus communis* Forst.) by Engineered Simultaneous Saccharification and Fermentation (ESSF) using Microbes Consortium. *Int. J. Renewable Energy Dev.* [Online] 2015, *4*, 25-31.

[20] Elshahed, M. S. Microbiological aspects of biofuel production: current status and future directions. *J. Adv. Res.* [Online] 2010, 1, 103-111.

[21] Goncalves, F. A.; Ruiz, H. A.; Nogueira, C. C.; Santos, E. S.; Teixeira, J. A.; Macedo, G. R. Comparison of delignified coconuts waste and cactus for fuel-ethanol production by the simultaneous and semi-simultaneous saccharification and fermentation strategies. *Fuel* [Online] 2014, *131*, 66-76.

[22] Bideaux, C.; Alfenore, S.; Cameleyre, X.; Molina-Jouve, C.; Uribelarrea; J. L.; Guillouet, S. E. Minimization of glycerol production during the high-performance fed-batch ethanolic fermentation process in *Saccharomyces cerevisiae*, using a metabolic model as a prediction tool. *Appl. Environ. Microbiol.* [Online] 2006, *72*, 2134-2140.

[23] Pagliardini, J.; Hubmann, G.; Alfenore, S.; Nevoigt, E.; Bideaux, C.; Guillouet, S. E. The metabolic costs of improving ethanol yield by reducing glycerol formation capacity under anaerobic conditions in *Saccharomyces cerevisiae*. *Microb. Cell Fact.* [Online] 2013, *12*, 1-14.

[24] Pandey, A. Solid-state fermentation. *Biochem. Eng. J.* [Online] 2003, *13*, 81-84.

[25] Galaction, A. I.; Lupasteanu, A. M.; Cascaval, D. Kinetic studies on alcoholic fermentation under substrate inhibition conditions using a bioreactor with stirred bed of immobilized yeast cells. *Open Syst. Biol. J.* [Online] 2010, *3*, 9-20.

[26] Takamitsu, I.; Izumida, H.; Akagi, Y.; Sakamoto, M. Continuous ethanol fermentation in molasses medium using *Zymomonas mobilis* immobilized in photo-crosslinkable resin gels. *J. Ferment. Bioeng.* [Online] 1993, *75*, 32-35.

[27] Najafpour, G.; Younsei, H.; Syahidah, K.; Ismail, K. Ethanol fermentation in an immobilized cell reactor using *Saccharomyces cerevisiae*. *Biores. Technol.* [Online] 2004, 92, 251-260.

[28] Staniszewski, M.; Kujawski, W.; Lewandowska, M. Semi-continuous ethanol production in bioreactor from whey with co-immobilized enzyme and yeast cells followed by pervaporative recovery of product -

kinetic model predictions considering glucose repression. *J. Food Eng.* [Online] 2009, *91*, 240-249.

[29] Luong, J. H. T. Cell immobilization in kappa- carrageenan for ethanol production. *Bioetechnol. Bioeng.* [Online] 1985, *27*, 1652-1661.

[30] Francesca, G.; Magherini, F.; Gamberi, T.; Borro, M.; Simmaco, M.; Modesti, A. Effect of different glucose concentrations on proteome of *Saccharomyces cerevisiae. Biochim. Biophys. Acta, Proteins Proteomics* [Online] 2010, *1804*, 1516-1525.

[31] Akinori, M.; Hiroyuki, I.; Tsutomu, K.; Shigeki, S. Ethanol production from xylose in engineered *Saccharomyces cerevisiae* strains: current state and perspectives. *Appl. Microbiol. Biotechnol.* [Online] 2009, *84*, 37-53.

[32] Luong, J. H. T. Kinetics of ethanol inhibition in alcohol fermentation. *Biotechnol. Bioeng.*[Online] 1985, *27*, 280-285.

[33] Luong, J. H. T. Generalization of monod kinetics for analysis of growth data with substrate inhibition. *Biotechnol. Bioeng.* [Online] 1987, 29, 242-248.

[34] Tabah, B.; Pulidindi, I. N.; Gedanken, A. Study on Fermentation Kinetics for Accelerated Production of Bioethanol from Glucose, Sucrose and Molasses. *J. Bioprocess. Biotech.* [Online] 2015, *5*, 232.

[35] Victor, A.; Pulidindi, I. N.; Gedanken, A. Assessment of holocellulose for the production of bioethanol by conserving *Pinus radiata* cones as renewable feedstock. *J. Environ. Manage.* [Online] 2015, *162*, 215-220.

[36] Whitmarsh, J.; Govindjee. The photosynthetic process. In *Concepts in Photobiology: Photosynthesis and Photomorphogenesis*; Singhal, G. S., Renger, G., Sopory, S. K., Irrgang, K-D., Govindjee, Eds.; Narosa Publishers: New Delhi and Kluwer Academic: Dordrecht, 1999; pp 11-51.

[37] LAMEDH Energy. Solar irradiance - central Israel outlook 2015. http://www.lnrg.technology/2016/02/28/solar-irradiance-central-israel-outlook-2015/ (accessed March, 15, 2016).

[38] Tabah, B.; Pulidindi, I. N.; Chitturi, V. R.; Arava, L. M. R., Gedanken, A. Simultaneous Saccharification and Fermentation of Starch to Bioethanol for Fuel-Cell Applications. *ChemSusChem* [Online] 2015, *8*, 3497-3503.

[39] Tabah, B.; Pulidindi, I. N.; Chitturi, V. R.; Arava, L. M. R.; Gedanken, A. Utilization of solar energy for continuous bioethanol production for energy applications. *RSC Adv.* [Online] 2016, *6*, 24203-24209.

[40] Vielstitch, W. *Fuel cells: Modern Process for the Electrochemical Production of Energy*; 1st ed.; Wiley-Interscience: London, 1965.

[41] Kordesch, K.; Simader, G. *Fuel cells and Their Applications,* 1st ed.; VCH Verlag GmbH: Weinheim, 1996.

[42] Winter, M.; Brodd, R. J. What are batteries, fuel cells, and supercapacitors? *Chem. Rev*. [Online] 2004, *104*, 4245-4269.

[43] Viswanathan, B.; Chitturi,V. R.; Varadaraju, U. V. On the search for non-noble metal based electrodes for oxygen reduction reaction. *Photo/Electrochem. Photobiol. Environ., Energy Fuel*[Online] 2006, 43-101.

[44] Li, J. Q.; Fang, C.; Xu, L. F. Current status and trends of the research and development for fuel cell vehicles**.** *J. Automot. Saf. Energy* [Online] 2014, *5*, 17-29.

[45] U.S. DRIVE Partnership/Fuel Cell Technical Team. *Fuel Cell Technical Team Roadmap*; U.S. Department of Energy/Office of Energy Efficiency & Renewable Energy: Washington, DC, June 2013.

[46] *Naik, S. N.; Goud, V. V.; Rout, P. K.; Dalai, A. K. Production of first and second generation biofuels: A comprehensive review.* Renewable Sustainable Energy Rev. *[Online] 2010,* 14*, 578-597.*

[47] Song, S. Q.; Tsiakaras P. Recent progress in direct ethanol proton exchange membrane fuel cells. *Appl Catal. B: Environ*. [Online] 2006, *63*, 187-193.

[48] Kamarudin, M. Z. F.; Kamarudin, S. K.; Masdar, M. S.; Daud, W. R. W. Direct ethanol fuel cells. *Int. J. Hydrogen Energy* [Online] 2013, *38,* 9438-9453.

[49] An, L.; Zhao, T. S.; Li, Y. S. Carbon-neutral sustainable energy technology: Direct ethanol fuel cells. *Renew. Sustainable Energy Rev.* [Online] 2015, *50*, 1462-1468.

[50] Song, S. Q.; Zhou, W. J.; Zhou, Z. H.; Jiang, L. H.; Sun, G. Q.; Xin, Q.; Leonditis, V.; Kontou, S.; Tsiakaras, P. Pt-based catalysts for direct ethanol fuel cells. *Int. J. Hydrogen Energy* [Online] 2005, *30*, 995-1001.

[51] Zhou, W. J.; Li, W. Z.; Song, S. Q.; Zhou, Z. H.; Jiang, L. H.; Sun, G. Q.; Xin, Q.; Poulianitis, K.; Kontou, S.; Tsiakaras P. Bi- and tri-metallic Pt based anode catalysts for direct ethanol fuel cells. *J. Power Sources* [Online] 2004, *131*, 217-223.

[52] Varcoe, J. R.; Slade, R. C. T. Prospects for alkaline anion-exchange membranes in low temperature fuel cells. *Fuel Cells* [Online] 2005, *5*, 187-200.

[53] Brouzgou, A.; Podias, A.; Tsiakaras, P. PEMFCs and AEMFCs directly fed with ethanol: a current status comparative review. *J. Appl. Electrochem.* [Online] 2013, *43*, 119-136.

[54] Chitturi, V. R.; Viswanathan, B. ORR activity and direct ethanol fuel cell performance of carbon-supported Pt-M (M=Fe, Co, and Cr) alloys prepared by polyol reduction method. *J. Phys. Chem. C* [Online] 2009,*113*, 18907-18913.

[55] Chitturi, V. R.; Viswanathan, B. Carbon supported Pd-Co-Mo alloy as an alternative to Pt for oxygen reduction in direct ethanol fuel cells. *Electrochim. Acta* [Online] 2010, *55*, 3002-3007.

[56] Zhao, T. S.; Li, Y. S.; Shen, S. Y. Anion-exchange membrane direct ethanol fuel cells: Status and perspective. *Front. Energy Power Eng. China* [Online] 2010, *4*, 443-458.

[57] Jiang, L. H.; Sun, G. Q.; Sun, S. G.; Liu, J. G.; Tang, S. H.; Li, H. Q.; Zhou, B.; Xin, Q. Structure and chemical composition of supported Pt-Sn electrocatalysts for ethanol oxidation. *Electrochim. Acta* [Online] 2005, *50*, 5384-5389.

[58] An, L.; Zhao, T. S. Performance of an alkaline-acid direct ethanol fuel cell. *Int. J. Hydrogen Energy* [Online] 2011, *36*, 9994-9999.

[59] Lange,N. A., Ed. *Handbook of Chemistry*, 10th ed.; McGraw-Hill: New York, NY, 1967; pp 1522-1524.

[60] Kumar, V. B.; Pulidindi, I. N.; Gedanken, A. Selective conversion of starch to glucose using carbon based solid acid catalyst. *Renewable Energy* [Online] 2015, *78*, 141-145.

[61] Anuradha, R.; Suresh, A. K.; Venkatesh, K. V. Simultaneous saccharification and fermentation of starch to lactic acid. *Process Biochem.* [Online] 1999, *35*, 367-375.

[62] Tabassum, R.; Khaliq, S.; Rajoka, M. I.; Agblevor, F. Solid State Fermentation of a Raw Starch Digesting Alkaline Alpha-Amylase from *Bacillus licheniformis* RT7PE1 and Its Characteristics. *Biotechnol. Res. Int.* [Online] 2014, *2014*, 495384.

[63] Baysal, Z.; Uyar, F.; Dogru, M.; Alkan, H. Production of Extracellular Alkaline α‐Amylase by Solid State Fermentation with a Newly Isolated *Bacillus sp. Prep. Biochem. Biotechnol.* [Online] 2008, *38*, 184-190.

[64] Van der Maarel, M. J. E. C.; Van der Veen, B.; Uitdehaag, J. C. M.; Leemhuis, H.; Dijkhuizen, L. Properties and applications of starch-converting enzymes of the α-amylase family. *J. Biotechnol.* [Online] 2002, *94*, 137-155.

[65] Sivaramakrishnan, S.; Gangadharan, D.; Nampoothiri, K. M.; Soccol, C. R.; Pandey, A. α-Amylases from Microbial Sources-An Overview on Recent Developments. *Food Technol. Biotechnol.* [Online] 2006, *44*, 173-184.

[66] Ballesteros, M.; Oliva, J. M.; Negro, M. J.; Manzanares, P.; Ballesteros, I. Ethanol from lignocellulosic materials by a simultaneous saccharification and fermentation process (SFS) with *Kluyveromyces marxianus* CECT 10875. *Process Biochem.* [Online] 2004, *39*, 1843-1848.

[67] Korzen, L.; Pulidindi, I. N.; Israel, A.; Abelson, A.; Gedanken, A. Single step production of bioethanol from the seaweed *Ulva rigida* using sonication. *RSC Adv.* [Online] 2015, *5*, 16223-16229.

[68] Korzen, L.; Pulidindi, I. N.; Israel, A.; Abelson, A.; Gedanken, A. Marine integrated culture of carbohydrate rich *Ulva rigida* for enhanced production of bioethanol. *RSC Adv.* [Online] 2015, *5*, 59251-59256.

[69] Wyman, C. E.; Hinman, N. D. Ethanol, Fundamentals of production from renewable feedstocks and use as a transportation fuel. *Appl. Biochem. Biotechnol.* [Online] 1990, *24*, 735-753.

[70] Wyman, C. E. Ethanol from lignocellulosic biomass: Technology, economics, and opportunities. *Bioresour. Technol.* [Online] 1994, *50*, 3-15.

[71] Novodarszki, G.; Retfalvi, N.; Dibo, G.; Mizsey, P.; Csefalvay, E.; Mika, T. L. Production of platform molecules from sweet sorghum. *RSC Adv.* [Online] 2014, *4*, 2081-2088.

[72] Chitturi, V. R.; Viswanathan, B. Monodispersed platinum nanoparticle supported carbon electrodes for hydrogen oxidation and oxygen reduction in proton exchange membrane fuel cells. *J. Phys. Chem. C* [Online] 2010, *114*, 8661-8667.

[73] Arava, L. M. R.; Ramaprabhu, S. Pt/SWNT-Pt/C nanocomposite electrocatalysts for proton-exchange membrane fuel cells. *J. Phys. Chem. C* [Online] 2007, *111*, 16138-16146.

[74] Pulidindi I. N.; Gedanken, A.; Schwarz, R.; Sendersky, E. Mild sonication accelerates ethanol production by yeast fermentation. *Energy Fuels* [Online] 2012, *26*, 2352-2356.

[75] Neves, C. M. S. S.; Granjo, J. F. O.; Freire, M. G.; Robertson, A.; Oliveira, N. M. C.; Coutinho, J. A. P. Separation of ethanol-water mixtures by liquid-liquid extraction using phosphonium-based ionic liquids. *Green Chem.* [Online] 2011, *13*, 1517-1526.

[76] Baeyens, J.; Kang, Q.; Appels, L.; Dewil, R.; Lv, Y.; Tan, T. Challenges and opportunities in improving the production of bio-ethanol. *Prog. Energy Combust. Sci.* [Online] 2015, *47*, 60-88.

[77] An, L.; Zhao, T. S. An alkaline direct ethanol fuel cell with a cation exchange membrane. *Energy Environ. Sci.* [Online] 2011, *4*, 2213-2217.

[78] Maiyalagan, T.; Scott, K. Performance of carbon nanofiber supported Pd-Ni catalysts for electro-oxidation of ethanol in alkaline medium. *J. Power Sources* [Online] 2010, *195*, 5246-5251.

[79] Lee, E.; Park, I.-S.; Manthiram, A. Synthesis and characterization of Pt-Sn-Pd/C catalysts for ethanol electro-oxidation reaction, *J. Phys. Chem.* [Online] 2010, *114*, 10634-10640.

[80] Ye, K.; Zhang, D.; Wang, X.; Cheng, K.; Cao, D. A novel three-dimensional gold catalyst prepared by simple pulse electrodeposition and its high electrochemical performance for hydrogen peroxide reduction. *RSC Adv*. [Online] 2015, *5*, 3239-3247.

[81] Gu, L.; Luo, N.; Miley, G. H. Cathode electrocatalyst selection and deposition for a direct borohydride/hydrogen peroxide fuel cell. *J. Power Sources* [Online] 2007, *173*, 77-85.

[82] An, L.; Zhao, T. S.; Chen, R.; Wu, Q. X. A novel direct ethanol fuel cell with high power density. *J. Power Sources* [Online] 2011, *196*, 6219-6222.

[83] An, L.; Zhao, T. S.; Xu, J. B. A bi-functional cathode structure for alkaline-acid direct ethanol fuel cells. *Int. J. Hydrogen Energy* [Online] 2011, *36*, 13089-13095.

[84] An, L.; Zhao, T. S.; Zeng, L.; Yan, X. H. Performance of an alkaline direct ethanol fuel cell with hydrogen peroxide as oxidant. *Int. J. Hydrogen Energy* [Online] 2014, *39*, 2320-2324.

[85] Priya, S. S.; Kumar, V. P.; Kantam, M. L.; Bhargava, S. K.; Chary, K. V. R. Catalytic performance of $Pt/AlPO_4$ catalysts for selective hydrogenolysis of glycerol to 1,3-propanediol in the vapour phase. *RSC Adv.* [Online] 2014, *4*, 51893-51903.

[86] Kaur, G.; Srivastava, A. K.; Chand, S. Advances in biotechnological production of 1,3-propanediol. *Biochem. Eng. J.* [Online] 2012, *64*, 106-118.

[87] Lee, C. S.; Aroua, M. K.; Daud, W. M. A. W.; Cognet, P.; Pérès-Lucchese, Y.; Fabre, P-L.; Reynes, O.; Latapie, L. A review: Conversion of bioglycerol into 1,3-propanediol via biological and chemical method.*Renew. Sust. Energ. Rev.* [Online] 2015, *42*, 963-972.

[88] Grahame, D. A. S.; Kang, T. S.; Khan, N. H.; Tanaka, T. Alkaline conditions stimulate the production of 1, 3-propanediol in *Lactobacillus panis* PM1 through shifting metabolic pathways. *World J. Microb. Biot.* [Online] 2013, *29*, 1207-1215.

[89] Leoneti, A. B.; Aragao-Leoneti, V.; De Oliveira, S. V. W. B. Glycerol as a by-product of biodiesel production in Brazil: Alternatives for the use of unrefined glycerol *Renew. Energ*. [Online] 2012, *45*, 138-145.

[90] Yazdani, S. S.; Gonzalez, R. Anaerobic fermentation of glycerol: a path to economic viability for the biofuels industry. *Curr. Opin. Biotech.* [Online] 2007, *18*, 213-219.

[91] Murarka, A.; Dharmadi, Y.; Yazdani, S. S.; Gonzalez, R. Fermentative Utilization of Glycerol by *Escherichia coli* and Its Implications for the Production of Fuels and Chemicals. *Appl. Environ. Microbiol.* [Online] 2008, *74*, 1124-1135.

[92] Clomburg, J. M.; Gonzalez, R. Anaerobic fermentation of glycerol: a platform for renewable fuels and chemicals. *Trends Biotechnol.* [Online] 2013, *31*, 20-28.

[93] Jun, S-A.; Moon, C.; Kang, C-H.; Kong, S. W.; Sang, B-I.; Um, Y. Microbial Fed-batch Production of 1,3-propanediol Using Raw Glycerol with Suspended and Immobilized *Klebsiella pneumoniae*. *Appl. Biochem. Biotechnol.* [Online] 2010, *161*, 491-501.

[94] Dobson, R.; Gray, V.; Rumbold, K. Microbial utilization of crude glycerol for the production of value-added products. *J. Ind. Microbiol. Biot.* [Online] 2012, *39*, 217-226.

[95] Fang, Z., Smith, Jr. R. L., Qi, X., Eds. *Production of Biofuels and Chemicals with Ultrasound*; The Biofuels and Biorefineries Series Volume 4; Springer: Dordrecht, 2015.

[96] Varisli, D.; Dogu, T.; Dogu, G. Ethylene and diethyl-ether production by dehydration reaction of ethanol over different heteropolyacid catalysts. *Chem. Eng. Sci.* [Online] 2007, *62*, 5349-5352.

[97] Kito-Borsa, T.; Pacas, D. A.; Selim, S.; Cowley, S.W. Properties of an ethanol diethyl ether water fuel mixture for cold start assistance of an ethanol-fueled vehicle. *Ind. Eng. Chem. Res.* [Online] 1998, *37*, 3366-3374.

[98] Pereira, C. J. New avenues in ethylene synthesis. *Science* [Online] 1999, *285*, 670-671.

[99] Gucbilmez, Y.; Dogu, T.; Balci, S. Ethylene and acetalehyde production by selective oxidation of ethanol using mesoporous V-MCM-41 catalysts. *Ind. Eng. Chem. Res.*[Online] 2006, *45*, 3496-3502.

[100] Vazquez, P.; Pizzio, L.; Caceres, C.; Blanco, M.; Thomas, H.; Alesso, E.; Finkielsztein, L.; Lantano, B.; Moltrasio, G.; Aguirre, J. Silica supported heteropolyacids as catalysts in alcohol dehydration reactions. *J. Mol. Catal.* [Online] 2000, *161*, 223-232.

[101] Haber, J.; Pamin, K.; Matachowski, L.; Napruszewska, B.; Poltowicz, J. Potassium and silver salts of tungstophosphoric acid as catalysts in dehydration of ethanol and hydration of ethylene. *J. Catal.* [Online] 2002, *207*, 296-306.

Reviewed by:

Prof. John H. T. Luong

Innovative Chromatography Group, Irish Separation Science Cluster (ISSC), Department of Chemistry and Analytical, Biological Chemistry Research Facility (ABCRF) University College Cork, Ireland.

E-mail address: j.luong@ucc.ie

BIOGRAPHICAL SKETCHES

Betina Tabah

Affiliation: Bar-Ilan University

Education: Betina Tabah received her B.Sc. in Biological Sciences and Bioengineering with minor honors in Chemistry from Sabanci University, Turkey (2009) and M.Sc. in Biotechnology from Ben-Gurion University of the Negev, Israel (2012). She is currently a Ph.D. candidate in Department of Chemistry and Institute for Nanotechnology and Advanced Materials at Bar-Ilan University, Israel.

Address: Department of Chemistry, Bar-Ilan University, Ramat-Gan, Israel 5290002.

Professional Appointments:

Ph.D. candidate under the supervision of Prof. Aharon Gedanken in Department of Chemistry and Institute for Nanotechnology and Advanced Materials at Bar-Ilan University.

Research and Professional Experience:

Betina's Ph.D. thesis focuses on novel methods for the conversion of biomass to bioethanol. She is passionate about finding green solutions to global problems. Her research interests include potential alternative energy sources, biofuels and renewable energy studies, utilizing different biomass for energy applications, developing biofuel production systems and up-scaling to industrial applications, and conversion of wastes and plant residues into value-added products.

Honors:

Betina was selected as a 2014 Rieger-JNF Fellow and 2015 Marshall Tulin Fellow in Environmental Studies by Rieger Foundation, USA. She has received many awards including Jewish National Fund-Keren Kayemeth LeIsrael prize for excellence in research (2011), The Robert Equey prize for excellence in desert studies (2011), Selim and Rachel Benin award of merit (2013), David Brekovsky award for academic excellence (2014), Turkish Union in Israel award of merit (2014), The Salti Foundation award of merit (2015), and Cyd Hessner prize for academic excellence and contribution to the community through volunteer work (2015). Her recent manuscript published in ChemSusChem was selected as a Key Scientific Article by Renewable Energy Global Innovations (Canada) for contributing to the excellence in energy research (2016).Her poster presentation entitled "Solar-energy driven

solid-state fermentation for continuous flow bioethanol production" has won the "Best Poster Award" at NanoIsrael 2016 conference.

Publications Last Three Years:

[1] Tabah, B., Varvak, A,Pulidindi, I. N., Foran, E., Banin, E., Gedanken, A. (2016) Production of 1,3-propanediol from glycerol via fermentation by *Saccharomyces cerevisiae*.*Green Chem.*(in press).

[2] Piker, A., Tabah, B., Perkas, N., Gedanken, A. (2016) A green and low-cost room temperature biodiesel production method from waste oil using egg shells as catalyst. *Fuel* (in press).

[3] Tabah, B., Pulidindi, I. N., Chitturi, V. R., Arava, L. M. R., Gedanken, A. (2016) Utilization of solar energy for continuous bioethanol production for energy applications. *RSC Adv.*, **6**, 24203-24209.

[4] Tabah, B., Pulidindi, I. N., Chitturi, V. R., Arava, L. M. R., Gedanken, A. (2015) Solar-energy driven simultaneous saccharification and fermentation (SSF) of starch to bioethanol for fuel cell applications. *ChemSusChem*, **8**, 3497-3503.

[5] Tabah, B**.**, Pulidindi, I. N., Gedanken, A. (2015) A study on fermentation kinetics for accelerated production of bioethanol from glucose, sucrose, and molasses. *Journal of Bioprocessing and Biotechniques*, **5**: 232.

Dr. Indra Neel Pulidindi

Affiliation: Bar-Ilan University

Education: Dr. Neel received his primary and secondary education from APPMills Model High School, Rajahmundry, India from 1985 to 1995. He received his M.Sc. from Andhra University, India in 2002. He received his Ph.D. from IIT Madras, India in 2010 with the doctoral thesis entitled "Development and exploitation of carbon materials from plant sources."
Address: Department of Chemistry, Bar-Ilan University, Ramat-Gan, Israel 5290002.

Professional Appointments:

Postdoctoral researcher under the supervision of Prof. Aharon Gedanken in Department of Chemistry, Bar-Ilan University, Israel since 2010.

Research and Professional Experience:

Dr. Pulidindi's research interests include nuclear chemistry, catalysis, electro chemistry, materials science, renewable energy, and biofuels. He has published 28peer-reviewed manuscripts and has applied for 4 patents. He has an h-index of 9and i10-index of 8with 289citations. He is passionate about identifying solutions for societal problems such as energy crisis or environmental pollution by means of utilizing natural resources such as solar energy, CO_2, and biomass. Energy crisis and environmental deterioration are the two major problems human society is currently facing. His research focuses on developing alternate renewable energy sources. Towards realization of this goal, it is imperative that one should utilize the solar energy which is abundantly available and also devise strategies to utilize CO_2 as an organic raw material for the production of fuels and chemicals. Dr. Pulidindi is currently working exclusively on the conversion of both terrestrial lignocellulosic and algal biomass to biofuels and biochemicals using solar energy for fuels production and lignin valorization. Mankind need to learn and mimic nature for sustainability and wellbeing; therefore, he focuses on understanding and mimicking nature by utilizing natural resources and trying to solve societal problems.

Honors:

Editorial board member of Journal of Catalyst and Catalysis, Editorial board member of Emerging trends in Chemical Engineering, Prof. M. N. Sastry Shastaibdpoorthi Celebration Gold Medal (2002, for 1st ranking in M. Sc., 2ndyear), Prof. B. S. V. Raghava Rao Memorial Prize (2001, for 1stranking in M. Sc., 1styear), Prof. R. Sambasiva Rao Prize (2001, for 1st ranking in M. Sc.,

1st year), Gold medalist (Best outgoing student in Xstd, 1995, APPMills Model High School, Rajahmundry).

Publications Last Three Years:

[1] Betina Tabah, Alexander Varvak, Indra Neel Pulidindi, Elizabeth Foran, Ehud Banin, Aharon Gedanken (2016) Production of 1,3-propanediol from glycerol via fermentation by *Saccharomyces cerevisiae, Green Chem*. (in press).

[2] Alex Tangy, Indra Neel Pulidindi, Aharon Gedanken (2016) SiO_2 beads decorated with SrO nanoparticles for biodiesel production from waste cooking oil using microwave irradiation, *Energy and Fuels*, 30 (4), 3151-3160.

[3] Miri Klein, Ofir Griess, Indra Neel Pulidindi, Nina Perkas, Aharon Gedanken (2016) Bioethanol production from *Ficus religiosa* leaves, *Journal of Environmental Management*, 177, 20-25.

[4] Vijay Bhooshan Kumar, Indra Neel Pulidindi, Aharon Gedanken (2016) Glucose production from potato peel waste under microwave irradiation, *J Mol Catal A Chem*, 417, 163-167.

[5] Betina Tabah, Indra Neel Pulidindi, Venkateswara Rao Chitturi, Leela Mohana Reddy Arava, Aharon Gedanken (2016) Utilization of solar energy for continuous production of bioethanol for energy applications, *RSC Adv.*, 6, 24203-24209.

[6] Vijay Bhooshan Kumar, Indra Neel Pulidindi, Yael Kinel, Yaron Yehoshuva, Aharon Gedanken (2016) Evaluation of the potential of *Chlorella vulgaris* for bioethanol production, *Energy and Fuels*, 30, 3161-3166.

[7] Rahul Kumar Mishra, Indra Neel Pulidindi, Eihab Kaba, and Aharon Gedanken (2016), *In situ* formation of carbon dots aid ampicillin sensing. *Analytical Methods*, 8, 2441-2447.

[8] Amudhavalli Victor, Indra Neel Pulidindi, Tae Hyun Kim, Aharon Gedanken (2016) Design of active solid acid catalyst for the optimization of glucose production from Oryza Sativa straw, *RSC Adv*, 6, 31-38.

[9] Indra Neel Pulidindi, Aharon Gedanken (2015) Employing novel techniques (microwave and sonochemitry) in the synthesis of biodiesel and bioethanol, Chapter 6, p. 159-188, in Springer Book Series - Production of Biofuels and Chemicals: Ultrasound, Editors: Zhen

Fang,Liang-shih Fan,John R. Grace, Yonghao Ni, Norman R. Scott, Richard L. Smith, Jr.

[10] Betina Tabah, Indra Neel Pulidindi, Venkateswara Rao Chitturi, Leela Mohana Reddy Arava, Aharon Gedanken (2015) Solar Energy Driven Simultaneous Saccharification and Fermentation (SSF) of Starch to Bioethanol for Fuel Cell Applications, *ChemSusChem*, 8, 3497-3503.

[11] Amudhavalli Victor, Indra Neel Pulidindi, Aharon Gedanken (2015) Assessment of Holocellulose for the production of Bioethanol by conserving Pinus radiata cones as renewable feedstock, *Journal of Environmental management*, 162, 215-220.

[12] Leor Korzen, Indra Neel Pulidindi, Alvaro Israel, Avigdor Abelson, Aharon Gedanken (2015) Marine integrated culture of carbohydrate rich Ulva rigida for enhanced production of bioethanol, *RSC Adv* 5, 59251-59256.

[13] Betina Tabah, Indra Neel Pulidindi, Aharon Gedanken (2015) A study on fermentation kinetics for accelerated production of bioethanol from glucose, sucrose, and molasses, *Journal of Bioprocessing and Biotechniques*, 5: 232 doi:10.4172/2155-9821.1000232.

[14] Vijay Bhooshan Kumar, Indra Neel Pulidindi, Aharon Gedanken (2015), Synergistic catalytic effect of ZnBr2-HCl system for levulinic acid production, *RSC Advances*, 5, 11043-11048.

[15] Vijay Bhooshan Kumar, Indra Neel Pulidindi, Aharon Gedanken (2015) Heteropoly acid supported on Carbon catalyzed conversion of Starch exclusively to glucose,*Renewable Energy*, 78, 141-145.

[16] Miri Klein, Alexander Varvak, Elad Segal, Boris Markovsky, Indra Neel Pulidindi, Nina Perkas, Aharon Gedanken (2015)Sonochemical synthesis of HSiW/graphene catalysts for enhanced biomass hydrolysis, *Green Chem*., 17, 2418-2425.

[17] Leor Korzen, Indra Neel Pulidindi, Alvaro Israel, Avigdor Abelson, Aharon Gedanken (2015) Single Step Production of Bioethanol from the Seaweed *Ulva rigida* using Sonication, *RSC Advances*, 5, 16223-16229.

[18] Miri Klein, Indra Neel Pulidindi, Nina Perkas, Aharon Gedanken (2015) Heteropoly acid catalyzed hydrolysis of glycogen to glucose, *Biomass Bioenergy*, 76, 61-68.

[19] Indra Neel Pulidindi, R. H. Mariana, M. Patricia, A. Gedanken (2014) Isosaccharinic Acid Mediated Fine Chemicals Production from Cellulose, *Journal of Fundamentals of Renewable Energy and Applications*, 4 (2), 143; doi: 10.4172/2090-4541.1000143.

[20] Amudhavalli Victor, Indra Neel Pulidindi, Aharon Gedanken (2014) Levulinic acid production from Cicer arietinum, Cotton, Pinus radiata and Sugar cane bagasse, *RSC Advances*, 4, 44706-44711.
[21] Oshrat Tzhayik, Indra Neel Pulidindi, Aharon Gedanken (2014) Forming Nano Spherical Cellulose Containers, *Industrial & Engineering Chemistry Research*, 53, 13871-13880.
[22] Indra Neel Pulidindi, Baruchi B Kimchi, Aharon Gedanken (2014) Selective chemical reduction of carbon dioxide to formate using microwave irradiation, *Journal of CO_2 utilization*, 7, 19-22.
[23] Indra Neel Pulidindi, Baruchi B Kimchi, Aharon Gedanken (2014) Can Cellulose be a sustainable feedstock for Bioethanol production? *Renewable energy*, 71, 77-80.
[24] Indra Neel Pulidindi, Aharon Gedanken (2014) Carbon Nanoparticles based Glucose Sensor, *International Journal of Analytical Environmental Chemistry*, 94 (1), 28-35.

Venkateswara Rao Chitturi

Affiliation: Nova-Kem LLC, US.

Education: Dr. Chitturi received his Ph.D. from Indian Institute of Technology Madras, India in 2008 and conducted post-doctoral research at Southern University, University of Puerto Rico, and Wayne State University, US.

Address: Nova-Kem LLC, Germantown, WI 53022, US.

Professional Appointments:

Dr. Chitturi is currently a Scientist at Nova-Kem LLC, US.

Research and Professional Experience:

Dr. Chitturi's research experiences include work with nanostructured materials, metal complexes, fuel cells, rechargeable lithium batteries, and molecular modeling. He has published 40 peer-reviewed articles in international journals, 1 book chapter, 3 e-book chapters and delivered more than 20 seminars and invited talks in academia and industry. His research has been cited more than 1000 times and has h-index of 16 and i10-index of 20.

Publications Last Three Years:

[1] N. Mosavati, Ch. Venkateswara Rao, Steven O. Salley and K.Y. Simon Ng. Nanostructured Titanium Nitride as a Novel Cathode for High Performance Lithium/Dissolved Polysulfide Batteries. *J. Power Sources* 2016 (accepted).

[2] B. Tabah, Indra Neel Pulidindi, Ch. Venkateswara Rao, L. M. R. Arava and A. Gedanken. Utilization of Solar Energy for Continuous Bioethanol Production for Energy Applications. *RSCAdv.* 2016, 6, 24203-24209.

[3] H. Al Salem, G. Babu, Ch. Venkateswara Rao and L. M. R. Arava. Electrocatalytic Polysulfide Traps for Controlling Redox Shuttle Process of Li–S Batteries. *J. Am. Chem. Soc.*2015,137, 11542–11545.

[4] B. Tabah, Indra Neel Pulidindi, Ch. Venkateswara Rao, L. M. R. Arava and A. Gedanken. Solar Energy Driven Simultaneous Saccharification and Fermentation (SSF) of Starch to Bioethanol for Fuel Cell Applications. *ChemSusChem*2015, 8, 3497-3503.

[5] N. Mosavati, Ch. Venkateswara Rao, L. M. R. Arava, Steven O. Salley and K.Y. Simon Ng. Effects of Nickel Particle Size and Graphene Support on the Electrochemical Performance of Lithium/Dissolved Polysulfide Batteries. *Electrochim. Acta*2015, 185, 297-303.

[6] Mahbuba Ara, Ch. Venkateswara Rao, Steven O. Salley and K.Y. Simon Ng. Nitrogen-doped Carbon-coated Sn_xO_y (x=1 and y=0 and 2) Nanoparticles for Rechargeable Li-Ion Batteries. *Electrochim. Acta*2015, 161, 269-278.

[7] Ch. Venkateswara Rao, K. Muthukumar, L. Hima Kumar and B. Viswanathan, Development of Cobalt based Non-precious Electrocatalyst for Oxygen Reduction Reaction. *Adv. Chem. Lett.*2015, 2, 9-15. (Invited article).

[8] Radhe Agarwal, S. Sahoo, Ch. Venkateswara Rao, J. D. Williams, O. Resto and R. S. Katiyar. Enhanced Photovoltaic Properties in Graphitic Carbon Nanospheres Networked TiO_2Nanocomposite Based Dye Sensitized Solar Cell. *J. Alloys Compd.*2015, 641, 99–105.

[9] Radhe Agarwal, S. Sahoo, Ch. Venkateswara Rao and R. S. Katiyar. Graphitic carbon nanospheres: A Raman Spectroscopic Investigation of Thermal Conductivity and Morphological Evolution by Pulsed Laser Irradiation. *J. Appl. Phys.*2015, 118, 214301-1–6.

[10] Jifi Shojan, Ch. Venkateswara Rao, Jesse Soler, William C. West and R. S. Katiyar. High Energy $x$$Li_2MnO_3$–(1−$x$)$LiNi_{2/3}Co_{1/6}Mn_{1/6}O_2$ Composite Cathode for Advanced Li-ion Batteries. *J. Power Sources* 2015, 274, 440-450.

[11] S. Sahoo, Ch. Venkateswara Rao, Radhe Agarwal, J. -W. Jiang, and R. S. Katiyar, Thermal Conductivity of Free-standing Single Wall Carbon Nanotube Sheet by Raman Spectroscopy.*ACS Appl. Mater. Interfaces* 2014, 6, 19958-19963.

[12] Ch. Venkateswara Rao, Rajesh Katiyar, Jifi Shojan, Jesse Soler, William C. West and R. S. Katiyar, Investigations on Electrochemical Behavior and Structural Stability of $Li_{1.2}Mn_{0.54}Ni_{0.13}Co_{0.13}O_2$Lithium-Ion Cathodes via in-Situ and ex-Situ Raman Spectroscopy. *J. Phys. Chem. C*2014, 118, 14133-14141.

[13] Dmitry Skachkov, Ch. Venkateswara Rao and Y. Ishikawa, A Combined First-Principles Molecular Dynamics/Density-Functional Theory Study of Ammonia Electrooxidation on Pt(100) Electrode. *J. Phys. Chem. C*2013, 117, 25451-25466.

[14] L. Hima Kumar, Ch. Venkateswara Rao and B. Viswanathan, Catalytic Effect of Nitrogen Containing Graphene and Carbon Nanotubes additives on Hydrogen Storage Properties of Sodium Alanate. *J. Mater. Chem. A*2013, 1, 3355-3361.

[15] Jifi Shojan, Ch. Venkateswara Rao, Loraine Torres, Gurpreet Singh and R. S. Katiyar, Lithium-ion Battery Performance of Layered $0.3Li_2MnO_3$-$0.7LiNi_{0.5}Mn_{0.5}O_2$ Composite Cathode Prepared by Co-precipitation and Sol-gel Methods. *Mater. Lett.* 2013, 104, 57-60.

[16] L. Cunci, Ch. Venkateswara Rao, Carlos Velez, Yasuyuki Ishikawa and C.R. Cabrera, Graphene-Supported Pt, Ir, and Pt-Ir Nanoparticles as

Electrocatalysts for the Oxidation of Ammonia. *Electrocatalysis* 2013, 4, 61-69.

Leela MohanaReddy Arava

Affiliation: Wayne State University.

Education: Dr. Arava received his Ph.D (2007) in Physics from Indian Institute of Technology Madras. He conducted his post-doctoral research at University of Pittsburgh and Rice University, US. He then spent a year as a research scientist at Rice University.

Address: Department of Mechanical Engineering, Wayne State University, Detroit, MI 48202, US.

Professional Appointments:

Asst. Prof.

Research and Professional Experience:

In 2013, Dr. Arava joined Wayne State University as an Assistant Professor of Mechanical Engineering. His research group is interested in fundamental electrochemical principles underlying in energy systems such as batteries,

supercapacitors, and fuel cells. His group is focused on designing variety of nanomaterials and understanding their transport phenomena, electrode kinetics, electrocatalytic activity, and thermal and electrochemical stabilities under extreme environments. His diverse activities in terms of applications include developing high energy and safe batteries for electric vehicles, micro-batteries to power micro-sensors, and flexible hybrid energy devices for wearable assistive technologies. Dr. Arava has published 65 peer-reviewed papers in international journals, 2 book chapters, 8 patents and delivered more than 35 invited talks and seminars in academia and industry. His research has been cited more than 4600 times and has h-index of 32 and i10-index of 44.

Publications Last Three Years:

[1] MTF Rodrigues, K Kalaga, H Gullapalli, G Babu, ALM Reddy, PM Ajayan, Hexagonal Boron Nitride-Based Electrolyte Composite for Li-Ion Battery Operation from Room Temperature to 150°C. *Advanced Energy Materials* 2016 (in press).

[2] B Tabah, IN Pulidindi, VR Chitturi, LMR Arava, A Gedanken, Utilization of solar energy for continuous bioethanol production for energy applications. *RSC Advances* 2016, 6 (29), 24203-24209.

[3] K Kalaga, MTF Rodrigues, H Gullapalli, G Babu, LMR Arava, PM Ajayan, Quasi-Solid Electrolytes for High Temperature Lithium Ion Batteries. *ACS Applied Materials & Interfaces* 2015, 7 (46), 25777-25783.

[4] B Tabah, IN Pulidindi, VR Chitturi, LMR Arava, A Gedanken, Solar-Energy Driven Simultaneous Saccharification and Fermentation of Starch to bioethanol for Fuel-Cell Applications. *ChemSusChem* 2015, 8 (20), 3497-3503.

[5] N Mosavati, VR Chitturi, LMR Arava, SO Salley, KYS Ng, Effects of Nickel Particle Size and Graphene Support on the Electrochemical Performance of Lithium/Dissolved Polysulfide Batteries, *Electrochimica Acta* 2015, 185, 297-303.

[6] H Al Salem, G Babu, VR Chitturi, LMR Arava, Electrocatalytic Polysulfide Traps for Controlling Redox Shuttle Process of Li–S Batteries. *Journal of the American Chemical Society* 2015, 137 (36), 11542-11545.

[7] P Thanikaivelan, TN Narayanan, BK Gupta, ALM Reddy, PM Ajayan, Nanobiocomposite from Collagen Waste Using Iron Oxide

Nanoparticles and Its Conversion Into Magnetic Nanocarbon. *Journal of Nanoscience and Nanotechnology* 2015, 15 (6), 4504-4509.

[8] G Babu, LMR Arava, Graphene-decorated graphite-sulfur composite as a high-tap-density electrode for Li-S batteries. *RSC Advances* 2015, 5 (59), 47621-47627.

[9] Raquel Borges, Arava Leela Mohana Reddy, Kaushik Balakrishnan, Glaura G. Silva and Pulickel M. Ajayan, Supercapacitor operating at 200 degrees Celsius. *Nature Scientific Reports* 2013, 3, 2572.

[10] Daniel P Cole, Arava Leela. M. Reddy, Myung Gwan Hahm, Ryan McCotter, Amelia HC Hart, Robert Vajtai, Pulickel M Ajayan, Shashi P Karna, Mark L Bundy, Electromechanical Properties of Polymer Electrolyte-Based Stretchable Supercapacitors, *Adv. Eng. Mater.*, 2013, 4(3), 1300844.

[11] Osama M Nayfeh, A Glen Birdwell, Cheng Tan, Madan Dubey, Hemtej Gullapalli, Zheng Liu, Arava Leela Mohana Reddy, Pulickel M Ajayan, Increased mobility for layer-by-layer transferred chemical vapor deposited graphene/boron-nitride thin films, *Appl. Phys. Lett.* 2013, 102, 103115.

[12] Rahul Rao, Gugang Chen, Tereza M. Paronyan, Arava Leela Mohana Reddy, Kaushik Kalaga, Masa Ishigami, Tony F. Heinz, Pulickel M. Ajayan, Avetik R. Harutyunyan, Graphene as an Atomically Thin Universal Interface for Aligned Carbon Nanotube Growth on any Substrate, *Nature Scientific Reports* 2013, 3, 1891.

[13] Adrienne E. Tanur, Jiesheng Wang, Arava L. M. Reddy, Daniel N. Lamont, Yoke Khin Yap, Gilbert C. Walker, Diameter-Dependent Bending Modulus of Individual Multiwall Boron Nitride Nanotubes, *J. Phys. Chem. B*, 2013, 117(16), 4618-4625.

[14] M. Ashokkumar, N. T. Narayanan, B. K. Gupta,A. L. M. Reddy, A. P. Singh, S. K. Dhawan, B. Chandrasekaran, D. Rawat, S. Talapatra, P. M. Ajayan, P. Thanikaivelan, Conversion of Industrial Bio-Waste into Useful Nanomaterials, *ACS Sustainable Chem. Eng.*, 2013, 1(6), 619-626.

[15] Sarah Claypool, Kaushik Kalaga, Arava Leela Mohana Reddy, Luke J. Currano, Madan Dubey, and Pulickel M. Ajayan, Graphene Based Energetic Materials: A Case Study,*Graphene* 2013, 1, 11-15.

[16] Dijo Damien, Binson Babu, T. N. Narayanan, A. Leela Mohana Reddy, P. M. Ajayan, and M. M. Shaijumon, Eco-Efficient Synthesis of Graphene Nanoribbons and Its Application in Electrochemical Supercapacitors, *Graphene* 2013, 1, 37-44.

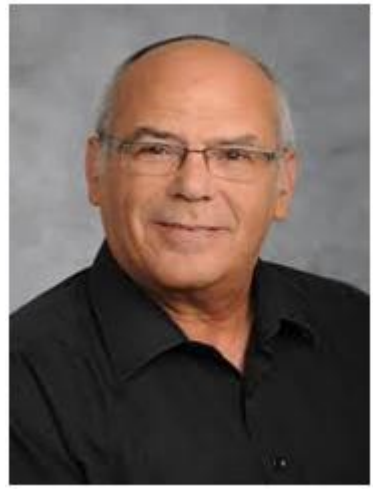

Aharon Gedanken

Affiliation: Bar-Ilan University.

Education: Prof. (Em.) Gedanken received his M.Sc. from Bar-Ilan University and his Ph.D. from Tel Aviv University, Israel.

Address: Department of Chemistry, Bar-Ilan University, Ramat-Gan, Israel 5290002.

Professional Appointments:

Emeritus Professor at Bar-Ilan University**.**

Research and Professional Experience:

After his post-doctoral research at USC, USA, Prof. (Em.) Gedanken returned to Bar-Ilan University in 1975 as a senior faculty in Chemistry Department. He was a visiting scientist at AT&T Bell Laboratories several times in 1980-1988, and at NIDDK, NIH, USA in the summers of 1989-1991. In 1999-2001, he was the chairman of national committee for strategic studies in advanced materials and chemical technologies. In the EC program FP7, he was the

Israeli representative to the Nanotechnology, Materials, and Processes (NMP) committee. He was also a partner in 12 EC projects, in which two of them were coordinated by him. From 2012 to 2016, he was a visiting chair professor in Department of Materials Science and Engineering, NCKU, Taiwan. Gedanken's research interests include sonochemistry, surface coating, synthesis of nanomaterials, microwave superheating, synthesis reactions under autogenic pressure at elevated temperatures, fuel cells, renewable energy (biomass conversion to biofuels), carbon materials, sensors, medicinal chemistry, and polymers. Gedanken has published over 725 papers in peer-reviewed journals, has 38 patent applications, and his h-index is 87.

Honors:

He is the recipient of 2009 Israel Vacuum Society and 2012 Israel Chemical Society awards of excellence in research.

Publications Last Three Years:

[1] Production of 1,3-propanediol from glycerol via fermentation by *Saccharomyces cerevisiae.* B. Tabah, A. Varvak, I. N. Pulidindi, E. Foran, E. Banin, A. Gedanken, *Green Chem.* (2016, *In Press*).

[2] A green and low-cost room temperature biodiesel production method from waste oil using egg shells as catalyst. A. Piker, B. Tabah, N. Perkas, A. Gedanken, Fuel (2016, *In Press*).

[3] In Vitro Studies of Polyethyleneimine coated miRNA Microspheres as AnticancerAgents. I. Reytblat, N. Wu, H. Xu, A. Gedanken, X. Lin, *Nano Research* DOI 10.1007/s12274-016-1055-4(2016).

[4] Facile sonochemical preparation and magnetic properties of strontium hexaferrite(SrFe12O19) nanoparticles. P. Sivakumar, A. Shaulov, L. Shani, Y. Yeshurun, A. Gedanken, *Journal of Materials Science: Materials in Electronics* DOI 10.1007/s10854-016-4482-9(2016).

[5] Fabrication of a Stable and Efficient Antibacterial Nanocoating of Zn-CuO on Contact Lenses. R. Tuby, S. Gutfreund,I. Perelshtein, G. Mircus, M. Ehrenberg,M. Mimouni, A. Gedanken, I. Bahar, *ChemNanoMat* DOI: 10.1002/cnma.201600066(2016).

[6] Sonochemical synthesis and electrochemical performance of Li1.2Ni0.13Co0.13Mn0.54O2 cathode material for Li-ion batteries application. P. Sivakumar, P. K. Nayak, J. Grinblat, N. Perkas, B.

Markovsky, D. Aurbach, A. Gedanken, *J. Solid State Electrochem.* (2016, *In Press*).

[7] Exceptionally active and stable spinel nickel manganese oxide electrocatalysts for urea oxidation reaction. S. Periyasamy, P. Subramanian, E. Levi, D. Aurbach, A. Gedanken, A. Schechterb, *ACS Appl. Mater. & Interf.* 8, 12176-12285, (*2016*).

[8] Bioethanol production from Ficus religiosa leaves using microwave irradiation. M. Klein, O. Griess, I. Pulidindi, N. Perkas, A. Gedanken, *J. Environm. Manage.* 177, 20-25 (2016).

[9] Facile One-Step Sonochemical Synthesis of Ultrafine and Stable Fluorescent C-dots. V. B. Kumar, Z. Porat, A. Gedanken, *Ultrason. Sonochem.* 27, 367-375 (2016).

[10] Simultaneous sonochemical-enzymatic coating of medical textiles with antibacterial ZnO nanoparticles. P. Petkova, A. Francesko, I. Perelshtein, A. Gedanken, T. Tzanov *Ultrason. Sonochem.* 29, 244-250 (2016).

[11] Can r-Graphene Oxide Replace the Noble Metals in SERS Studies: The Detection of Acrylamide. E. Segal, A. Gedanken, *Environ. Chem.* 13, 58-67 (2016).

[12] Design of selective solid acid catalyst for the optimization of glucose production from *Oryza Sativa* straw. A. Victor, I. Pulidindi, T. Kim, A. Gedanken, *RSC Adv.* 6, 31-38 (2016).

[13] Dispersion of Polymers in Metallic Gallium. V. B. Kumar, A. Gedanken, D. Avnir, Z. Porat, *ChemPhysChem* 17, 162-169 (2016).

[14] Nanotechnology solutions to restore antibiotic activity. U. Shimanovich, A. Gedanken *J. Mater. Chem. B: Materials for Biology and Medicine*, 4, 824-833 (2016).

[15] Sonochemical co-deposition of antibacterial nanoparticles and dyes on textiles. I. Perelshtein, A. Lipovsky, N. Perkas, T. Tzanov, A. Gedanken, *Beilstein J. of Nanotechnology* 7, 1-8 (2016).

[16] Sonochemical Formation of Ga-Pt Intermetallic Nanoparticles Embedded in Graphene and its Potential Use as an Electrocatalyst. V. B. Kumar, J. Sanetuntikul, P. Ganesan, Z. Porat, S. Shanmugam, A. Gedanken, *Electrochimica Acta* 190, 659-667 (2016).

[17] Sonochemical synthesis of CH3NH3PbI3 perovskite ultrafine nanocrystal sensitizers for solar energy applications. V. B. Kumar, L. Gouda, Z. Porat, A. Gedanken, *Ultrasonics Sonochemistry* 32, 54-59 (2016).

[18] Utilization of solar energy for continuous bioethanol production for energy applications. B. Tabah, I. Pulidindi, A. Varvak, E. Foran, E. Banin, A. Gedanken, *RSC Advances* 6, 24203-24209 (2016).

[19] In situ formation of carbon dots aids ampicillin sensing. R. Mishra, I. Pulidndi, A. Gedanken, *Analytical Methods* 8, 2441-2447 (2016).

[20] On the Nature of the nanospikes obtained in the sonication of a molten mixture of bismuth and Indium under silicon oil. V. B. Kumar, V. Ezersky, Z. Porat, A. Gedanken, *J. Alloys. & Comp.* 672, 476-480 (2016).

[21] A one-step sonochemical synthesis of ZnO-PVA nanofluid as a potential biocidal agent. A. P. Nagvenkar, A. Deokar, I. Perelshtein, A. Gedanken, *J. Mater. Chem. B.* 4, 2124-2132 (2016).

[22] Effects of the 3D sizing of polyacrylonitrile fabric with carbon nanotube-SP1 protein complex on the interfacial properties of polyacrylonitrile/ phenolic composites. I. Abramovitch, N. Hoter, H. Levy, A. Gedanken, A. Wolf, A. Eitan, T. Fine, L. Elmaleh, I. Shalev, G. Cohen, E. Grimberg, Y. Nevo, O. Shoseyov, *J. Compos. Mater.* 50, 1031-1036 (2016).

[23] DNA microspheres coated with bioavailable polymer as an efficient gene expression agent in yeasts. I. Reytblat, A. Lipovsky, A. Gedanken, *Journal of Nanomaterials* 5178029/1-5178029/9 (2016).

[24] Highly efficient silver particle layers on glass substrate synthesized by the sonochemical method for surface enhanced Raman spectroscopy purposes. P.Suchomel, R.Prucek, K.Černá, A.Fargašová, A.Panáček, A.Gedanken, R.Zbořil, L.Kvítek, *Ultrason. Sonochem.* 32, 165-172 (2016).

[25] Glucose production from potato peel waste under microwave irradiation. V. B. Kumar, I. Pulidindi, A. Gedanken, J. *of Mol. Catal. A: Chem.* 417, 163-167 (2016).

[26] Hydrophobic coating of GaAs surfaces with nanostructured ZnO. N. Perkas, G. Amirian, O. Girshevitz, A. Gedanken, *Mater. Lett.* 175, 101-105 (2016).

[27] SiO2 Beads Decorated with SrO Nanoparticles for Biodiesel Production from Waste Cooking Oil Using Microwave Irradiation. Tangy A., Pulidindi I., Gedanken A. *Energy & Fuels* 30, 3151-3160 (2016).

[28] Evaluation of the potential of *Chlorella vulgaris* for bioethanol production. Kumar V. B., Pulidindi I., Kinel-Tahan Y., Yehoshua, Y., Gedanken A., *Energy & Fuels* 30, 3161-3166 (2016).

[29] Two Are Better than One: Combining ZnO and MgF2 Nanoparticles Reduces *Streptococcus pneumoniae* and *Staphylococcus aureus* Biofilm

Formation on Cochlear Implants. M. Natan, F. Edin, N. Perkas, G. Yacobi, I. Perelshtein, E. Segal, A. Homsy,E. Laux, H. Keppner, H. Rask-Andersen, A. Gedanken, E. Banin, *Advanc. Funct. Mater.* 26, 2473-2481. (2016).

[30] A hydrothermal reaction of an aqueous solution of BSA yields highly fluorescent N doped C-dots used for imaging of live mammalian cells. V. B. Kumar, Y. Sheinberger, Z. Porat, Y. Shav-Tal, A. Gedanken, *J. Mater. Chem B.* 4, 2913 - 2920 (2016).

[31] A Novel Sonochemical Synthesis of Antlerite Nanorods. E. Segal, I. Perelshtein, A. Gedanken, *Ultrasonics Sonochemistry* 22, 30-4 (2015).

[32] Sonocatalytic degradation of oxalic acid in the presence of oxygen and Pt/TiO_2. T. Chave, N. M. Navarro, P. Pochon, N. Perkas, A. Gedanken, S. I. Nikitenko, *Catalysis Today* 241 (Part A),55-62. (2015).

[33] Antibiotic Nanoparticles Embedded into the Parylene C Layer as a New Method to Prevent Medical Device-Associated Infections. O. Grinberg, M. Natan, A. Lipovsky, A. Varvak, H. Keppner, A. Gedanken and E. Banin, *J. Mater. Chem. B* 3, 59-64 (2015).

[34] NMR Studies of DNA Nanospheres Prepared Using Sonochemical Methods. I. Reytblat, K. Keinan-Adamsky, J. Chill, H. E. Gottlieb, A. Gedanken, G. Goobes, *PCCP,* 17, 2235-2240 (2015).

[35] Protein Microgels from Amyloid Fibril Networks. Shimanovich U., E. Igor, Mason T. O., Flagmeier P., Buell A. K., Gedanken A., Linse S., Akerfeldt K. Stigsdotter, Dobson C. M., Weitz D. A., *ACS Nano* 9,43-51 (2015).

[36] Selective conversion of starch to glucose using carbon based solid acid catalyst. V. B. Kumar, I. Pulidindi, A. Gedanken, *Renewable Energy* 78,141-145 (2015).

[37] Sonochemically Synthesized Ag Nanoparticles as a SERS Active Substrate and Effect of Surfactant. N. Dar, K. Chen, Y. Nien, N. Perkas, A. Gedanken, I. Chen, *App.Surf. Sci.* 331, 219-224 (2015).

[38] Synergistic catalytic effect of $ZnBr_2$-HCl system for levulinic acid production using microwave irradiation. V. B. Kumar, I. Pulidindi, A. Gedanken, *RSC Advances* 5, 11043-11048 (2015).

[39] Single Step Production of Bioethanol from the Seaweed *Ulva rigida* using Sonication. L. Korzen, I. Pulidindi, A. Israel, A. Abelson, A. Gedanken, *RSC Advances*, 5, 16223-16229 (2015).

[40] The Influence of the Crystalline Nature of Nano Metal Oxides on Their Antibacterial and Toxicity Properties" I. Perelshtein, A. Lipovsky,N.

Perkas, A. Gedanken, E. Moschini, P. Mantecca, *Nano Research* 8 (2), 695-707. (2015).

[41] DSC measurements of the thermal properties of gallium particles in the micron and sub-micron size, obtained by sonication of molten gallium. V. B. Kumar, Z. Porat, A. Gedanken, *J. Therm. Anal. & Calorim.* 119, 1587-1592 (2015).

[42] The Sonochemical Synthesis of Ga@C-dots Particles. V. B. Kumar, Z. Porat, A. Gedanken, *RSC Advances*, 5, 25533-25540 (2015).

[43] Tetacycline Nanoparticles as Antibacterial Agentsand asGene-silencing Agents in Parasites. U.Shimanovich, A. Lypovsky, D. Eliaz, S. Zigdon, Y. Nitzan, S. Michaeli, A. Gedanken, *Advan. Healthcare Mater.* 4, 723-728 (2015).

[44] Carbon-based hybrid composites as advanced electrodes for supercapacitors. S. T. Senthilkumar, K. V. Sankar, J. S. Melo, A. Gedanken, R. K. Selvan. *Advanced Functional Materials*, 399-431 (2015).

[45] Making the Hospital a Safer Place by Sonochemical Coating of all its Textiles with Antibacterial Nanoparticles. I. Perelshtein, A. Lipovsky, N. Perkas, T. Tzanov, M. Argirova, M. Leseva,A. Gedanken*Ultrasonics Sonochemistry* 25,82-88 (2015).

[46] Sonochemical Synthesis of HSiW/Graphene Catalyst for Enhanced Biomass Hydrolysis. M. Klein, A. Varvak, E. Segal, B. Markovsky, I. Pulidindi, N. Perkas, A. Gedanken, *Green Chemistry* 17, 2418-2425 (2015).

[47] Chiral imprinting in molten gallium. V. B. Kumar, Y. Mastai, Z. Porat, A. Gedanken, *New J. Chem.* 39, 2690-2696 (2015).

[48] Heteropoly acid catalyzed hydrolysis of glycogen to glucose. M. Klein, I. Pulidindi, N. Perkas, A. Gedanken, *Biomass & Bioenergy* 76, 61-68. (2015).

[49] New Life for an Old Antibiotic. Mishra R., Segal E., Lipovsky A., Gedanken A., Banin E., Natan M., *ACS Appl. Mater. & Interf.* 7, 7324-7333 (2015).

[50] Reduction of metallic ions by molten gallium under ultrasonic irradiation and interactions between the formed metals and the gallium. V. B. Kumar, I. Perelshtein, G. Kimmel, Z. Porat, A. Gedanken, *J. Alloys & Comp.* 637, 538-544 (2015).

[51] Sonochemical synthesis of LiNi0.5Mn1.5O4 and its electrochemical performance as a cathode material for 5 V Li-ion batteries. P.

Sivakumar, P. K. Nayak, D. Aurbach, A. Gedanken, *Ultrasonics Sonochem.* 26, 332-339 (2015).

[52] Thermal and Structural Characterization of Ultrasonicated Bi-Sn Alloy in the Eutectic Composition. M. Pilloni, G. Ennas, V. Cabras, V. Denotti, V. B. Kumar, Z. Porat, A. Scano, A. Gedanken, *J. of Therm. Anal. & Calorim.* 120, 1543-1551 (2015).

[53] Facile synthesis of gallium oxide hydroxide by ultrasonic irradiation of molten gallium in water. V. B. Kumar, A. Gedanken, Z. Porat, *Ultrason. Sonochem.* 26, 340-344 (2015).

[54] Formation of particles of bismuth-based binary alloys and intermetallic compounds by ultrasonic cavitation. V. B. Kumar, G. Kimmel, Z. Porat, A. Gedanken, *New Journal of Chemistry* 39, 5374-5381 (2015).

[55] Ruthenium Phosphide Synthesis and Electroactivity towards Oxygen reduction in Acid Solutions. Teller H., Krichevski O., Gur M., Gedanken A., Schechter A. *ACS Catalysis* 5, 4260-4267 (2015).

[56] Marine integrated culture of carbohydrate rich *Ulva rigida* for enhanced production of bioethanol. L. Kortzen, I. Pulidindi, A. Israel, A. Abelson, A. Gedanken,*RSC Advances* 5, 59251-59256 (2015).

[57] Enhanced pharmacological activity of Vitamin B12 and Penicillin as nanoparticles. I. Yariv, A. Lipovsky, A. Gedanken, R. Lubart, D. Fixler, *Intern. J. Nanomedicine* 10, 3593-3601 (2015).

[58] Toxicity Evaluation of a New Zn-doped CuO Nanocomposite with Highly Effective Antibacterial Properties. P. Mantecca, E. Moschini, P. Bonfanti, U. Fascio, I. Perhelstein, A. Lipovsky, G. Chirico, R. Bacchetta, L. DelGiacco, A. Colombo, A. Gedanken, *Toxicologial Sciences* 146, 16-30 (2015).

[59] Ultrasound coating of polydimethylsiloxanes with antimicrobial enzymes. A. Lipovsky, B. Thallinger, I. Perelstein, R. Ludwig, C. Sygmund, G. S. Nyanhongo, G. M. Guebitz, A. Gedanken, *J. Mater. Chem.* B3, 7014-7019 (2015).

[60] Assessment of Holocellulose for the production of Bioethanol by conserving *Pinus radiata* cones as renewable feedstock. A. Victor, I. Pulidindi, A. Gedanken, *J. Environ. Manage.* 162, 215-220(2015).

[61] Novel Technology for Bio-diesel Production from Cooking and Waste Cooking Oil by Microwave Irradiation. R. Priambodo, T-C. Chen, M-C. Lu, A. Gedanken, J-D. Liao, Y-H. Huang, *Energy Procedia* 75, 84-91 (2015).

[62] Study on Fermentation Kinetics for Accelerated Production of Bioethanol from Glucose, Sucrose and Molasses. B. Tabah, I. Pulidindi, A. Gedanken, *J.Bioproc. & Biotechn.* 5, 232 (2015).

[63] Synthesis of WS2 and WSe2 nanowires on stainless steel coupon by reaction under autogenic pressure at elevated temperature method. Yuvasravan R., Apsana G., George P. P., Genish I., Maklouf S. B., Koltypin Y., Gedanken A. *Applied Nanoscience* 1-8 (2015).

[64] Solar Energy Driven Simultaneous Saccharification and Fermentation (SSF) of Starch to Bioethanol for Fuel Cell applications. B. Tabah, I. Pulidindi, V. R. Chitturi, L. M. R. Arava, A. Gedanken, *ChemSusChem*. 8, 3497-3503 (2015).

[65] Substrates Coated with Silver Nanoparticles as a Neuronal Regenerative Material. N. Alon, Y. Miroshnikov, N. Perkas, I. Nissan, A. Gedanken, O. Shefi, *Internat. J. Nanomed*. 9, 23 (2014).

[66] Sonochemical synthesis, structural, magnetic and grain size dependent electrical properties of NdVO4 nanoparticles. Yuvaraj S., Kalai S. R., Kumar V. B., Perelshtein I., Gedanken A., Isakkimuthu S., Arumugam, S.*Ultrason. Sonochem.* 21, 599-605(2014).

[67] Sonochemical coating of textiles with hybrid ZnO/chitosan antimicrobial nanoparticles. Petkova P., Francesko A., Fernandes M., Mendoza E., Perelshtein I., Gedanken A., Tzanov T. *ACS Appl. Mater. & Interf.* 6, 1164-1172 (2014).

[68] Ultrasonic Cavitation of Molten Gallium in Water :Entrapment of Organic Molecules in Gallium Microspheres. V. B. Kumar, A. Gedanken, Z. Porat, *J. Mater. Chem. A*, 2, 1309-1317(2014).

[69] Herpes Simplex Virus Type-1 Attachment Inhibition by Functionalized Graphene Oxide. M. Sametband, I. Kalt, A. Gedanken, R. Sarid, *ACS Appl. Mater. & Interf.* 6, 1228-1235 (2014).

[70] Ultrasonic cavitation of molten gallium: formation of micro- and nano-spheres. V. B. Kumar, A. Gedanken, Z. Porat, *Ultrasonics Sonochemistry*, 21, 1166-1173 (2014).

[71] Carbon Nanoparticles based Non-enzymatic Glucose Sensor. Pulidindi I., A. Gedanken, *International Journal of Environmental Analytical Chemistry* 94, 28-35, (2014).

[72] Sonochemically-induced spectral shift as a probe of green fluorescent protein release from nano capsules. Shimanovich U., Munder A., Azoia N. G., Cavaco-Paulo A., Gruzman Arie, Knowles T.P. J., Gedanken A., *RSC Advances* 4,10303-10309 (2014).

[73] Pre-miRNA expressing plasmid delivery for anti-cancer therapy. E. Benisvy-Aharonovich, U. Shimanovich, N. Kronfeld, N. Giladi, A. Bier, G. Kazimirsky, A. Gedanken, C. Brodi, *Medchemcomm.* 5, 459-462 (2014).

[74] Sonochemical approach improves the CuO-ZnO/TiO_2 catalyst for WGS reaction. N. Perkas, P. Gunawan, G. Amirian, Z. Wang, Z. Zhong, A. Gedanken *PCCP,* 16, 7521-7530 (2014).

[75] A Zn-doped CuO nanocomposite shows enhanced antibiofilm and antibacterial activities against *Streptococcus* mutans compared to nanosized CuO. M. Eshed, J. Lellouche, A. Gedanken, E. Banin, *Advanc. Funct. Mater.* 24, 1382-1390 (2014).

[76] An ultrasonic technology for production of anti-bacterial nanomaterials and their coating on textiles. A. V. Abramova, V. O. Abramov, A. Gedanken,
I. Perelshtein, V. M. Bayazitov, *Beilst. J. Nanotechn.* 5, 532-536 (2014).

[77] Can Cellulose be a sustainable feedstock for Bioethanol production? Baruchi B Kimchi, I. Pulidindi, A. Gedanken*Renewable Energy* 71, 77-80 (2014).

[78] Facile Synthesis of Self-Assembled Spherical and Mesoporous Dandelion Capsules of ZnO: Efficient Carrier for DNA and Anti-cancer Drugs. V. B. Kumar, K. Kumar, A. Gedanken, P. Paik, *J. Mater. Chem. B* 2, 3956-3964 (2014).

[79] Selective chemical reduction of carbon dioxide to formate using Microwave irradiation. I. Pulidindi, A. Gedanken, *Journal of CO_2 Utilization* 7, 19-22 (2014).

[80] Tannic Acid NPs-Synthesis and Immobilization Onto a Solid Surface in a One-Step Process and Their Antibacterial and Anti-inflammatory Properties. I. Perelshtein, E. Ruderman, A. Francesko, M. M. Fernandes, T. Tzanov, A. Gedanken, *Ultrason. Sonochem.* 21, 1916-1920 (2014).

[81] One-stepsonochemical preparation of redox-responsive nanocapsules forglutathione mediated RNA release. A. Francesko, T. Tzanov, I. Perelshtein, A. Gedanken, *J. Mater. Chem. B*, 2, 6020-6029 (2014).

[82] Forming Nano Spherical Cellulose Containers. Tzhayik O., Pulidindi I., Gedanken A. *Industrial & Engineering Chemistry Research* 53, 13871-13880 (2014).

[83] Gene silencing by siRNA nanoparticles synthesized via sonochemical method. U. Shimanovich,A. Munder, A. Loureiro, N. G. Azoia, A. Gomes, A. Cavaco-Paulo, A. Gedanken, A. Gruzman, *Journal of Nanomedicine & Nanotechn,* 5, 1000204/1-1000204/5(2014).

[84] Levulinic acid production from *Cicer arietinum*, Cotton, *Pinus radiata* and Sugar cane bagasse. A. Victor, I. Pulidindi, A. Gedanken, *RSC Advances* 4, 44706-44711 (2014).

[85] Enhanced Activity of Immobilized Pepsin Nanoparticles Coated on Solid Substrates Compared to Free Pepsin. D. Meridor, A. Gedanken, *Enzyme and Microbial Technology* 67, 67-76 (2014).

[86] Innovative Inorganic Nanoparticles with Antimicrobial Properties Attached to Textiles by Sonochemistry. A. Gedanken, N. Perkas, I. Perelshtein, A. Lipovsky, Y. Nitzan, R. Lubart, Chapter 9, in Cavitation Ed. Sivakumar Manickam and Muthupandian Ashokkumar, Pan Stanford Publishing Pte Ltd, 263-300 (2014) USA.

[87] Metal Oxide Nanoparticles as a Source for ROS: Their Application in the Fabrication of antimicrobial Textiles. A. Lipovsky, I. Perelshtein, N. Perkas, R. Lubart, A. Gedanken, Chapter 4 in a book " HANDBOOK on Reactive Oxygen Species (ROS) Eds. M. Suzuki, S. Yamamoto, Nova Pub. pp. 169-196 (2014).

[88] Optimizing Algal Lipid Production and its Efficient Conversion to Biodiesel
Biofuels, M. Topf, M. Koberg, Y. Kinel-Tahan, A. Gedanken, Z. Dubinsky, Y. Yehoshua, *Biofuels* 5, 405-413 (2014).

[89] Nanocrystalline Iron Oxides, Composites and Related Materials as a Platform for Electrochemical, Magnetic, and Chemical Biosensors. V. Urbanova, M. Magro, A. Gedanken, D. Baratella, F. Vianello, R. Zboril, *Chem. Mater.* 26, 6653-6673 (2014).

[90] Isosaccharinic Acid Mediated Fine Chemicals Production from Cellulose. I. Pulidindi, M. R. Hakim, P. Mayer, A. Gedanken,*J.Fundam.Renew. Energy and Appl.* 4, 143 (2014).

[91] Proteinaceous microspheres for targeted RNA delivery made by ultrasonic emulsification method. U. Shimanovich, D. Eliaz, S. Zigdon, V. Volkov, A. Aizer,A. Cavaco-Paulo, S. Michaeli, Y. Shav-Tal, A. Gedanken, *J. Mater. Chem. B*, 1, 82-90 (2013).

[92] Coating antibacterial nanoparticles on textiles: towards the future hospital in which all textiles will be antibacterial. Gedanken A., Perkas N., Perelshtein I., Inorganic Micro- and Nanomaterials Ed. Dibenedetto A., Aresta M., 3-33 (2013).

[93] Encapsulating Bioactive Materials in Micro and Nano Spheres Produced Sonochemically. O. Grinberg, U. Shimanovich, A. Gedanken *J. Mater. Chem. B:Mater.Biol. & Med.* 1, 595-605 (2013).

[94] The Magneto-caloric Properties of La0.7Ca0.11Sr0.19MnO3 Nanoparticles Prepared by a One-step, Nonaqueous Synthesis. E. Ohayon. A. Gedanken, *Journal of Magnetism and Magnetic Materials* 331, 45-52 (2013).

[95] A sonochemical technology for coating of textiles with antibacterial nanoparticles and equipment for its implementation. A. Abramova, V. Popov, A. Gedanken, Ean-Hin Ooi, T. J. Mason, E.M. Joyce, J. Beddow, I. Perelshtein, V. Bayazitov, *Mater. Letts.* 96, 121-124 (2013).

[96] Antibody modified Bovine Serum Albumin microspheres for targeted delivery of anticancer agent Gemcitabine. O. Grinberg, A. Gedanken, D. Mukhopadhyay, C. R. Patra, *Polymers for Advanced Technologies* 24, 294-299 (2013).

[97] Forming Nanoparticles of <alpha>-amylase and embedding them into solid surfaces. D. Meridor, A. Gedanken, *J. of Molecular Catalysis B: Enzymatic* 90, 43-48 (2013).

[98] Chitosan and Chitosan-Zn-based complex Nanoparticles: Formation, Characterization, and Antibacterial Activity. I. Perelshtein, E. Ruderman, N. Perkas, T. Tzanov, J. Beddow, E. Joyce, T. J. Mason, M. Blanes, K. Mollá, A. Patlolla, A. I. Frenkel, A. Gedanken, *J. Mater. Chem. B*., 1, 1968-1976 (2013).

[99] Fabrication of (La1-x Gdx)2/3Sr1/3MnO3 Manganite Perovskite Nanorods by Sonication-Assisted Coprecipation. Jiang X. L., Yao Y. J., Lai M., Jacob D. S., Gedanken A., Du Y. W.*J. Superconduct. Novel Magnet*. 26(4), 1385-1390 (2013).

[100] Preparation of Ge@Organosilicon Core-Shell Structures and Characterization by Solid State NMR and Other Techniques. Eshed M., Keinan-Adamsky K., Goobes G., Gedanken A., *J. Phys. Chem. C*117, 11086-11094 (2013).

[101] Silver Nanoparticles Promote Neuronal Growth. Alon N., Miroshnikov Y., Perkas N., Nissan I., Gedanken A., Shefi O., *Procedia Engineering*, 59,
25-29 (2013).

[102] The Sonochemical Coating of Cotton Withstands 65 Washing Cycles at Hospital Washing Standards and Retains its Antibacterial Properties. I. Perelshtein, Y. Ruderman, N. Perkas, J. Beddow, G. Singh, M. Vinatoru, E. Joyce, T. J Mason, M. Blanes, K. Mollá, A. Gedanken, *Cellulose* 20, 1215-1221 (2013).

[103] Low-Level Visible Light Irradiation (LLVL) Promotes Proliferation of Mesenchymal Stem Cells. A. Lipovsky, U. Oron, A. Gedanken, R. Lubart, *Lasers in Medical Science* 28, 1113-1117 (2013).

[104] MgF2 nanoparticles coated teeth inhibit *Streptocococcus* mutans biofilm formation on teeth model. M. Eshed, J. Lellouche, E. Banin, A. Gedanken, *J. Mater. Chem B,* 1, 3985-3991 (2013).

[105] Visible light-induced OH radicals in Ga_2O_3: An EPR study. Z. Tzitrinovich, A. Lipovsky, A. Gedanken, R. Lubart, *Phys. Chem.* 15, 12977-12981 (2013).

[106] Synthesis of mesoporous SiO2-ZnO nanocapsules: encapsulation of small biomolecules for drugs and ‘‘SiOZO-plex’’ for gene delivery. V. B. Kumar, M. Annamanedi, M. D. Prashad, K. M. Arunasree, Y. Mastai, A. Gedanken, P. Paik, *J. Nanopart. Res.* 15, 1904 (2013).

[107] The immobilization of PEI nano- and microspheres on glass using high intensity ultrasound. U. Shimanovich, A. Cavaco-Paulo, A. Gedanken, *International Journal of Applied Ceramic Technology* 10(s1), E267-E273 (2013).

[108] Biocidal properties of TiO_2 powder modified with Ag nanoparticles. N. Perkas, A. Lipovsky, G. Amirian, Y. Nitzan, A. Gedanken, *J. Mater. Chem. B Materials for Biology and Medicine*, 1, 5309-5316 (2013).

[109] Triangular core shell ZnO@SiO2 nanoparticles. Kumar V. B., Gedanken A., Pradip P., *Chem.Phys.Chem.* 14, 3215-3220 (2013).

[110] Visible Light-Induced Antibacterial Activity of Metaloxide Nanoparticles. Lipovsky A., Gedanken A., Lubart R., *Photomedicine and Laser Surgery* 31, 526-530 (2013).

[111] Using microwave radiation and SrO as a catalyst for the complete conversion of oils, cooked oils, and microalgae to biodiesel. Koberg M., Gedanken A., Ed. Suib S. L. New and Future Developments in Catalysis: Catalytic Biomass Conversion 209-227 (2013).

[112] Eradication of Multi-Drug Resistant Bacteria by a Novel Zn-doped CuO Nanocomposite. E. Malka, I. Perelshtein, A. Lipovsky, Y. Shalom, L.Naparstek, N. Perkas, T. Patick, R. Lubart, Y. Nitzan, E. Banin, A. Gedanken, *Small* 9, 4069-4076 (2013).

[113] Fabrication, Characterization and Printing of Conductive Ink Based on Multi Core-Shell Nanoparticles Synthesized by RAPET. E. Butovsky, I. Perelshtein, I. Nissan, A. Gedanken, *Advanc. Funct. Mater.* 23, 5794-5799 (2013).

In: Solar Energy and Solar Panels
Editor: Joel G. Carter
ISBN: 978-1-53610-380-9

Chapter 2

PV PANEL MODELING AND IDENTIFICATION

***Li Hong Idris Lim*[1,*], *Zhen Ye*[2] , *Dazhi Yang*[3] *and Han Chong Shaun Tay*[4]**
[1]School of Engineering, University of Glasgow, Glasgow, United Kingdom
[2]Renewable Energy Corporation (REC), Singapore
[3]Singapore Institute of Manufacturing Technology, Singapore
[4]Singapore Institute of Technology, Singapore

Abstract

In this chapter, the modelling techniques of PV panels from I-V characteristics are discussed. At the beginning, a necessary review on the various methods are presented, where difficulties in mathematics, drawbacks in accuracy, and challenges in implementation are highlighted. Next, a novel approach based on linear system identification is demonstrated in detail. Other than the prevailing methods of using approximation (analytical methods), iterative searching (classical optimization), or soft computing (artificial intelligence), the proposed method regards the PV diode model as the equivalent output of a dynamic system, so the diode model parameters can be linked to the transfer function coefficients of the same dynamic system. In this way, the problem of solving PV model parameters is equivalently converted to system identification in control theory, which can be perfectly solved by a simple integral-based linear least square method. Graphical meanings of the proposed method are illustrated to help readers understand the underlying principles. As compared

*E-mail address: LiHonIdris.Lim@glasgow.ac.uk

to other methods, the proposed one has the following benefits: 1) unique solution; 2) no iterative or global searching; 3) easy to implement (linear least square); 4) accuracy; 5) extendable to multi-diode models. The effectiveness of the proposed method has been verified by indoor and outdoor PV module testing results. In addition, possible applications of the proposed method are discussed like online PV monitoring and diagnostics, non-contact measurement of POA irradiance and cell temperature, fast model identification for satellite PV panels, and etc.

1. Introduction

PV panels are made of PV cells assembled in series/parallel and encapsulated in modules. The cell structure can be simplified as a *p-n* junction exposed to light, as depicted in Figure 1, which is a combination of two layers of differently doped semiconductor materials.

1.1. PV Modeling

Without the sunlight, the characteristics of the *p-n* junction is governed by the well-known Shockley diode equation [1]

$$I_D = I_o \left(\mathrm{e}^{\frac{V}{a}} - 1 \right), \tag{1}$$

where I_D is the diode current, I_o is the reverse saturation current, $a = nkT_c/q$ is the modified ideality factor [2], n is the ideality factor, k is Boltzmann's constant (1.380653×10^{-23} J/K), T_c is the cell temperature, and q is the electron charge ($1.60217646 \times 10^{-19}$ C). With the presence of sunlight, the *p-n* junction absorbs the photon and generates electron-hole pairs (or carriers) moving across the junction, which is known as the photovoltaic effect. The inclusion of the resulted photocurrent into Shockley equation (1) forms an ideal model of PV cells as

$$I = I_L - I_D = I_L - I_o \left(\mathrm{e}^{\frac{V}{a}} - 1 \right), \tag{2}$$

where photocurrent I_L is dependent on the flux of incident irradiation as well as the absorption capacity of the semiconductor materials [3]. However, the ideal model by (2) usually yields unacceptable errors in reality due to the lack of consideration on the current losses from the contact resistance between the silicon and electrodes surfaces, the current flow resistance in the silicon material

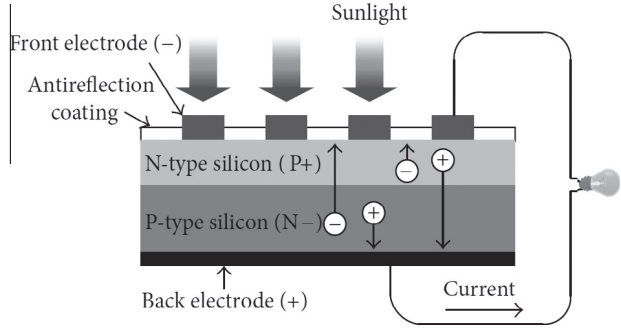

Figure 1. Equivalent circuit of diode models.

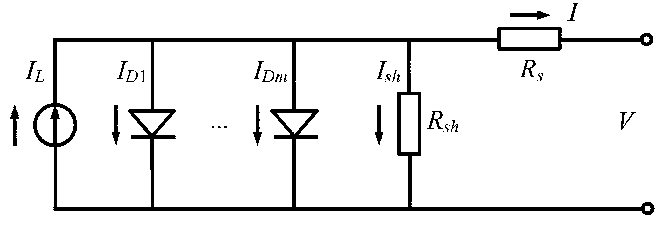

Figure 2. Equivalent circuit of diode models.

and the resistance of the electrodes. By incorporating the effects from all these resistances, a more realistic and accurate model [4] is derived as

$$I = I_L - \sum_{i=1}^{m} I_{D_i} - I_{sh} = I_L - \sum_{i=1}^{m} I_{o_i} \left(\mathrm{e}^{\frac{V+R_s I}{a_i}} - 1 \right) - \frac{V + R_s I}{R_{sh}}, \qquad (3)$$

where R_s and R_{sh} are resistances in series and parallel,respectively. The equivalent circuit for (3) is shown in Figure 2, where diode D_1 accounts for carriers diffusing across the *p-n* junction and recombining in the bulk or at surfaces, diode D_2 is sometimes attributed to carrier recombination by traps within the depletion region [5], or recombination at an unpassivated cell edge [6]. Theoretically, more diodes ($m > 2$) can be added to the circuit in Figure 2 to better account for distributed and localized effects in solar cells like Auger recombination, but their contributions are negligible as compared to D_1 and D_2 [7].

Note that (3) is applicable not only to PV cells, but also to PV modules.

For the latter, $a_i = N_s n_i k T_c/q$, where N_s is the number of cells connected in series. In the lumped-circuit model by (3) or Figure 2, only I and V are known variables from the data sheet or real measurements. The model identification is then to determine the unknown parameters I_L, I_{o_i}, a_i, R_s and R_{sh} from the known data of I and V.

1.2. PV Model Identification

Even in the case of the one diode model ($m = 1$ in (3)), it is not straightforward to determine the model parameters (I_L, I_o, a, R_s and R_{sh}) from the I-V characteristics of PV cells/modules due to the transcendental nature of (3). For such a one-diode PV model, the existing identification methods in literature can be divided into the following two categories.

1.2.1. Deterministic Solution

The deterministic solution is an unique solution of the five unknown parameters (I_L, I_o, a, R_s and R_{sh}) from five independent equations. Usually, the four independent equations are chosen from the open circuit, short circuit and maximum power points at STC (1000 W/m^2, $T_c = 25°$C, AM $= 1.5$) as follows.

At short circuit (SC), $V = 0$:

$$I_{sc} = I_L - I_o \left(\mathrm{e}^{\frac{R_s I_{sc}}{a}} - 1\right) - \frac{R_s I_{sc}}{R_{sh}}. \tag{4}$$

At open circuit (OC), $I = 0$:

$$I_L - I_o \left(\mathrm{e}^{\frac{V_{oc}}{a}} - 1\right) - \frac{V_{oc}}{R_{sh}} = 0. \tag{5}$$

At maximum power point (MPP), $\mathrm{d}P/\mathrm{d}V = 0$:

$$I_{mpp} = I_L - I_o \left(\mathrm{e}^{\frac{V_{mpp}+R_s I_{mpp}}{a}} - 1\right) - \frac{V_{mpp} + R_s I_{mpp}}{R_{sh}}. \tag{6}$$

$$\left.\frac{\mathrm{d}IV}{\mathrm{d}V}\right|_{mpp} = -\frac{V_{mpp}}{R_s + \frac{1}{\frac{I_o}{a}\mathrm{e}^{\frac{V_{mpp}+I_{mpp}R_s}{a}} + \frac{1}{R_{sh}}}} + I_{mpp} = 0. \tag{7}$$

As for the 5th independent equation, there are many options.

One way is to estimate one of the five parameters independently. For example, I_L can be estimated from the influence of the structure parameters of a silicon solar cell on photocurrent [8]. I_o is material independent and can be explicitly related to a solid state parameter, the $0K$ Debye temperature of the semiconductor [9]. a can be determined from the use of properties of special trans function theory (STFT) [10]. The estimation of R_s are well summarized in [11–15]. R_{sh} can be approximated by the reciprocal of slope at SC [16], i.e.,

$$R_{sh} \approx -\left.\frac{\mathrm{d}V}{\mathrm{d}I}\right|_{sc}. \tag{8}$$

For example, with equation (4)-(8), one-diode model parameters can be identified as [17]

$$\begin{aligned}
I_L &= I_{sc}\left(1+\frac{R_s}{R_{sh}}\right)+I_o\left(\mathrm{e}^{\frac{I_{sc}R_s}{a}}-1\right),\\
I_o &= \left(I_{sc}-\frac{V_{oc}}{R_{sh}}\right)\mathrm{e}^{-\frac{V_{oc}}{a}},\\
a &= \frac{V_{mpp}+I_{mpp}R_{s0}-V_{oc}}{\ln\left(I_{sc}-\frac{V_{mpp}}{R_{sh}}-I_{mpp}\right)-\ln\left(I_{sc}-\frac{V_{oc}}{R_{sh}}\right)+\frac{I_{mpp}}{I_{sc}-\frac{V_{oc}}{R_{sh}}}},\\
R_s &= R_{s0}-\frac{a}{I_0}\mathrm{e}^{-\frac{V_{oc}}{a}},
\end{aligned}$$

where $R_{s0} = -\left.\mathrm{d}V/\mathrm{d}I\right|_{oc}$ is the reciprocal of slope at OC.

The other way is to apply one of (4)-(7) to non-STC conditions. For example, applying (5) to $T_c^* = T_c + \Delta T$ ($\Delta T \neq 0$) gives

$$I_L^* - I_o^*\left(\mathrm{e}^{\frac{V_{oc}^*}{a^*}}-1\right)-\frac{V_{oc}^*}{R_{sh}^*}=0. \tag{9}$$

In the case of no irradiance change, non-STC parameters are given by [2, 18]

$$I_L^* = I_L + \alpha_T \Delta T, \tag{10}$$

$$I_o^* = I_o\left(\frac{T_c^*}{T_c}\right)^3 \mathrm{e}^{\frac{E_g}{kT_c}-\frac{E_g^*}{kT^*}}, \tag{11}$$

$$E_g^* = E_g(1 - 0.0002677\Delta T), \tag{12}$$

$$a^* = \frac{T_c^*}{T_c} a, \tag{13}$$

$$R_{sh}^* = R_{sh}, \tag{14}$$

$$V_{oc}^* = V_{oc} + \beta_T \Delta T, \tag{15}$$

where $E_g = 1.17 - 4.73 \times 10^{-4} T_c^2/(T_c + 636)$ is the band gap energy, α_T and β_T are the temperature coefficient of SC current and OC voltage, respectively. Substituting (10)-(15) into (9) yields the 5th independent equation as follows

$$I_L + \alpha_T \Delta T - I_o \left(\frac{T_c^*}{T_c}\right)^3 \mathrm{e}^{\frac{E_g}{kT_c} - \frac{E_g(1-0.0002677\Delta T)}{kT^*}} \left(\mathrm{e}^{\frac{V_{oc}+\beta_T\Delta T}{a}\frac{T_c}{T_c^*}} - 1\right) - \frac{V_{oc} + \beta_T \Delta T}{R_{sh}} = 0.$$

Different choices of non-STC equations yield different solutions for (I_L, I_o, a, R_s and R_{sh}), which can be found in [19–23].

No matter what the 5th equation is, a small variation in one parameter may lead to a large error in the other four parameters, due to the high sensitivity of the transcendental equation [24]. Even if there is no approximation in the 5th equation, there are no analytical solutions available due to the inherent nonlinearity. Usually, partial linearization has to be made to yield empirical formulas [25–29], which is a trade-off between simplicity and accuracy. Note that the greatest difficulty in solving (3) lies in its implicit format of I, i.e., I are both dependent and independent variable of the equation. Recent progress to overcome such difficulty is to apply the Lambert W function [30,31] to (3), then the implicit format of I is converted to its equivalent explicit format as [18, 32]

$$I = \frac{R_{sh}(I_L + I_o) - V}{R_s + R_{sh}} - \frac{a}{R_s} W\left(\frac{I_o R_s R_{sh}}{a(R_s + R_{sh})} \mathrm{e}^{\frac{R_{sh}(V + R_s(I_L + I_o))}{a(R_s + R_{sh})}}\right). \tag{16}$$

The benefit of (16) over (3) is that the former is not transcendental anymore, which makes it possible to find solutions to (4)-(7) by iterative algorithms.

1.2.2. Optimal Solution

Optimal solution employs nonlinear fitting procedures based on the minimization of deviations between modelled and measured I-V curves, in accordance with some metric function (usually least square) [33–36], e.g.,

$$\min f(I_L, I_o, a, R_s, R_{sh}) = \sum_{i=1}^{N} \left[I_i - \hat{I}_i(V_i, I_L, I_o, a, R_s, R_{sh})\right]^2,$$

where N is the number of data samples, $\hat{I}$ is the estimation of I with the optimal solution of I_L, I_o, a, R_s and R_{sh}. Iterative searching algorithms are usually used [37, 38], including Newton-Raphson [39], Levenberg-Marquardt [40], Gauss Siedal [16], and singular value decomposition [41], but their convergence and accuracy heavily depend on the initial values and are easily trapped in the local optimums. From different initial value guesses, such approaches can result in widely different parameter sets, all leading to satisfactory curve fitting [42]. Although a good match between estimation and measured data can be obtained, there is no guarantee that the estimated I-V curve would pass the SC, OC and MPP points.

To achieve the global optimum, soft computing techniques have to be used, which include genetic algorithm (GA) [43–46], particle swarm optimisation (PSO) [47–49], differential evolution (DE) [50–52], simulated annealing (SA) [53, 54] and artificial neural network (ANN) [55, 56]. But they are too complicated to be implemented and unsuitable for online calculation due to the heavy burden of computing.

Current trend of PV model identification is to combine the deterministic and optimal solutions, i.e.,employing both methods of solving algebraic equations and iterative searching [57–59]. With a single parameter fitting procedure, numerical solutions to (4)-(7) will be obtained by the empirical formulas or iterative algorithms. The drawbacks of the above two categories are mitigated in this way. With the help of Lambert W function as shown in (16), Laudani *et al.* further reduce the dimension of searching space from 5 to 2 by splitting the model parameters into two independent unknowns (a and R_s) and three dependent ones (I_L, I_o and R_{sh}). In this way, the burden of iterative searching is greatly relieved and it becomes easy to get a and R_s numerically or graphically. The review and comparison for the aforementioned all kinds of methods are well summarised in [60, 61].

This chapter opens a new angle to view the diode model from the systems perspective. Actually, one of the biggest application of Lambert W function is to solve differential equations, which is directly linked to the time-domain representation of a linear system. For example, the first-order linear system can be described as [62]

$$T\frac{\mathrm{d}y(t)}{\mathrm{d}t} + y(t) = u(t), \tag{17}$$

where T is the time constant of the system. The unit ramp ($u(t) = t$) response

of (17) is given by,

$$y(t) = t + T(\mathrm{e}^{-\frac{t}{T}} - 1),$$

which has the same format as (3). This motivates us that the I-V curve governed by (3) can be viewed as the output of some linear system, and the model parameters can be linked to the coefficients of a linear differential equation. Using system identification methods available in the literature [63], PV model parameters can be easily identified by a simple linear least squares method.

2. Dynamic System Formulation

Firstly, we show how to link one-diode model to an equivalent linear system. Next, the same method is extended to the general case of multi-diode model.

2.1. One-Diode Model

Recall the I-V curve described by (3) with $m = 1$. Let $y = I$ and $x = V + R_s I$, (3) then becomes

$$y = I_L + I_o - I_o \mathrm{e}^{\frac{x}{a}} - \frac{x}{R_{sh}}. \tag{18}$$

Taking differential once on both sides of (18) gives

$$\frac{\mathrm{d}y}{\mathrm{d}x} = -\frac{I_o}{a}\mathrm{e}^{\frac{x}{a}} - \frac{1}{R_{sh}}. \tag{19}$$

Differentiating one more time for (19) gives

$$\frac{\mathrm{d}^2 y}{\mathrm{d}x^2} = -\frac{I_o}{a^2}\mathrm{e}^{\frac{x}{a}}. \tag{20}$$

Eliminating $\mathrm{e}^{x/a}$ from (19) and (20) gives

$$a\frac{\mathrm{d}^2 y}{\mathrm{d}x^2} - \frac{\mathrm{d}y}{\mathrm{d}x} = \frac{1}{R_{sh}}. \tag{21}$$

Let $t = x$ and $u(t) \equiv 1$, (21) is equivalent to

$$a\frac{\mathrm{d}^2 y(t)}{\mathrm{d}t^2} - \frac{\mathrm{d}y(t)}{\mathrm{d}t} = \frac{u(t)}{R_{sh}}, \tag{22}$$

which is a standard differential equation representation of a second order linear system. t is the "time", $u(t)$ and $y(t)$ are the system "input" and "output", respectively. Since $u(t) \equiv 1$, $y(t)$ is the unit step response of the system in "time" domain. Taking Laplace transform, $F(s) = \mathcal{L}[f(t)] = \int_0^\infty \mathrm{e}^{-st} f(t)\mathrm{d}t$, on both sides of (22),

$$a[s^2Y(s) - sy(0) - y'(0)] - [sY(s) - y(0)] = \frac{U(s)}{R_{sh}}. \tag{23}$$

Utilize $sU(s) = 1$, and (23) is equivalent to

$$a\left[s^2Y(s) - s^2U(s)y(0) - sU(s)y'(0)\right] - [sY(s) - sU(s)y(0)] = \frac{1}{R_{sh}}U(s).$$

It follows from (18) that $y(0) = I_L$, $y'(0) = -I_o/a - 1/R_{sh}$, so the transfer function from $Y(s)$ to $U(s)$ is

$$\begin{aligned} G(s) := \frac{Y(s)}{U(s)} &= \frac{ay(0)s^2 + [ay'(0) - y(0)]s + \frac{1}{R_{sh}}}{as^2 - s} \\ &= \frac{aI_Ls^2 - (I_o + \frac{a}{R_{sh}} + I_L)s + \frac{1}{R_{sh}}}{as^2 - s}. \end{aligned} \tag{24}$$

The corresponding time domain differential equation is

$$a\frac{\mathrm{d}^2y(t)}{\mathrm{d}t^2} - \frac{\mathrm{d}y(t)}{\mathrm{d}t} = aI_L\frac{\mathrm{d}^2u(t)}{\mathrm{d}t^2} - \left(I_L + I_o + \frac{a}{R_{sh}}\right)\frac{\mathrm{d}u(t)}{\mathrm{d}t} + \frac{u(t)}{R_{sh}}. \tag{25}$$

It should be noted that (22) is different from (25) because of the non-zero initial conditions. In other words, (25) is the description of the same system of (22) but with zero initial conditions. This will facilitate the calculation of the integral-based identification proposed in Section 3

2.2. Multi-Diode Model

Similarly by letting $y = I$ and $x = V + R_sI$ in (3), it yields

$$y = I_L + \sum_{i=1}^{m} I_{o_i} - \sum_{i=1}^{m} I_{o_i}\mathrm{e}^{\frac{x}{a_i}} - \frac{x}{R_{sh}}. \tag{26}$$

Taking differential once on both sides of (26) gives

$$\frac{\mathrm{d}y}{\mathrm{d}x} = -\sum_{i=1}^{m}\frac{I_{o_i}}{a_i}\mathrm{e}^{\frac{x}{a_i}} - \frac{1}{R_{sh}}. \tag{27}$$

Differentiating (27) for k times, $k = 1, 2, \cdots, m$, yields

$$y^{(k+1)}(x) = -\sum_{i=1}^{m} \frac{I_{o_i}}{a_i^{k+1}} \mathrm{e}^{\frac{x}{a_i}}, \tag{28}$$

where $y^{(k)}(x) = \mathrm{d}^k y / \mathrm{d}x^k$. Rewrite (28) in matrix format,

$$\underbrace{\begin{bmatrix} y^{(2)}(x) \\ y^{(3)}(x) \\ \vdots \\ y^{(m+1)}(x) \end{bmatrix}}_{B} = \underbrace{\begin{bmatrix} a_1^{-1} & a_2^{-1} & \cdots & a_m^{-1} \\ a_1^{-2} & a_2^{-2} & \cdots & a_m^{-2} \\ \vdots & \vdots & \ddots & \vdots \\ a_1^{-m} & a_2^{-m} & \cdots & a_m^{-m} \end{bmatrix}}_{A} \begin{bmatrix} -\frac{I_{o1}}{a_1} \mathrm{e}^{\frac{x}{a_1}} \\ -\frac{I_{o2}}{a_2} \mathrm{e}^{\frac{x}{a_2}} \\ \vdots \\ -\frac{I_{om}}{a_m} \mathrm{e}^{\frac{x}{a_m}} \end{bmatrix}.$$

Since $a_k \neq 0$, A is a Vandermonde matrix with $\det(A) \neq 0$, so A^{-1} exists and

$$\left[-\frac{I_{o_1}}{a_1} \mathrm{e}^{\frac{x}{a_1}}, -\frac{I_{o_2}}{a_2} \mathrm{e}^{\frac{x}{a_2}}, \ldots - \frac{I_{o_m}}{a_m} \mathrm{e}^{\frac{x}{a_m}} \right]^T = A^{-1} B, \tag{29}$$

where $A^{-1} = [\xi_{i,j}] \in \mathbb{R}_{m \times m}$ with

$$\xi_{i,j} = \frac{\sum\limits_{\substack{1 \leq k_1 < \cdots < k_{n-j} \leq n \\ k_1, \cdots, k_{n-j} \neq i}} (-1)^{j-1} a_{k_1}^{-1} \cdots a_{k_{n-j}}^{-1}}{a_i^{-1} \prod\limits_{\substack{1 \leq k \leq n \\ k \neq i}} \left(a_k^{-1} - a_i^{-1} \right)}. \tag{30}$$

Substituting (29) into (27) yields

$$y^{(1)}(x) - \sum_{j=1}^{m} \sum_{i=1}^{m} \xi_{i,j} y^{(j+1)}(x) = -\frac{1}{R_{sh}}. \tag{31}$$

Let $t = x$ and $u(t) \equiv 1$, (31) becomes the differential equation representation of an mth-order "dynamic" system:

$$y^{(1)}(t) - \sum_{j=1}^{m} \sum_{i=1}^{m} \xi_{i,j} y^{(j+1)}(t) = -\frac{u(t)}{R_{sh}}. \tag{32}$$

Taking Laplace transform for both sides of (32) yields

$$sY(s) - y(0) - \sum_{j=1}^{m} \sum_{i=1}^{m} \xi_{i,j} \left(s^{j+1} Y(s) - \sum_{k=1}^{j+1} s^{k-1} y^{(j+1-k)}(0) \right) = -\frac{U(s)}{R_{sh}}. \tag{33}$$

It follows from (26)-(28) that $y(0) = I_L$, $y^{(1)}(0) = -\sum_{i=1}^{m} I_{o_i}/a_i - 1/R_{sh}$, $y^{(k+1)}(0) = -\sum_{i=1}^{m} I_{o_i}/a_i^{k+1}$ for $k = 1, 2, \cdots, m$. Since $sU(s) = 1$, (33) becomes

$$sY(s) - I_L sU(s) - \sum_{j=1}^{m}\sum_{i=1}^{m} \xi_{i,j} \left[s^{j+1}Y(s) - U(s) \times \left(\sum_{k=1}^{j} s^k \sum_{i=1}^{m} \frac{-I_{o_i}}{a_i^{j+1-k}} - \frac{s^j}{R_{sh}} + I_L s^{j+1} \right) \right] = -\frac{U(s)}{R_{sh}}.$$

The transfer function is $G(s) = Y(s)/U(s) = N/D$, where

$$D = \sum_{j=1}^{m}\sum_{i=1}^{m} \xi_{i,j} s^{j+1} - s,$$

$$N = \frac{1}{R_{sh}} - I_L s + \sum_{j=1}^{m}\sum_{i=1}^{m} \xi_{i,j} \left(I_L s^{j+1} - \frac{s^j}{R_{sh}} - \sum_{k=1}^{j} s^k \sum_{i=1}^{m} \frac{I_{o_i}}{a_i^{j+1-k}} \right).$$

The corresponding time domain differential equation with zero initial condition is

$$\begin{aligned} &\alpha_{m+1} y^{(m+1)}(t) + \cdots + \alpha_2 y^{(2)}(t) - y^{(1)}(t) \\ =&\beta_{m+1} u^{(m+1)}(t) + \cdots + \beta_1 u^{(1)}(t) + \frac{u(t)}{R_{sh}}, \end{aligned} \tag{34}$$

where for $j = 1, 2, \cdots, m$,

$$\alpha_1 = -1, \tag{35}$$

$$\alpha_{j+1} = \sum_{i=1}^{m} \xi_{i,j}, \tag{36}$$

$$\beta_j = \alpha_j I_L - \frac{\alpha_{j+1}}{R_{sh}} - \sum_{k=j}^{m}\sum_{i=1}^{m} \frac{\alpha_{k+1} I_{o_i}}{a_i^{k+1-j}}, \tag{37}$$

$$\beta_{m+1} = \alpha_{m+1} I_L. \tag{38}$$

In general, by introducing a virtual "time" of $t = x$, the static relationship between two variables y and x can be regarded as dynamics from the linear system governed by (34). Once α_i and β_i are determined from system identification, diode model parameters I_L, I_{o_i}, a_i and R_{sh} can be solved linearly from (36)-(37).

3. Integral-Based Linear Identification

For an integer $n \geq 1$, define the multiple integral as [63]

$$\int_{[T_1,T_2]}^{(n)} f(\tau) = \underbrace{\int_{T_1}^{T_2} \int_{T_1}^{\tau_n} \cdots \int_{T_1}^{\tau_2}}_{n} f(\tau_1) \mathrm{d}\tau_1 \mathrm{d}\tau_2 \cdots \mathrm{d}\tau_n. \tag{39}$$

3.1. One-Diode Model

Applying (39) to (25) for $T_1 = 0$, $T_2 = t$ and $n = 2$ gives

$$ay(t) - aI_L u(t) + \left(I_L + I_o + \frac{a}{R_{sh}}\right) \int_{[0,t]}^{(1)} u(\tau) - \frac{1}{R_{sh}} \int_{[0,t]}^{(2)} u(\tau) = \int_{[0,t]}^{(1)} y(\tau). \tag{40}$$

Let $\theta = [a, aI_L, I_L + I_o + \frac{a}{R_{sh}}, \frac{1}{R_{sh}}]^T$, $\phi(t) = [y(t), -u(t), \int_{[0,t]}^{(1)} u(\tau), -\int_{[0,t]}^{(2)} u(\tau)]^T$ and $\gamma(t) = \int_{[0,t]}^{(1)} y(\tau)$, (40) can be rewritten as the matrix format of $\phi^T(t)\theta = \gamma(t)$. Note that the matrix format holds for any $t_i \in [0, t]$, $i = 1, 2, \cdots, N$, where N is the the number of data samples on the I-V curve. This actually casts an equation group of $\Phi\theta = \Gamma$ with $\Phi = [\phi(t_1), \phi(t_2), \cdots, \phi(t_N)]^T$ and $\Gamma = [\gamma(t_1), \gamma(t_2), \cdots, \gamma(t_N)]^T$. If $\Phi^T\Phi$ is nonsingular, the linear least square solution for θ is given by

$$\theta = \left(\Phi^T\Phi\right)^{-1} \Phi^T\Gamma, \tag{41}$$

which will minimise the square error of $(\Gamma - \Phi\theta)^T(\Gamma - \Phi\theta)$. Once θ is determined from (41), the parameters of one-diode model can be obtained by

$$\begin{aligned} a &= \theta_1, \\ I_L &= \frac{\theta_2}{\theta_1}, \\ I_o &= \theta_3 - \frac{\theta_2}{\theta_1} - \theta_1\theta_4, \\ R_{sh} &= \frac{1}{\theta_4}. \end{aligned}$$

3.2. Multi-Diode Model

Applying (39) to (34) for $T_1 = 0$, $T_2 = t$ and $n = m + 1$,

$$\begin{aligned}&\alpha_{m+1}y(t) + \cdots + \alpha_2 \int_{[0,t]}^{(m-1)} y(\tau) - \int_{[0,t]}^{(m)} y(\tau)\\ =&\beta_{m+1}u(t) + \cdots + \beta_1 \int_{[0,t]}^{(m)} u(\tau) + \frac{1}{R_{sh}} \int_{[0,t]}^{(m+1)} u(\tau).\end{aligned}$$

Let $\theta = [\alpha_{m+1}, \cdots, \alpha_2, \beta_{m+1}, \cdots, \beta_1, \frac{1}{R_{sh}}]^T$, $\phi(t)$=$[y(t), \cdots, \int_{[o,t]}^{(m-1)} y(\tau), -u(t), \cdots,$ $- \int_{[0,t]}^{(m+1)} u(\tau)]^T$, $\gamma(t) = \int_{[0,t]}^{(m)} y(\tau)$, θ and $\phi(t) \in \mathbb{R}_{(2m+2)\times 1}$, we have $\phi^T(t)\theta = \gamma(t)$. For $t_i \in [0, t]$, $i = 1, 2, \cdots, N$, the equation group can be described by $\Phi\theta = \Gamma$ with $\Phi = [\phi(t_1), \phi(t_2), \cdots, \phi(t_N)]^T$ and $\Gamma = [\gamma(t_1), \gamma(t_2), \cdots, \gamma(t_N)]^T$. If $\Phi^T\Phi$ is nonsingular, the least square solution for θ will be

$$\theta = \left(\Phi^T\Phi\right)^{-1} \Phi^T\Gamma. \tag{42}$$

Once θ is determined from (42), $R_{sh} = 1/\theta_{2m+2}$ is immediately derived. It follows from (38) that $I_L = \beta_{m+1}/\alpha_{m+1} = \theta_{m+1}/\theta_1$.

a_i ($i = 1, 2, \cdots, m$) will be derived in the following way. Rewriting (36) in matrix format gives

$$[\alpha_2, \cdots, \alpha_{m+1}] = \underbrace{[1, \cdots, 1]}_{m} A^{-1}.$$

Right-multiplying A for both sides gives

$$[\alpha_2, \cdots, \alpha_{m+1}] \begin{bmatrix} a_1^{-1} & \cdots & a_m^{-1} \\ \vdots & \ddots & \vdots \\ a_1^{-m} & \cdots & a_m^{-m} \end{bmatrix} = \underbrace{[1, \cdots, 1]}_{m},$$

which implies that $1/a_i$ are the roots of the following characteristic equation

$$\alpha_{m+1}\lambda^m + \alpha_m\lambda^{m-1} + \cdots + \alpha_2\lambda - 1 = 0. \tag{43}$$

Solving (43) for λ_i, and $a_i = 1/\lambda_i$, I_{o_i} ($i = 1, 2, \cdots, m$) will be derived as follows. (37) can be rewritten as

$$\beta_j = \alpha_j I_L - \frac{\alpha_{j+1}}{R_{sh}} - \sum_{i=1}^{m} I_{o_i} \sum_{k=j}^{m} \frac{\alpha_{k+1}}{a_i^{k+1-j}}.$$

Rewriting further as matrix format,

$$\underbrace{\begin{bmatrix} \sum_{k=1}^{m} \frac{\alpha_{k+1}}{a_1^k} & \sum_{k=1}^{m} \frac{\alpha_{k+1}}{a_2^k} & \cdots & \sum_{k=1}^{m} \frac{\alpha_{k+1}}{a_m^k} \\ \sum_{k=2}^{m} \frac{\alpha_{k+1}}{a_1^{k-1}} & \sum_{k=2}^{m} \frac{\alpha_{k+1}}{a_2^{k-1}} & \cdots & \sum_{k=2}^{m} \frac{\alpha_{k+1}}{a_m^{k-1}} \\ \vdots & \vdots & \ddots & \vdots \\ \sum_{k=m}^{m} \frac{\alpha_{k+1}}{a_1^{k+1-m}} & \sum_{k=m}^{m} \frac{\alpha_{k+1}}{a_2^{k+1-m}} & \cdots & \sum_{k=m}^{m} \frac{\alpha_{k+1}}{a_m^{k+1-m}} \end{bmatrix}}_{\Psi} \begin{bmatrix} I_{o_1} \\ I_{o_2} \\ \vdots \\ I_{o_m} \end{bmatrix} = -\underbrace{\begin{bmatrix} \beta_1 + I_L + \frac{\alpha_2}{R_{sh}} \\ \beta_2 - \alpha_2 I_L + \frac{\alpha_3}{R_{sh}} \\ \vdots \\ \beta_m - \alpha_m I_L + \frac{\alpha_{m+1}}{R_{sh}} \end{bmatrix}}_{\Xi}$$

Note from (43) that $\sum_{k=1}^{m} \alpha_{k+1}/a_i^k = 1$ for $i = 1, 2, \cdots, m$, Ψ can be simplified as

$$\Psi = \underbrace{\begin{bmatrix} 1 & 1 & \cdots & 1 \\ a_1 & a_2 & \cdots & a_m \\ \vdots & \vdots & \ddots & \vdots \\ a_1^{m-1} & a_2^{m-1} & \cdots & a_m^{m-1} \end{bmatrix}}_{\Psi^*} - \begin{bmatrix} 0 & \cdots & 0 \\ \alpha_2 & \cdots & \alpha_2 \\ \vdots & \ddots & \vdots \\ \sum_{k=1}^{m-1} \alpha_{k+1} a_1^{m-1-k} & \cdots & \sum_{k=1}^{m-1} \alpha_{k+1} a_m^{m-1-k} \end{bmatrix}.$$

This implies that after elementary row operations, Ψ is similar to Ψ^*, which is a Vandermonde matrix with $\det(\Psi^*) \neq 0$. Therefore, Ψ^{-1} exists (Ψ is full rank) and $[I_{o_1}, I_{o_2}, \cdots, I_{o_m}]^T = \Psi^{-1}\Xi$.

3.3. Nonsingularity of $\Phi^T\Phi$

The existence of the linear least square solution by (41) and (42) depends on the nonsingularity of $\Phi^T\Phi$, which is shown by the following lemma.

Lemma 3.1. *$\Phi^T\Phi$ is nonsingular if $a_i \neq a_j$ for $i \neq j$, $i, j = 1, 2, \cdots, m$, and the sampling number $N \geq 2m + 2$.*

Proof. Consider the general case of multi-diode model with

$$\Phi = [\phi(t_1), \phi(t_2), \cdots, \phi(t_N)]^T := [\Phi_1, \Phi_2],$$

$$\Phi_1 = \begin{bmatrix} y(t_1) & \int_{[0,t_1]}^{(1)} y(\tau) & \cdots & \int_{[0,t_1]}^{(m-1)} y(\tau) \\ y(t_2) & \int_{[0,t_2]}^{(1)} y(\tau) & \cdots & \int_{[0,t_2]}^{(m-1)} y(\tau) \\ \vdots & \vdots & \ddots & \vdots \\ y(t_N) & \int_{[0,t_N]}^{(1)} y(\tau) & \cdots & \int_{[0,t_N]}^{(m-1)} y(\tau) \end{bmatrix} := [\phi_{i,j}],$$

$$\Phi_2 = -\begin{bmatrix} u(t_1) & \int_{[0,t_1]}^{(1)} u(\tau) & \cdots & \int_{[0,t_1]}^{(m+1)} u(\tau) \\ u(t_2) & \int_{[0,t_2]}^{(1)} u(\tau) & \cdots & \int_{[0,t_2]}^{(m+1)} u(\tau) \\ \vdots & \vdots & \ddots & \vdots \\ u(t_N) & \int_{[0,t_N]}^{(1)} u(\tau) & \cdots & \int_{[0,t_N]}^{(m+1)} u(\tau) \end{bmatrix} =: [\varphi_{i,l}].$$

Recall from (26) that

$$y(t) = I_L + \sum_{i=1}^{m} I_{o_i} - \sum_{i=1}^{m} I_{o_i} \mathrm{e}^{\frac{t}{a_i}} - \frac{t}{R_{sh}},$$

and $u(t) \equiv 1$ by the definition. For $i = 1, 2, \cdots, N$,

$$\phi_{i,j} = \int_{[0,t_i]}^{(j-1)} y(\tau) = \frac{I_L + \sum\limits_{i=1}^{m} I_{o_i}}{(j-1)!} t_i^{j-1} - \frac{t_i^j}{j! R_{sh}} + \sum_{k=0}^{j-2} \sum_{l=1}^{m} I_{o_l} a_l^{j-k-1} \frac{t_i^k}{k!} - \sum_{k=1}^{j} I_{o_k} a_k^{j-1} \mathrm{e}^{\frac{t_i}{a_k}},$$

$$\varphi_{i,l} = -\int_{[0,t_i]}^{(l-1)} u(\tau) = -\frac{1}{j!} t_i^l,$$

where $j = 1, 2, \cdots, m$ and $l = 1, 2, \cdots, m+2$. After elementary column operations for Φ, $\Phi_1 \to \tilde{\Phi}_1 := [\tilde{\phi}_{i,j}]$ with

$$\tilde{\phi}_{i,j} = \sum_{k=1}^{j} I_{o_k} a_k^{j-1} \mathrm{e}^{\frac{t_i}{a_k}}.$$

In matrix format,

$$\tilde{\Phi}_1 = \underbrace{\begin{bmatrix} \mathrm{e}^{\frac{t_1}{a_1}} & \mathrm{e}^{\frac{t_1}{a_2}} & \cdots & \mathrm{e}^{\frac{t_1}{a_m}} \\ \mathrm{e}^{\frac{t_2}{a_1}} & \mathrm{e}^{\frac{t_2}{a_2}} & \cdots & \mathrm{e}^{\frac{t_2}{a_m}} \\ \vdots & \vdots & \ddots & \vdots \\ \mathrm{e}^{\frac{t_N}{a_1}} & \mathrm{e}^{\frac{t_N}{a_2}} & \cdots & \mathrm{e}^{\frac{t_N}{a_m}} \end{bmatrix}}_{E} \underbrace{\begin{bmatrix} I_{o_1} & & & \\ & I_{o_2} & & \\ & & \ddots & \\ & & & I_{o_m} \end{bmatrix}}_{\Lambda} \underbrace{\begin{bmatrix} 1 & a_1 & \cdots & a_1^{m-1} \\ 1 & a_2 & \cdots & a_2^{m-1} \\ \vdots & \vdots & \ddots & \vdots \\ 1 & a_m & \cdots & a_m^{m-1} \end{bmatrix}}_{V^*}.$$

Since Λ is diagonal and V^* is a standard Vandermonde matrix, $\mathrm{rank}(\Lambda) = \mathrm{rank}(V^*) = m$. If $t_2 - t_1 = t_3 - t_2 = \cdots = t_m - t_{m-1} = T_s > 0$, as $N \geq 2m + 2$, the first m row of E

$$E_m = \begin{bmatrix} 1 & 1 & \cdots & 1 \\ \mathrm{e}^{\frac{T_s}{a_1}} & \mathrm{e}^{\frac{T_s}{a_2}} & \cdots & \mathrm{e}^{\frac{T_s}{a_m}} \\ \vdots & \vdots & \ddots & \vdots \\ (\mathrm{e}^{\frac{T_s}{a_1}})^{n-1} & (\mathrm{e}^{\frac{T_s}{a_2}})^{n-1} & \cdots & (\mathrm{e}^{\frac{T_s}{a_m}})^{m-1} \end{bmatrix} \begin{bmatrix} \mathrm{e}^{\frac{t_1}{a_1}} & & & \\ & \mathrm{e}^{\frac{t_1}{a_2}} & & \\ & & \ddots & \\ & & & \mathrm{e}^{\frac{t_1}{a_m}} \end{bmatrix},$$

so $\mathrm{rank}(E) = \mathrm{rank}(E_m) = m$. Otherwise, it is always possible to find some ΔT such that $t_i = n_i \Delta T$, $n_i \in \mathbb{N}$ for $i = 1, 2, \cdots, m$. Construct matrix

$$E^* = \begin{bmatrix} 1 & 1 & \cdots & 1 \\ \mathrm{e}^{\frac{\Delta T}{a_1}} & \mathrm{e}^{\frac{\Delta T}{a_2}} & \cdots & \mathrm{e}^{\frac{\Delta T}{a_m}} \\ \vdots & \vdots & \ddots & \vdots \\ \mathrm{e}^{\frac{n_m \Delta T}{a_1}} & \mathrm{e}^{\frac{n_m \Delta T}{a_2}} & \cdots & \mathrm{e}^{\frac{n_m \Delta T}{a_m}} \end{bmatrix} \in \mathbb{R}_{n_m \times n},$$

and E_m is sub-matrix of E^*. Since E^* is a Vandermonde matrix with full column rank, $\mathrm{rank}(E) = \mathrm{rank}(E_m) = \mathrm{rank}(E^*) = m$. So, Φ_1 is full column rank, i.e., $\mathrm{rank}(\Phi_1) = m$.

$$\Phi_2 = \underbrace{\begin{bmatrix} t_1 & t_1^2 & \cdots & t_1^{m+2} \\ t_2 & t_2^2 & \cdots & t_2^{m+2} \\ \vdots & \vdots & \ddots & \vdots \\ t_N & t_N^2 & \cdots & t_N^{m+2} \end{bmatrix}}_{V_2} \begin{bmatrix} -1 & & & \\ & \ddots & & \\ & & \frac{-1}{(m+1)!} & \\ & & & \frac{-1}{(m+2)!} \end{bmatrix}$$

As $N \geq 2m + 2$, the first $m + 2$ row of V_2 is a Vandermonde matrix, so $\mathrm{rank}(\Phi_2) = \mathrm{rank}(V_2) = m + 2$, i.e., Φ_2 is full column rank. Since $\Phi = [\Phi_1, \Phi_2]$ with the full column rank of both Φ_1 and Φ_2, Φ is also full column rank. $N \geq 2m + 2$ implies that the row number of Φ is no less than the column number. So, $\mathrm{rank}(\Phi) = 2m+2$ and $\Phi^T\Phi$ is full rank, i.e., $(\Phi^T\Phi)^{-1}$ exists. □

3.4. Calculation of Multiple Integrals

In practice, the integral shown as (39) is numerically estimated by rectangular or trapezoidal integration. For example, suppose there are N samples at

$t_1, t_2, \cdots, t_N$, the rectangular integration gives

$$\begin{aligned}
\int_{[t_1,t_i]}^{(1)} f(\tau) &= \int_{t_1}^{t_i} f(\tau_1)\mathrm{d}\tau_1 \approx \sum_{k=1}^{i-1} f(k)(t_{k+1}-t_k) := f_1(i),\\
\int_{[t_1,t_i]}^{(2)} f(\tau) &\approx \sum_{k=1}^{i-1} f_1(k)(t_{k+1}-t_k) := f_2(i),\\
&\vdots\\
\int_{[t_1,t_i]}^{(n)} f(\tau) &\approx \sum_{k=1}^{i-1} f_{n-1}(k)(t_{k+1}-t_k) := f_n(i).
\end{aligned}$$

for $i = 1, 2, \cdots, N$. The more number of samples, f_i, the more accurate the estimation to the multiple integrals will be.

3.5. Determination of R_s

To calculate θ from (41) or (42), Φ and Γ must be known. As both of them are integrals to t, t must be known as well. Since $t = V + R_s I$, R_s must be determined before applying integrals. It is clear to see that if R_s is bigger than its real value, t will increase so that the whole I-V curve will move to the right and the error between the real and estimated I-V curves will be positive; If R_s decreases, the whole I-V curve will move to the left and the error between the real and estimated I-V curves will be negative. Thus, R_s can be used as a tuning parameter such that the root mean square error (RMSE) is minimised.

It derives from (3) that

$$-\frac{1}{\left.\frac{\mathrm{d}I}{\mathrm{d}V}\right|_{oc}} = R_s + \frac{1}{\sum\limits_{i=1}^{m} \frac{I_{o_i}}{a_i}\mathrm{e}^{\frac{V_{oc}}{a_i}} + \frac{1}{R_{sh}}} > R_s,$$

which implies the upper bound of R_s, i.e., $R_s^{upp} = -1/\left.\frac{\mathrm{d}I}{\mathrm{d}V}\right|_{oc}$. The lower bound of R_s can be zero at first, i.e., $R_s^{low} = 0$. With such a band of $R_s \in [R_s^{low}, R_s^{upp}]$, binary search algorithm is applied to determine R_s in the following way:

Step 1. Arbitrarily choose R_s from $[R_s^{low}, R_s^{upp}]$ and calculate $\hat{a}_i$, $\hat{I}_L$, $\hat{I}_{o_i}$ and $\hat{R}_{sh}$ from the proposed linear least square (41) or (42);

Step 2. Calculate from (3) that

$$\hat{y}(t) = \hat{I}_L - \sum_{i=1}^{m} \hat{I}_{o_i}\left(\mathrm{e}^{\frac{V+R_s I}{\hat{a}_i}} - 1\right) - \frac{V + R_s I}{\hat{R}_{sh}},$$

and $RMSE = \sqrt{\sum_{i=1}^{N} \left[\hat{y}(t_i) - y(t_i)\right]^2 / N}$.

Step 3. Calculate $ERR = \sum_{i=1}^{N} [\hat{y}(t_i) - y(t_i)]$. If $ERR > 0$, adjust $R_s = (R_s + R_s^{low})/2$. Otherwise, adjust $R_s = (R_s + R_s^{upp})/2$.

Step 4. Update R_s^{upp} and R_s^{low} according to the sign of ERR. If $ERR > 0$, $R_s^{upp} = R_s$, otherwise, $R_s^{low} = R_s$.

Step 5. If $RMSE$ is less than some tolerance or the iterative cycle reaches some preset number, stop the searching. Otherwise, update R_s^{upp} and R_s^{low} according to the sign of ERR and go back to **Step 2**. The flowchart of the binary searching algorithm is shown in Figure 3.

3.6. Robustness Enhancement

From the viewpoint of control theory, the transfer function (24) has a pole of $s = 1/a > 0$, which implies the system (25) is unstable. This is also true for the general case of multi-diode model. Identification for unstable system is not preferred because the convergence of the proposed algorithm might be sensitive to the accuracy of the integral calculation in such a case. To improve the robustness of the proposed algorithm, $\tilde{V}$ is introduced to yield a stable system.

In case of one-diode model, let $V = V_{oc} - \tilde{V}$, $0 \le \tilde{V} \le V_{oc}$, and $\tilde{x} = \tilde{V} - R_s I$, thus $x = V + R_s I = V_{oc} - (\tilde{V} - R_s I) = V_{oc} - \tilde{x}$. It follows from (18)-(20) that

$$
\begin{aligned}
y &= I_L + I_o - \frac{V_{oc}}{R_{sh}} - I_o \mathrm{e}^{\frac{V_{oc}}{a}} \mathrm{e}^{-\frac{\tilde{x}}{a}} + \frac{\tilde{x}}{R_{sh}}, \\
\frac{\mathrm{d}y}{\mathrm{d}\tilde{x}} &= \frac{I_o}{a} \mathrm{e}^{\frac{V_{oc}}{a}} \mathrm{e}^{-\frac{\tilde{x}}{a}} + \frac{1}{R_{sh}}, \\
\frac{\mathrm{d}^2 y}{\mathrm{d}\tilde{x}^2} &= -\frac{I_o}{a^2} \mathrm{e}^{\frac{V_{oc}}{a}} \mathrm{e}^{-\frac{\tilde{x}}{a}}.
\end{aligned}
$$

Let $t = \tilde{x}$ and $u(t) \equiv 1$, by eliminating $\mathrm{e}^{-\tilde{x}/a}$ it gives

$$
a \frac{\mathrm{d}^2 y(t)}{\mathrm{d}t^2} + \frac{\mathrm{d}y(t)}{\mathrm{d}t} = \frac{u(t)}{R_{sh}}.
$$

The corresponding transfer function is

$$
G(s) = \frac{Y(s)}{U(s)} = \frac{ay(0)s^2 + [ay'(0) + y(0)]s + \frac{1}{R_{sh}}}{as^2 + s},
$$

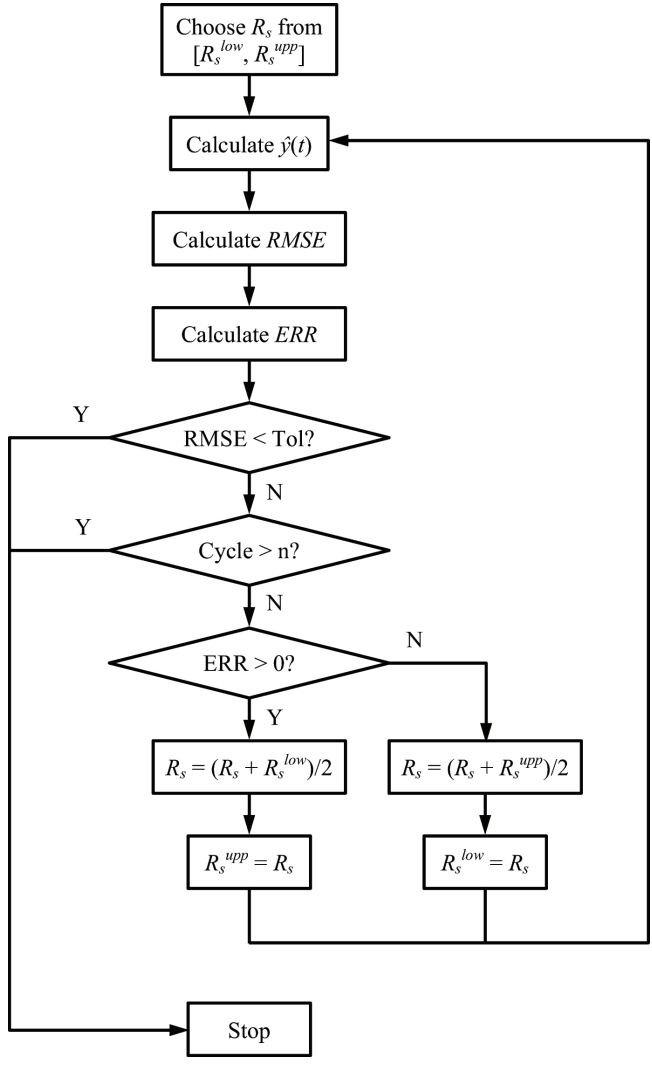

Figure 3. Flowchart of the binary searching algorithm.

where $y(0) = I_L - I_o(\mathrm{e}^{V_{oc}/a} - 1) - V_{oc}/R_{sh}$, $y'(0) = I_o\mathrm{e}^{V_{oc}/a}/a + 1/R_{sh}$. In this way, the unstable pole $s = 1/a > 0$ becomes stable as $s = -1/a < 0$.

The remaining procedures are the same as aforementioned. Let $\gamma(t) =$

$-\int_{[0,t]}^{(1)} y(\tau), \phi(t) = \left[y(t), -u(t), -\int_{[0,t]}^{(1)} u(\tau), -\int_{[0,t]}^{(2)} u(\tau)\right]^T$, and

$$\theta = \begin{bmatrix} a \\ aI_L - aI_o(\mathrm{e}^{\frac{V_{oc}}{a}} - 1) - \frac{aV_{oc}}{R_{sh}} \\ I_L + I_o - \frac{V_{oc}-a}{R_{sh}} \\ \frac{1}{R_{sh}} \end{bmatrix},$$

the linear least square solution is $\theta = \left(\Phi^T\Phi\right)^{-1}\Phi^T\Gamma$ with $\Phi = [\phi(t_1), \phi(t_2), \cdots, \phi(t_N)]^T$ and $\Gamma = [\gamma(t_1), \gamma(t_2), \cdots, \gamma(t_N)]^T$. Once θ is determined, the parameters of one-diode model are obtained by

$$\begin{aligned} a &= \theta_1, \\ I_L &= \frac{\theta_2}{\theta_1} + \left(\theta_3 - \frac{\theta_2}{\theta_1} - \theta_1\theta_4\right)\left(1 - \mathrm{e}^{-\frac{V_{oc}}{\theta_1}}\right) + V_{oc}\theta_4, \\ I_o &= \frac{\theta_3 - \frac{\theta_2}{\theta_1} - \theta_1\theta_4}{\mathrm{e}^{\frac{V_{oc}}{\theta_1}}}, \\ R_{sh} &= \frac{1}{\theta_4}. \end{aligned}$$

In the case of a multi-diode model, with the same transform of $x = V_{oc} - \tilde{x}$, (26) becomes

$$y = I_L + \sum_{i=1}^{m} I_{o_i} - \sum_{i=1}^{m} I_{o_i}\mathrm{e}^{\frac{V_{oc}}{a_i}}\mathrm{e}^{-\frac{\tilde{x}}{a_i}} - \frac{V_{oc}}{R_{sh}} + \frac{\tilde{x}}{R_{sh}}. \tag{44}$$

Let $\tilde{a}_i = -a_i$, $\tilde{I}_L = I_L + \sum_{i=1}^{m} I_{o_i}(1 - \mathrm{e}^{V_{oc}/a_i}) - V_{oc}/R_{sh}$, $\tilde{I}_{o_i} = I_{o_i}\mathrm{e}^{V_{oc}/a_i}$, $\tilde{R}_{sh} = -R_{sh}$, and (44) is equivalent to

$$y = \tilde{I}_L + \sum_{i=1}^{m} \tilde{I}_{o_i} - \sum_{i=1}^{m} \tilde{I}_{o_i}\mathrm{e}^{\frac{\tilde{x}}{\tilde{a}_i}} - \frac{\tilde{x}}{\tilde{R}_{sh}},$$

which has the same format as (26). This means that all the derivation aforementioned are applicable to the parameter set $\{\tilde{a}_i, \tilde{I}_L, \tilde{I}_{o_i}, \tilde{R}_{sh}\}$. Once they are

determined, the parameter set $\{a_i, I_L, I_{o_i}, R_{sh}\}$ is derived immediately by

$$\begin{aligned} a_i &= -\tilde{a}_i, \\ R_{sh} &= -\tilde{R}_{sh}, \\ I_{o_i} &= \tilde{I}_{o_i} \mathrm{e}^{-\frac{V_{oc}}{a_i}}, \\ I_L &= \tilde{I}_L - \sum_{i=1}^{m} I_{o_i} \left(1 - \mathrm{e}^{\frac{V_{oc}}{a_i}}\right) + \frac{V_{oc}}{R_{sh}}. \end{aligned}$$

4. Validation

4.1. Indoor Flash Test

The I-V characteristics of full-sized commercial modules were measured indoor by a pulsed solar simulator (PASAN IIIB) with a constant illumination intensity plateau of about $12ms$ used. The data acquisition, which requires about $10ms$, occurs during the plateau period, whereby the light intensity varies by less than $\pm 1\%$. The intensity of the solar simulator is calibrated with a c-Si reference cell certified by Fraunhofer ISE. The overall uncertainty of module power measurement is within $\pm 2\%$.

Consider the I-V characteristic of a crystalline PV module from the indoor flash test under STC ($1000W/m^2$, $25°C$, AM $= 1.5$) is shown in Figure 4. Both one-diode and two-diode models are considered for this case study.

4.1.1. One-Diode Model

Firstly, use the last 10 points at OC to derive a linear fitting: $I = kV + p$, where $k = -0.9131$. $R_s^{upp} \approx -1/k = 1.0952$. $R_s^{low} = 0$. Arbitrarily choose $R_s \in [R_s^{low}, R_s^{upp}]$, e.g., $R_s = 1.0952$, and follow the proposed integral-based linear identification presented in Section 3.1, R_s converges to $R_s = 0.655$ after about 30 steps with the proposed binary searching, as shown in Figure 6. Multiple integrals from (39) are estimated by the numerical integration presented in Section 3.4. It follows from (41) that $\theta_1 = 1.9891$, $\theta_2 = 9.8295$, $\theta_3 = 4.9434$,

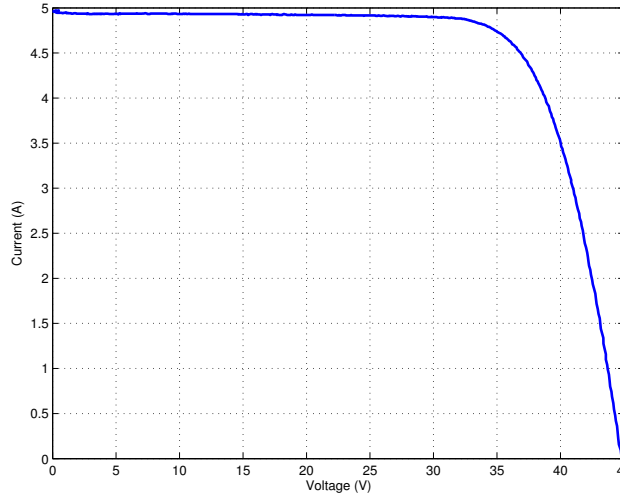

Figure 4. The I-V characteristic of a crystalline PV module.

$\theta_4 = 8.9631 \times 10^{-4}$. Thus,

$$
\begin{aligned}
a &= \theta_1 = 1.9891 \text{ (V)}, \\
I_L &= \frac{\theta_2}{\theta_1} = 4.9416 \text{ (A)}, \\
I_o &= \theta_3 - \frac{\theta_2}{\theta_1} - \theta_1\theta_4 = 4.1785 \times 10^{-9} \text{ (A)}, \\
R_{sh} &= \frac{1}{\theta_4} = 1.1157 \times 10^{3} \text{ } (\Omega).
\end{aligned}
$$

The comparison between the I-V curves from the real measurement and the one-code model is shown in Figure 5, where the average absolute error $\bar{E} = 1/N \sum_{i=1}^{N} |ERR| = 0.0085$. The $RMSE$ is shown in Figure 6, which converges to 1.67% at last after 35 steps with $\mathrm{Tol} = 2\%$.

4.1.2. Two-Diode Model

It is clear to see from Figure 5 that one-diode model is good enough to represent the whole I-V curve accurately. This implies that if two-diode model is applied,

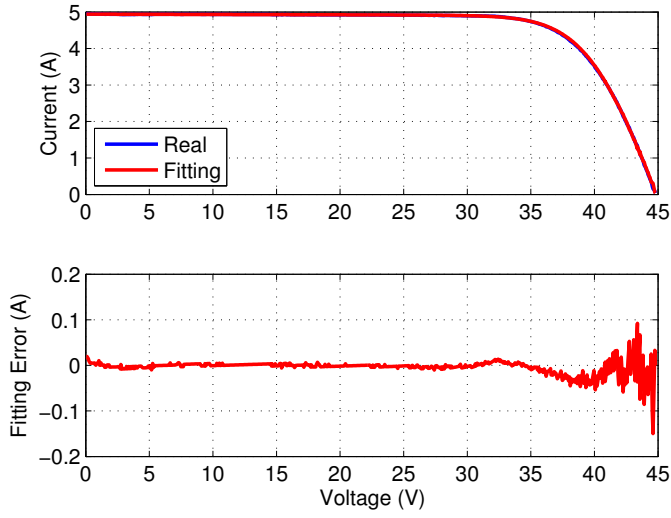

Figure 5. Accuracy of the proposed method for c-Si module.

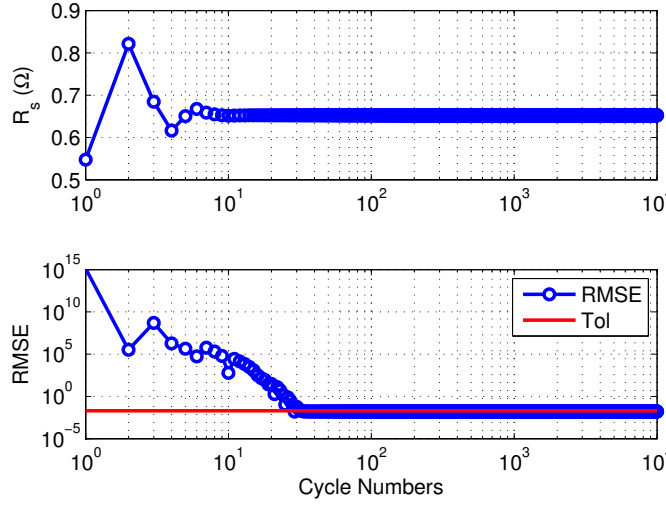

Figure 6. Convergence of R_s and $RMSE$ for c-Si module.

$I_{o_2} \to 0$, which will cause a singular matrix in the identification of Section 3.2 To avoid such a potential problem, robustness enhancement discussed in Section 3.6 will be applied. With $m = 2$, (44) becomes

$$y = I_L + I_{o_1}\left(1 - \mathrm{e}^{\frac{V_{oc}-\tilde{x}}{a_1}}\right) + I_{o_2}\left(1 - \mathrm{e}^{\frac{V_{oc}-\tilde{x}}{a_2}}\right) - \frac{V_{oc} - \tilde{x}}{R_{sh}},$$

where $\tilde{x} = \tilde{V} - R_s I$, $\tilde{V} = V_{oc} - V$. And its multiple differentials are

$$\frac{\mathrm{d}y}{\mathrm{d}\tilde{x}} = \frac{I_{o_1}}{a_1}\mathrm{e}^{\frac{V_{oc}-\tilde{x}}{a_1}} + \frac{I_{o_2}}{a_2}\mathrm{e}^{\frac{V_{oc}-\tilde{x}}{a_2}} + \frac{1}{R_{sh}}, \tag{45}$$

$$\frac{\mathrm{d}^2y}{\mathrm{d}\tilde{x}^2} = -\frac{I_{o_1}}{a_1^2}\mathrm{e}^{\frac{V_{oc}-\tilde{x}}{a_1}} - \frac{I_{o_2}}{a_2^2}\mathrm{e}^{\frac{V_{oc}-\tilde{x}}{a_2}}, \tag{46}$$

$$\frac{\mathrm{d}^3y}{\mathrm{d}\tilde{x}^3} = \frac{I_{o_1}}{a_1^3}\mathrm{e}^{\frac{V_{oc}-\tilde{x}}{a_1}} + \frac{I_{o_2}}{a_2^3}\mathrm{e}^{\frac{V_{oc}-\tilde{x}}{a_2}}. \tag{47}$$

(46) and (47) in matrix format are

$$\begin{bmatrix} \dfrac{\mathrm{d}^2y}{\mathrm{d}\tilde{x}^2} \\ \dfrac{\mathrm{d}^3y}{\mathrm{d}\tilde{x}^3} \end{bmatrix} = \begin{bmatrix} -\dfrac{I_{o_1}}{a_1^2} & -\dfrac{I_{o_2}}{a_2^2} \\ \dfrac{I_{o_1}}{a_1^3} & \dfrac{I_{o_2}}{a_2^3} \end{bmatrix} \begin{bmatrix} \mathrm{e}^{\frac{V_{oc}-\tilde{x}}{a_1}} \\ \mathrm{e}^{\frac{V_{oc}-\tilde{x}}{a_2}} \end{bmatrix}.$$

Thus,

$$\begin{aligned} \begin{bmatrix} \mathrm{e}^{\frac{V_{oc}-\tilde{x}}{a_1}} \\ \mathrm{e}^{\frac{V_{oc}-\tilde{x}}{a_2}} \end{bmatrix} &= \begin{bmatrix} -\dfrac{I_{o_1}}{a_1^2} & -\dfrac{I_{o_2}}{a_2^2} \\ \dfrac{I_{o_1}}{a_1^3} & \dfrac{I_{o_2}}{a_2^3} \end{bmatrix}^{-1} \begin{bmatrix} \dfrac{\mathrm{d}^2y}{\mathrm{d}\tilde{x}^2} \\ \dfrac{\mathrm{d}^3y}{\mathrm{d}\tilde{x}^3} \end{bmatrix} \\ &= \begin{bmatrix} \dfrac{a_1^3}{I_{o_1}(a_2 - a_1)} & \dfrac{a_1^3 a_2}{I_{o_1}(a_2 - a_1)} \\ -\dfrac{a_2^3}{I_{o_2}(a_2 - a_1)} & -\dfrac{a_1 a_2^3}{I_{o_2}(a_2 - a_1)} \end{bmatrix} \begin{bmatrix} \dfrac{\mathrm{d}^2y}{\mathrm{d}\tilde{x}^2} \\ \dfrac{\mathrm{d}^3y}{\mathrm{d}\tilde{x}^3} \end{bmatrix}. \end{aligned}$$

Substitute it into (45), it yields

$$a_1 a_2 \frac{\mathrm{d}^3y(t)}{\mathrm{d}t^3} + (a_1 + a_2)\frac{\mathrm{d}^2y(t)}{\mathrm{d}t^2} + \frac{\mathrm{d}y(t)}{\mathrm{d}t} = \frac{u(t)}{R_{sh}}, \tag{48}$$

where $t = \tilde{x}$ and $u(t) \equiv 0$. After Laplace transform, (48) becomes

$$a_1a_2\left[s^3Y(s) - y''(0) - sy'(0) - s^2y(0)\right] + (a_1 + a_2)\left[s^2Y(s) - y'(0) - sy(0)\right] + [sY(s) - y(0)] = \frac{U(s)}{R_{sh}}, \tag{49}$$

where

$$y(0) = I_L + I_{o_1}\left(1 - \mathrm{e}^{\frac{V_{oc}}{a_1}}\right) + I_{o_2}\left(1 - \mathrm{e}^{\frac{V_{oc}}{a_2}}\right) - \frac{V_{oc}}{R_{sh}}, \tag{50}$$

$$y'(0) = \frac{I_{o_1}}{a_1}\mathrm{e}^{\frac{V_{oc}}{a_1}} + \frac{I_{o_2}}{a_2}\mathrm{e}^{\frac{V_{oc}}{a_2}} + \frac{1}{R_{sh}}, \tag{51}$$

$$y''(0) = -\frac{I_{o_1}}{a_1^2}\mathrm{e}^{\frac{V_{oc}}{a_1}} - \frac{I_{o_2}}{a_2^2}\mathrm{e}^{\frac{V_{oc}}{a_2}}. \tag{52}$$

Utilize $sU(s) = 1$, and (49) is equivalent to

$$a_1a_2s^3Y(s) + (a_1 + a_2)s^2Y(s) - a_1a_2y(0)s^3U(s) - \left[a_1a_2y'(0) + (a_1 + a_2)y(0)\right]s^2U(s) - \frac{U(s)}{R_{sh}} - \left[a_1a_2y''(0) + (a_1 + a_2)y'(0) + y(0)\right]sU(s) = -sY(s).$$

Therefore, the differential equation representation with zero initial conditions are

$$a_1a_2\frac{\mathrm{d}^3y(t)}{\mathrm{d}t^3} + (a_1 + a_2)\frac{\mathrm{d}^2y(t)}{\mathrm{d}t^2} - a_1a_2y(0)\frac{\mathrm{d}^3u(t)}{\mathrm{d}t^3} - \left[a_1a_2y'(0) + (a_1 + a_2)y(0)\right]\frac{\mathrm{d}^2u(t)}{\mathrm{d}t^2} - \frac{u(t)}{R_{sh}} - \left[a_1a_2y''(0) + (a_1 + a_2)y'(0) + y(0)\right]\frac{\mathrm{d}u(t)}{\mathrm{d}t} = -\frac{\mathrm{d}y(t)}{\mathrm{d}t}. \tag{53}$$

Applying triple integral (39) (with $n = 3$) to (53), we have

$$a_1a_2y(t) + (a_1 + a_2)\int_{[0,t]}^{(1)} y(\tau) - a_1a_2y(0)u(t) - \left[a_1a_2y'(0) + (a_1 + a_2)y(0)\right]\int_{[0,t]}^{(1)} u(\tau) - \frac{1}{R_{sh}}\int_{[0,t]}^{(3)} u(\tau) - \left[a_1a_2y''(0) + (a_1 + a_2)y'(0) + y(0)\right]\int_{[0,t]}^{(2)} u(\tau) = -\int_{[0,t]}^{(2)} y(\tau). \tag{54}$$

Let $\phi(t) = [y(t), \int_{[0,t]}^{(1)} y(\tau), -u(t), -\int_{[0,t]}^{(1)} u(\tau), -\int_{[0,t]}^{(2)} u(\tau), -\int_{[0,t]}^{(3)} u(\tau)]^T$,

$$\theta := \begin{bmatrix} \theta_1 \\ \theta_2 \\ \theta_3 \\ \theta_4 \\ \theta_5 \\ \theta_6 \end{bmatrix} = \begin{bmatrix} a_1a_2 \\ a_1 + a_2 \\ \theta_1y(0) \\ \theta_1y'(0) + \theta_2y(0) \\ \theta_1y''(0) + \theta_2y'(0) + y(0) \\ 1/R_{sh} \end{bmatrix}, \tag{55}$$

and $\gamma(t) = -\int_{[0,t]}^{(2)} y(\tau)$, then (54) can be rewritten in matrix format of $\phi(t)^T\theta = \gamma(t)$. The linear least solution to θ is given by (42). Immediately, $a_{1,2} = (\theta_2 \pm \sqrt{\theta_2^2 - 4\theta_1})/2$, $R_{sh} = 1/\theta_6$, and

$$\begin{bmatrix} \theta_3 \\ \theta_4 \\ \theta_5 \end{bmatrix} = \begin{bmatrix} \theta_1 & 0 & 0 \\ \theta_2 & \theta_1 & 0 \\ 1 & \theta_2 & \theta_1 \end{bmatrix} \begin{bmatrix} y(0) \\ y'(0) \\ y''(0) \end{bmatrix}.$$

Therefore,

$$\begin{bmatrix} y(0) \\ y'(0) \\ y''(0) \end{bmatrix} = \begin{bmatrix} \theta_1 & 0 & 0 \\ \theta_2 & \theta_1 & 0 \\ 1 & \theta_2 & \theta_1 \end{bmatrix}^{-1} \begin{bmatrix} \theta_3 \\ \theta_4 \\ \theta_5 \end{bmatrix}.$$

It follows from (50)-(52) that

$$\begin{bmatrix} y(0) + V_{oc}/R_{sh} \\ y'(0) - 1/R_{sh} \\ y''(0) \end{bmatrix} = \begin{bmatrix} 1 & 1 - \mathrm{e}^{\frac{V_{oc}}{a_1}} & 1 - \mathrm{e}^{\frac{V_{oc}}{a_2}} \\ 0 & \mathrm{e}^{\frac{V_{oc}}{a_1}}/a_1 & \mathrm{e}^{\frac{V_{oc}}{a_2}}/a_2 \\ 0 & -\mathrm{e}^{\frac{V_{oc}}{a_1}}/a_1^2 & -\mathrm{e}^{\frac{V_{oc}}{a_2}}/a_2^2 \end{bmatrix} \begin{bmatrix} I_L \\ I_{o_1} \\ I_{o_2} \end{bmatrix}.$$

Thus,

$$\begin{bmatrix} I_L \\ I_{o_1} \\ I_{o_2} \end{bmatrix} = \begin{bmatrix} 1 & 1 - \mathrm{e}^{\frac{V_{oc}}{a_1}} & 1 - \mathrm{e}^{\frac{V_{oc}}{a_2}} \\ 0 & \mathrm{e}^{\frac{V_{oc}}{a_1}}/a_1 & \mathrm{e}^{\frac{V_{oc}}{a_2}}/a_2 \\ 0 & -\mathrm{e}^{\frac{V_{oc}}{a_1}}/a_1^2 & -\mathrm{e}^{\frac{V_{oc}}{a_2}}/a_2^2 \end{bmatrix}^{-1} \begin{bmatrix} y(0) + V_{oc}/R_{sh} \\ y'(0) - 1/R_{sh} \\ y''(0) \end{bmatrix}.$$

In this way, with the same I-V characteristics data as shown in Figure5, we got $\theta_1 = 0.6849$, $\theta_2 = 2.2356$, $\theta_3 = 0.0247$, $\theta_4 = 3.3348$, $\theta_5 = 4.9034$ and $\theta_6 = 0.0010$. The two-diode model parameters are identified as

$$\begin{aligned} a_1 &= 1.8691\,(\mathrm{V}), \\ a_2 &= 0.3664\,(\mathrm{V}), \\ I_{o_1} &= 1.5168 \times 10^{-10}\,(\mathrm{A}), \\ I_{o_2} &= 7.9060 \times 10^{-54}\,(\mathrm{A}), \\ I_L &= 4.9480\,(\mathrm{A}), \\ R_{sh} &= 955.1229\,(\Omega), \\ R_s &= 0.6845\,(\Omega). \end{aligned}$$

The average absolute error $\bar{E} = 0.0080$ and $RMSE = 1.35\%$, both of which are slightly reduced as compared to the one-diode model result. As expected, I_{o_2} is indeed extremely close to zero, whereas other parameters are comparable to their counter parts in one-diode model result.

It should be highlighted that the diode model parameters derived from the indoor flash test are not constant. Actually, they are varying with temperature and solar radiation. Therefore, it is necessary to check the online computability of the proposed method for PV modules under non-constant environment, which is demonstrated by the outdoor module testing as follows.

4.2. Outdoor Module Testing

Outdoor module testing (OMT) is usually carried out by many PV panel manufacturers and solar research institutes for the module performance evaluation under the real operating environments. DC parameters including full I-V curves, V_{oc}, I_{sc}, V_{mpp}, I_{mpp}, P_{mpp} together with module temperature are measured and logged every minute. Environmental parameters including in-plane solar irradiance G_{si}, ambient temperature T_{amb}, module temperature T_{mod}, wind speed and wind direction are logged simultaneously with the DC parameters. Between I-V measurements, electrical energy is maintained at the module maximum power point (MPP). The uncertainty of all electrical measured parameters is within $\pm 0.1\%$ for full scale. With these I-V data in time series, the diode model parameters can be identified online by the proposed method and correlated to the environmental factors like irradiance, temperature, etc.

Figure 7 shows the time series of G_{si}, T_{amb} and T_{mod} on a typical day from the OMT testbed of Solar Energy Research Institute of Singapore (SERIS). The plot is centred around the solar noon, which was at $13:10$ on the 5 August 2010.

By applying the proposed method in Section 3, the time-varying one-diode model parameters I_L, I_o, a, R_s and R_{sh} for the same day are identified, as shown in Figure 8. The variation of the identified parameters reflects the dynamics of the PV module under different environmental conditions, which cannot be seen from the static I-V curves.

The relationships between the identified parameters and the environmental operating conditions are further illustrated in Figure 9-12. A proportional relationship between I_L and irradiance intensity is observed in Figure 9. It is also apparent from Figure 10 that I_o generally shows an increasing trend with rising

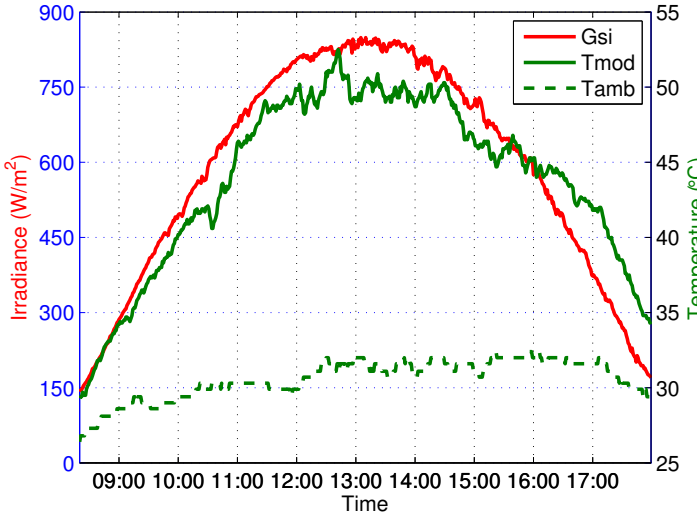

Figure 7. Environmental factors of a typical day in SERIS' OMT testbed.

module temperature. This also agrees with the theoretical temperature dependence of I_o, as given by $I_o = BT^3 \mathrm{e}^{-E_g/(kT)}$, where E_g is the band gap of silicon and B is a temperature independent constant [14]. Figure 11 illustrates that a generally decreases with increasing irradiance for $G_{si} < 300$ W/m^2 and increases beyond that, which is as reported in [64]. When irradiance decreases in Figure 12, the series resistance R_s decreases and the shunt resistance R_{sh} increases, which is consistent with previous reported results [65]. The decrease in R_s is due to the decreased thermal loss ($I^2 R_s$) with decreasing irradiance.

The RMSE of the proposed algorithm in OMT case is shown in Figure13, where the burden of the online calculation for convergence (iterative steps for R_s until Tol or maximum cycle is achieved) is presented as well. Among 600 plus I-V scans during the day, there are only three cases with the RMSE exceeding the preset 1% Tol when the maximum number (100) of steps is reached. Even for these three cases, the RMSE is still below 1.5%. The iterative steps are very stable, and they are usually less than 30. This indicates that the online calculation burden of the proposed algorithm is low and the identification can be done by an industrial PC locally between two consecutive I-V scan (1 min in our case).

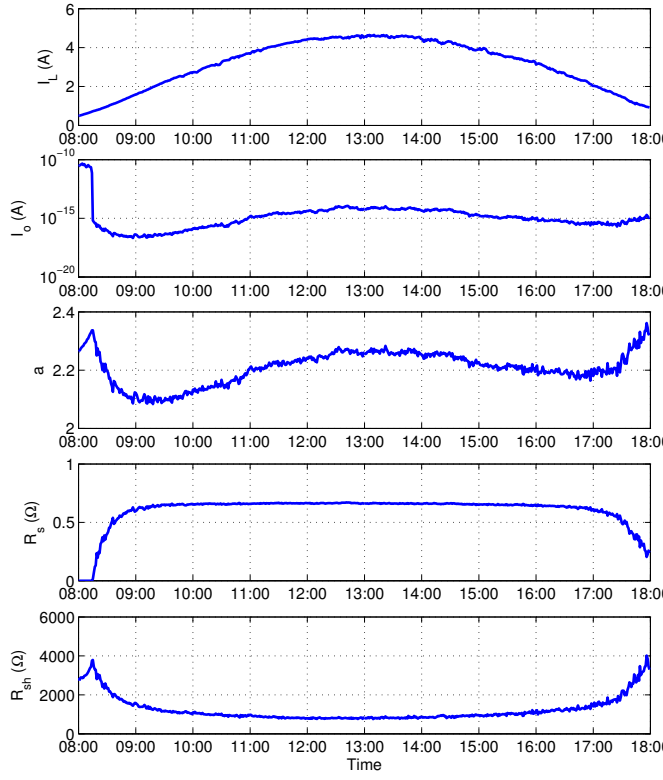

Figure 8. Identified one-diode model parameters.

5. Comparison with Other Methods

In this section, the comparison of the proposed method with the approaches of iterative searching (based on Lambert W function) and evolutionary algorithms (mainly DE and GA) are discussed because they represent the most accurate estimation of PV model parameters.

5.1. Lambert W Function Based Method

In [32], two data sets of I-V curves (26 points) are presented, which are initially proposed in [39] and are commonly used to test the effectiveness of the extraction algorithms. One refers to a solar module (Photowatt-PWP 201) at

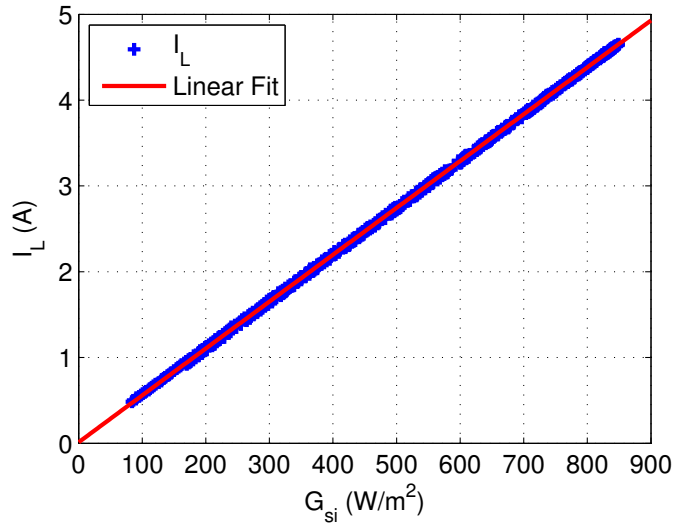

Figure 9. Proportional relationship between I_L and G_{si}.

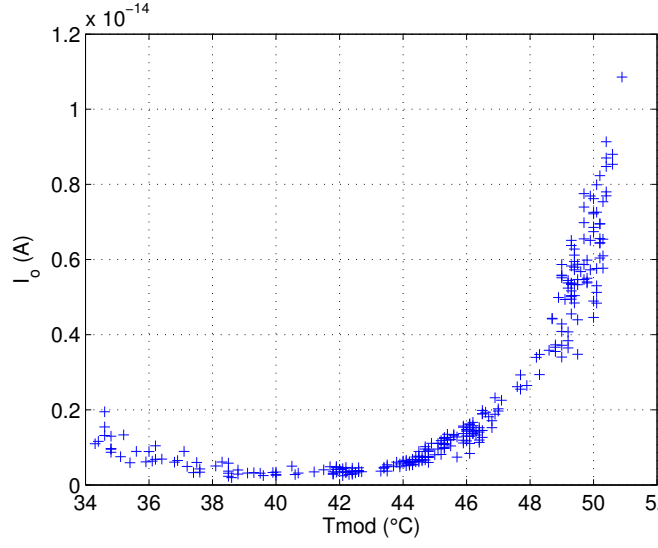

Figure 10. Relationship between I_o and T_{mod}.

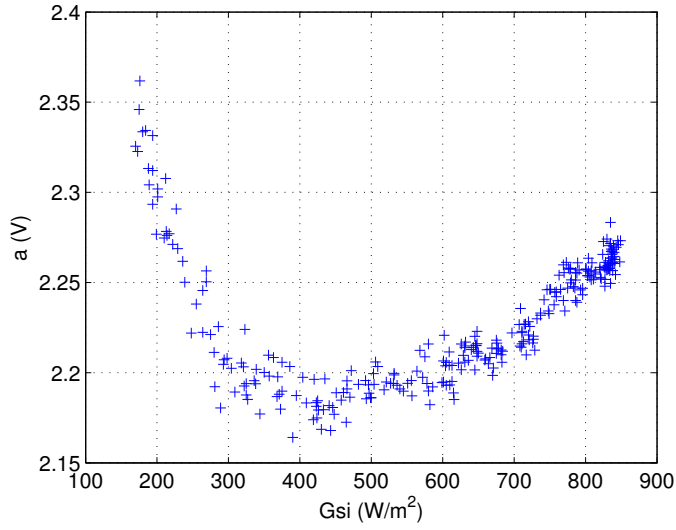

Figure 11. Relationship between a and G_{si}.

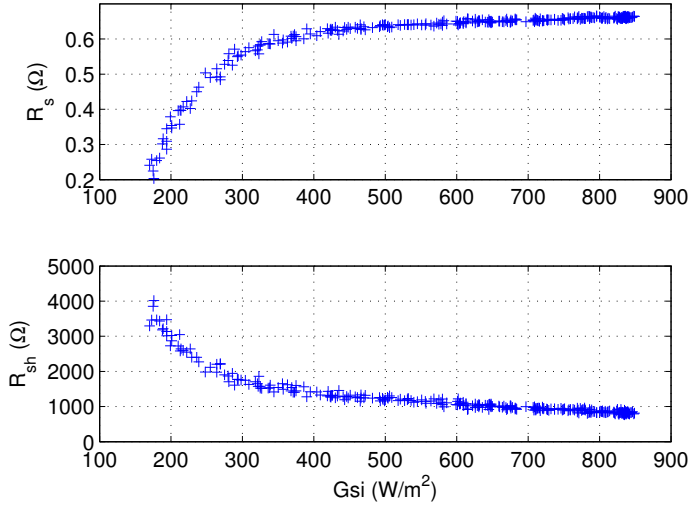

Figure 12. Relationship between R_s, R_sh and G_{si}.

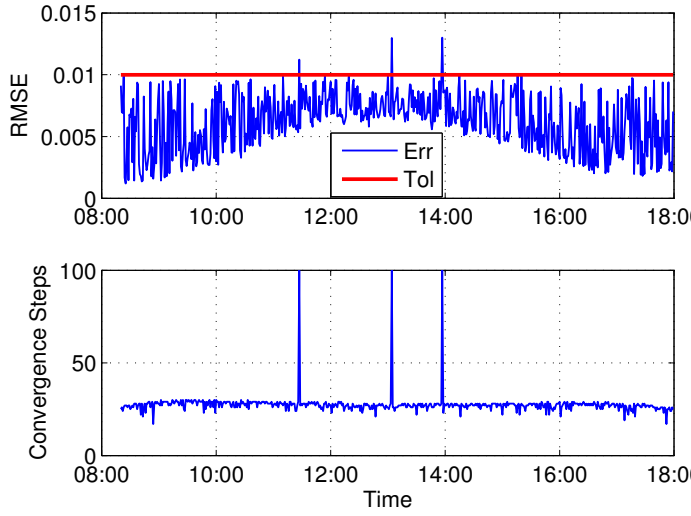

Figure 13. RMSE and burden of online calculation.

45°C and the other refers to a solar cell (c-Si) at 33°C, as shown in Table 1. The one-diode model parameters I_L, I_o and R_{sh} are proved to be functions of R_s and a. So the searching in the two-dimensional parameter space of R_s and a with the constrained conditions of (4), (5) and (7) yields Solution A; with the constrained conditions of (4), (5) and (6) yields Solution B. These two solutions are then fine tuned as the initial values of some nonlinear least square for the experimental data, which yields Solution C and D, respectively.

The comparison of the solutions of one-diode model by the propose and Lambert W function based method are shown in Table 2, where "MAE" is the mean absolute error and "Step" is the number of iterative searching cycle before convergence. It is clear to see that the proposed method gives a very close results to Lambert W function based method. Although the error is slightly bigger, the number of iteration steps is less.

The error mainly arises from the numerical integrations presented in Section 3.4 and the few I-V data samples available (26 points only). If more data samples on the I-V curve are known, the error of the proposed method will be reduced. To illustrate this point, model parameters from the solution of Laudani 1D was used to reproduce the whole I-V curve with the help of (16). The

Table 1. Experimental I-V data [32]

SN	Module		Cell	
	Voltage (V)	**Current (A)**	**Voltage (V)**	**Current (A)**
1	−1.9426	1.0345	−0.2057	0.7640
2	0.1248	1.0315	−0.1291	0.7620
3	1.8093	1.0300	−0.0588	0.7605
4	3.3511	1.0260	0.0057	0.7605
5	4.7622	1.0220	0.0646	0.7600
6	6.0538	1.0180	0.1185	0.7590
7	7.2364	1.0155	0.1678	0.7570
8	8.3189	1.0140	0.2132	0.7570
9	9.3097	1.0100	0.2545	0.7555
10	10.2163	1.0035	0.2924	0.7540
11	11.0449	0.9880	0.3269	0.7505
12	11.8018	0.9630	0.3585	0.7465
13	12.4929	0.9255	0.3873	0.7385
14	12.6490	0.9120	0.4137	0.7280
15	13.1231	0.8725	0.4373	0.7065
16	14.2221	0.7265	0.4590	0.6755
17	14.6995	0.6345	0.4784	0.6320
18	15.1346	0.5345	0.4960	0.5730
19	15.5311	0.4275	0.5119	0.4990
20	15.8929	0.3185	0.5265	0.4130
21	16.2229	0.2085	0.5398	0.3165
22	16.5241	0.1010	0.5521	0.2120
23	16.7987	−0.0080	0.5633	0.1035
24	17.0499	−0.1110	0.5736	−0.0100
25	17.2793	−0.2090	0.5833	−0.1230
26	17.4885	−0.3030	0.5900	−0.2100

number of samples are selected to be 50, 100, 200. Based on such samples on the I-V curve derived from Laudani 1D solution, the RMSE of the proposed method to the whole I-V and the experimental data are shown in Table 3. As expected, the more data samples, the smaller RMSE. When data samples in-

Table 2. Solution comparison for solar module

Parameters	Proposed	Laudani 1A	Laudani 1B	Laudani 1C	Laudani 1D
I_L (A)	1.0334262	1.032173	1.033537	1.0323759	1.0323759
I_o (μA)	2.4424001	3.035367	2.825571	2.5188885	2.5188848
R_s (Ω)	1.2307473	1.218407	1.224053	1.2390187	1.2390187
R_{sh} (kΩ)	0.6034037	0.783516	0.689321	0.7456443	0.7456431
a ($N_s nkT_c/q$)	1.2975122	1.319345	1.312115	1.3002458	1.3002456
RMSE (10^{-3})	2.4777	2.1176	2.1547	2.0465	2.0465
MAE (10^{-3})	1.8461	1.6425	1.6060	1.6917	1.6917
Steps	8	12	10	19	28

creased to 100, the RMSE for the experimental data is already better than the solutions of Laudani 1A/B and all the other results compared in [32].

Table 3. RMSE with different data samples (Module)

Source	Solutions	RMSE[1]	RMSE[2]	Steps
Module[3]	From 50 pts	3.3085×10^{-4}	2.2290×10^{-3}	8
	From 100 pts	8.5583×10^{-5}	2.0939×10^{-3}	13
	From 200 pts	2.0177×10^{-5}	2.0874×10^{-3}	12
Cell[4]	From 50 pts	3.6098×10^{-4}	9.9881×10^{-4}	8
	From 100 pts	8.8401×10^{-5}	8.6810×10^{-4}	9
	From 200 pts	2.2234×10^{-5}	8.5153×10^{-4}	10

[1] for the whole I-V curve [2] for the experimental data in [32]
[3] I-V curve is produced from Laudani 1D
[4] I-V curve is produced from Laudani 2D

The result comparison for the solar cell I-V data in [32] is shown in Table 4. The RMSE of the proposed method is smaller than the results of Laudani 2A/C, and only slightly bigger than Laudani 2B/D. When data samples increased to 100, the proposed method already outperformed Laudani 2B, as shown in Table 3.

Table 4. Solution comparison for solar cell

Parameters	Proposed	Laudani 2A	Laudani 2B	Laudani 2C	Laudani 2D
I_L (A)	0.7609438	0.764114	0.761060	0.7706871	0.7607884
I_o (μA)	0.3456572	0.003496	0.290125	0.003668522	0.3102482
R_s (mΩ)	36.14233	45.438	36.8	49.11298	36.55304
R_{sh} (Ω)	49.482205	11.103851	49.973561	11.103904	52.859056
a (10^{-2})	3.9256187	2.9929942	3.8784080	2.997888	3.8965248
RMSE (10^{-3})	1.0548	11.388	0.88437	8.9605	0.77301
MAE (10^{-3})	0.85202	9.4014	0.69732	7.2064	0.67810
Steps	8	8	7	14	16

In general, Lambert W function based method has many benefits in two aspects:

- It utilizes the Lambert W function to convert a non-concave optimal problem into a concave optimal problem;
- It utilizes reduced forms to decrease the dimension of the parameter space from five to two.

This method can deal with the I-V data from the data sheet (points at SC, OC, MPP) or experiment (full I-V curve), and in most of cases, it yields the best results in terms of RMSE and/or MAE.

The deficiencies of Lambert W function based method may be:

- No unique solutions;
- Inapplicable to the multi-diode model ($m > 1$) parameter identification due to the limitations of Lambert W function;
- Not easy to be implemented and unsuitable for online parameter identification.

The proposed method further reduces the dimension of the parameter space to one. It uses linear square other than nonlinear optimal algorithms to derive diode model parameters, so the drawbacks of nonlinear algorithms are avoided. It can also be used for multiple-diode model and simple enough to be implemented as online calculation. The deficiencies is that it requires the knowledge of the full I-V curve data.

5.2. Evolution Algorithms

As mentioned in the Introduction, evolution algorithms are very suitable for the search of a global optimal solution. Recently, two types of evolution algorithms using differential evolution (DE) [50] and genetic algorithm (GA) [45] yield good results for diode model parameter identification. Since no full I-V curve data are provided in [45,50], we do the comparison in an indirect way as follows. Firstly, use the identified parameters (I_L, I_o, a, R_s and R_{sh}) to reconstruct the I-V curve by (16); Secondly, use that I-V curve data to identify diode-model parameters with the proposed method. Since DE and GA are applied to derive a, R_s and R_{sh} only (I_L and I_o are derived by formulas in [2, 58]), we only compare the results of a, R_s and R_{sh}. Table 5 shows the results of a, R_s and R_{sh} from the proposed method and DE/GA. It is clear to see that the differences in between are very minor.

Table 5. Solution comparison with evolution algorithms

Module	**Solutions**	a ($N_s nkT_c/q$)	R_s (Ω)	R_{sh} (Ω)
Shell SM55	Proposed	1.2666	0.3001	2.3165×10^3
(mono-cSi)	DE	1.2665	0.3	2.34×10^3
Shell S75	Proposed	1.2300	0.2000	1.7834×10^3
(multi-cSi)	DE	1.2295	0.2	1.79×10^3
Sanyo 215	Proposed	2.1778	0.7821	851.2464
(HIT)	GA	2.1780	0.782	852.177
Kyocera 200	Proposed	1.5340	0.3310	882.7933
(multi-cSi)	GA	1.5337	0.331	883.925

The result of the two-diode model for the aforementioned Kyocera module (Kyocera - KC200GT) was also reported in [45]. It is interesting to comparing this result with ours. If looking carefully at the comparison shown in Table 6, the GA algorithm gives comparable I_{o_1} and I_{o_2} (both in 10^{-9} A). a_1 and a_2 are also near to each other. If ignoring the differences between them, the two-diode can be combined as one. This implies that GA algorithm actually gives a result of one-diode model but mathematically divides it into two diodes format with no physical meaning. That's a common issue for the global optimization algorithm like DE and GA, whereas the proposed method has no such problems.

Table 6. Comparison of two-diode models

Parameters	GA	Proposed
a_1 (V)	1.5420	1.4936
a_2 (V)	1.9095	0.4944
R_s (Ω)	0.29	0.4095
R_{sh} (Ω)	480.496	842.8287
I_{o_1} (A)	4.23×10^{-9}	1.6044×10^{-9}
I_{o_2} (A)	9.1478×10^{-9}	2.6559×10^{-29}
MAE	0.02	0.0058

6. Graphical Meaning

In the previous sections, we showed the effectiveness of the proposed method to accurately extract diode model parameters from the I-V characteristics. This section illustrates the underlying principle from the angle of control theory by an illustration of the graphical meanings of the proposed method.

As control theory is usually studied for stable systems, coordinate transformation in Section 3.6 is applied, i.e., $\tilde{V} = V_{oc} - V$ so that I-$\tilde{V}$ is corresponding to some stable linear system. After transformation, I-V curve in Figure 4 is changed to I-$\tilde{V}$ (blue line) in Figure 14. Draw a straight line (black) starting from $O(0,0)$ with the slope of $1/R_s$, i.e., $Y = X/R_s$, with the same I, the coordinates of the points on the black and blue lines will be $Q(R_sI, I)$ and $P(\tilde{V}, I)$, respectively. Therefore, $\tilde{x} = \tilde{V} - R_sI$ actually represents the distance between P and Q (green arrow). If $Y' = X/R_s$ is constructed as the new Y-axis, then only in XOY' coordinate system, I-$\tilde{V}$ curve is equivalent to a response of some linear system. In normal XOY coordinate system, this is not the case unless each point on the I-$\tilde{V}$ curve is shifted a variable distance of R_sI to the Y-axis, which is shown by red dash line in Figure 14.

Note that for the response of a stable linear system with zero initial conditions, both x and y values are monotonically increasing, which means distance $|PQ|$ is monotonically increasing with I. If $1/R_s < \mathrm{d}I/\mathrm{d}\tilde{V}|_{\tilde{V}=0} = -\mathrm{d}I/\mathrm{d}V|_{V=V_{oc}}$, the black line will intersect with the blue one so that the monotonically increasing of $|PQ|$ is violated, see Figure 15. Therefor, $1/R_s \geq -\mathrm{d}I/\mathrm{d}V|_{V=V_{oc}}$, which yields the upper bound of R_s discussed in Section 3.5

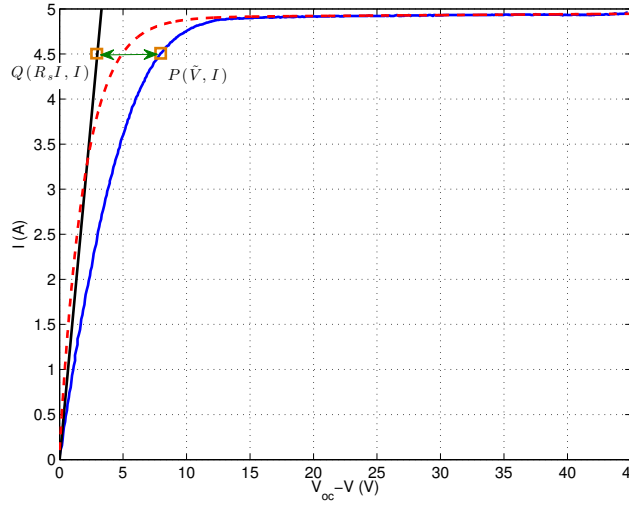

Figure 14. The I-$\tilde{V}$ characteristic from I-V.

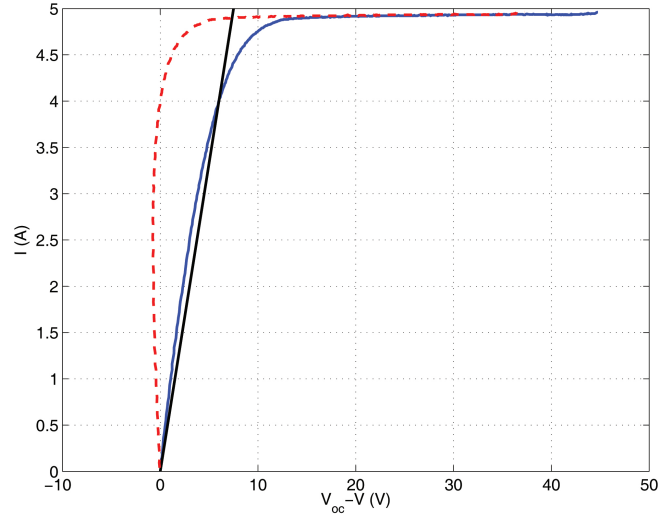

Figure 15. Impact of R_s on the profile of I-$\tilde{V}$.

Figure 16 shows the impact of Rs on the RMSE of the proposed method, where I-V characteristic data are from the same indoor flash test module discussed in Section 4.1, and $0 \leq R_s \leq -\mathrm{d}V/\mathrm{d}I|_{V=V_{oc}}$. One sees clearly that the accuracy of the proposed method is very sensitive to R_s, which implies that only when R_s is properly selected, the resulted I-$\tilde{V}$ is the response of a linear system. Such high sensitivity results in the unique solution of R_s and the rest of PV model parameters, and the effectiveness of the binary search algorithm proposed in Section 3.5.

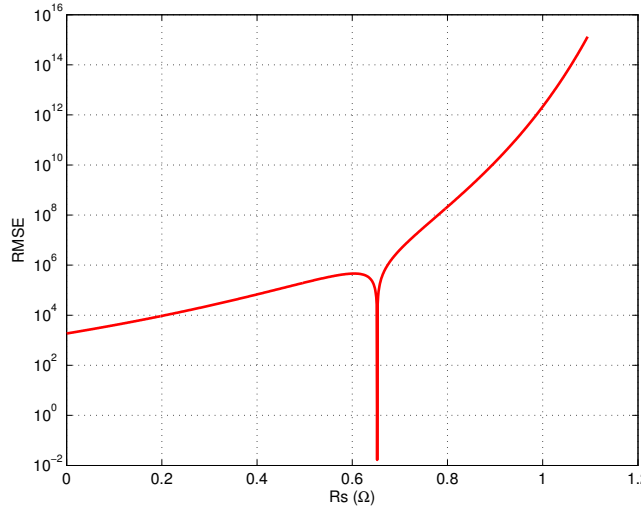

Figure 16. Impact of R_s on the RMSE of the proposed method.

7. Applications

7.1. Non-Contact Measurement of POA Irradiance and Cell Temperature

Irradiance on plane of array (POA) and cell temperature are important to PV systems because system performance, evaluated by performance ratio (PR), is derived from them. Usually, silicon sensors are applied in PV systems to measure the irradiance level on POA, as shown in Figure 17. Their structure is com-

Figure 17. POA irradiance measurement by silicon sensor.

posed of a high-quality mono-crystalline solar cell connected to a high accuracy shunt, which is the same as Figure 2, where I_L is the photocurrent proportional to the POA irradiance, the diode represents the mono-crystalline cell, and R_{sh} is the shunt. The low shunt ($R_{sh} = 0.1\Omega$) causes the cell to operate close to the short-circuit point, which makes $I_{sh} \rightarrow I_L$ so that POA irradiance can be calibrated from I_{sh} according to the proportionality.

Essentially, silicon sensors use an internal reference cell as a benchmark to sense the POA irradiance of PV modules/systems. The measurement accuracy highly depends on the differences between: 1) reference cell and PV modules; 2) I_L and I_{sh}. However, mismatch between reference cell and PV modules is inevitable and $I_L \neq I_{sh}$ although compensation measures for temperature are taken into account. All of them cause the mismatch error up to $\pm 5\%$, and the sensor needs to be recalibrated every two years to avoid the measurement shift caused by the degradation of reference cell.

A more accurate irradiance sensor is pyranometer, which covers the full spectrum of solar radiation (300-2, 800 nm) from a field of view of 180 degrees. It is seldom deployed in PV systems due to: 1) much higher cost as compared to silicon sensor; 2) mismatch in spectrum as crystalline is not a full spectrum absorber; 3) is not applicable to measure POA irradiance.

Temperature measurement for PV systems is even worse than POA irradiance measurement because what is measured is not the true cell temperature but the temperature of the back sheet of modules. This is because cells are encapsulated between the layers of glass, EVA, back sheet during the process of lamination. However, it is also impractical to incorporate a sensor within the

module, in direct contact with an individual cell, to measure the cell temperature. In addition, the non-uniformity of module temperature across the module area, which was assumed to be $\pm 1\,^{\circ}\mathrm{C}$ in [66], is not accounted for with this approach. The current compromise is to put a sensor attached to the back sheet, which causes the cell temperature measurement to be roughly $2-3^{\circ}\mathrm{C}$ lower than the true value. At a standard irradiance level of $1000W/m^2$, a mean cell-to-back temperature difference of $2.5 \pm 1\,^{\circ}\mathrm{C}$ was adopted in [67] for c-Si modules with plastic back encapsulation.

It is much desired to find a more accurate way to measure the POA irradiance and cell temperature as more and more PV systems are installed all over the world, not only for the academic research, but also for the commercial investment evaluation. Motivated by the recent progress in the diode model parameter identification [68, 69], photocurrent I_L and reverse saturation I_o can be linearly determined from the I-V characteristics of PV modules. Immediately, POA irradiance $G_s = \lambda I_L$, where λ is a constant slope (to be calibrated) and independent of irradiance or temperature [2]. Cell temperature T_c is derived from $I_o = BT_c^3 \mathrm{e}^{-E_g/(kT_c)}$, where E_g is the band gap of silicon and B is a temperature independent constant [14]. No external sensors for irradiance or temperature is required once the I-V curve is known.

7.1.1. Calibration of POA Irradiance

As mentioned before, the photocurrent I_L is proportional to POA irradiance G_s, i.e., $G_s = \lambda I_L$, and λ is the slope. To calibrate λ, the I-V characteristics of a full-sized commercial module were measured indoor by a PASAN IIIB with the constant illumination intensity of $200, 400, 600, 800, 1000, 1200W/m^2$. The temperature for such flash tests is fixed at $25^{\circ}\mathrm{C}$.

Figure 18 shows the family I-V characteristic of a PV module (crystalline) from the proposed indoor flash test, where estimation results by the identification method from Section 3 are indicated by circles. The estimation results obtained from the identified diode model parameters match closely to the I-V curves from the indoor flash test. The identified diode model parameters and RMSE compared to the real I-V curves are listed in Table 7, which illustrate the accuracy of the proposed identification.

Based on the results from Table 7, Figure 19 shows the correlation between G_s and I_L. As expected, I_L is proportional to G_s. The non-zero intercept is caused by measurement error, which brings the uncertainty of irradiance esti-

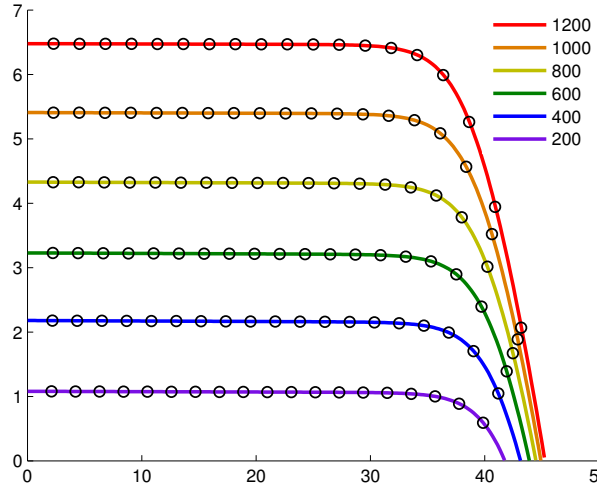

Figure 18. Indoor flash test at different illumination intensity.

Table 7. Identification results

Illumination (**W/m**^{2})	I_L (A)	I_o (10^{-9}A)	a (V)	R_s (Ω)	R_{sh} (kΩ)	**RMSE** ($\times 10^{-3}$)
200	1.08	0.4782	1.9411	0.5293	1.8321	0.0849
400	2.18	0.4757	1.9407	0.6278	1.3512	0.1410
600	3.23	0.4745	1.9404	0.6339	1.3414	0.1809
800	4.33	0.4741	1.9401	0.6345	1.5710	0.2130
1000	5.41	0.4725	1.9399	0.6347	1.8408	0.2380
1200	6.48	0.4786	1.9397	0.6347	2.1330	0.2569

mation up to $0.006/0.0054 = 1.11\ W/m^2$. The slope λ from $G_s = \lambda I_L$ is determined by $\lambda = 1/0.0054 = 185.1852$.

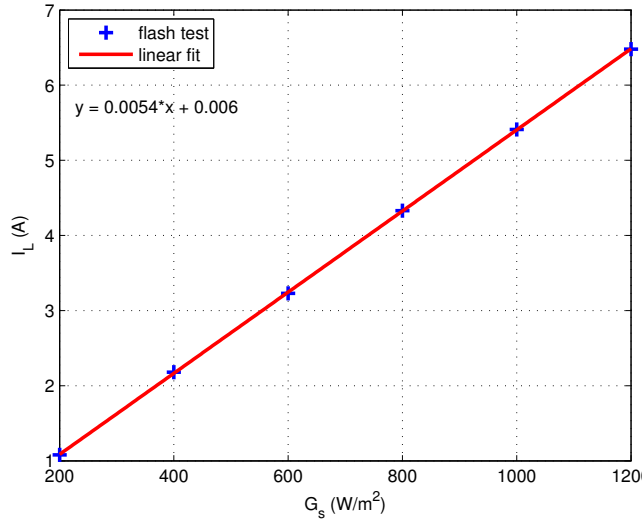

Figure 19. Determination of λ from $G_s = \lambda I_L$.

7.1.2. Calibration of Cell Temperature

Cell temperature is derived from $I_o = BT_c^3 \mathrm{e}^{-E_g/(kT_c)}$, where E_g is the band gap of silicon and B is a temperature independent constant [14]. Both B and E_g are required to be calibrated. To do the calibration, the I-V characteristics of the same module in Section 7.1.1 were measured by the PASAN IIIB in a thermal chamber. The illumination intensity is fixed at $1000W/m^2$ and the chamber temperature are set at $15°C$, $25°C$, $35°C$, $45°C$, $55°C$, $65°C$.

Figure 20 shows the results of the flash test at different temperature levels, where the circles represent the estimated I-V curves by the proposed identification. The identified diode model parameters and RMSE compared to the real I-V curves are listed in Table 8.

With the identified I_o from Table 8, taking logarithmic to I_o gives,

$$\ln I_o = \ln B + 3 \ln T_c - \frac{E_g}{kT_c}, \quad \Rightarrow$$

$$\ln I_o - 3 \ln T_c = -\frac{E_g}{k} T_c^{-1} + \ln B. \tag{56}$$

Let $y = \ln I_o - 3 \ln T_c$, $x = 1/T_c$, $\alpha = -E_g/k$ and $\beta = \ln B$, (56) becomes $y =$

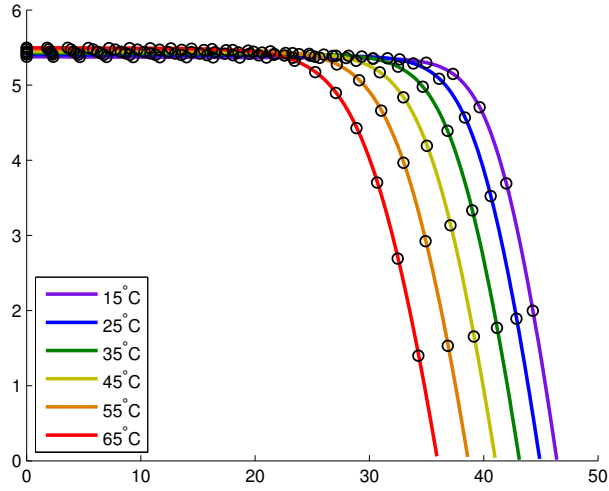

Figure 20. Indoor flash test at different temperatures.

Table 8. Identification results

Temperature (°C)	I_L (A)	I_o (10^{-9}A)	a (V)	R_s (Ω)	R_{sh} (kΩ)	**RMSE** ($\times 10^{-3}$)
15	5.38	0.0326	1.7970	0.6326	1.8486	0.2676
25	5.41	0.4756	1.9399	0.6347	1.8409	0.2375
35	5.43	5.8101	2.0883	0.6367	1.8335	0.2089
45	5.45	61.544	2.2420	0.6378	1.8283	0.1810
55	5.48	564.16	2.4012	0.6388	1.8180	0.1550
65	5.50	4546.3	2.5659	0.6399	1.8075	0.1305

$\alpha x + \beta$. The relationship between x and y are shown in Figure 21. With linear fitting, $\alpha = -22122$ and $\beta = 35.637$. Thus, $E_g = -k\alpha = 3.0543 \times 10^{-19}$ and $B = \mathrm{e}^{\beta} = 2.9988 \times 10^{15}$. After E_g and B are known, the cell temperature T_c can be numerically determined by Newton-Raphson method with the initial $T_c = 300$ K.

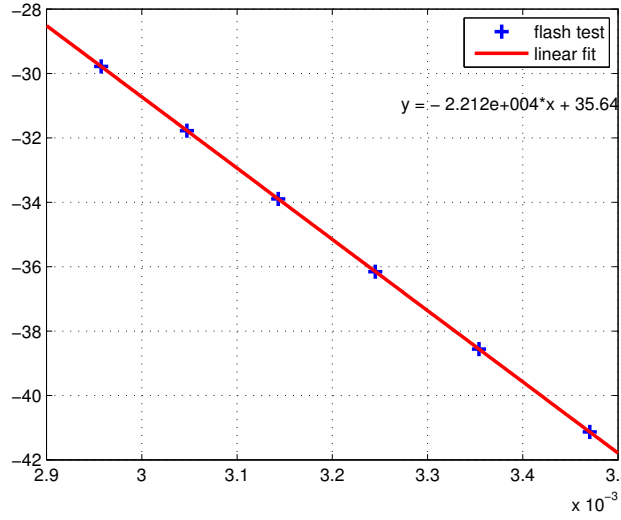

Figure 21. Calibration of E_g and B.

7.1.3. Outdoor Verification

To validate the proposed non-contact measurement for POA irradiance and cell temperature, the same module after the indoor calibration was put at outdoor module testing bed for a whole day with the continuous recording of I-V curves and meteorological data. By applying the proposed method in Section 3, the time-varying one-diode model parameters I_L, I_o, a, R_s and R_{sh} for the same day are identified, which has been discussed in Section 4.2 and the results are shown in Figure 8. The variation of the identified parameters reflects the dynamics of the PV module under different environmental conditions, which cannot be seen from the static I-V curves. With the identified diode model parameters, the POA irradiance and cell temperature can then be derived.

Based on the calibration value λ from Section 7.1.1, the POA irradiance can be determined from I_L by $G_s = \lambda I_L$. Figure 22 illustrates the comparison to the results from a reference silicon sensor which has the same inclined angle as the PV module. As seen from Figure 22, the non-contact measurement POA irradiance matches the irradiance measurement from the silicon sensor well.

With the calibrated E_g and B from Section 7.1.2, cell temperature T_c is numerically determined by Newton-Raphson method. The comparison between

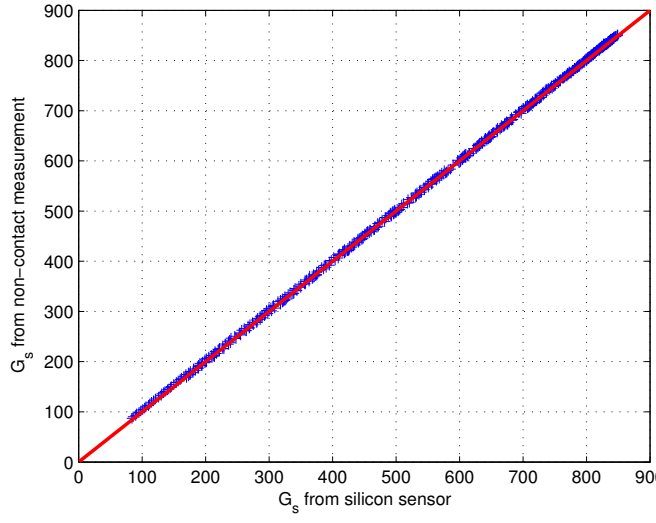

Figure 22. POA irradiance: non-contact measurement vs. reference cell.

T_c and T_{mod} (backsheet measurement) is shown in Figure 23. One can see that when irradiance increases in the morning, T_c is usually higher than T_{mod}, which is due to the positive temperature gradient (from cell to backsheet) during that time. Whereas after solar noon when irradiance decreases, temperature gradient becomes negative due to the thermal delay, so T_c is lower than T_{mod}. But the difference in between is within ± 2°C.

7.2. PV Panel Characterisation for Satellites

When PV panels are used in satellites, it is usually not allowed to do the flash test sweeping from OC to SC because the power supply must be stable to maintain the normal operation of satellites. Hence, to do the PV panel characterisation for satellites in operation, I-V scan is limited within a small range around MPP, i.e., $I \in [I_1, I_2]$ and $V \in [V_1, V_2]$. With the example of one-diode model, it

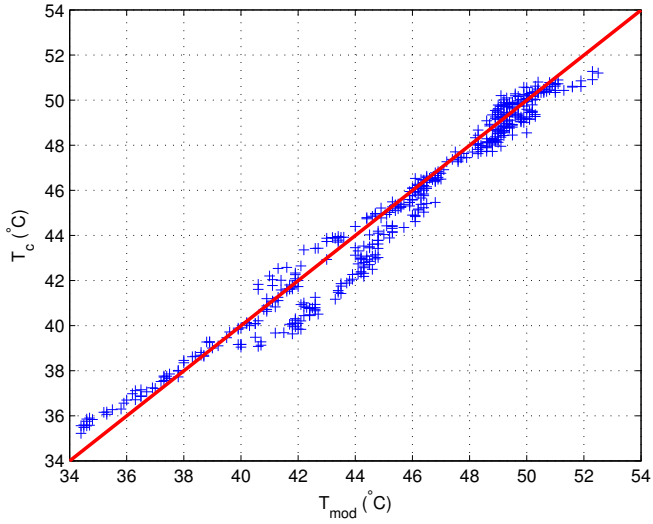

Figure 23. Cell temperature: non-contact measurement vs. backsheet-attached sensors.

follows from (3) that

$$I_1 = I_L + I_o - I_o \mathrm{e}^{\frac{V_1 + R_s I_1}{a}} - \frac{V_1 + R_s I_1}{R_{sh}}, \tag{57}$$

$$I = I_L + I_o - I_o \mathrm{e}^{\frac{V + R_s I}{a}} - \frac{V + R_s I}{R_{sh}}. \tag{58}$$

Let $\Delta I = I - I_1$ and $\Delta V = V - V_1$, (58) $-$ (57) yields

$$\Delta I = I_o \mathrm{e}^{\frac{V_1 + R_s I_1}{a}} \left(1 - \mathrm{e}^{\frac{\Delta V + R_s \Delta I}{a}}\right) - \frac{\Delta V + R_s \Delta I}{R_{sh}}. \tag{59}$$

Let $y = \Delta I$ and $x = \Delta V + R_s \Delta I$, (59) becomes

$$y = I_o \mathrm{e}^{\frac{V_1 + R_s I_1}{a}} \left(1 - \mathrm{e}^{\frac{x}{a}}\right) - \frac{x}{R_{sh}}. \tag{60}$$

Taking differential once for (60) gives

$$\frac{\mathrm{d}y}{\mathrm{d}x} = -\frac{I_o}{a} \mathrm{e}^{\frac{V_1 + R_s I_1}{a}} \mathrm{e}^{\frac{x}{a}} - \frac{1}{R_{sh}}. \tag{61}$$

Differentiating twice gives

$$\frac{\mathrm{d}^2 y}{\mathrm{d}x^2} = -\frac{I_o}{a^2}\mathrm{e}^{\frac{V_1+R_sI_1}{a}}\mathrm{e}^{\frac{x}{a}}. \tag{62}$$

Eliminating $\mathrm{e}^{x/a}$ from (61) and (62) gives

$$a\frac{\mathrm{d}^2 y}{\mathrm{d}x^2} - \frac{\mathrm{d}y}{\mathrm{d}x} = \frac{1}{R_{sh}},$$

which is just the same as (21). The remaining procedures are very similar to what we did in Section 2.1 except for the initial conditions. From (60) and (61), $y(0) = 0$ and $y'(0) = -I_o\mathrm{e}^{(V_1+R_sI_1)/a}/a - 1/R_{sh}$, respectively. According to (24), the transfer function

$$G(s) = \frac{ay(0)s^2 + [ay'(0) - y(0)]s + \frac{1}{R_{sh}}}{as^2 - s} = \frac{-(I_o\mathrm{e}^{\frac{V_1+R_sI_1}{a}} + \frac{a}{R_{sh}})s + \frac{1}{R_{sh}}}{as^2 - s}.$$

The corresponding time domain differential equation is

$$a\frac{\mathrm{d}^2 y(t)}{\mathrm{d}t^2} - \frac{\mathrm{d}y(t)}{\mathrm{d}t} = -\left(I_o\mathrm{e}^{\frac{V_1+R_sI_1}{a}} + \frac{a}{R_{sh}}\right)\frac{\mathrm{d}u(t)}{\mathrm{d}t} + \frac{u(t)}{R_{sh}}, \tag{63}$$

where $t = x$ and $u(t) \equiv 1$. With the help of double integral in (39), (63) is equivalent to

$$ay(t) + \left(I_o\mathrm{e}^{\frac{V_1+R_sI_1}{a}} + \frac{a}{R_{sh}}\right)\int_{[0,t]}^{(1)} u(\tau) - \frac{1}{R_{sh}}\int_{[0,t]}^{(2)} u(\tau) = \int_{[0,t]}^{(1)} y(\tau).$$

Let $\theta = [a, I_o\mathrm{e}^{\frac{V_1+R_sI_1}{a}} + \frac{a}{R_{sh}}, \frac{1}{R_{sh}}]^T$, $\phi(t) = [y(t), \int_{[0,t]}^{(1)} u(\tau), -\int_{[0,t]}^{(2)} u(\tau)]^T$ and $\gamma(t) = \int_{[0,t]}^{(1)} y(\tau)$, then the least square solution for θ is given by

$$\theta = \left(\Phi^T\Phi\right)^{-1}\Phi^T\Gamma,$$

where $\Phi = [\phi(t_1), \cdots, \phi(t_N)]^T$ and $\Gamma = [\gamma(t_1), \cdots, \gamma(t_N)]^T$. Thus,

$$\begin{aligned} a &= \theta_1, \\ I_o &= (\theta_2 - \theta_1\theta_3)\mathrm{e}^{-\frac{V_1+R_sI_1}{\theta_1}}, \\ R_{sh} &= \frac{1}{\theta_3}. \end{aligned}$$

R_s is determined by the same binary search algorithm in Section 3.5 as before, and I_L is derived from (57) as follows once I_o, a, R_s and R_{sh} are all determined.

$$I_L = I_1 - I_o + I_o \mathrm{e}^{\frac{V_1 + R_s I_1}{a}} + \frac{V_1 + R_s I_1}{R_{sh}}.$$

Conclusion

In this chapter, an approach on linear system identification is developed, which links the diode model parameters to the transfer function coefficients of a dynamic system. This approach solves the PV model parameters by an integral-based linear least square method, which reduces the dimension of the search space from 5 to 1, so the drawbacks of nonlinear algorithms are avoided. Graphical meanings of the proposed method are illustrated to help readers understand the underlying principles. Finally, a discussion of the possible applications of the proposed method like online PV monitoring and diagnostics, non-contact measurement of POA irradiance and cell temperature, fast model identification for satellite PV panels are presented.

References

[1] William Shockley. The theory of p-n junctions in semiconductors and p-n junction transistors. *The Bell System Technical Journal*, 28(3):435489, July 1949.

[2] W. De Soto, S.A. Klein, and W.A. Beckman. Improvement and validation of a model for photovoltaic array performance. *Sol. Energy*, 80(1):7888, 2006.

[3] J. Surya Kumari and Ch. Sai Babu. Mathematical modeling and simulation of photovoltaic cell using matlab-simulink environment. *International Journal of Electrical and Computer Engineering (IJECE)*, 2(1):2634, February 2012.

[4] Jing Jun Soon, Kay-Soon Low, and Shu Ting Goh. Multi-dimension diode photovoltaic (PV) model for different PV cell technologies. In *IEEE 23rd ISIE*, pages 24962501, 2014.

[5] B. G. Streetman and S. Banerjee. *Solid state electronic devices*. Prentice Hall, New Jersey, 5th edition, 2000.

[6] K. R. McIntosh. Lumps, humps and bumps: three detrimental effects in the currentvoltage curve of silicon solar cells. PhD thesis, University of New SouthWales, 2001.

[7] D. Macdonald and A. Cuevas. Reduced fill factors in multicrystalline silicon solar cells due to injection-level dependent bulk recombination lifetime. *Prog. Photovolt: Res. Appl.*, (8):363375, 2000.

[8] F. Pelanchon, P. Mialhe, and J.P. Charles. The photocurrent and the open-circuit voltage of a silicon solar cell. *Sol. Cells*, 28(1):4155, 1990.

[9] N.M. Ravindra and Basudev Prasad. Saturation current in solar cells: an analysis. *Sol. Cells*, 2(2):109113, 1980.

[10] N. Santakrus Singh, Amit Jain, and Avinashi Kapoor. Determination of the solar cell junction ideality factor using special trans function theory (STFT). *Sol. Energ. Mat. Sol. C.*, 93(8):14231426, 2009.

[11] Chan DS and Phang JC. Analytical methods for the extraction of solar cell singleand double-diode model parameters from i-v characteristics. *IEEE Trans. Electron Devices*, 34(2):286293, 1987.

[12] D. Pysch, A. Mette, and S.W. Glunz. A review and comparison of different methods to determine the series resistance of solar cells. *Sol. Energ. Mat. Sol. C.*, 91(18):16981706, 2007.

[13] D. Sera and R. Teodorescu. Robust series resistance estimation for diagnostics of photovoltaic modules. In 35th IEEE IECON, pages 800805, 2009.

[14] Georgi Hristov Yordanov, Ole-Morten Midtgøard, and Tor Oskar Saetre. Series resistance determination and further characterization of c-si PV modules. *Renew. Energ.*, 46(10):7280, 2012.

[15] Yong Sin Kim, Sung-Mo Kang, Bruce Johnston, and RolandWinston. A novel method to extract the series resistances of individual cells in a photovoltaic module. *Sol. Energ. Mat. Sol. C.*, 115(8):2128, 2013.

[16] A. Chatterjee, A. Keyhani, and D. Kapoor. Identification of photovoltaic source models. *IEEE Trans. Energy Convers.*, 26(3):883889, Sep. 2011.

[17] Hadj Arab A, Chenlo F, and Benghanem M. Loss-of-load probability of photovoltaic water pumping systems. *Solar Energy*, 76:713723, 2004.

[18] Antonino Laudani, Francesco Riganti Fulginei, and Alessandro Salvini. Identification of the one-diode model for photovoltaic modules from datasheet values. *Sol. Energy*, 108:432446, 2014.

[19] de Blas MA, Torres JL, Prieto E, and Garía A. Selecting a suitable model for characterizing photovoltaic devices. *Renew. Energ.*, 25:371380, 2002.

[20] Lo Brano V, Orioli A, Ciulla G, and Di Gangi A. An improved five-parameter model for phtotvoltaic modules. *Sol. Energ. Mat. Sol. C.*, 94:13581370, 2010.

[21] Orioli A and Di Gangi A. A procedure to calculate the five-parameter model of crystalline silicon photovoltaic modules on the basis of the tabular performance data. *Appl. Energ.*, 102(1160-1177), 2013.

[22] S. Lineykin, Averbukh M, and A. Kuperman. An improved approach to extract the single-diode equivalent circuit parameters of a photovoltaic cell/panel. *Renew. Sustain. Energy. Rev.*, 30:282289, 2014.

[23] Peng L, Sun Y, and Meng Z. An improved model and parameters extraction for photovoltaic cells using only three state points at standard test condition. *J. Power Sources*, 248(621-631), 2014.

[24] S. Lineykin and A. Kuperman. Issues in modeling amorphous silicon photovoltaic modules by single-diode equivalent circuit. *IEEE Trans. Ind. Electron.*, 61(99), 2014.

[25] Y. A. Mahmoud, W. Xiao, and H. H. Zeineldin. A parameterization approach for enhancing PV model accuracy. *IEEE Trans. Ind. Electron.*, 60(12):57085716, 2013.

[26] F. Adamo, F. Attivissimo, A. Di Nisio, and M. Spadavecchia. Characterization and testing of a tool for photovoltaic panel modeling. *IEEE Trans. Instrum. Meas.*, 60(5):16131622, May 2011.

[27] Y. Mahmoud, W. Xiao, and H. H. Zeineldin. A simple approach to modeling and simulation of photovoltaic modules. *IEEE Trans. Sustain. Energy*, 3(1):185186, Jan. 2012.

[28] S. Lineykin, M. Averbukh, and A. Kuperman. Five-parameter model of photovoltaic cell based on STC data. In 27th IEEE Conv. Electr. Electron. Eng., pages 15, Eilat, Israel, Nov. 2012.

[29] A. Izadian, A. Pourtaherial, and S. Motahari. Basic model and governing equation of solar cells used in power and control applications. In IEEE Energy Conv. Congr. Expo., pages 14831488, Raleigh, NC, Sep. 2012.

[30] F. Ghani, M. Duke, and J. Carson. Numerical calculation of series and shunt resistances and diode quality fator of a photovoltaic cell using the Lambert W-function. *Sol. Energy*, 91:422431, 2013.

[31] F. Ghani, M. Duke, and J. Carson. Numerical calculation of series and shunt resistance of a photovoltaic cell using the Lambert W-function: Experimental evaluation. *Sol. Energy*, 87:246253, 2013.

[32] Antonino Laudani, Francesco Riganti Fulginei, and Alessandro Salvini. High performing extracton procedure for the one-diode model of a photovoltaic panel from experimental I-V curves by using reduced forms. *Sol. Energy*, 103:316326, 2014.

[33] M. Al-Rashidi, M. Al-Hajri, K. El-Naggar, and A. Al-Othman. A new estimation approach for determining the I-V characteristics of solar cells. *Sol. Energy*, 85(7):15431550, 2011.

[34] H. Qin and J. W. Kimball. Parameter determination of photovoltaic cells from field testing data using particle swarm optimization. In *IEEE PECI*, number 1-4, 2011.

[35] Jing Jun Soon and Kay-Soon Low. Optimizing photovoltaic model parameters for simulation. In *IEEE 21st ISIE*, pages 18131818, 2012.

[36] Y. Li, W. Huang, H. Huang, C. Hewitt, Y. Chen, G. Fang, and D. Carroll. Evaluation of methods to extract parameters from current-voltage characteristics of solar cells. *Sol. Energy*, 90:5157, Apr. 2013.

[37] Kien F. Teng and Ping Wu. PV module characterization using Q-R decomposition based on the least square method. *IEEE Trans. Ind. Electron.*, 36(1):7175, 1989.

[38] Hyeonah Park and Hyosung Kim. PV cell modeling on single-diode equivalent circuit. In *39th IEEE IECON*, pages 18451849, 2013.

[39] T. Easwarkhanthan, J. Bottin, I. Bouhouch, and C. Boutrit. Nonlinear minimization algorithm for determining the solar cell parameters with microcomputers. *Int. J. Solar Energ.*, 4:112, 1986.

[40] Dkhichi F, Oukarfi B, Fakkar A, and Belbounaguia N. Parameter identification of solar cell model using levenberg-marquardt algorithm combined with simulated annealing. *Sol. Energy*, 110:781788, 2014.

[41] Zhang K, Jia W, Koplowitz J, Marzocca P, and Cheng MC. Modeling of photovoltaic cells and arrays based on singular value decomposition. *Semicond. Sci. Technol.*, 28(3):035002, 2013.

[42] J. Appelbaum, A. Chait, and D. Thompson. Parameter estimation and screening of solar cells. *Prog. Photovolt: Res. Appl.*, 1(2):93106, February 1993.

[43] Jervase JA, Bourdoucen H, and Al-Lawati A. Solar cell parameter extraction using genetic algorithms. Meas. *Sci. Technol.*, 12(11):1922, 2001.

[44] Zagrouba M, Sellami A, Bouaïcha M, and Ksouri M. Identification of PV solar cells and modules parameters using the genetic algorithms: application to maximum power extraction. *Sol. Energy*, 84(5):860866, 2010.

[45] M. S. Ismail, M. Moghavvemi, and T. M. I. Mahlia. Characterization of pv panel and global optimization of its model parameters using genetic algorithm. *Energ. Convers. Manage.*, 73:1025, 2013.

[46] Dizqah A.M., Maheri A., and Busawon K. An accurate method for the PV model identification based on a genetic algorithm and the interior-point method. *Renew. Energ.*, 72:212222, 2014.

[47] Wang X.M. and Xu Y. Parameter extraction of solar cells using particle swarm optimization. *J. Appl. Phys.*, 105(9):094502, 2009.

[48] Jing Jun Soon and Kay-Soon Low. Photovoltaic model identification using particle swarm optimization with inverse barrier constraint. *IEEE Trans. Power Electron.*, 27(9):39753983, Sep. 2012.

[49] Khanna V, Das BK, Bisht D, and Singh PK. A three diode model for industrial solar cells and estimation of solar cell parameters using pso algorithm. *Renew. Energ.*, 78:105113, 2015.

[50] K Ishaque and Z. Salam. An improved modeling method to determine the model parameters of photovoltaic (PV) modules using differential evolution (DE). *Sol. Energy*, 85:23492359, 2011.

[51] W. Gong and Z. Cai. Parameter extraction of solar cell models using repaired adaptive differential evolution. *Sol. Energy*, 94:209220, 2013.

[52] L.L Jiang, D.L. Maskell, and J.C. Patra. Parameter estimation of solar cells and modules using an improved adaptive differential evolution algorithm. *Appl. Energ.*, 112:185193, 2013.

[53] Asif S. and Li Y. Solar cell modeling and parameter optimization using simulated annealing. *J. Propuls Power*, 24(5):10181022, 2008.

[54] K. El-Naggar, M. AlRashidi, M. AlHajri, and A. Al-Othman. Simulated annealing algorithm for photovoltaic parameters identification. *Sol. Energy*, 86:266274, 2012.

[55] Celik AN. Artificial neural network modeling and experimental verification of the operating current of mono-ctystalline photovoltaic modules. *Sol. Energy*, 85(10):25072517, 2011.

[56] Almonacid F, Rus C, Hontoria L, Fuentes M, and Nofuentes G. Characterisation if Sicrystalline PV modules by artificial neural networks. *Renew. Energ.*, 34(4):941949, 2009.

[57] W. Xiao, P. R. Dunford, W. G. Palmer, and A. Capel. Regulation of photovoltaic voltage. *IEEE Trans. Ind. Electron.*, 54(3):13651374, 2007.

[58] M. G. Villalva, J. R. Gazoli, and Filho E. R. Comprehensive approach to modeling and simulation of photovoltaic arrays. *IEEE Trans. Power Electron.*, 24(5):11981208, 2009.

[59] Soon J.J. and Low K.S. Optimizing photovoltaic model for different cell technologies using a generalized multi-dimension diode model. *IEEE Trans. Ind. Electron.*, 62(10):63716380, 2015.

[60] Debashisha Jena and Vanjari Venkata Ramana. Modeling of photovoltaic system for uniform and non-uniform irradiance: A critial review. *Renew. Sustain. Energy. Rev.*, 52:400417, 2015.

[61] Vun Jack Chin, Zainal Salam, and Kashif Ishaque. Cell modeling and model parameters estimation techniques for phtotvoltaic simulation application: A review. *Appl. Energ.*, 154:500519, 2015.

[62] K. Ogata. *Modern Control Engineering*. Prentice Hall, 2002.

[63] Qing-Guo Wang and Yong Zhang. Robust identification of continuous systems with dead-time from step responses. *Automatica*, 37(3):377390, 2001.

[64] M. Hamdy and R. Call. The effect of the diode ideality factor on the experimental determination of series resistance of solar cells. *Sol. Cells*, 20(2):119126, 1987.

[65] M. C. Di Piazza and G. Vitale. *Photovoltaic Sources: Modeling and Emulation*. Springer, 2012.

[66] W. Zaaiman H. Mullejans and R. Galleano. Analysis and mitigation of measurement uncertainties in the traceability chain for the calibration of photovoltaic devices. *Measurement Science and Technology*, 20, 2009.

[67] K. Whitfield and C.R. Osterwald. Procedure for determining the uncertainty of photovoltaic module outdoor electrical performance. *Progress in Photovoltaics: Research & Applications*, 9:87 102, 2001.

[68] Li Hong Idris Lim, Zhen Ye, Jiaying Ye, Dazhi Yang, and Hui Du. A linear identification of diode models from single I-V characteristics of PV panels. *IEEE Trans. Ind. Electron.*, 62(7):41814193, 2015.

[69] Li Hong Idris Lim, Zhen Ye, Jiaying Ye, Dazhi Yang, and Hui Du. A linear method to extract diode model parameters of solar panels from a single I-V curve. *Renewable Energy*, 76:135142, 2015.

In: Solar Energy and Solar Panels
Editor: Joel G. Carter
ISBN: 978-1-53610-380-9

Chapter 3

STATISTICAL MODELING, PARAMETER ESTIMATION AND MEASUREMENT PLANNING FOR PV DEGRADATION

***Dazhi Yang*[1,*], *Licheng Liu*[2], *Carlos David Rodríguez-Gallegos*[3], *Zhen Ye*[4], *Li Hong Idris Lim*[5] *and Omid Geramifard*[1]**
[1]Singapore Institute of Manufacturing Technology,
Agency for Science, Technology and Research,
Singapore, Singapore
[2]Saferay Pte Ltd., Singapore, Singapore
[3]Solar Energy Research Institute of Singapore,
National University of Singapore, Singapore, Singapore
[4]Modules Division, REC Solar Pte Ltd., Singapore, Singapore
[5]Department of Electronic Systems,
University of Glasgow (Singapore),
Singapore, Singapore

Abstract

Photovoltaics (PV) degradation is a key consideration during PV performance evaluation. Accurately predicting power delivery over the course of lifetime of PV is vital to manufacturers and system owners. With many systems exceeding 20 years of operation worldwide, degradation rates have been reported abundantly in the recent years. PV degradation is a complex function of a variety of factors, including but not limited

*E-mail address: yangdazhi.nus@gmail.com

to climate, manufacturer, technology and installation skill. As a result, it is difficult to determine degradation rate by analytical modeling; it has to be measured.

As one set of degradation measurements based on a single sample cannot represent the population nor be used to estimate the true degradation of a particular PV technology, repeated measures through multiple samples are essential. In this chapter, linear mixed effects model (LMM) is introduced to analyze longitudinal degradation data. The framework herein introduced aims to address three issues: 1) how to model the difference in degradation observed in PV modules/systems of a same technology that are installed at a shared location; 2) how to estimate the degradation rate and quantiles based on the data; and 3) how to effectively and efficiently plan degradation measurements.

1. Introduction

The installed photovoltaic (PV) capacity has exceeded 227 GW around the globe in April 2016 [1], with the majority of installations realized only in the past few years. Aside from various environmental benefits of adopting PV power, the increasing PV installation is also motivated by financial benefits that have become apparent in the recent years, when grid parity has occurred in many places in the world. PV degradation is a key consideration during PV performance evaluation, not only concerning the manufacturers, but also system developers and owners. This chapter studies the PV degradation through a statistical model. More importantly, the degradation measurement planning is discussed.

1.1. Motivations

Typically, the installation of a PV power plant consists of three phases, namely, the development, construction, as well as operations and maintenance (O&M) phases. Having an accurate estimation of PV degradation is highly critical for the owners and investors of PV power plants, especially during the development and the O&M phases. Despite the substantial drop in the cost of PV power world-wide, the initial capital cost required to set up a sizable, utility-scale PV power plant can still be very taxing on the liquidity of PV power plant owners. Consequently, the owners typically turn to development banks or other financial institutions with deep pockets for financing. The estimation of PV degrada-

tion rate thus plays an important role in securing significant equity and/or debt financing, which is a key step in the development phase of a project. The development banks or financial institutions would generally involve third-party technical advisors to estimate the levelized cost of electricity (LCOE), the ratio of the total cost of the PV power plant to the total energy yield produced by the PV power plant over its entire lifecycle, and thus calculate the return on investment for a PV power plant. As the estimation of the degradation rate directly affects the LCOE of a PV power plant, it relates to the amount of financing obtainable.

In the event of an overestimation of the degradation rate (predicted degradation is greater than the actual degradation), resulting in a lower predicted total energy yield produced over the lifetime of a PV power plant, the financing can be undesirably decreased, or in the worst case scenario, unapproved. In the case of an underestimation of the degradation rate (predicted degradation is smaller than the actual degradation), the predicted total energy yield may become higher than the actual yield. This seemingly favors the securing of financing in the development phase, but ultimately it will be detrimental for the O&M phase, which typically stretches over a long period of 20 to 25 years. Although it is possible to justify a couple of years of underperformance of the PV power plant with the unforeseen "bad" weather, an underestimation of the degradation rate would potentially imply consecutive years of underperformance of the PV power plant. In such situation, depending on the financing terms and conditions from the development banks or financial institutions, a full or partial lock-down of the revenues from the sale of electricity of the PV power plant through power purchased agreements, or feed-in tariffs, will be triggered until certain release conditions are fulfilled. Thus, in order to secure a significant amount of financing, while protecting the owners of the PV power plants from the possibility of a revenue lockdown, an accurate estimation of degradation rate is required.

Aside from being the interest of PV plant owners and investors, PV degradation is also important for the manufacturers to set their warranty. In the increasingly competitive market, it has become popular for the manufacturers to provide peak power warranty for their PV modules. The typical module manufacturer power output warranty increased from 5 years to 25 five years since 1985 [2]. Such warranty usually comes in one of two forms: 1) warranting the maximum annual power decline of PV modules to be less than a certain percentage (such as 0.7%), and 2) warranting the peak power to be above a certain percentage of the nameplate power (such as 80%) at the end of a period (such

as 25 years). Both warranty schemes require accurate information on degradation, or more specifically, the information on PV power degradation quantile. In statistics and probability theory, quantiles are points that divide a probability distribution into contiguous intervals with equal probabilities. The definition itself may be less known, but the examples of quantiles, namely, quartiles and percentiles, are well-known. As degradation rate is only a point estimate, i.e., a number; it does not provide the information on PV degradation distribution. Manufacturers would thus need to consider the degradation quantile in their warranty setting. For example, if the degradation rate is estimated to be 0.7% per year (this can be thought of as the median, if a normal distribution is assumed), it is impractical for the manufacturers to set their warranty exactly at 0.7%, since 50% of the modules are likely to experience a degradation larger than that. Such improper warranty would lead to mass replacement or repair of modules, and thus harm the manufacturers financially.

1.2. PV Degradation Preliminaries

As degradation rate is receiving more attention, many researchers have reported degradation rates based on available data. Comprehensive reviews of published degradation rates can be found in Refs. [2, 3]. Ref. [4] reviewed some of the mechanisms which cause PV degradation. Degradation in PV can be quantified at the module level [5, 6] and system level [7, 8]. Based on the study by Jordan and Kurtz [2], the mean degradation rates of modules and systems differ by only small margins, despite their distinct degradation mechanisms. For such reasons, this chapter only provides a simulation example on module degradation. Nevertheless, the methods to measure system degradation are provided for referencing.

PV degradation is studied across different technologies [9, 10, 11, 12]. Five mainstream technologies are often seen in the literature, namely, amorphous silicon, cadmium telluride, copper indium gallium selenide, mono-crystalline silicon and multi-crystalline silicon. Among these technologies, crystalline silicon received the most attention at the reported time [2]. Therefore, in the later analysis, without loss of generality, crystalline silicon modules are used. For crystalline silicon technologies, the degradation rates observed in the first year of operation are much higher due to early degradation mechanisms, such as the light induced degradation (LID) [13]. Therefore, it is more amenable to remove this “burn-in” year from the simulation.

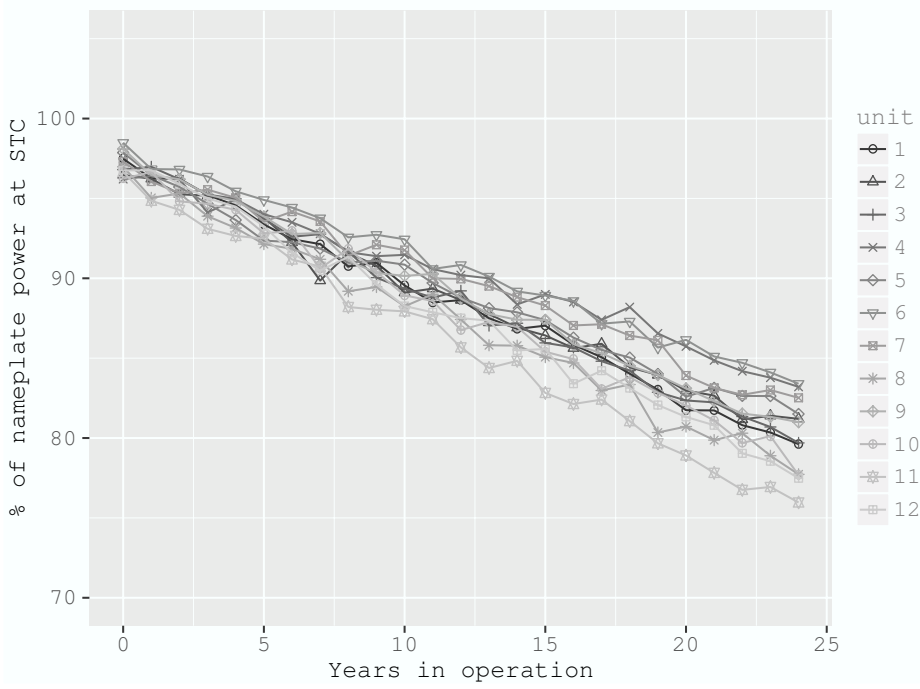

Figure 1. Simulated degradation paths for 12 collocated crystalline silicon modules from the same manufacturing batch. Simulation is performed based on Eq. (6), see below.

As mentioned earlier, the nameplate power measured under standard test conditions (STC) is a commonly used parameter to describe the expected module energy output. However, even for modules with the same nameplate power, the actual energy production may be significantly different [13]. Some factors that lead to these differences are climate, manufacturing process and installation skill, etc. During a degradation study, these factors can be eliminated by considering PV modules of a same manufacturing batch and installed at a shared location. Nevertheless, other factors that affect the peak power, such as different degrees of LID, as well as the intricate loss propagation in each module, are difficult to control, if not to eliminate at all. The degradation rate estimation thus cannot depend on few measurements of a single sample; repeated measures are essential.

Before we describe the degradation model based on repeated measures, a set of typical degradation curves is shown. Figure 1 shows the degradation curves for 12 crystalline silicon modules; simulation (detailed in Section 3) is used to generate these curves. It is assumed that these modules have identical nameplate information and are installed at a shared climatic condition. Furthermore, the early degradation effects are removed from the simulation, so that the degradation of the remaining years can be assumed to be linear. Although some publications use an exponential degradation model [14]; it is shown that for a typical starting degradation rate, the models do not differ significantly up to 25 years [15].

In the following sections, we are going to look at: 1) how the degradation curves shown in Figure 1 can be modeled using the linear mixed effect model (LMM); 2) how to estimate the parameter values and quantile information through the LMM; and 3) how to effectively and efficiently plan the degradation measurement. Degradation measurement planning in this case refers to the design of degradation experiment, which includes design parameters such as the sample size, period of study, measurement frequency and types of measurement.

2. Modeling, Parameter Estimation and Measurement Planning

Repeated measures are defined if an outcome is measured repeatedly within a set of *units* [16]. In our current context, a unit could be a PV module or system, depending on the type of degradation measurements. These collected data are called *longitudinal data* if they are taken over time [17].

2.1. Degradation Model

Suppose we collect m_i degradation measurements of unit i, where $i = 1, \cdots, n$ denotes the samples, and let y_{ij} be the measured degradation of unit i at time t_{ij}, where $j = 1, \cdots, m_i$, the linear degradation model is given by:

$$y_{ij} = b_{0,i} + b_{1,i} t_{ij} + \varepsilon_{ij}, \tag{1}$$

where $b_{0,i}$ and $b_{1,i}$ denote the intercept and the gradient of the linear model for unit i; ε_{ij} denotes a random effect. The term $\mathcal{D}_i = b_{0,i} + b_{1,i} t_{ij}$ is called the

true degradation path for unit i. Symbol m_i is used to denote the (possibly) different numbers of measurements for each unit, as longitudinal data are often unbalanced [18, 19].

We have discussed earlier that PV degradation is a complex function of a variety of factors. In this chapter, we do not consider contributing factors that may have significant impacts on degradation, such as environmental and climate condition, technology and manufacturer. Under such arrangement, the intercept and gradient in Eq. (1) can be modeled using a bivariate normal distribution, $(b_0, b_1)^\top \sim \mathrm{BVN}(\boldsymbol{\beta}, \boldsymbol{V})$ with mean vector

$$\boldsymbol{\beta} = (\beta_0, \beta_1)^\top \tag{2}$$

and covariance matrix

$$\boldsymbol{V} = \begin{pmatrix} \sigma_{b_0}^2 & \rho\sigma_{b_0}\sigma_{b_1} \\ \rho\sigma_{b_0}\sigma_{b_1} & \sigma_{b_1}^2 \end{pmatrix}. \tag{3}$$

It should be noted that b_0 and b_1 are random variables, and $b_{0,i}$ and $b_{1,i}$ are a particular realization of these random variables, i.e., the intercept and gradient for unit i. The practical relevance and implications of the above BVN assumption are more described in Section 3. The probability density function (pdf) of BVN distribution is:

$$f(b_0, b_1; \boldsymbol{\beta}, \boldsymbol{V}) = \frac{1}{2\pi\sigma_{b_0}\sigma_{b_1}\sqrt{1-\rho^2}} \exp\left[-\frac{\kappa}{2(1-\rho^2)}\right], \tag{4}$$

where

$$\kappa = \left(\frac{b_1-\beta_1}{\sigma_{b_0}}\right)^2 + \left(\frac{b_2-\beta_2}{\sigma_{b_1}}\right)^2 - 2\rho\left(\frac{b_1-\beta_1}{\sigma_{b_0}}\right)\left(\frac{b_2-\beta_2}{\sigma_{b_1}}\right). \tag{5}$$

2.2. Linear Mixed Effects Model

Linear mixed effects model is perhaps the most fundamental model for analyzing longitudinal data. Its general form is given as:

$$\boldsymbol{Y}_i = \boldsymbol{X}_i\boldsymbol{\beta} + \boldsymbol{Z}_i\boldsymbol{b}_i^* + \boldsymbol{\varepsilon}_i, \tag{6}$$

where $\boldsymbol{X}_i$ and $\boldsymbol{Z}_i$ are matrices of known covariates [18]. In this model, $\boldsymbol{\beta}$ is the *fixed effects* and $\boldsymbol{b}_i^*$ is the *unit-specific effects*. The degradation model, Eq. (1),

can be related to the above matrix equation with notations used in Section 2.1, i.e., $\boldsymbol{Y}_i = (y_{i1}, \cdots, y_{im_i})^\top$, $\boldsymbol{\varepsilon}_i = (\varepsilon_{i1}, \cdots, \varepsilon_{im_i})^\top$ and $\boldsymbol{b}_i^* = (b_{0,i}^*, b_{1,i}^*)^\top$; it can be expressed as:

$$y_{ij} = (\beta_0 + b_{0,i}^*) + (\beta_1 + b_{1,i}^*)t_{ij} + \varepsilon_{ij}, \tag{7}$$

where $(b_0^*, b_1^*)^\top \sim \mathrm{BVN}(\boldsymbol{0}, \boldsymbol{V})$. Furthermore, we have:

$$\boldsymbol{\varepsilon}_i \sim \mathrm{MVN}(\boldsymbol{0}, \sigma^2 \boldsymbol{I}_i); \tag{8}$$

$$\mathbb{V}(\boldsymbol{b}_i^*, \boldsymbol{\varepsilon}_i) = \boldsymbol{0}; \tag{9}$$

$$\boldsymbol{X}_i = \boldsymbol{Z}_i = \begin{pmatrix} 1 & t_{i1} \\ \vdots & \vdots \\ 1 & t_{im_i} \end{pmatrix} \tag{10}$$

and $\boldsymbol{I}_i$ is an m_i by m_i identity matrix. We do not distinguish between LMM and degradation model hereafter.

Eq. (8) implies that $\boldsymbol{\varepsilon}_i$ is independent and normally distributed. Eq. (9) reveals that $\boldsymbol{b}_i^*$ and $\boldsymbol{\varepsilon}_i$ are independent. Under these settings, $\boldsymbol{Y}_i$ has a multivariate normal distribution with mean vector $\boldsymbol{X}_i\boldsymbol{\beta}$ and covariance

$$\boldsymbol{\Sigma}_i = \mathbb{V}(\boldsymbol{Y}_i) = \boldsymbol{Z}_i \boldsymbol{V} \boldsymbol{Z}_i^\top + \sigma^2 \boldsymbol{I}_i, \tag{11}$$

which is a special case of the repeated-measured models in Ref. [19], i.e, $\boldsymbol{Y}_i \sim \mathrm{MVN}(\boldsymbol{X}_i\boldsymbol{\beta}, \boldsymbol{\Sigma}_i)$. The multivariate normal random vector $\boldsymbol{Y}_i$ has pdf:

$$f(\boldsymbol{y}_i; \boldsymbol{X}_i\boldsymbol{\beta}, \boldsymbol{\Sigma}_i) = \frac{1}{(\sqrt{2\pi})^{m_i}|\boldsymbol{\Sigma_i}|^{1/2}} \exp\left[-\frac{1}{2}(\boldsymbol{y}_i - \boldsymbol{X}_i\boldsymbol{\beta})^\top \boldsymbol{\Sigma}_i^{-1}(\boldsymbol{y}_i - \boldsymbol{X}_i\boldsymbol{\beta})\right], \tag{12}$$

where $|\boldsymbol{\Sigma}_i|$ is the determinant of $\boldsymbol{\Sigma}_i$.

2.3. Parameter Estimation

We have presented the degradation model in the previous sections. In order to use the model to describe a particular set of data, model parameters need to be estimated. Standard ways for parameter estimation include method of moments, maximum likelihood (ML) method and Bayesian method; we use ML method in this chapter. *Maximum likelihood estimator* (MLE) of a parameter θ is the value of θ that maximizes $\mathcal{L}(\theta)$, the *likelihood function* of θ. As maximizing a *log-likelihood function*, $\ell(\theta)$, leads to the same answer as maximizing $\mathcal{L}(\theta)$, we consider $\ell(\theta)$ here. In this case, it is easier to work with $\ell(\theta)$.

By observing Eq. (12), we know that the MVN is controlled by its mean vector $\boldsymbol{X}_i\boldsymbol{\beta}$ and covariance matrix $\boldsymbol{\Sigma}_i$. These two parameters are controlled by:

$$\boldsymbol{\theta} = (\beta_0, \beta_1, \sigma_{b_0}, \sigma_{b_1}, \rho, \sigma)^\top. \tag{13}$$

Suppose $\boldsymbol{y}_1, \cdots, \boldsymbol{y}_n$ are independent observations from $\boldsymbol{Y}_1, \cdots, \boldsymbol{Y}_n$, respectively, following Ref. [19], the total log-likelihood for n units is:

$$\ell(\boldsymbol{\theta}) = \sum_{i=1}^{n} \ell_i(\boldsymbol{\theta}) = \text{const.} - \frac{1}{2}\sum_{i=1}^{n}(\boldsymbol{y}_i - \boldsymbol{X}_i\boldsymbol{\beta})^\top \boldsymbol{\Sigma}_i^{-1}(\boldsymbol{y}_i - \boldsymbol{X}_i\boldsymbol{\beta}) - \frac{1}{2}\sum_{i=1}^{n}\log|\boldsymbol{\Sigma}_i|, \tag{14}$$

where $\ell_i(\boldsymbol{\theta})$ is the log-likelihood for observational unit i. We use $\widehat{\boldsymbol{\theta}}$ to denote the ML estimate of $\boldsymbol{\theta}$.

2.4. Degradation Quantiles

The parameters of an LMM are estimated through the ML method. The information attained so far is sufficient for many PV degradation applications. For example, $\widehat{\beta}_1$ (the ML estimate of β_1) can be considered as the estimated degradation rate. Other quantities, such as the degradation quantile, can also be derived from $\widehat{\boldsymbol{\theta}}$.

Recall that the true degradation at time t is $\mathcal{D} = b_0 + b_1 t$, $\mathcal{D}$ can be considered as a function of random variables. For the present case, b_0 and b_1 follow a BVN distribution, their sum can be shown to be normally distributed with mean and variance being:

$$\mathbb{E}(\mathcal{D}) = \mathbb{E}(b_0 + b_1 t) = \beta_0 + \beta_1 t \tag{15}$$

and

$$\mathbb{V}(\mathcal{D}) = \mathbb{V}(b_0 + b_1 t) = \sigma_{b_0}^2 + t^2\sigma_{b_1}^2 + 2t\rho\sigma_{b_0}\sigma_{b_1}, \tag{16}$$

respectively. The p quantile of the degradation distribution at time t is:

$$d_p(t) = \mathbb{E}(\mathcal{D}) + \sqrt{\mathbb{V}(\mathcal{D})}\Phi^{-1}(p), \tag{17}$$

where $\Phi^{-1}(p)$ is the *probit* function. Mathematically, it is the inverse of $\Phi(z)$, the standard normal CDF. For example, $\Phi(-1.96) = 0.025$ and $\Phi^{-1}(0.025) = -1.96$. Let $\widehat{d}_p(t)$ be the ML estimate of $d_p(t)$, it can be directly obtained by evaluating Eq. (17) at $\widehat{\boldsymbol{\theta}}$:

$$\widehat{d}_p(t) = \widehat{\beta}_0 + \widehat{\beta}_1 t + \Phi^{-1}(p)\sqrt{\widehat{\sigma}_{b_0}^2 + t^2\widehat{\sigma}_{b_1}^2 + 2t\widehat{\rho}\widehat{\sigma}_{b_0}\widehat{\sigma}_{b_1}}. \tag{18}$$

2.5. Preliminaries for Degradation Measurement Planning

In statistics, estimators (such as MLE) are random variables; their distributions are called *sampling distribution*. On the other hand, estimates are numbers computed from data. For simplicity, we do not distinguish them in terms of notations in this chapter. However, the concept should not be mixed up.

The estimates $\widehat{\boldsymbol{\theta}}$ and $\widehat{d}_p(t)$ are known as *point estimates*; point estimation provides a single "best guess" of some quantity of interest [20]. However, point estimates are often insufficient; the knowledge of the sampling distributions is also important, especially during measurement planning where confidence intervals are of interest. The standard deviation of an estimator is called the *standard error*, denoted by $\mathbf{se}$. In particular, we are interested in the standard error of the MLE of the p quantile, namely, $\mathbf{se}(\widehat{d}_p)$. To derive $\mathbf{se}(\widehat{d}_p)$, Fisher information is useful.

2.5.1. Fisher Information

Let random variable X have a distribution $f(x;\theta)$, the *score function* (a function of θ) is defined to be:

$$s(X;\theta) = \frac{\partial \ell(\theta)}{\partial \theta} = \frac{\partial \log f(x;\theta)}{\partial \theta}, \tag{19}$$

i.e., the derivative of the log-likelihood. The *Fisher information* $\mathcal{I}(\theta)$ is defined as:

$$\mathcal{I}(\theta) = \mathbb{E}_\theta\left[s^2(X;\theta)\right] = \int \left(\frac{\partial \ell(\theta)}{\partial \theta}\right)^2 f(x;\theta)dx. \tag{20}$$

As Eq. (20) can be difficult to evaluate sometimes, an alternative definition can be used:

$$\mathcal{I}(\theta) = -\mathbb{E}_\theta\left(\frac{\partial^2 \ell(\theta)}{\partial \theta^2}\right). \tag{21}$$

A proof of Eq. (21) can be found in Ref. [21], page 242.

In our present case, the parameter $\boldsymbol{\theta}$ can be written into $\boldsymbol{\theta} = (\beta_0, \beta_1, \sigma_{b_0}, \sigma_{b_1}, \rho, \sigma)^\top = (\boldsymbol{\beta}^\top, \boldsymbol{\vartheta}^\top)^\top$, the Fisher information of unit i can be

evaluated by considering the Hessian matrix [19]:

$$\boldsymbol{H}_i = \begin{pmatrix} \boldsymbol{H}_{\boldsymbol{\beta\beta},i} & \boldsymbol{H}_{\boldsymbol{\beta\vartheta},i} \\ \boldsymbol{H}_{\boldsymbol{\vartheta\beta},i} & \boldsymbol{H}_{\boldsymbol{\vartheta\vartheta},i} \end{pmatrix} = \begin{pmatrix} \dfrac{\partial^2 \ell_i(\boldsymbol{\theta})}{\partial \boldsymbol{\beta} \partial \boldsymbol{\beta}} & \dfrac{\partial^2 \ell_i(\boldsymbol{\theta})}{\partial \boldsymbol{\beta} \partial \boldsymbol{\vartheta}} \\ \dfrac{\partial^2 \ell_i(\boldsymbol{\theta})}{\partial \boldsymbol{\vartheta} \partial \boldsymbol{\beta}} & \dfrac{\partial^2 \ell_i(\boldsymbol{\theta})}{\partial \boldsymbol{\vartheta} \partial \boldsymbol{\vartheta}} \end{pmatrix}. \tag{22}$$

We thus have

$$\mathcal{I}_i(\boldsymbol{\theta}) = \begin{pmatrix} \boldsymbol{X}_i^\top \boldsymbol{\Sigma}_i^{-1} \boldsymbol{X}_i & \mathbf{0} \\ \mathbf{0} & \boldsymbol{M}_i \end{pmatrix}, \tag{23}$$

where the element on row r and column s of the symmetrical 4 by 4 matrix $\boldsymbol{M}_i$ is:

$$M_{i,rs} = \frac{1}{2} tr(\boldsymbol{\Sigma}_i^{-1} \dot{\boldsymbol{\Sigma}}_{ir} \boldsymbol{\Sigma}_i^{-1} \dot{\boldsymbol{\Sigma}}_{is}), \tag{24}$$

$r, s = 1, \cdots, 4$ and the explicit representations of $\dot{\boldsymbol{\Sigma}}_{ir}$ or $\dot{\boldsymbol{\Sigma}}_{is}$ are obtained by differentiating Eq. (11) with respect to each parameter in $\boldsymbol{\vartheta}$:

$$\dot{\boldsymbol{\Sigma}}_{i1} = \frac{\partial \boldsymbol{\Sigma}_i}{\partial \vartheta_1} = \frac{\partial \boldsymbol{\Sigma}_i}{\partial \sigma_{b_0}} = \boldsymbol{Z}_i \begin{pmatrix} 2\sigma_{b_0} & \rho\sigma_{b_1} \\ \rho\sigma_{b_1} & 0 \end{pmatrix} \boldsymbol{Z}_i^\top; \tag{25}$$

$$\dot{\boldsymbol{\Sigma}}_{i2} = \frac{\partial \boldsymbol{\Sigma}_i}{\partial \vartheta_2} = \frac{\partial \boldsymbol{\Sigma}_i}{\partial \sigma_{b_1}} = \boldsymbol{Z}_i \begin{pmatrix} 0 & \rho\sigma_{b_0} \\ \rho\sigma_{b_0} & 2\sigma_{b_1} \end{pmatrix} \boldsymbol{Z}_i^\top; \tag{26}$$

$$\dot{\boldsymbol{\Sigma}}_{i3} = \frac{\partial \boldsymbol{\Sigma}_i}{\partial \vartheta_3} = \frac{\partial \boldsymbol{\Sigma}_i}{\partial \rho} = \boldsymbol{Z}_i \begin{pmatrix} 0 & \sigma_{b_0}\sigma_{b_1} \\ \sigma_{b_0}\sigma_{b_1} & 0 \end{pmatrix} \boldsymbol{Z}_i^\top; \tag{27}$$

$$\dot{\boldsymbol{\Sigma}}_{i4} = \frac{\partial \boldsymbol{\Sigma}_i}{\partial \vartheta_4} = \frac{\partial \boldsymbol{\Sigma}_i}{\partial \sigma} = 2\sigma \boldsymbol{I}_i. \tag{28}$$

The Fisher information for all n units is the sum of the Fisher information for each unit:

$$\mathcal{I}(\boldsymbol{\theta}) = \sum_{i=1}^{n} \mathcal{I}_i(\boldsymbol{\theta}). \tag{29}$$

2.5.2. Standard Error of MLE

The Fisher information matrix is used to calculate the standard error and covariance matrices associated with ML estimates. Wasserman [20] states the following theorem:

Theorem 1. *(Asymptotic Normality of the MLE) Let* $\mathbf{se} = \sqrt{\mathbb{V}(\widehat{\theta})}$. *Under appropriate regularity conditions, the following hold:*
1. $\mathbf{se} \approx \sqrt{1/\mathcal{I}(\theta)}$ *and*

$$\frac{(\widehat{\theta} - \theta)}{\mathbf{se}} \rightsquigarrow \mathrm{N}(0, 1). \tag{30}$$

2. Let $\widehat{\mathbf{se}} = \sqrt{1/\mathcal{I}(\widehat{\theta})}$. *Then,*

$$\frac{(\widehat{\theta} - \theta)}{\widehat{\mathbf{se}}} \rightsquigarrow \mathrm{N}(0, 1). \tag{31}$$

Symbol $\rightsquigarrow$ *denotes convergence in distribution. (end of theorem)*

The first statement of the theorem says that $\widehat{\theta} \approx \mathrm{N}(\theta, \mathbf{se})$. The second statements says that even when the standard error is replaced by the estimated standard error, the asymptotic normality is still true. This theorem can thus be used to construct the asymptotic confidence interval for $\widehat{\theta}$. If we extend the theorem to multi-parameter cases [20], we have:

Theorem 2. *Under appropriate regularity conditions,*

$$(\widehat{\boldsymbol{\theta}} - \boldsymbol{\theta}) \approx \mathrm{MVN}(\mathbf{0}, \boldsymbol{J}(\boldsymbol{\theta})), \tag{32}$$

where $\boldsymbol{J}(\boldsymbol{\theta}) = [\mathcal{I}(\boldsymbol{\theta})]^{-1}$ *is the inverse of the Fisher information matrix. (end of theorem)*

The details of those regularity conditions mentioned in the above theorems can be found in Chapter 12 of Ref. [21]. Following Theorem 2, we have:

$$\mathbb{V}(\widehat{\boldsymbol{\theta}}) = [\mathcal{I}(\boldsymbol{\theta})]^{-1}, \tag{33}$$

where $\mathbb{V}(\cdot)$ denotes the *approximated variance-covariance matrix* of the MLE. In other words, the $\widehat{\mathbf{se}}^2$ of each parameter is given by the corresponding diagonal term of $\boldsymbol{J}(\boldsymbol{\theta})$; the covariance between the parameters are given the off-diagonal terms of $\boldsymbol{J}(\boldsymbol{\theta})$. An estimate of $\mathbb{V}(\cdot)$ at the ML estimates is denoted by $\widehat{\mathbb{V}}(\widehat{\boldsymbol{\theta}})$.

2.5.3. Standard Error and Confidence Interval of the Degradation Quantiles

The estimate of the approximated variance-covariance matrix of the MLE can be obtained through the inverse of the Fisher information matrix. With this information, together with the degradation quantile d_p evaluated at the ML estimates (denoted by $\widehat{d}_p(\widehat{\boldsymbol{\theta}})$ or simply $\widehat{d}_p$), the standard error of the quantile can be estimated through the delta method. In statistics, the *delta method* is used to estimate the approximate probability distribution for a smooth function, g, of an asymptotically normal statistical estimator (such as MLE). In the present case, $g(\widehat{\boldsymbol{\theta}})$ is Eq. (17), namely, the quantile function of the degradation.

Wasserman [20] states the following theorem:

Theorem 3. *(Multiparameter delta method) Suppose that ∇g evaluated at $\widehat{\boldsymbol{\theta}}$ is not 0. Let $\widehat{\tau} = g(\widehat{\boldsymbol{\theta}})$. Then*

$$\frac{(\widehat{\tau} - \tau)}{\widehat{\mathbf{se}}(\widehat{\tau})} \rightsquigarrow \mathrm{N}(0, 1), \tag{34}$$

where

$$\widehat{\mathbf{se}}(\widehat{\tau}) = \sqrt{(\widehat{\nabla} g)^{\top} \widehat{\mathbb{V}}(\widehat{\boldsymbol{\theta}})(\widehat{\nabla} g)}, \tag{35}$$

$\widehat{\nabla} g$ is ∇g evaluated at $\boldsymbol{\theta} = \widehat{\boldsymbol{\theta}}$. (end of theorem)

In our case, ∇g is the (column) vector of partial derivatives of d_p with respect to the parameters. The elements of this vector are:

$$\partial d_p / \partial \beta_0 = 1; \tag{36}$$
$$\partial d_p / \partial \beta_1 = t; \tag{37}$$
$$\partial d_p / \partial \sigma_{b_0} = \zeta(2\sigma_{b_0} + 2t\rho\sigma_{b_1}); \tag{38}$$
$$\partial d_p / \partial \sigma_{b_1} = \zeta(2t^2\sigma_{b_1} + 2t\rho\sigma_{b_0}); \tag{39}$$
$$\partial d_p / \partial \rho = \zeta(2t\sigma_{b_0}\sigma_{b_1}); \tag{40}$$
$$\partial d_p / \partial \sigma = 0, \tag{41}$$

where

$$\zeta = \frac{\Phi^{-1}(p)}{2\sqrt{\sigma_{b_0}^2 + t^2\sigma_{b_1} + 2t\rho\sigma_{b_0}\sigma_{b_1}}}. \tag{42}$$

The estimated standard error of the quantile of degradation distribution at the ML estimates is thus given by:

$$\widehat{\mathbf{se}}(\widehat{d}_p) = \sqrt{\widehat{\boldsymbol{c}}^\top \widehat{\mathbb{V}}(\widehat{\boldsymbol{\theta}})\widehat{\boldsymbol{c}}}, \tag{43}$$

where $\boldsymbol{c}$ is the (column) vector of partial derivatives of d_p. The $1-\alpha\%$ confidence interval of the estimated quantile is thus given by:

$$\widehat{d}_p \pm z_{\alpha/2}\widehat{\mathbf{se}}(\widehat{d}_p), \tag{44}$$

under the normal-based interval.

2.6. Section Summary

This section discusses the modeling and parameter estimation for PV degradation. A linear degradation model is first presented. Its equivalent LMM is then outlined. A total of six parameters, namely, $\beta_0, \beta_1, \sigma_{b_0}, \sigma_{b_1}, \rho$ and σ, are estimated using the ML method. With the estimated parameters, the degradation quantile $d_p(t)$ at time t could be evaluated through Eq. (18). However, as a single value (a point estimate) carries limited information about the distribution of $\widehat{d}_p$, the standard error and confidence interval of $\widehat{d}_p$ are given in Eqs. (43) and (44), respectively. To derive the representations of standard error and confidence interval, the Fisher information and several theorems are used.

3. Simulation Study on PV Degradation Planning

In this section, we use simulation to describe the planning method for PV degradation. In particular, we are going to look at how degradation measurement settings would affect the uncertainties in degradation estimates. In our context, *degradation measurement settings* refer to factors such as type of degradation measurements, number of test units and number of measurements for each unit. We note that this simulation study does not advise on the "optimal" settings for degradation measurements, because the appropriate settings depend on a variety of factors. Furthermore, the tolerance for standard error and the acceptable range for confidence intervals may also vary based on different expert views. We thus present a visual representation of various concepts outlined in the previous section.

In the simulation study below, we consider PV modules as the degradation test units. More specifically, a total of 12 crystalline modules are assumed. By assuming the units are collocated modules from a same manufacturing batch, some factors (e.g., climate, technology and manufacturer) that can affect the degradation are eliminated.

3.1. Low- and High- Accuracy Degradation Experiments

Three methods of measurement are commonly used for PV degradation studies [22]: 1) the regression-based low-accuracy experiment (LE) through outdoor monitoring data, 2) the LE through outdoor I–V measurements, and 3) the high-accuracy experiment (HE) though the indoor I–V measurements. Similar to many other engineering problems (see Refs. [23, 24, 25] for other examples on low- and high-accuracy experiments), the LE data in PV degradation are more accessible as compared to the HE data. To fully utilize the results from LE, the outcomes from the HEs are often used to benchmark various LEs to determine their accuracies [22]. Although LEs in general have a lower cost as compared to HE, the limitation of the LEs is obvious during the decision making process of the manufacturers, for example, setting the degradation warranty based on inaccurate degradation rates leads to financial risks [26].

Among the three degradation experiments listed above, the first experiment is commonly used to determine the degradation of PV systems or sub-systems, while the latter two experiments are used when the test units are PV modules. Although the units used in this simulation study are set to be modules, we describe all three experiments below to give the readers a general understanding on each experiment.

3.1.1. Low-Accuracy Degradation Methods

Low-accuracy degradation experiments use regressions and outdoor monitoring data to determine degradation rates. The regressor (explanatory variable) is usually time, while the regressands (explained variable) are different metrics. Consider a linear regression problem $y = b_0 + b_1 t + \varepsilon$, the term *metric* is used by Jordan and Kurtz [22] to denote y. After the regression, the degradation rate is reflected by the fitted value $\widehat{b}_1$, i.e., the gradient of the fitted line.

When the test units are PV systems, examples of metrics include performance ratio (PR), PR with temperature correction [27], $\mathrm{DC}/G_{\mathrm{POA}}$ [28] and PVUSA [29]. These four metrics were summarized by Jordan and Kurtz [22].

While these metrics depend on irradiance data (see below) which is not always available, other irradiance-independent metrics have been proposed [30]. On the other hand, when the units are modules, examples of metrics include maximum power ($P_{\max}$), open-circuit voltage ($V_{\rm oc}$), short-circuit current ($I_{\rm sc}$) and fill factor (FF). These metrics were described and used by Smith *et al.* [31].

The core idea of LEs is to use the drops in certain metrics to represent degradation in PV modules/systems over time. It is therefore important to consider various types of corrections and data filtering. PR is perhaps the most commonly used metric to measure system performance. In mid-latitude regions, PR varies within a year with winter showing a relatively higher PR than summer. This observation is mainly due to the lower module temperature in winter. Module temperature is thus commonly used to adjust the seasonal variation in PR. For example, Dierauf *et al.* [32] proposed a PR correlation method where PR is normalized by removing the weather dependency. Conventional PR is given by:

$$\text{PR} = \frac{\sum_t EN_{\text{AC},t}}{\sum_t \left[P_{\text{STC}} \left(\dfrac{G_{\text{POA},t}}{G_{\text{STC}}} \right) \right]}, \tag{45}$$

while the weather-corrected performance ratio, $PR_{\rm corr}$, is:

$$\text{PR}_{\text{corr}} = \frac{\sum_t EN_{\text{AC},t}}{\sum_t \left\{ P_{\text{STC}} \left(\dfrac{G_{\text{POA},t}}{G_{\text{STC}}} \right) \left[1 - \gamma (T_{\text{mod\_typ\_avg}} - T_{\text{mod},t}) \right] \right\}}, \tag{46}$$

with γ being the temperature coefficient for power, with a typically value of $-0.4\%/^{\circ}\text{C}$; $EN_{\rm AC}$ being the measured AC power generation (in kW); $P_{\rm STC}$ being the nameplate power (in kW); $G_{\rm POA}$ being the in-plane irradiance (in kW/m^2); $G_{\rm STC}$ being the STC irradiance (1 kW/m^2); $T_{\rm mod}$ being the module temperature (in $^{\circ}$C) and $T_{\rm mod\_typ\_avg}$ being the average cell temperature computed from a typical meteorological year.

The summation in the above equations can be calculated over any defined period of time, may it be days, weeks, months or years. It is shown that the seasonal cycles in the PR can be effectively removed using this weather correction regardless if monthly or daily PR is used [32]. Besides the corrections in PR, data filtering is also commonly used to remove certain data points. For example, an irradiance filter can be applied to remove data points far from STC; a module temperature filter can be used to remove data points which deviate

largely from the $T_{\mathrm{mod\_typ\_avg}}$. In addition, outlier filters and stability filters are also frequently involved in the data quality control process [22].

As previously mentioned, the metrics used to determine module degradation are usually different from those for systems. In order to compute metrics such as $P_{\max}$, V_{oc} and I_{sc}, I–V measurements (I–V curves) are required. The commercial I–V curve tracers are commonly equipped with the capability of generating the values of these metrics. More advanced mathematical models [33] that are only suitable for off-chip computation are also available. On this point, we refer the readers to another chapter of this book, namely, *PV Panel Modeling and Identification*, for a detailed tutorial. Comparing to the indoor measurement (see below), a drawback of the outdoor I–V measurement is that the ambient condition is uncontrolled in this experiment. This leads to the need of minimizing the effect of weather on degradation rate determination; data filtering is essential in this LE. Data filtering here aims at identifying the data points that are close to the STC, for example, an irradiance filter that includes only data points with deviations of ± 20 W/m^2 from the STC irradiance could be considered. We refer the readers to [31] for a detailed example on data filtering, in which the authors studied the degradation of 12 crystalline silicon modules over a period of 17 years.

The advantage of conducting LEs is that the experiments can be performed remotely once the measurement devices are in place. As compared to the HE, the cost of LE can be lower as well, especially when the monitoring equipment becomes more affordable and reliable. On the other hand, although appropriate measurement equipment setup and data filtering could minimize the uncertainty in the LEs to a certain extent, the outdoor experiments still suffer from soiling and other degradation mechanisms that are hard to trace through monitoring data. In the later sections, we further discuss the trade-off between cost and accuracy for different degradation experiments.

3.1.2. High-Accuracy Degradation Methods

High-accuracy degradation experiments rely on measuring the I–V curves of a PV panel at fixed time intervals under indoor conditions [2]. Due to the dependency on indoor test facilities, HE is usually performed by shipping the modules back to the manufacturers. This embeds high costs into the degradation experiment. For such reasons, it is common (about 74% of all degradation rates reported in the literature) to conduct indoor I–V measurements only once; the

measurements are then compared to the nameplate rating of a module [3]. The inherent assumption is the accuracy of the nameplate rating, which may possess significant variance, especially when early degradation mechanisms are not excluded from the experiments.

3.2. Examples on Parameter Estimation Using MLE

In Section 3.1, low- and high-accuracy degradation experiments are discussed. As the degradation study can be based on different metrics, without loss of generality, we consider percentage of nameplate power at STC as the regressand. We begin our simulation study by setting the degradation parameters. A total of six parameters, namely, β_0, β_1, σ_{b_0}, σ_{b_1}, ρ and σ, are used to parameterize the degradation model. The numeric values of these parameters are justified and set as follows.

PV modules experience early degradation such as LID during the first year of operation. To simulate the approximate 3% drop in the first year, the intercept of true degradation curve β_0 is set at 97. It was reported that some crystalline modules may have more than 4% power loss after the first weeks of operation [13], $\sigma_{b_0} = 0.5$ is used to represent the variations of early degradation among the sample modules. This means that the PV modules under simulation preserve 97% of the nameplate power at STC at time $t = 0$ with a standard deviation of 0.5. It is noted that $t = 0$ denotes the beginning of the simulation, one can consider this to be the beginning of the second actual operating year. Only the simulation time reference t will be used hereafter.

In Ref. [2], a rich literature review is presented on the degradation rate of crystalline silicon technology. It was found that the average degradation rate of crystalline silicon technology is 0.7%/year, i.e., $\beta_1 = -0.7$. Further to that, $\sigma_{b_1} = 0.1$ is interpreted from Ref. [2] to denote the variation in the degradation rate distribution, see Fig. 5 from Ref. [2] for this interpretation.

We assume that the intercept and gradient of the degradation path can be modeled using a BVN distribution with correlation ρ. In reality, this parameter does not carry significant physical implication. However, it is reasonable to assume modules with higher β_0 values degrade slower. Therefore, a small positive correlation between b_0 and b_1, $\rho = 0.3$, is set.

The final model parameter σ represents the error term. It should be set differently for HE and LE. In HE, it can be assumed that the error is small; $\sigma = 0.5$ is set to represent the year-to-year experimental variations in practicing

the HE. In LE, experimental errors are higher; $\sigma = 2$ is set to represent the uncertainties due to imperfect data filtering, soiling and other mechanisms that may affect the variance in module power output.

Considering an expected PV lifetime of 25 years, the simulated output power (in % of the nameplate power) for the 12 modules over a period of 24 years (the burn-in year is not simulated) is plotted in Fig. 1 using the HE assumptions and Eq. (1). To obtain these curves, 12 sets of (b_0, b_1) values are first drawn from the BVN distribution parameterized by $\boldsymbol{\beta}$ and $\boldsymbol{V}$. The true degradation paths ($\mathcal{D}_i$) are then produced using $\mathcal{D}_i = b_{0,i} + b_{1,i} t_{ij}$, where $i = 1, \cdots, 12$, $j = 1, \cdots, m_i$ and $m_i = 24, \forall i$. Noise terms are then added to $\mathcal{D}_i$ using random samples drawn from $\mathrm{N}(0, \sigma^2)$, where $\sigma = 0.5$. Using MLE, the estimated HE parameters are: $\widehat{\beta}_0 = 96.982$, $\widehat{\beta}_1 = -0.706$, $\widehat{\sigma}_{b_0} = 0.481$, $\widehat{\sigma}_{b_1} = 0.087$, $\widehat{\rho} = 0.443$ and $\widehat{\sigma} = 0.516$. These estimated parameters agree with our earlier simulation settings, showing the precise estimations from MLE. Similarly, using the LE simulated data, the ML estimates are $\widehat{\beta}_0 = 96.858$, $\widehat{\beta}_1 = -0.709$, $\widehat{\sigma}_{b_0} = 0.405$, $\widehat{\sigma}_{b_1} = 0.086$, $\widehat{\rho} = 0.631$ and $\widehat{\sigma} = 2.062$.

3.3. Degradation Quantiles Evaluated at ML Estimates

True degradation $\mathcal{D}$ is normally distributed. This is visualized in Figure 2; the data used for plotting are computed with the LE settings. At any time t, the expected value and variance of the normal distribution can be evaluated at the ML estimates through Eqs. (15) and (16). Figure 2 shows the pdfs of $\mathcal{D}$ at $t = 0, 4, \cdots, 24$, the evolution of the pdfs of $\mathcal{D}$ is apparent. In Section 2.4, degradation quantiles are formulated based on the distribution of $\mathcal{D}$. Using the ML estimates we obtained earlier, degradation quantiles can be computed via Eq. (18). Three example quantiles, namely, $\widehat{d}_{0.001}$ (dotted line on x–y plane), $\widehat{d}_{0.5}$ (solid line) and $\widehat{d}_{0.95}$ (dashed line), are shown. This quantile information is critical for manufacturers or system developers to set their warranty.

As mentioned earlier, point estimates have their limitations. Considering standard errors and confidence intervals of the degradation quantiles may help manufacturers or system developers to make their decisions. Standard errors and confidence intervals can be computed via Eqs. (43) and (44), respectively. Figure 3 shows the 95% confidence intervals for $\widehat{d}_{0.5}$ based on 5 and 15 years of LE data.

The computation for the confidence intervals depends on the amount of information available. By examining Eq. (44), it is noted that the confidence

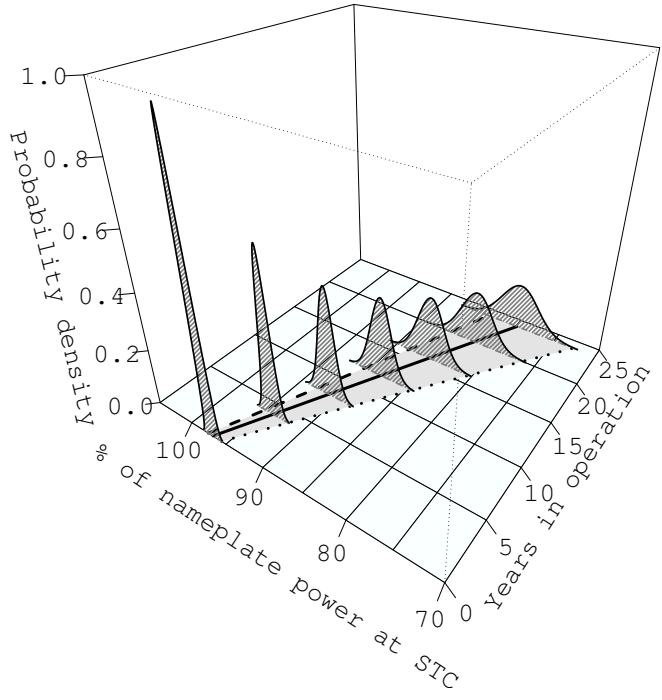

Figure 2. Evaluations of the 0.001 (dotted line on x–y plane), 0.50 (solid line), 0.95 (dashed line) degradation quantiles at ML estimates of the LE.

interval depends on $\widehat{d}_p$ and $\widehat{\mathbf{se}}(\widehat{d}_p)$. After the model parameter $\boldsymbol{\theta}$ is estimated based on whatever available data, may it be 5, 10 or 15 years of data, $\widehat{d}_p$ can be evaluated for any time t. The solid black lines in Figure 3(a) and 3(b) are $\widehat{d}_{0.5}$ for $t = 1, \cdots, 24$; and the two lines are identical. In other words, quantiles do not depend on the amount of information but depend only on $\widehat{\boldsymbol{\theta}}$, see Eq. (18). On the other hand, $\widehat{\mathbf{se}}(\widehat{d}_p) = \sqrt{\widehat{\boldsymbol{c}}^\top \widehat{\mathbb{V}}(\widehat{\boldsymbol{\theta}}) \widehat{\boldsymbol{c}}}$ depends on the amount of information, since $\widehat{\mathbb{V}}(\widehat{\boldsymbol{\theta}})$ is the inverse of the estimated Fisher information matrix. From Eq. (23), we know that $\mathcal{I}(\boldsymbol{\theta})$ depends on the amount of data, i.e., $\boldsymbol{X}_i$ and $\boldsymbol{Z}_i$ represent the available data. Thus, the confidence intervals estimated based on 5 and 15 years of data are different.

Going back to Figure 3, as expected, the width of the confidence interval

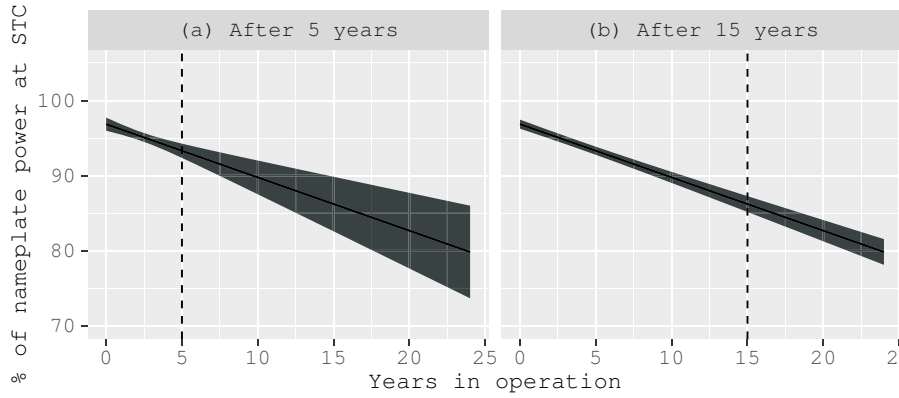

Figure 3. The 95% confidence intervals of 0.50 degradation quantile based on 5 and 15 years of data. The estimated 0.5 quantiles are shown as the solid black line. The shaded regions denote the confidence intervals.

is narrower when more information is available. It should be noted that the confidence intervals plotted in Figure 3 are for the 0.5 quantile; they should not be mixed up with the gray band plotted on the x–y plane of Figure 2.

3.4. Degradation Measurement Planning Using a Simple Test Plan

The discussion so far has assumed that the degradation measurements are available at the time of analyses. However, from a planner's perspective, it is necessary to decide the type of experiments, number of measurements and number of test units, as degradation monitoring is often associated with financial constraints. The cost of LE includes equipment cost and overheads. While it is common to employ monitoring systems at PV farms, when the farm scale becomes large, setting up a single weather station is most likely insufficient. On the other hand, gauging every sub-system may be an overkill. A trade-off needs to be made between degradation estimation accuracy and cost. The composition of the HE cost is different from that of the LE. HE in PV degradation is indoor I–V measurements. Once the modules/systems are deployed, it becomes difficult to conduct I–V measurements especially when the installation is remote. If the manufacturers were to conduct the degradation studies, shipping cost is predominant. In either of the LE or HE case, the number of measurements and

number of units are of interest.

We use the standard error of degradation quantile to reflect the degradation estimation accuracy. As shown in Figure 2, the confidence interval of degradation quantile is a function of time t. From Eq. (44), it is seen that this time dependency is originated from the standard error, i.e., $\widehat{\mathbf{se}}(\widehat{d}_p)$ is also a function of time. However, it should be noted that although the $\widehat{\mathbf{se}}$ at different time $t = 1, \cdots, 24$ are different, the discussion below is applicable for all t. We use $t = 15$ as an example, i.e., the degradation quantile at the end of 15 years is of interest.

Figure 4 (a) shows the contour plot of the estimated standard error of the estimated 0.50 quantile for an HE, $\widehat{\mathbf{se}}(\widehat{d}_{0.50})$, at the end of the evaluation period. The contour plot can be interpreted as follows. The case of $n = 3$ and $m = 3$ corresponds to the situation whereby three units are each measured three times during the course of 15 years at $t = 0$, $t = 7.5$ and $t = 15$, respectively. Under this setting, the estimated standard error is $\widehat{\mathbf{se}}(\widehat{d}_{0.50}) = 0.95$, reflected by the contour line at the bottom left corner of Fig. 4 (a). Similarly, $\widehat{\mathbf{se}}(\widehat{d}_{0.50}) = 0.5$, a smaller standard error, is found for the setup with $n = 11$ units and $m = 3$ measurements. It can be concluded from the "vertical" contour lines that in the HE simulation, fewer number of measurements (per module) can be used without losing much accuracy. Instead, the degradation standard error relies more on the number of units used in HE.

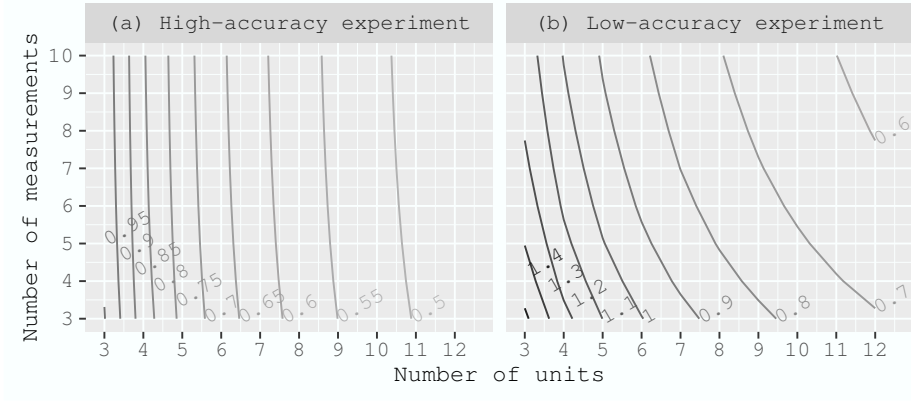

Figure 4. Contour plot of $\widehat{\mathbf{se}}(\widehat{d}_{0.50})$ at the end of evaluation period using different number of units and different number of measurements.

For a comparison of HE and LE errors, Figure 4 (b) shows the contour plot of the estimated standard error for an LE setting. The time of evaluation is also set as $t = 15$; and the contour lines correspond to $\widehat{\mathbf{se}}(\widehat{d}_{0.50})$. In contrast to the HE, standard error for the LE is more sensitive to the number of measurements. The improvement in accuracy can be achieved in the LE by increasing either the number of measurements or the number of units. However, it is observed that for same m and n values, LE yields a higher standard error than HE. This is largely owing to the higher measurement uncertainties embedded in the LE.

Figure 4 shown above demonstrates how the number of units (n) and measurements (m) can affect the standard error estimation, and thus affect the planning method for degradation studies. However, 15 years (as used in Figure 4) may be considered long for a PV degradation study; a shorter period of study such as 5 or 10 years may be more appropriate. On this point, we analyze the extrapolation of degradation quantile standard error below. In other words, we are going to look at how $\widehat{\mathbf{se}}(\widehat{d}_p)$ will be projected (up to 25 years for example) when different runtimes of the experiment are considered.

Fig. 5 (a) shows the standard error of the 0.5 quantile, $\widehat{d}_{0.5}$, as a function of time, for different HE studies. The HE degradation studies are assumed to be conducted over periods of 5, 10 and 15 years. In all three simulations, the number of units is set as 12, and the degradation for each unit is measured once every year throughout the period of study. For example, for the 5 year study, a total of 60 measurements are made to compute the standard error curve shown in Fig. 5 (a). Based on the available data of each case, the standard errors are extrapolated using the degradation model for the remaining years of a typical PV lifetime. It can be seen that the standard error projection at 25 years decreases as the runtime of the experiment increases.

The simulation result of the LE with the same degradation measurement settings is shown in Fig. 5 (b). With no surprise, the standard errors of the LE are higher than those of HE. Nevertheless, it is found that the standard error from the LE is comparable to that of the HE when the study period is long enough, such as a period of 15 years.

The above simple test plan enables PV module manufacturers to plan the degradation studies effectively. Although the examples were given for 0.5 quantile, the approach can be readily applied to any quantile. For example, a similar analysis on the 0.001 quantile can be useful during warranty policy making. The particular choice of experiment and setup can be decided by experts based on some specific tolerable upper bound of the standard error. Together with the

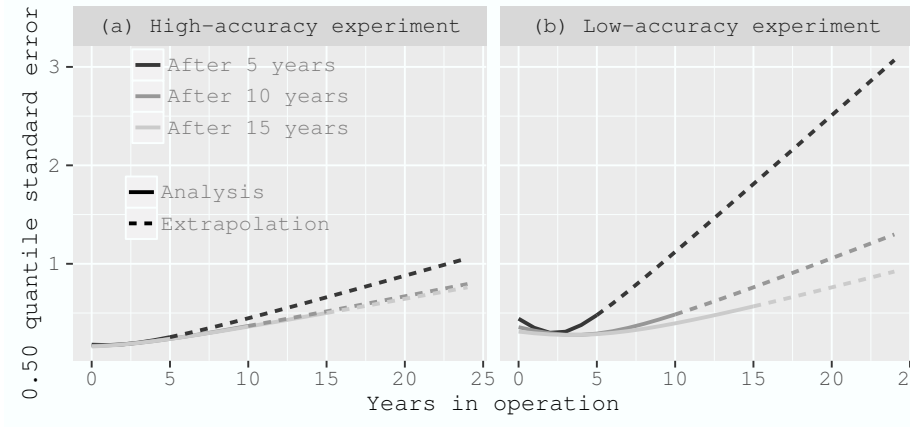

Figure 5. $\widehat{\mathbf{se}}(\widehat{d}_{0.50})$ as functions of time for the HE and LE.

above mentioned cost constraints for HE and LE, the problem can be considered as a multi-objective optimization task. However, the solution to this task is not within the scope of this chapter.

Conclusion

A practical PV degradation model is introduced in this chapter. The degradation model is based on the linear mixed effect model and contains six parameters; it enables flexible simulation and design exercises for photovoltaic degradation. Instead of using the conventional regression based methods for gradient estimation, maximum likelihood estimation is used to identify the degradation rate together with other parameters, simultaneously. The degradation model used here not only provides accurate estimates of the most used parameter, the degradation rate, it also gives quantile estimates of PV degradation. The quantile information gives additional insights for making warranty policy.

Three types of PV degradation experiments are discussed in detail. The low-accuracy experiments are performed in the outdoor conditions; their accuracy is limited by various uncertainties primarily due to ambient weather condition and soiling, which can otherwise be controlled in an indoor measurement environment. It is found that the accuracy of the high-accuracy experiment is rather

independent of the number of measurements made over the period of a degradation study. To improve the accuracy of an HE, more degradation test units should be considered. On the other hand, the accuracies of the LEs depend on both the number of measurements and number of units.

All the degradation experiments described in this chapter depend on the length of the evaluation period, number of measurements and cost. Therefore, due the design of an degradation experiment, a multi-objective optimization could be formulated.

References

[1] E. Meza, "IEA PVPS: Installed PV capacity at 227 GW worldwide." http://www.pv-magazine.com/news, Apr 2016.

[2] D. C. Jordan and S. R. Kurtz, "Photovoltaic degradation rates – an analytical review," *Progress in Photovoltaics: Research and Applications*, vol. 21, no. 1, pp. 12–29, 2013.

[3] D. C. Jordan, S. R. Kurtz, K. VanSant, and J. Newmiller, "Compendium of photovoltaic degradation rates," *Progress in Photovoltaics: Research and Applications*, vol. 24, no. 7, pp. 978–989, 2016.

[4] A. Ndiaye, A. Charki, A. Kobi, C. M. Kèbé, P. A. Ndiaye, and V. Sambou, "Degradations of silicon photovoltaic modules: A literature review," *Solar Energy*, vol. 96, no. 0, pp. 140–151, 2013.

[5] A. Skoczek, T. Sample, and E. D. Dunlop, "The results of performance measurements of field-aged crystalline silicon photovoltaic modules," *Progress in Photovoltaics: Research and Applications*, vol. 17, no. 4, pp. 227–240, 2009.

[6] E. D. Dunlop and D. Halton, "The performance of crystalline silicon photovoltaic solar modules after 22 years of continuous outdoor exposure," *Progress in Photovoltaics: Research and Applications*, vol. 14, no. 1, pp. 53–64, 2006.

[7] J. H. So, Y. S. Jung, G. J. Yu, J. Y. Choi, and J. H. Choi, "Performance results and analysis of 3-kW grid-connected PV systems," *Renewable Energy*, vol. 32, no. 11, pp. 1858–1872, 2007.

[8] S. H. Alawaji, "Evaluation of solar energy research and its applications in saudi arabia-20 years of experience," *Renewable and Sustainable Energy Reviews*, vol. 5, no. 1, pp. 59–77, 2001.

[9] T. Ishii, K. Otani, and T. Takashima, "Effects of solar spectrum and module temperature on outdoor performance of photovoltaic modules in round-robin measurements in Japan," *Progress in Photovoltaics: Research and Applications*, vol. 19, no. 2, pp. 141–148, 2011.

[10] G. Makrides, B. Zinsser, G. Georghiou, M. Schubert, and J. Werner, "Degradation of different photovoltaic technologies under field conditions," in *Photovoltaic Specialists Conference (PVSC), 2010 35th IEEE*, pp. 002332–002337, June 2010.

[11] G. Makrides, B. Zinsser, G. Georghiou, M. Schubert, and J. Werner, "Evaluation of grid-connected photovoltaic system performance losses in cyprus," in *Power Generation, Transmission, Distribution and Energy Conversion (MedPower 2010), 7th Mediterranean Conference and Exhibition on*, pp. 1–7, Nov 2010.

[12] B. Marion, J. Adelstein, K. Boyle, H. Hayden, B. Hammond, T. Fletcher, B. Canada, D. Narang, A. Kimber, L. Mitchell, G. Rich, and T. Townsend, "Performance parameters for grid-connected PV systems," in *Proceedings of the 31st PV Specialists Conference*, (Lake Buena, FL, USA), pp. 1601–1606, 2005.

[13] N. Cereghetti, E. Bura, D. Chianese, G. Friesen, A. Realini, and A. Rezzonico, "Power and energy production of PV modules statistical considerations of 10 years activity," in *Photovoltaic Energy Conversion, 2003. Proceedings of 3rd World Conference on*, vol. 2, pp. 1919–1922 Vol.2, May 2003.

[14] S.-L. Chuang, A. Ishibashi, S. Kijima, N. Nakayama, M. Ukita, and S. Taniguchi, "Kinetic model for degradation of light-emitting diodes," *Quantum Electronics, IEEE Journal of*, vol. 33, pp. 970–979, Jun 1997.

[15] M. Vázquez and I. Rey-Stolle, "Photovoltaic module reliability model based on field degradation studies," *Progress in Photovoltaics: Research and Applications*, vol. 16, no. 5, pp. 419–433, 2008.

[16] G. Verbeke, G. Molenberghs, and D. Rizopoulos, "Random effects models for longitudinal data," in *Longitudinal research with latent variables* (K. van Montfort, J. H. L. Oud, and A. Satorra, eds.), pp. 37–96, Berlin: Springer, 2010.

[17] J. J. Faraway, M. A. Tanner, J. Zidek, and C. Chatfield, *Extending the Linear Model with R*. Routledge, 2004.

[18] G. Verbeke and G. Molenberghs, *Linear Mixed Models for Longitudinal Data*. New York: Springer-Verlag, 2000.

[19] R. I. Jennrich and M. D. Schluchter, "Unbalanced repeated-measures models with structured covariance matrices," *Biometrics*, vol. 42, no. 4, pp. 805–820, 1986.

[20] L. Wasserman, *All of Statistics: A Concise Course in Statistical Inference*. Springer, 2003.

[21] R. B. Millar, *Maximum Likelihood Estimation and Inference: With Examples in R, SAS and ADMB*. John Wiley & Sons, 2011.

[22] D. Jordan and S. Kurtz, "The dark horse of evaluating long-term field performance–data filtering," *Photovoltaics, IEEE Journal of*, vol. 4, no. 1, pp. 317–323, 2014.

[23] P. Z. G. Qian and C. F. J. Wu, "Bayesian hierarchical modeling for integrating low-accuracy and high-accuracy experiments," *Technometrics*, vol. 50, no. 2, pp. 192–204, 2008.

[24] Q. Zhang, X. Deng, P. Z. G. Qian, and X. Wang, "Spatial modeling for refining and predicting surface potential mapping with enhanced resolution," *Nanoscale*, vol. 5, pp. 921–926, 2013.

[25] R. A. Escobar, C. Cortés, A. Pino, E. B. Pereira, F. R. Martins, and J. M. Cardemil, "Solar energy resource assessment in Chile: Satellite estimation and ground station measurements," *Renewable Energy*, vol. 71, pp. 324–332, 2014.

[26] D. C. Jordan, "NREL PV module reliability workshop." http://www.nrel.gov/pv/pvmrw.html, Feb 2011.

[27] H. Haeberlin and C. Beutler, "Normalized representation of energy and power for analysis of performance and on-line error detection in PV systems," in *the 13th Eur. Photovoltaic Sol. Energy Conf.*, (Nice, France), 1995.

[28] D. C. Jordan and S. R. Kurtz, "PV degradation risk," in *World Renewable Energy Forum*, (Denver, Colorado), May 2012.

[29] C. Jennings, "PV module performance at PG&E," in *Photovoltaic Specialists Conference, 1988., Conference Record of the Twentieth IEEE*, pp. 1225–1229 vol.2, 1988.

[30] S. Pulver, D. Cormode, A. Cronin, D. Jordan, S. Kurtz, and R. Smith, "Measuring Degradation Rates Without Irradiance Data," Tech. Rep. NREL/CP-5200-47597, National Renewable Energy Laboratory, Golden, CO, USA, 2010.

[31] R. M. Smith, D. C. Jordan, and S. R. Kurtz, "Outdoor PV module degradation of current-voltage parameters," Tech. Rep. NREL/CP-5200-53713, National Renewable Energy Laboratory, Golden, CO, USA, 2012.

[32] T. Dierauf, A. Growitz, S. Kurtz, J. L. B. Cruz, E. Riley, and C. Hansen, "Weather-corrected performance ratio," tech. rep., NREL, April 2013.

[33] L. H. I. Lim, Z. Ye, J. Ye, D. Yang, and H. Du, "A linear identification of diode models from single I–V characteristics of PV panels," *IEEE Transactions on Industrial Electronics*, vol. 62, pp. 4181 – 4193, July 2015.

In: Solar Energy and Solar Panels ISBN: 978-1-53610-380-9
Editor: Joel G. Carter

Chapter 4

COMPARISON FOR POLICY AND PROMOTION STRATEGY OF SOLAR ENERGY DEVELOPMENTS BETWEEN TAIWAN AND JAPAN

Tzu-Yi Pai[1,2,*], Keisuke Hanaki[2], Yi-Ti Tung[3] and Pei-Yu Wang[1]

[1]Master Program of Environmental Education and Management,
Department of Science Education and Application,
National Taichung University of Education, Taichung, Taiwan, ROC
[2]Department of Urban Engineering, School of Engineering,
University of Tokyo, Bunkyo-ku, Tokyo, Japan
[3]Department of Social Work, National Taipei University,
New Taipei City, Taiwan, ROC

ABSTRACT

Solar power is always the ultimate energy source on earth. Solar energy not drives the hydrologic cycle and wind, but also produces biomass including ancient fossil fuels and present foods. Solar energy is one of the potential renewable energy and has been actively promoted by many countries. In this study, the policy and promotion strategy of solar energy

* Corresponding author: E-mail address: bai@ms6.hinet.net, Tel.: +886-4-22183541, Fax: +886-4-22183540.

developments between Taiwan and Japan were surveyed and compared. The results showed that the solar power increased significantly in the past ten years. The cumulative capacity of solar energy (CCSE), solar power generation (SPG), and the ratio of SPG to total power generation for Taiwan in 2014 gave on 615.2, 533.1, and 466.2 times than those in 2005. The CCSE, SPG, and the ratio of SPG to TPG for Japan in 2014 gave on 16.5, 16.4, and 17.6 times than those in 2005. Besides, an analytic hierarchy process (AHP) structure was proposed for decision makers to make decisions to prioritize and select policy and promotion strategy of solar energy developments. Taiwan and Japan have launched solar PV R&D in the 1980s and 1970s, respectively. In the early 2000s, Taiwan enacted the RED Act and rewarded the solar power generation system invested by folk investment to increase the use of renewable energy. Japan enacted the RPS Law and Feed-in Tariffs policy towards the aim of promoting the new energy electricity.

INTRODUCTION

Energy resources have massively deteriorated because human beings consume unlimitedly. Currently, fossil fuels account for about 88 percent of all commercial energy worldwide. The energy supply will be a serious challenge in the future because of the almost diminished reserves. According to the report from World Energy Council, the oil shale and other nontraditional deposits still contain massive amount of petroleum, therefore several countries actively extract the shale oil at present. Even the extraction of shale oil lowers the increase trend of oil price, high oil price strongly affects energy security of Taiwan and Japan because both nations mainly export overseas energy from other countries. Consequently, the combustion of fossil fuel releases a large amount of carbon dioxide and enhance the global warming [1-2].

Renewable energy is the type of energy that can be harvested from nature and can naturally replenish on a human timescale including solar energy, wind energy, geothermal heat, hydraulic energy, tide energy, and wave energy. Renewable energy can eliminate the demand for fossil fuels because it can replace conventional fossil fuels in several distinct areas [3-8].Therefore active promotion of renewable energy has become an important option among many countries to simultaneously conquer the problem of global warming and energy stress. Solar energy is regarded as the most potential renewable energy and has been aggressively promoted by many nations' governments in the world.

Solar power is always the ultimate energy source on earth. Solar energy not drives the hydrologic cycle and wind, but also produces biomass including ancient fossil fuels and present foods. The average amount of solar energy that

the earth receives is about 10000 times all the energy consumed in one year [1].

Solar energy exhibits advantages in several aspects. Although the amount of solar energy that reaches the earth's surface varies geographically, the solar energy is still sufficient and competitive for economical production even at high latitudes, as in northern Europe or Japan. In 2014, the U.S. utility-scale solar energy costs as little as 5.6 cents per kWh, as compared to gas at 6.1 cents and coal at 6.6 cents [1].

A typical solar energy usage is solar thermal system. A typical solar thermal system consists of a glass vacuum tube or a glass-covered flat panel, heat exchanger, some thin pipes, and driving liquid. The hot water can be made by running the driving liquid (such as antifreeze contained water) through thin pipes in the tube or panel. The driving liquid often reaches high temperatures of 95 Centigrade.

The driving liquid with high temperature then is introduced into a heat exchanger. The water in heat exchanger is subsequently heated for direct use or for space heating. At least 330 GW of solar thermal systems have been built worldwide, more than two times of the installed solar-photovoltaic (PV) capacity. Solar thermal systems are common in some countries such as China, but they are less common in the North America and Europe than solar PV systems.

Another way for capturing solar energy is concentrating solar power (CSP) system. CSP often use parabolic mirrors to concentrate and reflect sunlight on a central tube containing a heat-adsorbing liquid. Then the heat-adsorbing liquid is introduced into a hot exchanger for making hot water for direct use or producing steam for electricity generation.

In addition to solar thermal system and CSP, solar PV system can transfer the solar energy to electrical current directly. In the past three decades, the energy efficiency of PV cell has increased from less than 1 % to more than 10 % under field condition. At least 140 GW of solar PV systems have been installed globally [1].

To actively promote solar energy, many studies have pointed out that the policy and promotion strategy of solar energy developments are the successful key.

Therefore the policy and promotion strategy of solar energy developments between Taiwan and Japan were compared in this study. By studying the survey results, the viewpoints will be summarized to serve as a reference for the government to promote the solar energy in the future.

SOLAR POWER GENERATION IN TAIWAN AND JAPAN

Total Power Generation

According to Figure 1, Taiwan's total power generation (TPG) continuously increased from 227419.9GWh in 2005 to 260026.7GWh in 2014, i.e. increased by 14.3 % in the past twenty years [9, 10].

Contrarily, Japan's TPG slightly increased from 882558.6GWh in 2005, peaked in 2007 (919543.891GWh), gradually decreased to 823004.9GWh in 2014, i.e. totally decreased by 6.7 %. Especially, after the Fukushima No.1 nuclear incident in 2011, Japan's TPG significantly decreased from 906417.2GWh in 2010 to 859808.7 GWh in 2011, i.e. decreased by 5.1 % in the single year [11]. Since the impact of Fukushima No.1 nuclear incident was broad and long-lasting, not only the public's behavior of energy usage changed dramatically, but also the public opinion switched from "accepting-nuclear" stance to "anti-nuclear and pro-renewables".

Cumulative Capacity of Solar Energy

In 2005, the cumulative capacity of solar energy (CCSE) was only 1.0 MW in Taiwan. In the recent ten years, the solar energy was developed in Taiwan.

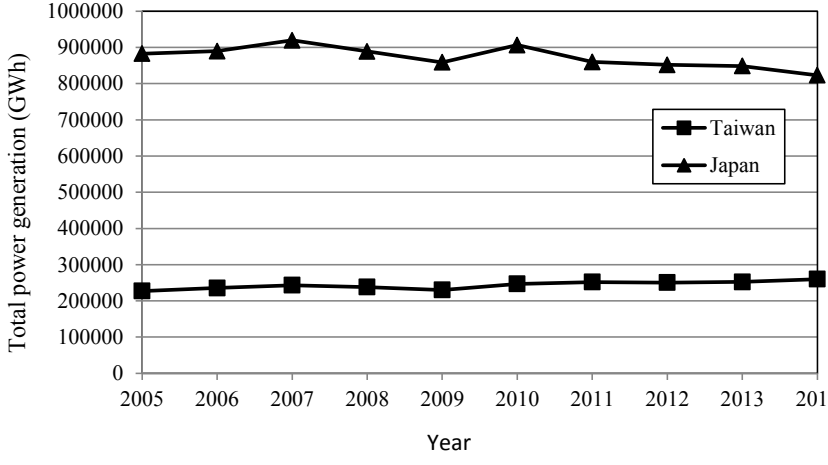

Figure 1. The total power generation for Taiwan and Japan from 2005 to 2014.

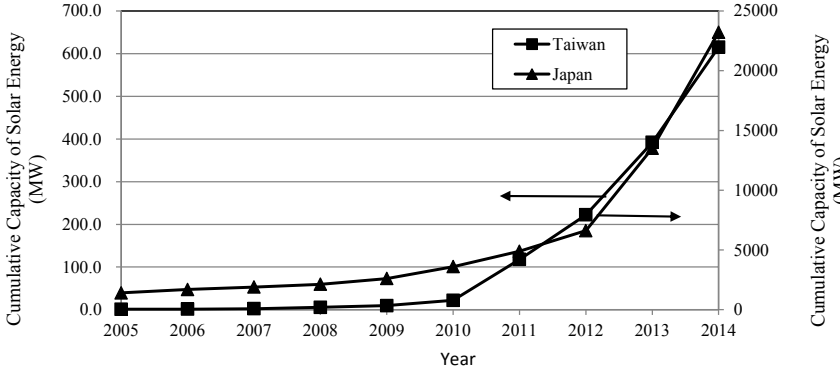

Figure 2. The cumulative capacity of solar energy for Taiwan and Japan from 2005 to 2014.

According to Figure 2, the CCSE in Taiwan significantly increased from 1.0 MW in 2005 to 615.2 MW in 2014. The CCSE for Taiwan in 2014 gave on 615.2 times more capacity than that in 2005 [9-10].

In 2005, the CCSE was 1403.0 MW in Japan. According to Figure 2, the CCSE in Japan significantly increased from 1403.0 MW in 2005 to 23213.0 MW in 2014. The CCSE for Japan in 2014 gave on 16.5 times more capacity than that in 2005 [11].

Solar Power Generation

Since the CCSE is actively installed in both Taiwan and Japan, the solar power generation (SPG) increased significantly from 2005 to 2014 as shown in Figure 3. In accordance with Figure 3, the SPG in Taiwan significantly increased from 0.96GWh in 2005 to 511.73GWh in 2014. The SPG for Taiwan in 2014 gave on 533.1 times more generation than that in 2005 [9-10].

Japan's SPG also increased continuously from 1421.0 GWh in 2005 to 23339.0 GWh in 2014. The SPG for Japan in 2014 gave on 16.4 times more generation than that in 2005 [11].

Ratio of SPG to TPG

With the SPG and TPG data, the ratio of SPG to TPG could be calculated further.

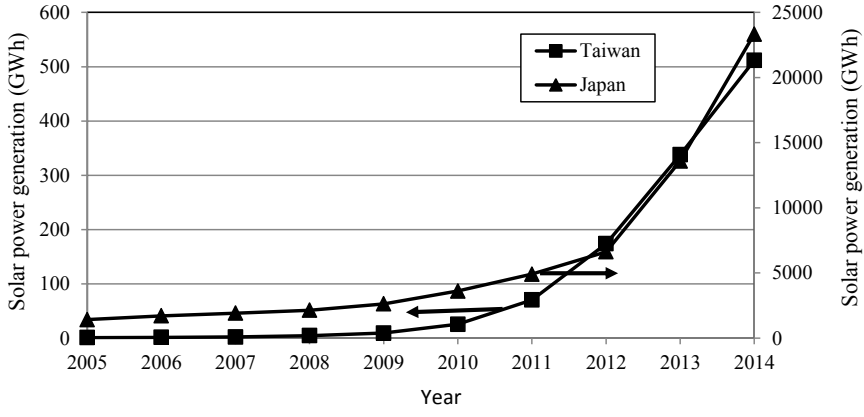

Figure 3. The solar power generation for Taiwan and Japan from 2005 to 2014.

In the past decade, the ratio of SPG to TPG was promoted in both Taiwan and Japan. According to Figure 4, the ratio in Taiwan significantly increased from 0.0004 in 2005 to 0.1968 in 2014. The ratio for Taiwan in 2014 gave on 466.2 times than that in 2005.

Japan's ratio also increased continuously from 0.161 in 2005 to 2.836 in 2014. The ratio for Japan in 2014 gave on 17.6 times than that in 2005.

APPLICATION OF ANALYTICAL HIERARCHY PROCESS

For promoting solar energy, the analytic hierarchy process (AHP) theory was used to identify the priority of the policy and promotion strategy for solar energy developments [3-6]. AHP is a priority measurement proposed by Saaty in the 1970s [12-13]. A chaotic problem can be decomposed into several hierarchy levels using AHP. With this method, the chaotic problem forms a hierarchy structure in which the hierarchical relationships between different levels are constructed [3-6].

First Stage Test

The criteria relating to the policy and promotion strategy of solar energy developments were collected and selected. According to literature review, several evaluation criteria were selected to form the questionnaire of first stage test.

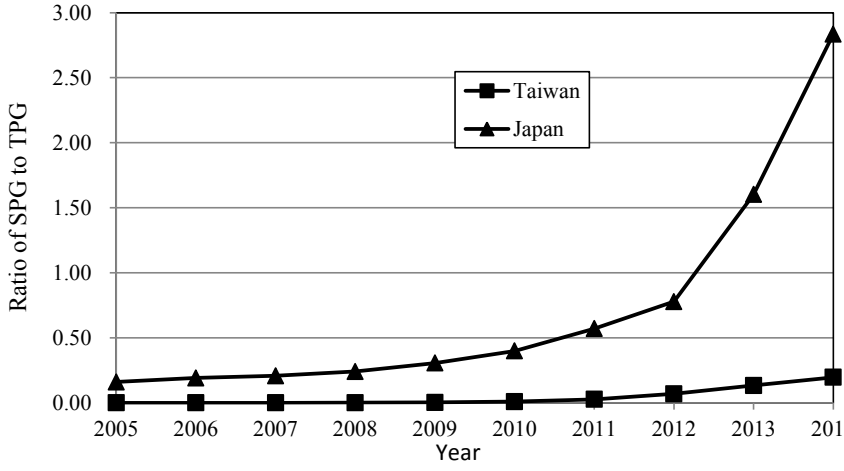

Figure 4. The ratio of SPG to TPG for Taiwan and Japan from 2005 to 2014.

The Likert 5-point scale was employed to compile the questionnaire of first stage test. Thirty six experts from governments, universities, environmental organizations, and community associations of Taiwan were invited to fill in the questionnaires. The items were chosen according to the means and standard deviation.

By calculation, 16 items with the mean top 16 weights were selected as the evaluation criteria to design the hierarchy structure of policy and promotion strategy of wind energy developments. The structure was decomposed in the second level containing four major criteria: (1) policies aspect, (2) educational promotion, (3) technical research and development, and (4) economic incentives. There are total 16 sub-criteria in the third level, as shown in Figure5 [6]. Subsequently, the criteria were used to edit the AHP relative weight questionnaire.

Second Stage Test

According to the first stage questionnaire test, the criteria were used to form the AHP relative weight questionnaire of second stage test. The questionnaire of first stage test was edited using pair-wise comparison. Eighteen practitioners from environmental organizations and community associations of Taiwan were invited to answer the questionnaires of second stage test.

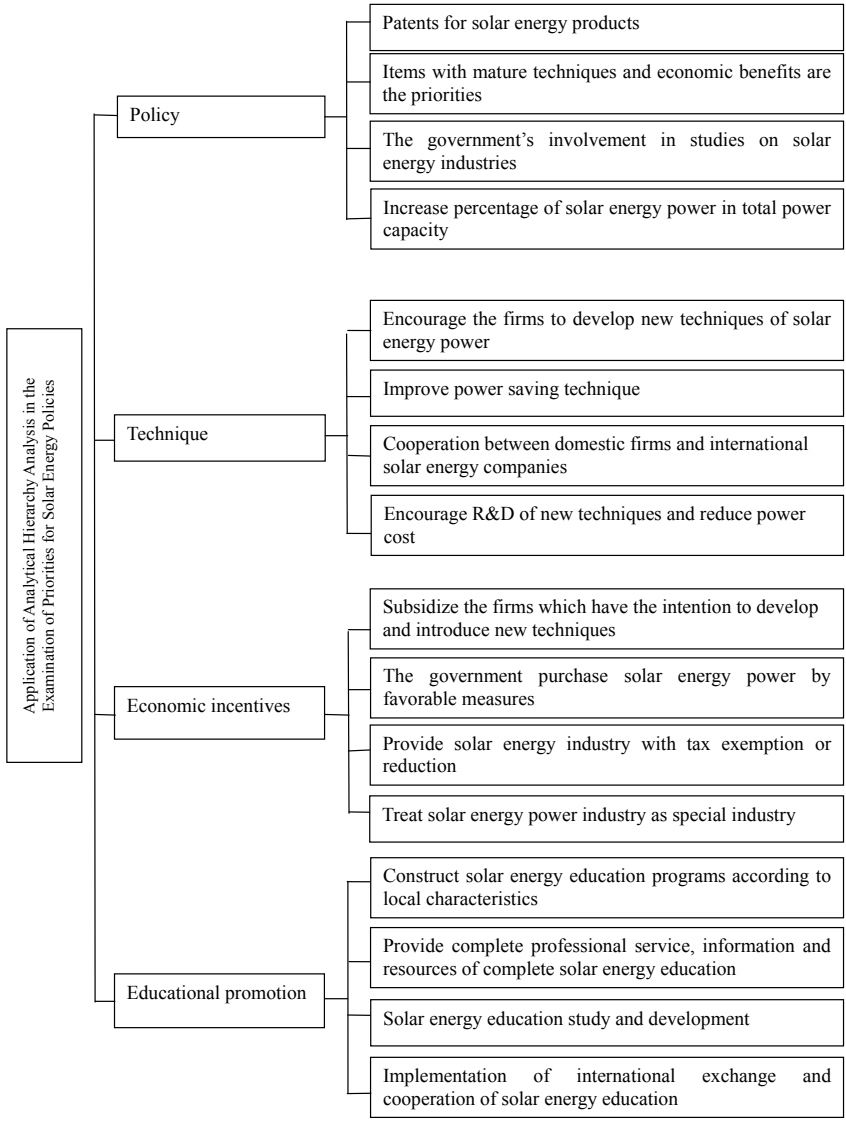

Figure 5. The hierarchical structure to promote solar energy [4].

The pair-wise comparison data were allocated in the pattern of a matrix and calculated based on the eigenvector procedure [12-13].

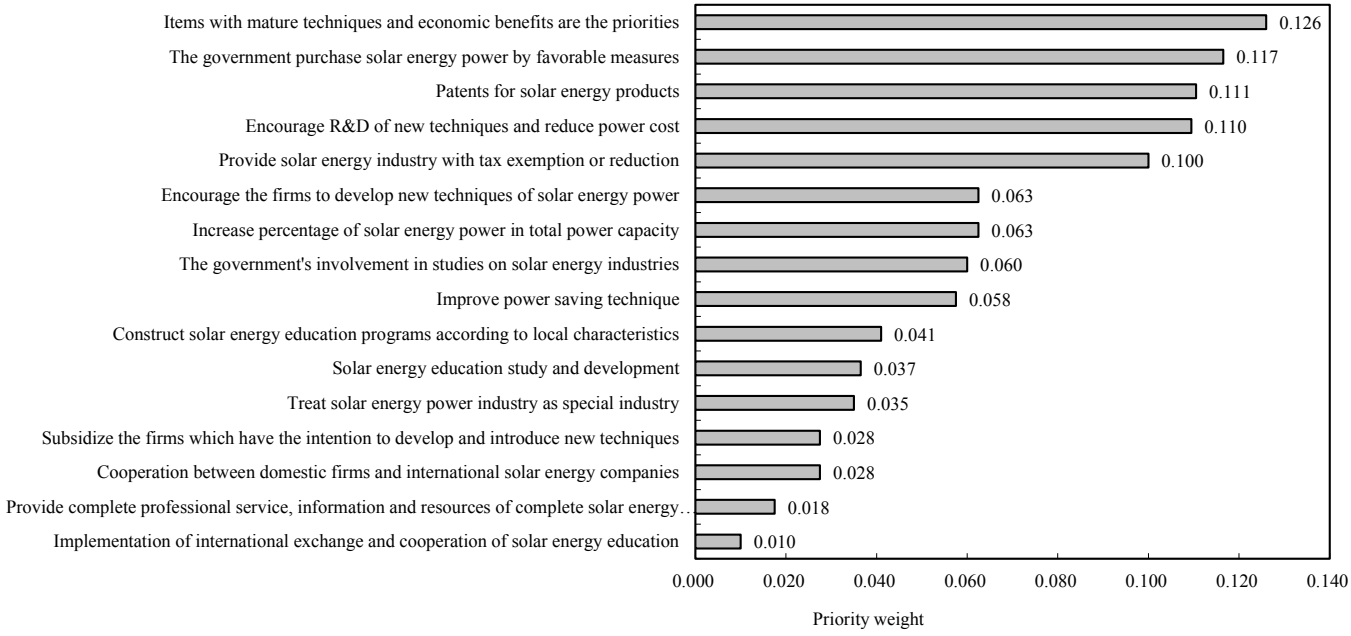

Figure 6. The weights of all sub-criteria for policy and promotion strategy of solar energy developments.

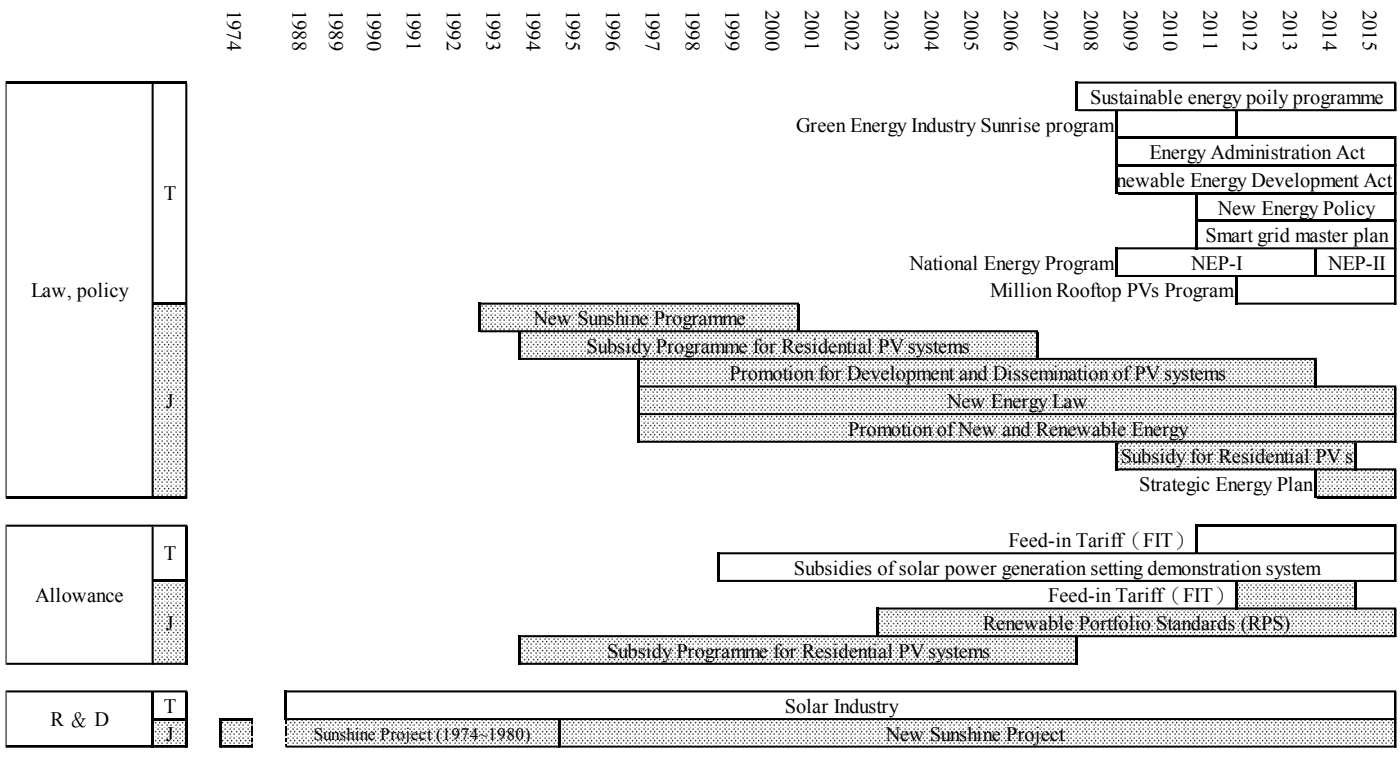

Figure 7. The evolution and progress for policy and promotion strategy of solar energy developments in both Taiwan and Japan.

To ensure the suitability of AHP, the consistency ratio for each of the matrices and overall inconsistency for the hierarchy were calculated. After calculation, the global weights of 16 sub-criteria were depicted in Figure 6.

POLICY AND PROMOTION STRATEGY OF SOLAR ENERGY DEVELOPMENTS

Although R&D support for solar energy began with Sunshine Project in 1970s in Japan, the main development for solar energy began in 1990s. Therefore the policy and promotion strategy of solar energy developments in both Taiwan and Japan were mainly surveyed from 1990 to present [11, 14-18].

In 1974, Japan began the Sunshine Project for R&D of PV. When this project was closed, another new project entitled New Sunshine Project was launched. Compared to Japan, Taiwan began R&D for PV in 1988.

In the middle 1990s, two projects including the regional new energy promotion business and new energy companies support measures were carried out in Japan. In the late 1990s, the Environmental Impact Assessment Law was enacted in Taiwan to protect environment and to reduce the negative effects of development activities. In some development activities, the introduction of renewable energy was obligated.

The Renewable Energy Development (RED) Act was enacted in Taiwan in the early 2000s to increase the application of renewable energy, to enhance the diversification of energy, to conserve the quality of environment, to impel the development of related industries, and to ensure the sustainable development of Taiwan. At the same time, the government began to reward the solar power generation system invested by folk investment

In the early 2000s, the Special Measures Law Concerning the Use of New Energy by Electric Utilities or Renewables Portfolio Standards Law (hereinafter referred to as RPS Law) was enacted by Japan government. The RPS Law obligated the electric utilities to use a certain amount of new energy towards the aim of promoting the new energy electricity.

In 2015, the Greenhouse Gas Reduction and Management Act (GGRM) was enacted in Taiwan. The objectives of GGRM Act includes (1) managing and reducing the release of greenhouse gas, (2) implementing the environmental justice, (3) taking the responsibility to protect the global environment, and (4) ensuring that national sustainable development in response to global climate change. Japan implemented Feed-in Tariffs policy to set prices for the renewable

power to compensate electric utilities for the higher cost of producing new energy electricity.

The evolution and progress for policy and promotion strategy of solar energy developments in both Taiwan and Japan are summarized in Figure 7.

According to the results of AHP, 5 sub-criteria were ranked most importantly, including "Implementation of international exchange and cooperation of solar energy education", "Provide complete professional service, information and resources of complete solar energy education", "Cooperation between domestic firms and international solar energy companies", "Subsidize the firms which have the intention to develop and introduce new techniques", and "Treat solar energy power industry as special industry". Both Taiwan and Japan have launched the R&D in 1980s and 1970s, respectively. The RED Act was formulated to promote the renewable energy in Taiwan in the early 2000s. Taiwan government also began to reward the solar power generation system invested by folk investment. Japan formulated the RPS Law in the early 2000s to obligate the electric utilities to use a certain amount of new energy towards the aim of promoting the new energy electricity. In addition, Japan implemented Feed-in Tariffs policy to set prices for the renewable power.

It revealed that the actions of governments and viewpoints of practitioners from environmental organizations were consistent. By studying the survey results, the consistent common viewpoints and actions were summarized to serve as a reference to promote the solar energy in the future.

CONCLUSION

In this study, the policy and promotion strategy of solar energy developments between Taiwan and Japan were surveyed and compared from 1990 to present. The results showed that the solar power increased significantly in the past ten years. The CCWE, SPG, and the ratio of SPG to TPG for Taiwan in 2014 gave on 615.2, 533.1, and 466.2 times than those in 2005. The CCWE, SPG, and the ratio of SPG to TPG for Japan in 2014 gave on 16.5, 16.4, and 17.6 times than those in 2005.

Besides, an AHP structure was proposed for decision makers to prioritize and select policy and promotion strategy of solar energy developments.

Taiwan and Japan have launched solar PV R&D in the 1980s and 1970s, respectively. In the early 2000s, Taiwan enacted the RED Act and rewarded the solar power generation system invested by folk investment to increase the use of renewable energy. Japan enacted the RPS Law and Feed-in Tariffs policy towards the aim of promoting the new energy electricity.

The consistent common viewpoints and actions obtained from this study could serve as a reference to promote the solar energy in the future.

Acknowledgments

The authors are grateful to the Ministry of Science and Technology of R.O.C. for financial support under the grant number MOST 104-2621-M-142-001.

REFERENCES

[1] Cunningham W.P. and Cunningham M.A. (2012). *Principles of Environmental Science. Inquiry and Applications*. McGraw-Hill, New York.

[2] Tung Y.T. and Pai T.Y. (2015). Water management for agriculture, energy and social security in Taiwan. *CLEAN-Soil Air Water*, 43 (5), 627-632.

[3] Tung Y.T., Pai T.Y., Lin S.H., Chih C.H., Lee H.Y., Hsu H.W., Tong Z.D., Lu H.F. and Shih L.H. (2014). Analytic hierarchy process of academic scholars for promoting energy saving and carbon reduction in Taiwan. *Procedia Environmental Sciences*, 20, 526–532.

[4] Tung Y.T., Pai T.Y., Yu J.J., Lin M.S., Yang P.Y., Shih L.H. and Su J.W. (2014). A social publics' evaluation for promotion priority of solar energy policy in Taiwan based on analytical hierarchy process. *Advanced Materials Research*, 1008-1009, 3-6.

[5] Tung Y.T., Pai T.Y., Kang Y.C., Chen Y.P., Huang T.C., Lai W.J. and Lee H.Y. (2014). Analytic hierarchy process of environmental social groups for promoting biomass energy in Taiwan. *Advanced Materials Research*, 1008-1009, 89-92.

[6] Tung Y.T., Pai T.Y., Li I.T., Ou T.Y., Lin C.P., Jiang Y.Z. and Su J.W. (2014). Identifying the attitude of environmental practitioners toward policy for promoting wind energy in Taiwan using analytical hierarchy process. *Advanced Materials Research*, 1008-1009, 133-136.

[7] Tung Y.T., Pai T.Y., Lee H.Y., Jiang Y.Z., and Chan L.Y. (2014). Effect of gas and electricity price on energy consumption rate for residential sector in Taiwan based on fuzzy rules. *Advanced Materials Research*, 1044-1045, 1737-1740.

[8] Tung Y.T., Pai T.Y., Shih L.H., Fan S.W., Lin W.C. and Lu T.H. (2014). Using ANN to forecast transportation sector's energy consumption in

Taiwan based on oil and gas price. *Advanced Materials Research*, 1044-1045, 1872-1875.

[9] Bureau of Energy (2014). *Taiwan Energy Statistics Yearbook*. Bureau of Energy, Taipei.

[10] Directorate - General of Budget, Accounting and Statistics (2014). *National Accounts Yearbook*. Directorate - General of Budget, Accounting and Statistics, Taipei.

[11] International Energy Agency. Retrieved April 25, 2016 from http://www.iea.org/policiesandmeasures/pams/japan/name-21048-en.php

[12] Saaty T.L. (1980). *The Analytical Hierarchy Process*. McGraw Hill, New York.

[13] Saaty T.L. (1994). *Fundamentals of Decision Making and Priority Theory with the Analytic Hierarchy Process*. RWS Publications, PA.

[14] Council for Economic Planning and Development (2014). *Adaptation Strategy to Climate Change in Taiwan.* Council for Economic Planning and Development, Taipei.

[15] Institute for Sustainable Energy Policies (2014). *Renewables Japan Status Report 2014 – Executive Summary.* Institute for Sustainable Energy Policies, Tokyo.

[16] Pai T.Y., Hanaki K., Tung Y.T. and Wang P.Y. (2015). Comparison for policy and promotion strategy of wind energy developments between Taiwan and Japan. In: *Wind Energy: Developments, Potential and Challenges*. Ed: Desiree Fleming, Nova Science Publishers, New York, U.S.

[17] Tatsuta M. (1996). New sunshine project and new trend of PV R&D program in Japan. *Renewable energy*, 8(1), 40-43.

[18] Federation of Electric Power Companies of Japan (2015). *Electric Power Report*. Federation of Electric Power Companies of Japan, Tokyo.

In: Solar Energy and Solar Panels
Editor: Joel G. Carter
ISBN: 978-1-53610-380-9

Chapter 5

THE FUTURE OF ORGANIC SOLAR ENERGY HARVESTING COMPLEXES

Julie L. H. Kho[1,2,3,4], Margaux Airey[1,2,4] and M. Cather Simpson[1,2,3,4,*]

[1]The Photon Factory, Faculty of Science, The University of Auckland, Auckland, New Zealand
[2]School of Chemical Sciences, The University of Auckland, Auckland, New Zealand
[3]Department of Physics, The University of Auckland, Auckland, New Zealand
[4]The Dodd Walls Centre for Photonic and Quantum Technologies and The MacDiarmid Institute for Advanced Materials and Nanotechnology, New Zealand

ABSTRACT

Recent advances in solar harvesting technology are transforming the renewable energy landscape. Despite the plunging cost of silicon and the ground-breaking efficiencies of new perovskite materials, research into "traditional" biomimetic, organic solar energy harvesting complexes remains important for the future success of solar energy. Here we discuss recent findings from studies of molecular donor-acceptor complexes that show promise as the active light harvesting components in organic solar energy systems. In particular, we focus upon self-assembled and covalent complexes of porphyrins (and related

* Corresponding author: E-mail address: c.simpson@auckland.ac.nz; Address: The University of Auckland, Private Bag 92019, New Zealand.

molecules) and fullerenes as facile electron transfer partners, and highlight several new results. Finally, we discuss the role these types of "soft" organic-based materials play in the solar energy marketplace, and explore how that role is likely to change in the future.

Keywords: organic solar cells, porphyrin, fullerene, electron donor-acceptor

INTRODUCTION

Harvesting energy from our planet's brightest star – the sun, is no longer an unfamiliar concept to us in this generation. The three critical steps in harnessing this abundant renewable energysource is to capture, convert, and store. Solar power has been achieved now in our every-day lives. There are solar panels on the rooftops of our, people drive solar powered cars, and we can harness the energy of the sun with our personal electronic devices. However, as the demand of global energy consumption increases, solar cells will need to perform ever more efficiently to fulfill the rising demand. The important question becomes: Will solar power be ever sufficient enough to replace the role of fossil fuels when the supply runs out eventually?

The continous development of solar cells technology shows a lot of promise for answering this question in the affirmative. At present, there are five major categories of solar cell types classified by the National Renewable Energy Laboratory [1]. The top two highest efficiency catergories: multijunction cells (46%) and single-junction GaAs (29%) were developed in the late 1980's. These types of cells are not easily accesible to most consumer applications due to their hefty price tag. They have been mainly installed on satelites and for space related research that require higher solar conversion efficiencies, and for which cost is not as much of an issue. The other three catergories are more commonly known. These are: crystalline silicon (c-Si), thin-film, and emerging photovoltaics (PV). Both c-Si and thin-film solar cells have been studied for more than 40 years. The emerging PV were developed just in the last two decades. Dye-sensitized solar cells (DSSC), organic solar cells (OSC), and perovskite solar cells (PSC), are amongst the highlights of emerging PV (Figure 1), and these hold great potential for making solar energy inexpensive and widespread.

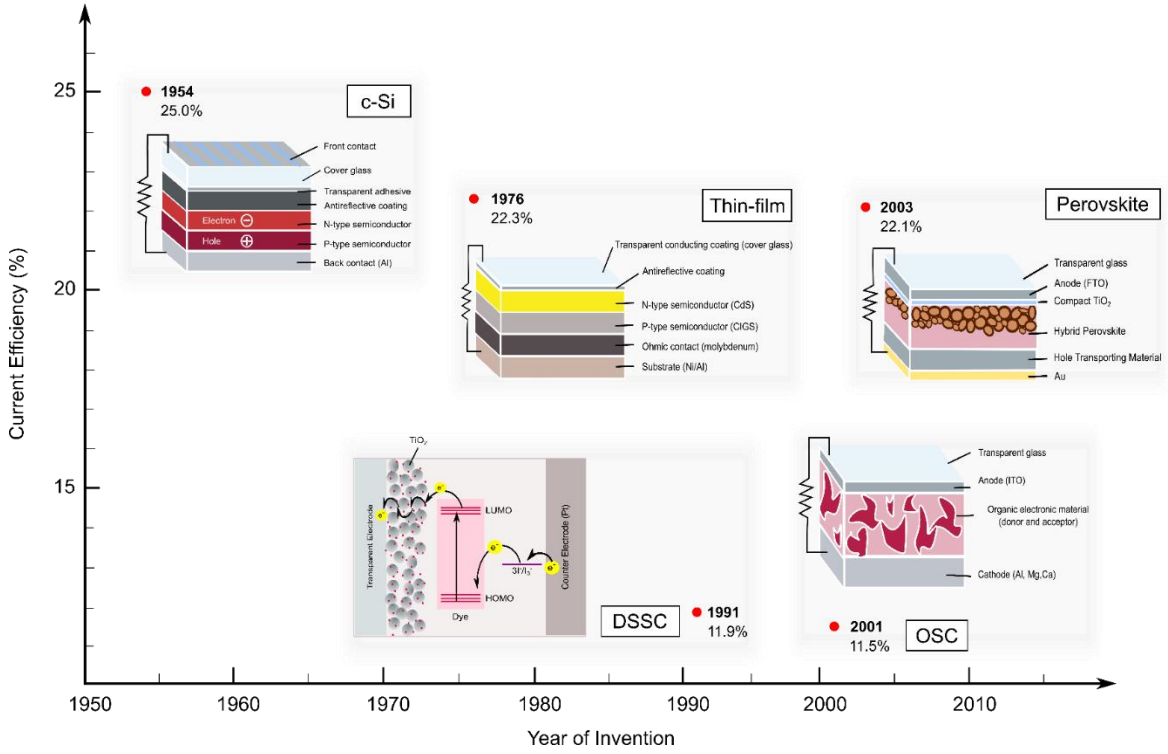

Figure 1. The types of solar cells with their respective year of invention (bold) and their current certified efficiency. Data obtained from the latest NREL efficiency chart (20 April 2016). Clockwise from top left: crystalline silicon (c-Si), thin-film, perovskite, organic solar cell (OSC), and dye-sensitized solar cell (DSSC).

The current commercial market in PV is dominated by c-Si cells, with the best module efficiency of 25% [2]. The cost of c-Si modules has dropped more than 50% in the last 6 years from $1.9 USD per Watt-peak ($W_p$) to $0.6 USD/$W_p$ due to the plunging cost of silicon [3].Ever since the first silicon cell from Bell labs reported an efficiency of 6% [4], rapid progress has been made to improve various components. These include adding athin layer of metal oxide to themetal contact to reduce charge recombination (CR) at the surface, texturing the surface of the silicon to increase absorption of light, and adding a layer of anti-reflective coating [5-7]. Yet, the efficiency of c-Si cells has not increased significantly in the last decade. It is, in fact, reaching the Shockley-Queisser limit predicted at 29% [8]. The manufacturing cost for a wafer-based Si cell is relatively high and the process is complex. A high purity of c-Si is also required to fabricate a working solar cell. For these reasons, research effortshave been moving away from c-Si cells and concentrating more towards improving thin-film and other emerging PV technologies.

Thin-film solar cells have a similar layered construction and operating principle as c-Si cells, except these use a direct bandgap semiconductor rather than the indirect bandgap one used in c-Si cells. This allows thin-film materials to be made of *very* thin layers, typically ranging from 1-3 μm. The flexible pairing of semiconductor layers is a major advantage of thin-film technologies, where a variety of inorganic materials (e.g., amorphous Si, CdTe, CIGS, Cu_2O, Cu_2ZnSnS_4) can be tested [9-13]. CdTe and CIGS are currently the best perfomance materials, capable of delivering 22% certified efficiency [2].

Among the emerging PV technologies, DSSC has been around the longest, and is often classified under thin-film cells. The modern form of DSSC is called a Grätzel cell, named after one of the co-inventors – Michael Grätzel. Even though the efficiency of DSSCs sits around 11%, these cells have the advantage of simpler preparation process, low cost, and flexibility. DSSC can be printed roll-to-roll and can be made transparent or multi-coloured. These features are demonstrated in one of the most fascinating solar material installments, in which 300 square metres of DSSC cells were used as the building façade on the SwissTech convention centre (Figure 2).

OSC technology bears similar advantages and efficiency as DSSC. The construction of OSCs is simpler, with a layer of mixed organic donor-acceptor materials sandwiched between two electrodes. Most of the organic materials consist of polymer blends such as P3HT and functionalized-C_{60} PCBM, that are relatively cheap and easy to synthesize [14].

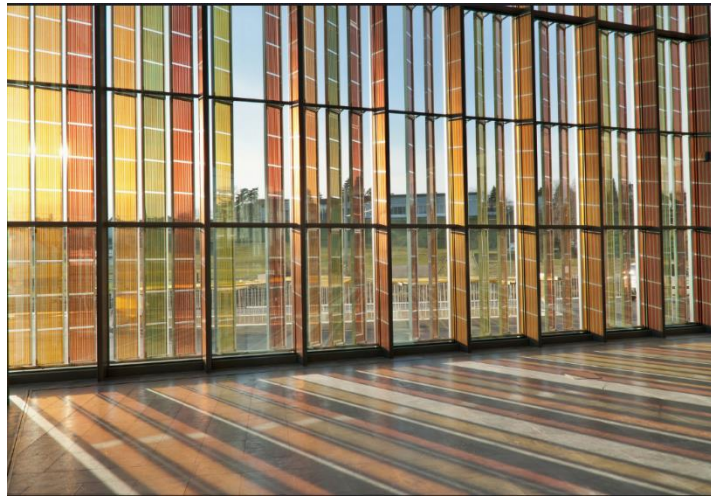

Figure 2. The SwissTech Convention Center where DSSC were installed as part of the building façade. The DSSC cells were made by Solaronix. Photo credit: Solaronix.

The latest addition to solar tehcnology is the rapidly advancing PSC. Within 4 years since the first invention by Kojima et al. [15], the efficiency of PSC has risen exponentially from 3% to the current 22.1% demonstrated by Michael Grätzel and Anders Hagfeldt at EPFL [16]. This is a very promising breakthrough that has attracted vast attention from researchers in the field. The architecture of PSC is an evolution from solid state DSSC [17-18], with the main difference in the active material layer. Perovskite has the general formula of ABX_3 and the most studied example is $CH_3NH_3PbI_3$. Perovskites not only function as light absorbers for electron injection into the TiO_2 semiconductor, they also act as electron hole carriers [19-21]. The ability to exhibit appealing aspects of both inorganic thin-film and organic PV is the key to current success of perovskites [22]. Despite all the enormous potential that PSC exhibit, the technology is yet to be commercialized due to several crucial drawbacks. Some of these issues include stability upon exposure to the UV-Vis region of the spectrum, toxicity of the main active element (Pb), sensitivity to moisture, and unreliable device performance [22-28]. Researchers remain very optimistic that PSCswill surpass silicon technology in the near future, with a prediction of real commercialization of PSC modules on the 2019-21 time frame [29].

The solar technology sector is certainly competitve in both energy conversion efficiency and cost per module. Emerging PV cells are leading with more cost effective materials and manufacturing process. In particular, there are still countless possibilities of improving DSSC and OSC in terms of active materials

selection. Finding the right combination of electron donor-acceptor is the key to optimizing the cell performance. The donor-acceptor molecules are primarily responsible for the first two steps of the aforemention 'capture, convert, and store' process. In this chapter, we focused upon organic molecules that have been designed specifically for this purpose, understanding how energy can be captured and converted efficiently into metastable species with opposing charges which later recombine.

ENERGY HARVESTING SYSTEMS IN ORGANIC SOLAR CELLS

Electron donor-acceptor pairs were first observed in natural photosynthetic systems. Plants and photosynthetic bacteria have complex protein architectures with light harvesting antennas to absorb sunlight, and a series of enzymes that works as an electron transport chain to create a long-lived charge separated state. In plants, the process is divided into photosystem I and II where chlorophylls act as the light absorber, generating electrons to pass onto the next phases for converting ADP to ATP and NADP to NADPH (Figure 3). The quantum yield of this process is near unity and the charge-separated species in photosynthetic systems last for ~1 s [30-32].

The goal of biomimetic systems is to achieve the unity quantum yield of electron transfer in photosynthesis with simple molecules. To design efficient artificial molecules, the selection of a suitable electron donor and acceptor pair is vital. The electron donor needs to have a broad absorption spectrum to fully utilize the solar radiation across the visible and near-IR. Absorption of the light by the donor molecules should not lead to degradation, and is ideally followed by fast and efficient electron transfer to the electron acceptor. Subsequently, the electron acceptor should have a lower energy level than the donor, with high electron affinity, and promotes slow charge recombination.

There is an extensive list of potential electron donors and acceptors that have been designed for different solar cells. In OSC, polymer blends of donor-acceptor are primarily used. The donor consists of π-conjugated long chains, and acceptors are functionalized fullerenes [33-38]. Polymer blends suffer from low efficiency compared to hard materials, and could also undergo photochemical degradation [39]. Inorganic molecules such as ruthenium complexes [40-42] and BODIPY dyes [43-45] are widely used as sensitizers in DSSC. These complexes are limited by their absorption bandwidth in the visible region, and the rare earth metals are also costly. Organic molecules are also popular in artificial systems, since their chemical properties can be more readily tailored by structural modifications. One

of the earliest examples was a pair of chlorophyll dimers, synthesized with similar photochemical properties to P700 chlorophyll in plants [46]. Combinations of chlorophylls, carotenoids, porphyrins, and phthalocyanine donors were paired up with quinone acceptors to demonstrate long-lived, charge-separated states that last for microseconds [47-51]. In the following discussion, we focus on one of the globally important class of organic donor-acceptor pairs: porphyrins and fullerenes.

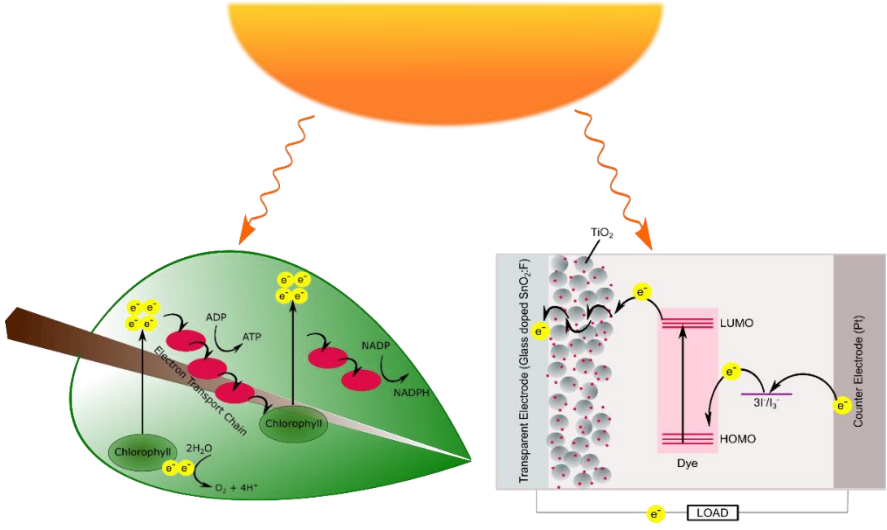

Figure 3. Both the photosynthetic system in plants and DSSC absorb solar energy to create a cascade of electron transfer steps forming charge-separated species.

The employment of porphyrins as electron-donor light-harvesters in the design of these organic arrays is particularly attractive due to the primary role of porphyrin-type molecules in natural photosynthetic systems. Alongside their ability to harvest light within the visible and near-IR region, analogous to chlorophylls, their structural malleability is also an important feature for allowing the optimisation of electronic properties by chemical modification. Fullerenes are especially favourable as electron acceptors in the design of these synthetic reaction centres due to their low-energy first excited singlet state, and their readiness to accept energy alongside multiple electrons [52]. The particularly small reorganisation energies of fullerenes associated with photoinduced electron transfer reactions, for example, are attractive for improving the efficiency of electron transfer within artificial photosynthetic reaction centres [53]. It is responsible for decreasing energy waste, and allows the investigation of rates and

yields of charge separation and charge recombination mechanisms. Furthermore, these three-dimensional building blocks readily form multiple isomers which facilitate the attachment of other molecules [54-55].

COVALENTLY BOUND PORPHYRIN-FULLERENE COMPLEXES

Covalently-bound porphyrin-fullerene systems has been around for a few decades. They are a popular synthetic choice to construct polyads (triads, tetrads, pentads, etc.) due to the natural attraction of fullerene to the porphyrin macrocycle. Often these are tethered using appropriate molecular linkers (e.g., aromatic groups, π-conjugation) in various structural arrangements, along with peripheral substitutions on the porphyrin for one purpose – that is to optimize the electron transfer process resulting in a long-lived charge-separated state with high quantum yield [56-61].

The early design of free-base and zinc porphyrin-fullerenedyads largely satisfied the goals of a synthetic light-harvesting system by exhibiting very rapid photoinduced electron transfer to produce long-lived charge-separated states and quantum yields nearing unity[62-64]. The single-step electron transfer associated with a dyad system is based upon two basic processes over a short range. Following excitation of the donor or acceptor moiety, the dyad forms a donor radical cation and acceptor radical anion pair that subsequently undergoes charge recombination before returning to its initial ground state [65]. Employing single-step electron transfer in a dyad complex was therefore particularly attractive because of the reduction in loss of photon input energy that could occur with a longer-range multi-step process. However with the resulting intense electronic coupling between the radical anion and cation donor-acceptor pair, in many cases charge recombination could take place too rapidly to produce the desired efficiency of a photosynthetic reaction centre. Despite these disadvantages, the selection of donor-acceptor pairs with suitable redox potentials and excitation energies has been shown to improve the photochemical properties of dyads [55, 65-67]. With the goal of extending the lifetime of the charge-separated state while minimising the loss of photon input energy, a series of zinc chlorin-C_{60} dyads with short linkages were successfully designed [68-71]. It was predicted based on theory that both charge-separation and recombination processes could be optimised by decreasing the separation distance between the donor and acceptor pair. Nevertheless, despite exhibiting an exceptionally long-lived charge-separated state, the quantum yield of formation reached only 12% of an ideally-

estimated 100% [69]. Therefore an approach towards multi-step electron transfer in complexes of higher structural hierarchy was made.

Donor-acceptor systems with higher orders than dyads can undergo multi-step electron transfer – an approach that is observed in natural photosynthetic systems [65]. Despite its unfavourable loss of input photon energy unseen in single-step transfer, in the multi-step process the photoinduced radical ion pair substantially reduces the electronic coupling and therefore increases the lifetime of the final charge-separated state. This new approach yielded a variety of particularly attractive complexes: with the employment of specific porphyrin-fullerene donor-acceptor pairs for example, the achievement of a long-lived charge-separated state with a high quantum yield was made possible [52, 63, 65, 72]. Furthermore, increasing the hierarchy of porphyrin-fullerene systems from dyad to heptad assemblies [65], an excellent synthetic analogy to photosynthetic systems in nature could be achieved.

In rigid conjugated dendrimer arrays, the excitation of peripheral chromophores exhibits an efficient electron transfer process to an electron-accepting core that quenches the fluorescence of the fringe electron acceptors[57, 66-67, 73-74]. Moreover, dendrimers allow a multi-step electron transfer process that extends the lifetime of the final charge-separated state of the molecule [54, 65, 75-77].

The structural details of porphyrin-fullerene triads and higher order complexes play an important role in influencing the rate and efficiency of electron transfer from the donor to acceptor moieties. For example, the role played by linkages in optimizing electron transfer by reorganisation energy is crucial in the balance between efficient charge separation and unfavourable back-electron transfer; an effect that can be solved by causing charge-separation to occur in multiple short-distance steps by structural design[55, 60, 78-80]. Notably, the organisation of the photosynthetic reaction centers vary in nature: for example, symmetric macrocyclic structures have been found in purple bacteria chlorophylls, whereas rod-like aggregates have been observed in green bacteria chlorophylls [81].

Moreover, designing a multi-component system with conformationally restrained linkages restricts the possible values of electronic coupling between the initial excited state and the charge-separated state of the porphyrin and fullerene [58, 82]. Thus a macro assembly could be designed a variety of different ways with its ultimate photosynthetic properties depending on that structural conformation. Generally, these porphyrin-fullerenes have been arranged cyclically or linearly. The cyclic arrangement of photoactive molecules has been observed for example in particular chlorophyll pairs in bacterial reaction centres, and is

therefore one attractive design prospect [82]. Cyclic complexes can be organised over a three-dimensional or two-dimensional framework, where the former is characterised by a double-bridge covalent bond between two porphyrin moieties and a fullerene.

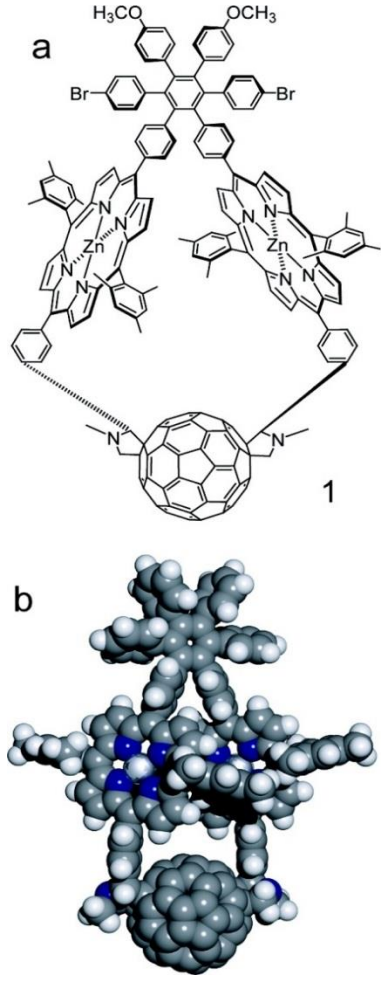

Figure 4. a) The structure of a diporphyrin-fullerene triad three-dimensional macrocycle, where the two zinc-porphyrins are bridged by a hexaphenylbenzene. b) The space-filling model of the same triad. Fullerene is connected via two bonds to each porphyrin moiety. Figure reproduced with permission from ACS Publications.

The double-bridging three-dimensional macrocycle has been shown to counter the rate of undesirable charge recombination while preventing free rotation about bonds that would normally occur with a single bond [78, 82]. By preventing this movement, the distance between the donor and acceptor, angles, and electronic coupling can be restricted. In a 42-atom diporphyrin-fullerene triad macrocycle featuring two zinc-porphyrins bridged by a hexaphenylbenzene, both the cyclic and doubly-bridged structural features are shown to significantly benefit the electronic efficiency of the complex by the strain exacted on the porphyrins (Figure 4). In the solvent 2-methyltetrahydrofuran for example, a particularly long-lived charge separated state with a decay rate constant of 2.7 ns occurs with a quantum yield of 1.0. This was matched with a favourably short time constant for electron transfer from the first singlet excited state of the porphyrin to the fullerene to generate the cation-anion radical pair. Thus compacting the structure of these macromolecules into a rigid cyclic conformation satisfies the energetically-favourable face-to-face contact required in their design, and limits the effects of solvent reorganisation energy by restricting the exposure of the donor and acceptor moieties [83]. These combined factors produced a porphyrin-fullerene three-dimensional macrocycle with notably superior properties to dyad counterparts [84-85].

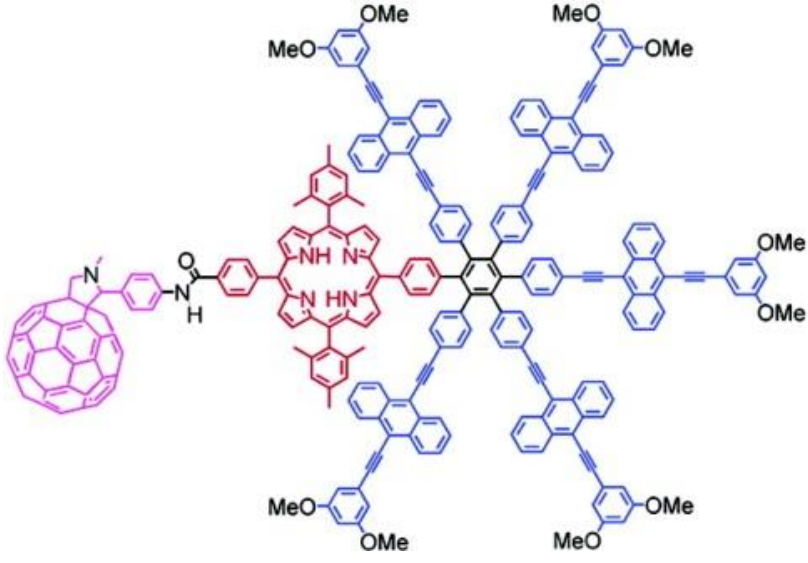

Figure 5. The antenna-based structure of a two-dimensional macrocycle. Five bis(phenylethynyl)anthracene (BPEA) antennas encircle a central hexaphenylbenzene core that is covalently attached to a porphyrin-fullerene pair. Figure reproduced with permission from ACS Publications.

Two-dimensional cyclic arrays with higher structural order also have exhibited improved electronic qualities. This is likely due to the antenna-based design that imitates the broadened light-harvesting capacity of a natural photosynthetic system. With this knowledge, the covalent attachment of five bis(phenylethynyl)anthracene (BPEA) antennas arranged around a central hexaphenylbenzene core to a porphyrin-fullerene pair has achieved numerous favourable properties (Figure 5). Firstly, a highly efficient and rapid singlet energy transfer from the antenna periphery to the porphyrin electron acceptor has been demonstrated. The structure also impeded a variety of unfavourable electronic mechanisms that could interfere with the very decisive charge separation and recombination in the donor-acceptor pair[57]. Both a quantum yield of near unity and a charge-separated state lifetime exceeding that of the diporphyrin-fullerene triad macrocycle above suggests that the antennas play a crucial function in the design of these synthetic systems.

Carotenoid-tethered porphyrin-fullerene molecules have been an attractive area of research for the design of linear arrays [77, 86-87]. For example, imitating the role of carotenoid polyenes may provide the analogous capacity of broader spectral absorption. Following charge recombination of these compounds, the carotenoids also exhibit spin-polarised triplet states as well as triplet-triplet energy transfer phenomena seen in the photoprotective characteristics of carotenes in natural antenna function [77]. Thus the design of carotene-based assemblies has been oriented around the unique properties of the carotene moiety. Based on the main processes of electron transfer, charge shifts, and triplet-states, it is first favourable to yield the initial charged state on a picosecond timescale form photoinduced electron transfer. This must be followed by a very rapid charge shift to produce the charge-separated state with a quantum yield of near unity, which must be subsequently long-lived and recombine to yield the triplet state of the carotenoid. Ideally, the resulting triad would exhibit good resistivity to oxidative damage, have high solubility in a variety of solvents, and could be synthesised with ease. With these existing goals, a carotene-porphyrin-fullerene triad was synthesised with properties matching those in nature [88-90]. This compound bearing mesityl groups bonded to the porphyrin moiety presented both synthetic and chemical advantages, with a more rapid charge recombination to yield the carotenoid triplet state in comparison to other linear triads.

A remarkably long lifetime of a charge-separated state was reported in an artificial photosynthetic reaction centre bearing a ferrocene-zinc porphyrin-zinc porphyrin-fullerene *meso-meso*linkage [56]. This tetrad exhibited an improved charge-separated state and quantum yield in comparison to an analogue bearing a free-base porphyrin moiety. Generally, the improved excited-state energy and

oxidation potential attributed to the use of the zinc porphyrin over the free-base[91]. It is therefore notable that a pentad with an additional zinc porphyrin in the light-harvesting structure produced a charge-separated state that did not match the extremely long lifetime of 1.6 s observed in the tetrad, but significantly improved its quantum yield from approximately 0.34 to 0.83 [91]. The improvements associated with an increase in zinc porphyrins could be due to improved exciton coupling in the trimer, but in the case for both the tetrad and pentad systems such positive values could only be achieved in frozen media to minimise competing mechanisms such as back electron-transfer[75, 91].

SELF-ASSEMBLED PORPHYRIN-FULLERENE COMPLEXES

Compared to the literature published on covalently tethered porphyrin-fullerene complexes, much less research is reported for self-assembled systems. The latter approach is appealing for several reasons, including simple building blocks that avoid complicated synthetic pathways, higher flexibility and free rotation, and resemblance to the natural photosynthetic reaction centre's self-assembled entities [92-94].

Two different types of self-assembled methods have been demonstrated: (1) through Van der Waals interactions, and (2) through 'commanded assembly'. Examples of each of the methods will be described in the following section. D'Souza, Ito, Imahori, and Guldi are among the few researchers who have investigated the coordination of fullerene to porphyrin, particularly on their photoinduced electron transfer behaviour to generate long-lived charge-separated species [92-93, 95-102].

Van der Waals Interactions

Molecular self-assembly between porphyrins and fullerenes is conducted via Van der Waals interactions to form various complex arrangements, including: sandwich, dendritic, interstice, and nanorods [103-106]. In solution, metal-ligand axial coordination is often employed to bind functionalized fullerenes to porphyrins with unsaturated metal ion centers such as Zn or Mg [92-93, 95-96, 99, 102, 107]. Photoinduced electron transfer has been shown to be successful in coordinated complexes, forming the charge-separated species $P^{\cdot+}C_{60}^{\cdot-}$.An example of a simple dyad, Zn-tetraphenylporphyrin (Zn-TPP) axially coordinated with fulleropyrrolidine designed by D'Souza *et. al* exhibits a charge-separated lifetime of 1.1 ns [95].

Higher order complexes that self-assemble are often more challenging to design and synthesize due to space restrictions. With axial ligation, a maximum of two fullerenes can coordinate to the porphyrin face to form triads. Following the first successful axial ligation of a porphyrin and a fullerene, D'Souza created a triad using a 'two-point' axial binding approach, in which a covalently linked dimer, Zn-porphyrin-Zn-phthalocyanine (ZnP-ZnPc) was coordinated to fulleropyrrolidine [108]. After photoexcitation, energy transfer from ZnP to ZnPc was initially observed, followed by the formation of a charge-separated state ZnP-$ZnPc^{\cdot+}$-$C_{60}^{\cdot-}$that lasted for 1.7 ns. From this result, the triad complex did not show a significant increase in lifetime compared to the previous dyad.

Cyclic dimers of porphyrins also have been employed to facilitate non-covalent binding of fullerenes [109-112]. Pristine fullerenes can be encapsulated within the cyclic porphyrin cage via π-π interaction. Aida and co-workers first reported the effects of various metalloporphyins (Co, Ni, Cu, Ag, Zn, Rh) on the binding affinity for fullerenes in the cyclic dimers and found anomalously high binding constants when using rhodium ions in porphyrins [113]. This result led to further studies using more complex structures of cyclic porphyrin dimers for binding fullerenes [112, 114-116]. On the other hand, Fukuzumi's group investigated the use of Lithium-ion encapsulated fullerene ($Li^+@C_{60}$) in cyclic dimers [105, 117]. The binding constant for $Li^+@C_{60}$in cyclic porphyrin dimers have been reported to be higher than pristine C_{60}thanks to the higher electron affinity of $Li^+@C_{60}$. Photoinduced electron transfer studies of this supramolecular complex yielded one of longest lived non-covalent porphyrin-fullerene charge-separated state of 0.6 ms at the time. This promising result was attributed to the lower charge-separated energies of the complex compared to the triplet energy of both the cyclic porphyrin and $Li^+@C_{60}$.

In recent years, Fukuzumi has continued to explore the combination of cyclic porphyrin dimers and $Li^+@C_{60}$as electron donor-acceptor pairs. Structural modifications were made to the linkage between the porphyrin dimers to increase their binding affinity to fullerenes, and the widely employed electron acceptors in organic PV, PCBM and C_{60} were used [118-119]. The result satisfyingly yielded an even longer charge-separated state of 0.71 ms (Figure 6).

Acyclic porphyrin hosts for binding fullerene emerged in early 2000, around the same time as did cyclic porphyrins. Boyd *et al.* first prepared a palladium-linked, metallated porphyrins that acted as "*jaws"* to trap the fullerene [120-121]. Successful complexation of the "jaws" porphyrins with C_{60}- and with C_{70} was demonstrated. Subsequently, a new porphyrin linkage, a calix[4]-arene scaffold, was synthesized to improve the binding affinity of the porphyrin pair to fullerenes [122]. The charge transfer mechanism of the

calixarene-linked Zn-bisporphyrin jaws with C_{60} was investigated using transient absorption spectroscopy. Charge-separated state lifetime of the dyad was 0.5 ns in a non-polar medium, toluene [123].

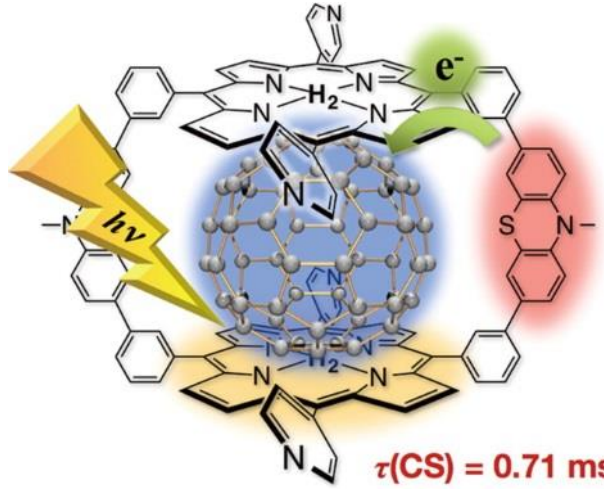

Figure 6. Cyclic porphyrin dimer with phenothiazine linkers self-assembled with C_{60} designed and characterized by Fukuzumi et al. The charge-separated state lifetime of this complex was one of the longest reported for non-covalent systems. Figure reproduced with permission from ACS Publications.

Following that, Boyd and co-workers designed a fully self-assembled triad, with a ferrocene pyridine entity coordinated to each of the Zn-porphryin core (Figure 7). Upon photoexcitation, electron transfer occurred from the singlet porphyrin to the $C_{60}$to create a radical ion pair $ZnP^{\cdot+}$-$C_{60}^{\cdot-}$with lifetime of 1.2 ns. Ideally, a secondary electron transfer would create a hole shift from $ZnP^{\cdot+}$ to $Fc^{\cdot+}$. However, this stepwise electron transfer was not evident from the transient absorption lifetime measurement result [124].

To synthesize more complex porphyrin structures for self-assembly with fullerenes, “click chemistry” has been employed as a synthetic technique by several groups [125-127].“Click chemistry” is a cycloaddition process often used to create elaborate 3D nanostructures of the porphyrin hosts [128]. Such systems often possess complex donor-acceptor architectures that could promote multi-cascade electron transfer. Obviously, the major drawback is the complexity in synthesizing pieces of compatible molecules so that they “click” together [129]. One particularly interesting example by Takaiet al. is a novel Zn-porphyrin tripod synthesized via this pathway [126].A fullerene derivative with pyridine moiety

was assembled within the Zn-porphyrin tripod via π-π interaction as well as coordination between the pyridine and Zn^{2+}. This strong electron donor-acceptor complex exhibited a charge-separated state lifetime of 0.53 ns in toluene.

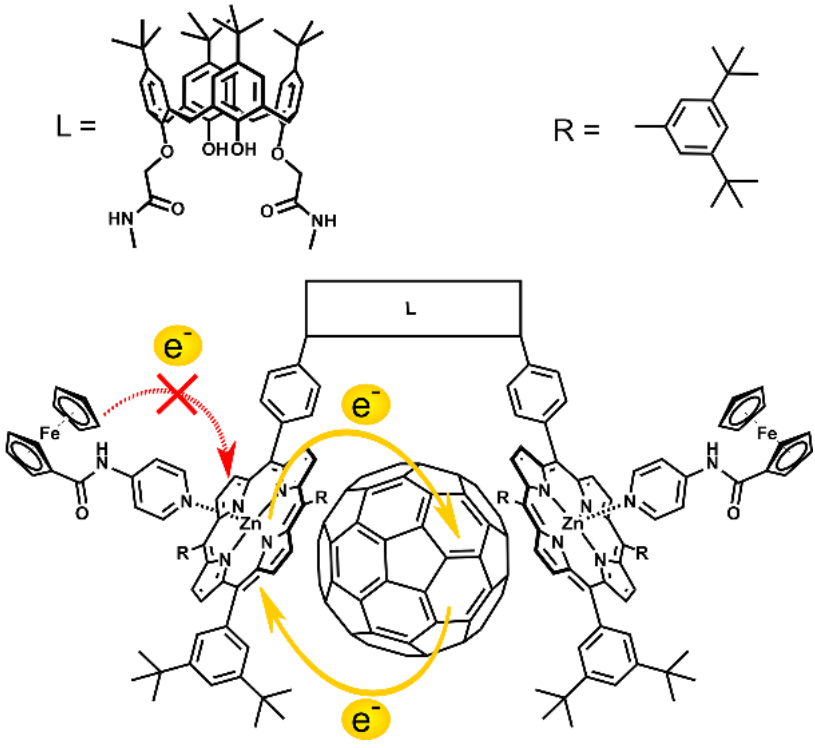

Figure 7. Self-assembled ferrocene-porphyrin-fullerene triad by Boyd et al. Transient absorption studies evaluated the charge-separated species formed lasted for 1.2 ns in cyclohexane. Evidence of hole shift from porphyrin to ferrocene was not observed.

Commanded Assembly for Device Fabrication

On the aspect of device fabrication, commanded assembly via an external stimuli has emerged as a new strategy to gain control over the arrangement of functional units. The stimuli can be conducted through either electrostatic interactions, magnetic fields, or mechanical flows [128]. Multilayers of materials can be formed by this bottom-up fabrication technique using electrochemical coupling, to assemble alternating positively and negatively charged materials in sequence [130-132]. Commanded assembly is also useful in terms of creating area-selective

patterns, by varying the spatial application of voltage across the surface[133]. The major advantage of this technique is the precision and control of the functional units. It is predicted that the research focus on self-assembly of molecules will preferentially shift to commanded assembly in the coming years, as the technique develops into a more practically useful technology.

CONCLUSION AND OUTLOOK

Incorporating porphyrin-fullerene light-harvesting units into photovoltaic devices is the next important step towards exploiting their energetic properties. Organic photovoltaic devices have not achieved a comparable level of efficiency as photosynthetic systems yet, but a step-by-step approach to their design may provide key information to their improvement in the future. In particular, the internal quantum yield of photocurrent generation serves as an important marker for electrode capability. The most practical method of incorporating porphyrin-fullerene complexes onto electrode surfaces is by self-assembled monolayers (SAMs), where the presence of an additional functional molecule such as thiols or disulfides on these compounds allows the tethering of the layers onto a gold surface[81]. Assembling these light-harvesting monolayers onto a gold surface has been a particularly attractive prospect for a variety of reasons. For example, the fullerene plays an important role in allowing the acceleration of the forward electron transfer and the deceleration of charge-recombination, producing a high quantum yield of photocurrent generation on the gold surface that largely quenches the porphyrin singlet excited state. In the case of a dyad monolayer assembly, a distinct improvement photocurrent generation from zinc porphyrin-to free-base-fullerenes was observed thanks to the increased quantum yield of the charge-separated state from the former to the latter. In comparison with ferrocene-porphyrin-fullerene triads with alkanethiols, optimal conditions yielded an equal improvement from the zinc to free-base analogue (from 20% to 25% efficiency). It is noted that the presence of the ferrocenium cation also plays an important role, where the electron transfer rate from the gold surface to the cation increases when the potential applied is decreased, thus overall increasing the photocurrent of the system.

Significant improvements also have been seen by a different approach: incorporating an additional light-harvesting chromophore alongside the porphyrin-fullerene compounds to add a singlet-singlet energy transfer step. A boron-dipyrrin dye was chosen for this purpose, motivated in part by its favourable absorption that extends the overall absorption range of the entire system with particular emphasis in the blue and green region. The efficient singlet-singlet energy transfer directly from

the dipyrrin to the porphyrin moiety of a ferrocene-porphyrin-fullerene alkanethiol triad tethered to a gold surface helped improve the photocurrent generation, likely assisted by a single-step to multi-step transfer mechanism. With the free-base porphyrin analogue, a photocurrent efficiency 30 times greater than that of a device bearing only the boron-dipyrrin unit was observed. Despite the very high quantum yield achieved by SAM systems on metal electrodes, achieving natural photosynthetic efficiencies of almost 100% has been hindered by the potent quenching effect of the porphyrin singlet excited state by gold surfaces. Thus the high optical transparency and electrical conductivity of ITOs provide the next step to designing photosynthetic electrodes, with a predicted internal quantum yield of 280 times larger than respective porphyrin SAM gold electrodes. The problem with ITOs however has been the difficulties associated with attaching SAMs onto their surface, and as a result only single chromophores have been successfully linked. Furthermore, despite improved internal quantum yields of photocurrent generation, the light-harvesting capacities of these systems still behave poorly with low values of incident photon-to-photocurrent efficiency attributed to the monolayer.

Based on a successful approach towards improving light-harvesting efficiency, dyad clusters of porphyrin-fullerenes were deposited by electrophoresis onto a nanostructured SnO_2 electrode [134-136]. This showed significant improvement over the monolayer system, but low external quantum yield values were attributed to the cancellation of the charge-separated state in the porphyrin-fullerene dyad clusters. In an attempt to improve the absorbance of the system by enhancing charge-transfer type interactions between molecules, larger composite porphyrin-fullerene clusters were assembled via primary organisation before electrodeposition onto the SnO_2 surface. Likewise, these provided enhanced photocurrent generation, encouraging the design of quarternary self-organised porphyrin-fullerene-gold nanoparticle clusters for incorporation onto an SnO_2 electrode[137]. From these electrode designs, it was found that the three-dimensional network of the porphyrin dyes was directly responsible for the improvements seen in photoelectrochemical properties by facilitating the injection of the parted electron into the conduction band.

In DSSC, porphyrin-fullerene sensitizers have been incorporated for performance testing [138-139]. The overall power-conversion efficiency of the cells remains less than 10%; much lower than existing inorganic solar cells which have reached up to 25% in practical efficiency. Although the development of organic complexes in solar harvesting is slower compared to the rise of other technology such as perovskites, there is still a positive outlook for future breakthroughs. Even so, a commercial market currently exists for organic PV. They might not be efficient enough to provide electricity in a household yet, but

they are extremely useful in portable consumer products such as watches, remote control, phone charger, clothing and sensors [140-141]. These applications require the flexibility and low-cost that organic PV offers. Of course, the most powerful advantage of organic solar harvesting complexes is their potential to be chemically tuned, with virtually unlimited possibilities for achieving desirable properties. Finally, with the amount of research directed towards numerous promising solutions to the pressing renewable energy problem, it would be wise not to close doors on an outcome bearing at least one viable technology for widespread use.

REFERENCES

[1] National Renewable Energy Laboratory. http://www.nrel.gov/ncpv/ (accessed 1 May).

[2] Green, M. A.; Emery, K.; Hishikawa, Y.; Warta, W.; Dunlop, E. D., Solar cell efficiency tables (version 47). *Prog. Photovoltaics* 2016, *24* (1), 3-11.

[3] Louwen, A.; van Sark, W.; Schropp, R.; Faaij, A., A cost roadmap for silicon heterojunction solar cells. *Sol. Energy Mater. Sol. Cells* 2016, *147*, 295-314.

[4] Perlin, J., Good As Gold: The Silicon Solar Cell Turns 50. *Solar Today* 2004, pp 24-27.

[5] Wenham, S. R.; Green, M. A., Silicon solar cells. *Prog. Photovoltaics* 1996, *4* (1), 3-33.

[6] Green, M. A., Crystalline and thin-film silicon solar cells: state of the art and future potential. *Solar Energy* 2003, *74* (3), 181-192.

[7] Green, M. A., The path to 25% silicon solar cell efficiency: History of silicon cell evolution. *Prog. Photovoltaics* 2009, *17* (3), 183-189.

[8] Swanson, R. M. In: *Approaching the 29% limit efficiency of silicon solar cells*, Photovoltaic Specialists Conference, 2005. Conference Record of the Thirty-first IEEE, 3-7 Jan. 2005; 2005; pp 889-894.

[9] Chopra, K. L.; Paulson, P. D.; Dutta, V., Thin-film solar cells: an overview. *Prog. Photovoltaics* 2004, *12* (23), 69-92.

[10] Gordon, I.; Carnel, L.; Van Gestel, D.; Beaucarne, G.; Poortmans, J., Fabrication and characterization of highly efficient thin-film polycrystalline-silicon solar cells based on aluminium-induced crystallization. *Thin Solid Films* 2008, *516* (20), 6984-6988.

[11] Jackson, P.; Hariskos, D.; Lotter, E.; Paetel, S.; Wuerz, R.; Menner, R.; Wischmann, W.; Powalla, M., New world record efficiency for

Cu(In,Ga)Se2 thin-film solar cells beyond 20%. *Prog. Photovoltaics* 2011, *19* (7), 894-897.

[12] Kumar, V.; Masudy-Panah, S.; Tan, C. C.; Wong, T. K. S.; Chi, D. Z.; Dalapati, G. K. In *Copper oxide based low cost thin film solar cells*, Nanoelectronics Conference (INEC), 2013 IEEE 5th International, 2-4 Jan. 2013; 2013; pp 443-445.

[13] Nguyen, R. H., Galliumarsenide. Its uses in photovoltaic applications. *Potentials, IEEE* 1998, *17* (5), 33-35.

[14] Liang, Y.; Xu, Z.; Xia, J.; Tsai, S.-T.; Wu, Y.; Li, G.; Ray, C.; Yu, L., For the Bright Future—Bulk Heterojunction Polymer Solar Cells with Power Conversion Efficiency of 7.4%. *Adv. Mater.* 2010, *22* (20), E135-E138.

[15] Kojima, A.; Teshima, K.; Shirai, Y.; Miyasaka, T., Organometal Halide Perovskites as Visible-Light Sensitizers for Photovoltaic Cells. *J. Am. Chem. Soc.* 2009, *131* (17), 6050-6051.

[16] Ltd, D., EPFL Achieves 21% Efficiency for Perovskites. Queanbeyan, 2015.

[17] Chung, I.; Lee, B.; He, J.; Chang, R. P. H.; Kanatzidis, M. G., All-solid-state dye-sensitized solar cells with high efficiency. *Nature* 2012, *485* (7399), 486-489.

[18] Lee, M. M.; Teuscher, J.; Miyasaka, T.; Murakami, T. N.; Snaith, H. J., Efficient Hybrid Solar Cells Based on Meso-Superstructured Organometal Halide Perovskites. *Science* 2012, *338* (6107), 643-647.

[19] Gonzalez-Pedro, V.; Juarez-Perez, E. J.; Arsyad, W.-S.; Barea, E. M.; Fabregat-Santiago, F.; Mora-Sero, I.; Bisquert, J., General Working Principles of CH3NH3PbX3 Perovskite Solar Cells. *Nano Lett.* 2014, *14* (2), 888-893.

[20] Etgar, L.; Gao, P.; Xue, Z.; Peng, Q.; Chandiran, A. K.; Liu, B.; Nazeeruddin, M. K.; Grätzel, M., Mesoscopic CH3NH3PbI3/TiO2 Heterojunction Solar Cells. *J. Am. Chem. Soc.* 2012, *134* (42), 17396-17399.

[21] Boix, P. P.; Nonomura, K.; Mathews, N.; Mhaisalkar, S. G., Current progress and future perspectives for organic/inorganic perovskite solar cells. *Mater. Today* 2014, *17* (1), 16-23.

[22] Zhu, X., The Perovskite Fever and Beyond. *Acc. Chem. Res.* 2016, *49* (3), 355-356.

[23] Docampo, P.; Bein, T., A Long-Term View on Perovskite Optoelectronics. *Acc. Chem. Res.* 2016, *49* (2), 339-346.

[24] Noel, N. K.; Stranks, S. D.; Abate, A.; Wehrenfennig, C.; Guarnera, S.; Haghighirad, A.-A.; Sadhanala, A.; Eperon, G. E.; Pathak, S. K.; Johnston, M. B.; Petrozza, A.; Herz, L. M.; Snaith, H. J., Lead-free organic-inorganic

tin halide perovskites for photovoltaic applications. *Energy Environ. Sci.* 2014, *7* (9), 3061-3068.

[25] Niu, G.; Li, W.; Meng, F.; Wang, L.; Dong, H.; Qiu, Y., Study on the stability of CH3NH3PbI3 films and the effect of post-modification by aluminum oxide in all-solid-state hybrid solar cells. *J. Mater. Chem. A* 2014, *2* (3), 705-710.

[26] Leong, W. L.; Ooi, Z.-E.; Sabba, D.; Yi, C.; Zakeeruddin, S. M.; Graetzel, M.; Gordon, J. M.; Katz, E. A.; Mathews, N., Identifying Fundamental Limitations in Halide Perovskite Solar Cells. *Adv. Mater.* 2016, *28* (12), 2439-2445.

[27] Reddy, S. S.; Gunasekar, K.; Heo, J. H.; Im, S. H.; Kim, C. S.; Kim, D.-H.; Moon, J. H.; Lee, J. Y.; Song, M.; Jin, S.-H., Solar Cells: Highly Efficient Organic Hole Transporting Materials for Perovskite and Organic Solar Cells with Long-Term Stability (Adv. Mater. 4/2016). *Adv. Mater.* 2016, *28* (4), 685-685.

[28] Egger, D. A.; Rappe, A. M.; Kronik, L., Hybrid Organic–Inorganic Perovskites on the Move. *Acc. Chem. Res.* 2016, *49* (3), 573-581.

[29] Jacoby, M., The future of low-cost solar cells. *Chemical & Engineering News* 2016, pp 30-35.

[30] Woodbury, N.; Allen, J., The Pathway, Kinetics and Thermodynamics of Electron Transfer in Wild Type and Mutant Reaction Centers of Purple Nonsulfur Bacteria. In *Anoxygenic Photosynthetic Bacteria*, Blankenship, R.; Madigan, M.; Bauer, C., Eds. Springer Netherlands: 1995; Vol. 2, pp 527-557.

[31] Yoder, L.; Cole, A.; Sension, R., Structure and function in the isolated reaction center complex of Photosystem II: energy and charge transfer dynamics and mechanism. *Photosynth. Res.* 2002, *72* (2), 147-158.

[32] Savikhin, S., Ultrafast Optical Spectroscopy of Photosystem I. In *Photosystem I*, Golbeck, J., Ed. Springer Netherlands: 2006; Vol. 24, pp 155-175.

[33] Veldman, D.; Meskers, S. C. J.; Janssen, R. A. J., The Energy of Charge-Transfer States in Electron Donor–Acceptor Blends: Insight into the Energy Losses in Organic Solar Cells. *Adv. Funct. Mater.* 2009, *19* (12), 1939-1948.

[34] Yu, G.; Gao, J.; Hummelen, J. C.; Wudl, F.; Heeger, A. J., Polymer photovoltiac cells: Enhanced efficiencies via a network of internal donor-acceptor heterojunctions. *Science* 1995, *270* (5243), 1789.

[35] Dennler, G.; Scharber, M. C.; Brabec, C. J., Polymer-Fullerene Bulk-Heterojunction Solar Cells. *Adv. Mater.* 2009, *21* (13), 1323-1338.

[36] Chen, H.-Y.; Hou, J.; Zhang, S.; Liang, Y.; Yang, G.; Yang, Y.; Yu, L.; Wu, Y.; Li, G., Polymer solar cells with enhanced open-circuit voltage and efficiency. *Nat Photon* 2009, *3* (11), 649-653.

[37] Li, G.; Zhu, R.; Yang, Y., Polymersolarcells. *Nat Photon* 2012, *6* (3), 153-161.

[38] Chen, J.; Cao, Y., Development of Novel Conjugated Donor Polymers for High-Efficiency Bulk-Heterojunction Photovoltaic Devices. *Acc. Chem. Res.* 2009, *42* (11), 1709-1718.

[39] Jørgensen, M.; Norrman, K.; Krebs, F. C., Stability/degradation of polymer solar cells. *Sol. Energy Mater. Sol. Cells* 2008, *92* (7), 686-714.

[40] Johansson, O.; Borgström, M.; Lomoth, R.; Palmblad, M.; Bergquist, J.; Hammarström, L.; Sun, L.; Åkermark, B., Electron Donor−Acceptor Dyads Based on Ruthenium(II) Bipyridine and Terpyridine Complexes Bound to Naphthalenediimide. *Inorg. Chem.* 2003, *42* (9), 2908-2918.

[41] Borgström, M.; Johansson, O.; Lomoth, R.; Baudin, H. B.; Wallin, S.; Sun, L.; Åkermark, B.; Hammarström, L., Electron Donor−Acceptor Dyads and Triads Based on Tris(bipyridine)ruthenium(II) and Benzoquinone: Synthesis, Characterization, and Photoinduced Electron Transfer Reactions. *Inorg. Chem.* 2003, *42* (17), 5173-5184.

[42] Grätzel, M., Solar Energy Conversion by Dye-Sensitized Photovoltaic Cells. *Inorg. Chem.* 2005, *44* (20), 6841-6851.

[43] Erten-Ela, S.; Yilmaz, M. D.; Icli, B.; Dede, Y.; Icli, S.; Akkaya, E. U., A Panchromatic Boradiazaindacene (BODIPY) Sensitizer for Dye-Sensitized Solar Cells. *Org. Lett.* 2008, *10* (15), 3299-3302.

[44] Kolemen, S.; Cakmak, Y.; Erten-Ela, S.; Altay, Y.; Brendel, J.; Thelakkat, M.; Akkaya, E. U., Solid-State Dye-Sensitized Solar Cells Using Red and Near-IR Absorbing Bodipy Sensitizers. *Org. Lett.* 2010, *12* (17), 3812-3815.

[45] Mao, M.; Zhang, X.; Cao, L.; Tong, Y.; Wu, G., Design of Bodipy based organic dyes for high-efficient dye-sensitized solar cells employing double electron acceptors. *Dyes Pigm.* 2015, *117*, 28-36.

[46] Wasielewski, M. R.; Studier, M. H.; Katz, J. J., Covalently linked chlorophyll a dimer: A biomimetic model of special pair chlorophyll. *Proc. Natl. Acad. Sci. U. S. A.* 1976, *73* (12), 4282-4286.

[47] Gust, D.; Moore, T. A.; Moore, A. L., Molecular mimicry of photosynthetic energy and electron transfer. *Acc. Chem. Res.* 1993, *26* (4), 198-205.

[48] Moore, T. A.; Gust, D.; Mathis, P.; Mialocq, J.-C.; Chachaty, C.; Bensasson, R. V.; Land, E. J.; Doizi, D.; Liddell, P. A.; Lehman, W. R.; Nemeth, G. A.; Moore, A. L., Photodriven charge separation in a carotenoporphyrin-quinone triad. *Nature* 1984, *307* (5952), 630-632.

[49] Palacios, R. E.; Kodis, G.; Gould, S. L.; de la Garza, L.; Brune, A.; Gust, D.; Moore, T. A.; Moore, A. L., Artificial Photosynthetic Reaction Centers: Mimicking Sequential Electron and Triplet-Energy Transfer. *Chem Phys Chem* 2005, *6* (11), 2359-2370.

[50] Gust, D.; Moore, T. A.; Moore, A. L.; Lee, S.-J.; Bittersmann, E.; Luttrull, D. K.; Rehms, A. A.; DeGraziano, J. M.; Ma, X. C.; Gao, F.; Belford, R. E.; Trier, T. T., Efficient Multistep Photoinitiated Electron Transfer in a Molecular Pentad. *Science* 1990, *248* (4952), 199-201.

[51] Kuciauskas, D.; Liddell, P. A.; Hung, S.-C.; Lin, S.; Stone, S.; Seely, G. R.; Moore, A. L.; Moore, T. A.; Gust, D., Structural Effects on Photoinduced Electron Transfer in Carotenoid−Porphyrin−Quinone Triads. *J. Phys. Chem. B* 1997, *101* (3), 429-440.

[52] Kuciauskas, D.; Lin, S.; Seely, G. R.; Moore, A. L.; Moore, T. A.; Gust, D.; Drovetskaya, T.; Reed, C. A.; Boyd, P. D. W., Energy and photoinduced electron transfer in porphyrin-fullerene dyads. *J. Phys. Chem.* 1996, *100* (39), 15926-15932.

[53] Guldi, D. M., Fullerenes: three dimensional electron acceptor materials. *Chem. Commun.* 2000, (5), 321-327.

[54] Guldi, D. M., Molecular porphyrinfullerene architectures. *Pure Appl. Chem.* 2003, *75* (8), 1069-1075.

[55] Imahori, H.; Tamaki, K.; Guldi, D. M.; Luo, C.; Fujitsuka, M.; Ito, O.; Sakata, Y.; Fukuzumi, S., Modulating charge separation and charge recombination dynamics in porphyrin-fullerene linked dyads and triads: Marcus-normal versus inverted region. *J. Am. Chem. Soc.* 2001, *123* (11), 2607-2617.

[56] Robinson, I. Metal dipyrrin and aryl-linked bis-porphyrin hosts for fullerenes and the supramolecular assembly of multi-chromophore porphyrin -- fullerene systems. 2012.

[57] Kodis, G.; Terazono, Y.; Liddell, P. A.; Andréasson, J.; Garg, V.; Hambourger, M.; Moore, T. A.; Moore, A. L.; Gust, D., Energy and photoinduced electron transfer in a wheel-shaped artificial photosynthetic antenna-reaction center complex. *J. Am. Chem. Soc.* 2006, *128* (6), 1818-1827.

[58] Bothner-By, A. A.; Dadok, J.; Johnson, T. E.; Lindsey, J. S., Molecular dynamics of covalently-linked multi-porphyrin arrays. *J. Phys. Chem.* 1996, *100* (44), 17551-17557.

[59] Terazono, Y.; Liddell, P. A.; Garg, V.; Kodis, G.; Brune, A.; Hambourger, M.; Moore, A. L.; Moore, T. A.; Gust, D., Artificial photosynthetic

antenna-reaction center complexes based on a hexaphenylbenzene core. *J. Porphyrins Phthalocyanines* 2005, *9* (10), 706-723.

[60] Chukharev, V.; Tkachenko, N. V.; Efimov, A.; Guldi, D. M.; Hirsch, A.; Scheloske, M.; Lemmetyinen, H., Tuning the ground-state and excited-state interchromophore interactions in porphyrin-fullerene π-stacks. *J. Phys. Chem. B.* 2004, *108* (42), 16377-16385.

[61] Dietel, E.; Hirsch, A.; Eichhorn, E.; Rieker, A.; Hackbarth, S.; Röder, B., A macrocyclic [60] fullerene–porphyrin dyad involving π–π stacking interactions. *Chem. Commun.* 1998, (18), 1981-1982.

[62] Kuciauskas, D.; Lin, S.; Seely, G. R.; Moore, A. L.; Moore, T. A.; Gust, D.; Drovetskaya, T.; Reed, C. A.; Boyd, P. D., Energy and photoinduced electron transfer in porphyrin-fullerene dyads. *The Journal of Physical Chemistry* 1996, *100* (39), 15926-15932.

[63] Imahori, H.; Hagiwara, K.; Aoki, M.; Akiyama, T.; Taniguchi, S.; Okada, T.; Shirakawa, M.; Sakata, Y., Linkage and solvent dependence of photoinduced electron transfer in zincporphyrin-C60 dyads. *J. Am. Chem. Soc.* 1996, *118* (47), 11771-11782.

[64] Imahori, H.; Sakata, Y., Donor-Linked Fullerenes: Photoinduced electron transfer and its potential application. *Adv. Mater.* 1997, *9* (7), 537-546.

[65] Imahori, H., Porphyrin-fullerene linked systems as artificial photosynthetic mimics. *Org. Biomol. Chem.* 2004, *2* (10), 1425-1433.

[66] Kuciauskas, D.; Liddell, P. A.; Lin, S.; Johnson, T. E.; Weghorn, S. J.; Lindsey, J. S.; Moore, A. L.; Moore, T. A.; Gust, D., An artificial photosynthetic antenna-reaction center complex. *J. Am. Chem. Soc.* 1999, *121* (37), 8604-8614.

[67] Kodis, G.; Liddell, P. A.; de la Garza, L.; Clausen, P. C.; Lindsey, J. S.; Moore, A. L.; Moore, T. A.; Gust, D., Efficient energy transfer and electron transfer in an artificial photosynthetic antenna-reaction center complex. *J. Phys. Chem. A.* 2002, *106* (10), 2036-2048.

[68] Tkachenko, N. V.; Rantala, L.; Tauber, A. Y.; Helaja, J.; Hynninen, P. H.; Lemmetyinen, H., Photoinduced electron transfer in phytochlorin-[60] fullerene dyads. *J. Am. Chem. Soc.* 1999, *121* (40), 9378-9387.

[69] Ohkubo, K.; Kotani, H.; Shao, J.; Ou, Z.; Kadish, K. M.; Li, G.; Pandey, R. K.; Fujitsuka, M.; Ito, O.; Imahori, H., Production of an Ultra-Long-Lived Charge-Separated State in a Zinc Chlorin–C60 Dyad by One-Step Photoinduced Electron Transfer. *Angew. Chem.* 2004, *116* (7), 871-874.

[70] Fukuzumi, S.; Ohkubo, K.; Imahori, H.; Shao, J.; Ou, Z.; Zheng, G.; Chen, Y.; Pandey, R. K.; Fujitsuka, M.; Ito, O., Photochemical and electrochemical properties of zinc chlorin-C60 dyad as compared to

corresponding free-base chlorin-C60, free-base porphyrin-C60, and zinc porphyrin-C60 dyads. *J. Am. Chem. Soc.* 2001, *123* (43), 10676-10683.

[71] Zilbermann, I.; Anderson, G. A.; Guldi, D. M.; Yamada, H.; Imahori, H.; Fukuzumi, S., Layer-by-layer assembly of porphyrin-fullerene dyads. *J. Porphyrins Phthalocyanines*2003, *7* (05), 357-364.

[72] Hauke, F.; Swartz, A.; Guldi, D. M.; Hirsch, A., Supramolecular assembly of a quasi-linear heterofullerene–porphyrin dyad. *J. Mater. Chem.* 2002, *12* (7), 2088-2094.

[73] Swiegers, G. F., *Bioinspiration and biomimicry in chemistry: reverse-engineering nature*. Wiley: 2012.

[74] Garg, V.; Kodis, G.; Liddell, P. A.; Terazono, Y.; Moore, T. A.; Moore, A. L.; Gust, D., Artificial photosynthetic reaction center with a coumarin-based antenna system. *J. Phys. Chem. B.* 2013, *117* (38), 11299-11308.

[75] Imahori, H.; Sekiguchi, Y.; Kashiwagi, Y.; Sato, T.; Araki, Y.; Ito, O.; Yamada, H.; Fukuzumi, S., Long-Lived Charge-Separated State Generated in a Ferrocene–meso,meso-Linked Porphyrin Trimer–Fullerene Pentad with a High Quantum Yield. *Chemistry – A European Journal* 2004, *10* (13), 3184-3196.

[76] Terazono, Y.; Kodis, G.; Liddell, P. A.; Garg, V.; Moore, T. A.; Moore, A. L.; Gust, D., Multiantenna artificial photosynthetic reaction center complex. *J. Phys. Chem. B.* 2009, *113* (20), 7147-7155.

[77] Kodis, G.; Liddell, P. A.; Moore, A. L.; Moore, T. A.; Gust, D., Synthesis and photochemistry of a carotene–porphyrin–fullerene model photosynthetic reaction center. *J. Phys. Org. Chem.* 2004, *17* (9), 724-734.

[78] Isosomppi, M.; Tkachenko, N. V.; Efimov, A.; Lemmetyinen, H., Photoinduced electron transfer in double-bridged porphyrin-fullerene triads. *J. Phys. Chem. A.* 2005, *109* (22), 4881-4890.

[79] El-Khouly, M. E.; Ito, O.; Smith, P. M.; D'Souza, F., Intermolecular and supramolecular photoinduced electron transfer processes of fullerene–porphyrin/phthalocyanine systems. *J. Photochem. Photobiol., C* 2004, *5* (1), 79-104.

[80] Schuster, D. In *Electron transfer in the marcus inverted region in fullerene-porphyrin dyads*, Abstracts of Papers of the American Chemical Society, *Amer. Chemical Soc* 1155 16th St, NW, Washington, DC 20036 USA: 2000; pp U240-U240.

[81] Imahori, H.; Fukuzumi, S., Porphyrin-and Fullerene-Based Molecular Photovoltaic Devices. *Adv. Funct. Mater.* 2004, *14* (6), 525-536.

[82] Garg, V.; Kodis, G.; Chachisvilis, M.; Hambourger, M.; Moore, A. L.; Moore, T. A.; Gust, D., Conformationally Constrained Macrocyclic

Diporphyrin-Fullerene Artificial Photosynthetic Reaction Center. *J. Am. Chem. Soc.* 2011, *133* (9), 2944-2954.

[83] Imahori, H.; El-Khouly, M. E.; Fujitsuka, M.; Ito, O.; Sakata, Y.; Fukuzumi, S., Solvent dependence of charge separation and charge recombination rates in porphyrin-fullerene dyad. *J. Phys. Chem. A.* 2001, *105* (2), 325-332.

[84] Guldi, D. M.; Hirsch, A.; Scheloske, M.; Dietel, E.; Troisi, A.; Zerbetto, F.; Prato, M., Modulating Charge-Transfer Interactions in Topologically Different Porphyrin–C60 Dyads. *Chemistry–A European Journal* 2003, *9* (20), 4968-4979.

[85] Guldi, D. M.; Luo, C.; Prato, M.; Troisi, A.; Zerbetto, F.; Scheloske, M.; Dietel, E.; Bauer, W.; Hirsch, A., Parallel (face-to-face) versus perpendicular (edge-to-face) alignment of electron donors and acceptors in fullerene porphyrin dyads: The importance of orientation in electron transfer. *J. Am. Chem. Soc.* 2001, *123* (37), 9166-9167.

[86] Liddell, P. A.; Kuciauskas, D.; Sumida, J. P.; Nash, B.; Nguyen, D.; Moore, A. L.; Moore, T. A.; Gust, D., Photoinduced charge separation and charge recombination to a triplet state in a carotene-porphyrin-fullerene triad. *J. Am. Chem. Soc.* 1997, *119* (6), 1400-1405.

[87] Kuciauskas, D.; Liddell, P. A.; Lin, S.; Stone, S. G.; Moore, A. L.; Moore, T. A.; Gust, D., Photoinduced electron transfer in carotenoporphyrin-fullerene triads: Temperature and solvent effects. *J. Phys. Chem. B.* 2000, *104* (18), 4307-4321.

[88] Platt, J. R., Carotene-Donor-Acceptor Complexes in Photosynthesis The predicted lowering of the excited states of carotenoids may offer a new photosynthetic pathway. *Science* 1959, *129* (3346), 372-374.

[89] Yasushi, K., New trends in photobiology: structures and functions of carotenoids in photosynthetic systems. *J. Photochem. Photobiol., B* 1991, *9* (3), 265-280.

[90] Frank, H. A.; Cogdell, R. J., Carotenoids in photosynthesis. *Photochem. Photobiol.* 1996, *63* (3), 257-264.

[91] Guldi, D. M.; Imahori, H.; Tamaki, K.; Kashiwagi, Y.; Yamada, H.; Sakata, Y.; Fukuzumi, S., A Molecular Tetrad Allowing Efficient Energy Storage for 1.6 s at 163 K. *J. Phys. Chem. A* 2004, *108* (4), 541-548.

[92] D'Souza, F.; Chitta, R.; Gadde, S.; Zandler, M. E.; Sandanayaka, A. S. D.; Araki, Y.; Ito, O., Supramolecular porphyrin-fullerene via 'two-point' binding strategy: Axial-coordination and cation-crown ether complexation. *Chem. Commun.* 2005, (10), 1279-1281.

[93] D'Souza, F.; Deviprasad, G. R.; Rahman, M. S.; Choi, J.-p., Self-Assembled Porphyrin−C_{60} and Porphycene−C_{60} Complexes via Metal Axial Coordination. *Inorg. Chem.* 1999, *38* (9), 2157-2160.

[94] Swiegers, G. F.; Malefetse, T. J., New Self-Assembled Structural Motifs in Coordination Chemistry. *Chem. Rev.* 2000, *100* (9), 3483-3538.

[95] D'Souza, F.; Ito, O., Photoinduced electron transfer in supramolecular systems of fullerenes functionalized with ligands capable of binding to zinc porphyrins and zinc phthalocyanines. *Coord. Chem. Rev.* 2005, *249* (13–14), 1410-1422.

[96] D'Souza, F.; Smith, P. M.; Gadde, S.; McCarty, A. L.; Kullman, M. J.; Zandler, M. E.; Itou, M.; Araki, Y.; Ito, O., Supramolecular Triads Formed by Axial Coordination of Fullerene to Covalently Linked Zinc Porphyrin−Ferrocene(s): Design, Syntheses, Electrochemistry, and Photochemistry. *J. Phys. Chem. B* 2004, *108* (31), 11333-11343.

[97] D'Souza, F.; Deviprasad, G. R.; Zandler, M. E.; El-Khouly, M. E.; Fujitsuka, M.; Ito, O., Photoinduced Electron Transfer in "Two-Point" Bound Supramolecular Triads Composed of N,N-Dimethylaminophenyl-Fullerene-Pyridine Coordinated to Zinc Porphyrin. *J. Phys. Chem. A* 2003, *107* (24), 4801-4807.

[98] Kira, A.; Umeyama, T.; Matano, Y.; Yoshida, K.; Isoda, S.; Park, J. K.; Kim, D.; Imahori, H., Supramolecular Donor−Acceptor Heterojunctions by Vectorial Stepwise Assembly of Porphyrins and Coordination-Bonded Fullerene Arrays for Photocurrent Generation. *J. Am. Chem. Soc.* 2009, *131* (9), 3198-3200.

[99] D'Souza, F.; Deviprasad, G. R.; Zandler, M. E.; Hoang, V. T.; Klykov, A.; VanStipdonk, M.; Perera, A.; El-Khouly, M. E.; Fujitsuka, M.; Ito, O., Spectroscopic, Electrochemical, and Photochemical Studies of Self-Assembled via Axial Coordination Zinc Porphyrin−Fulleropyrrolidine Dyads. *J. Phys. Chem. A* 2002, *106* (13), 3243-3252.

[100] Das, S. K.; Song, B.; Mahler, A.; Nesterov, V. N.; Wilson, A. K.; Ito, O.; D'Souza, F., Electron Transfer Studies of High Potential Zinc Porphyrin–Fullerene Supramolecular Dyads. *Journal of Physical Chemistry C* 2014, *118* (8), 3994-4006.

[101] de Miguel, G.; Wielopolski, M.; Schuster, D. I.; Fazio, M. A.; Lee, O. P.; Haley, C. K.; Ortiz, A. L.; Echegoyen, L.; Clark, T.; Guldi, D. M., Triazole Bridges as Versatile Linkers in Electron Donor–Acceptor Conjugates. *J. Am. Chem. Soc.* 2011, *133* (33), 13036-13054.

[102] El-Khouly, M. E.; Gadde, S.; Deviprasad, G. R.; Fujitsuka, M.; Ito, O.; D'Souza, F., Self-assembled supramolecular triad composed of

fulleropyrrolidine bearing two pyridine moieties axially coordinated to two zinc porphyrins. *J. Porphyrins Phthalocyanines* 2003, *07* (01), 1-7.

[103] Katsuhiko, A.; Jonathan, P. H.; Michael, V. L.; Ajayan, V.; Richard, C.; Somobrata, A., Challenges and breakthroughs in recent research on self-assembly. *Sci. Technol. Adv. Mater.* 2008, *9* (1), 014109.

[104] Tashiro, K.; Aida, T., Metalloporphyrin hosts for supramolecular chemistry of fullerenes. *Chem. Soc. Rev.* 2007, *36* (2), 189-197.

[105] Kamimura, T.; Ohkubo, K.; Kawashima, Y.; Nobukuni, H.; Naruta, Y.; Tani, F.; Fukuzumi, S., Submillisecond-lived photoinduced charge separation in inclusion complexes composed of Li+@C60 and cyclic porphyrin dimers. *Chemical Science* 2013, *4* (4), 1451-1461.

[106] Yamaguchi, T.; Ishii, N.; Tashiro, K.; Aida, T., Supramolecular Peapods Composed of a Metalloporphyrin Nanotube and Fullerenes. *J. Am. Chem. Soc.* 2003, *125* (46), 13934-13935.

[107] Kim, H. J.; Park, K.-M.; Ahn, T. K.; Kim, S. K.; Kim, K. S.; Kim, D.; Kim, H.-J., Novel fullerene-porphyrin-fullerene triad linked by metal axial coordination: Synthesis, X-ray crystal structure, and spectroscopic characterizations of trans-bis([60]fullerenoacetato)tin(iv) porphyrin. *Chem. Commun.* 2004, (22), 2594-2595.

[108] Kc, C. B.; Ohkubo, K.; Karr, P. A.; Fukuzumi, S.; D'Souza, F., A 'two-point' bound zinc porphyrin-zinc phthalocyanine-fullerene supramolecular triad for sequential energy and electron transfer. *Chem. Commun.* 2013, *49* (69), 7614-7616.

[109] Yanagisawa, M.; Tashiro, K.; Yamasaki, M.; Aida, T., Hosting Fullerenes by Dynamic Bond Formation with an Iridium Porphyrin Cyclic Dimer: A "Chemical Friction" for Rotary Guest Motions. *J. Am. Chem. Soc.* 2007, *129* (39), 11912-11913.

[110] Ouchi, A.; Tashiro, K.; Yamaguchi, K.; Tsuchiya, T.; Akasaka, T.; Aida, T., A Self-Regulatory Host in an Oscillatory Guest Motion: Complexation of Fullerenes with a Short-Spaced Cyclic Dimer of an Organorhodium Porphyrin. *Angew. Chem. Int. Ed.* 2006, *45* (21), 3542-3546.

[111] Shoji, Y.; Tashiro, K.; Aida, T., Sensing of Chiral Fullerenes by a Cyclic Host with an Asymmetrically Distorted π-Electronic Component. *J. Am. Chem. Soc.* 2006, *128* (33), 10690-10691.

[112] Sakaguchi, K.-i.; Kamimura, T.; Uno, H.; Mori, S.; Ozako, S.; Nobukuni, H.; Ishida, M.; Tani, F., Phenothiazine-Bridged Cyclic Porphyrin Dimers as High-Affinity Hosts for Fullerenes and Linear Array of C60 in Self-Assembled Porphyrin Nanotube. *J. Org. Chem.* 2014, *79* (7), 2980-2992.

[113] Zheng, J.-Y.; Tashiro, K.; Hirabayashi, Y.; Kinbara, K.; Saigo, K.; Aida, T.; Sakamoto, S.; Yamaguchi, K., Cyclic Dimers of Metalloporphyrins as Tunable Hosts for Fullerenes: A Remarkable Effect of Rhodium(III). *Angew. Chem. Int. Ed.* 2001, *40* (10), 1857-1861.

[114] Garcia-Simon, C.; Costas, M.; Ribas, X., Metallosupramolecular receptors for fullerene binding and release. *Chem. Soc. Rev.* 2016, *45* (1), 40-62.

[115] Uno, H.; Furukawa, M.; Fujimoto, A.; Uoyama, H.; Watanabe, H.; Okujima, T.; Yamada, H.; Mori, S.; Kuramoto, M.; Iwamura, T.; Hatae, N.; Tani, F.; Komatsu, N., Porphyrin molecular tweezers for fullerenes. *J. Porphyrins Phthalocyanines*2011, *15* (09n10), 951-963.

[116] Canevet, D.; Pérez, E. M.; Martín, N., Wraparound Hosts for Fullerenes: Tailored Macrocycles and Cages. *Angew. Chem. Int. Ed.* 2011, *50* (40), 9248-9259.

[117] Fukuzumi, S.; Ohkubo, K., Long-lived photoinduced charge separation for solar cell applications in supramolecular complexes of multi-metalloporphyrins and fullerenes. *Dalton Transactions* 2013, *42* (45), 15846-15858.

[118] Kamimura, T.; Ohkubo, K.; Kawashima, Y.; Ozako, S.; Sakaguchi, K.-i.; Fukuzumi, S.; Tani, F., Long-Lived Photoinduced Charge Separation in Inclusion Complexes Composed of a Phenothiazine-Bridged Cyclic Porphyrin Dimer and Fullerenes. *J. Phys. Chem. C.* 2015, *119* (45), 25634-25650.

[119] Kawashima, Y.; Ohkubo, K.; Okada, H.; Matsuo, Y.; Fukuzumi, S., Supramolecular Formation of Li+@PCBM Fullerene with Sulfonated Porphyrins and Long-Lived Charge Separation. *ChemPhysChem*2014, *15* (17), 3782-3790.

[120] Sun, D.; Tham, F. S.; Reed, C. A.; Chaker, L.; Boyd, P. D. W., Supramolecular Fullerene-Porphyrin Chemistry. Fullerene Complexation by Metalated "Jaws Porphyrin" Hosts. *J. Am. Chem. Soc.* 2002, *124* (23), 6604-6612.

[121] Sun, D.; Tham, F. S.; Reed, C. A.; Chaker, L.; Burgess, M.; Boyd, P. D. W., Porphyrin−Fullerene Host−Guest Chemistry. *J. Am. Chem. Soc.* 2000, *122* (43), 10704-10705.

[122] Hosseini, A.; Taylor, S.; Accorsi, G.; Armaroli, N.; Reed, C. A.; Boyd, P. D. W., Calix[4]arene-Linked Bisporphyrin Hosts for Fullerenes: Binding Strength, Solvation Effects, and Porphyrin−Fullerene Charge Transfer Bands. *J. Am. Chem. Soc.* 2006, *128* (49), 15903-15913.

[123] Grimm, B.; Schornbaum, J.; Cardona, C. M.; van Paauwe, J. D.; Boyd, P. D. W.; Guldi, D. M., Enhanced binding strengths of acyclic porphyrin hosts

with endohedral metallofullerenes. *Chemical Science* 2011, *2* (8), 1530-1537.

[124] Kho, J. L.H., Rohde, C.A, Boyd, P. D. W., Simpson, M. C., Hosseini, A. "Structure, Computational, Binding, and Photophysical Studies of Fully Self-assembled Bisporphyrin-fullerene Dyads and Triads" (To Be Submitted).

[125] Trabolsi, A.; Elhabiri, M.; Urbani, M.; Delgado de la Cruz, J. L.; Ajamaa, F.; Solladie, N.; Albrecht-Gary, A.-M.; Nierengarten, J.-F., Supramolecular click chemistry for the self-assembly of a stable Zn(ii)-porphyrin-C60 conjugate. *Chem. Commun.* 2005, (46), 5736-5738.

[126] Takai, A.; Chkounda, M.; Eggenspiller, A.; Gros, C. P.; Lachkar, M.; Barbe, J.-M.; Fukuzumi, S., Efficient Photoinduced Electron Transfer in a Porphyrin Tripod−Fullerene Supramolecular Complex via π−π Interactions in Nonpolar Media. *J. Am. Chem. Soc.* 2010, *132* (12), 4477-4489.

[127] Marois, J.-S.; Cantin, K.; Desmarais, A.; Morin, J.-F., [3]Rotaxane−Porphyrin Conjugate as a Novel Supramolecular Host for Fullerenes. *Org. Lett.* 2008, *10* (1), 33-36.

[128] Li, M.; Ishihara, S.; Ji, Q.; Akada, M.; Hill, J. P.; Ariga, K., Paradigm shift from self-assembly to commanded assembly of functional materials: recent examples in porphyrin/fullerene supramolecular systems. *Sci. Technol. Adv. Mater.* 2012, *13* (5), 053001.

[129] Ladomenou, K.; Nikolaou, V.; Charalambidis, G.; Coutsolelos, A. G., "Click"-reaction: An alternative tool for new architectures of porphyrin based derivatives. *Coord. Chem. Rev.* 2016, *306, Part 1*, 1-42.

[130] Li, M.; Ishihara, S.; Akada, M.; Liao, M.; Sang, L.; Hill, J. P.; Krishnan, V.; Ma, Y.; Ariga, K., Electrochemical-Coupling Layer-by-Layer (ECC–LbL) Assembly. *J. Am. Chem. Soc.* 2011, *133* (19), 7348-7351.

[131] Ikeda, A.; Hatano, T.; Shinkai, S.; Akiyama, T.; Yamada, S., Efficient Photocurrent Generation in Novel Self-Assembled Multilayers Comprised of [60]Fullerene−Cationic Homooxacalix[3]arene Inclusion Complex and Anionic Porphyrin Polymer. *J. Am. Chem. Soc.* 2001, *123* (20), 4855-4856.

[132] Guldi, D. M.; Pellarini, F.; Prato, M.; Granito, C.; Troisi, L., Layer-by-Layer Construction of Nanostructured Porphyrin−Fullerene Electrodes. *Nano Lett.* 2002, *2* (9), 965-968.

[133] Li, M.; Ishihara, S.; Ji, Q.; Ma, Y.; Hill, J. P.; Ariga, K., Electrochemical Coupling Layer-by-layer (ECC-LbL) Assembly in Patterning Mode. *Chem. Lett.* 2012, *41* (4), 383-385.

[134] Sudeep, P. K.; Ipe, B. I.; Thomas, K. G.; George, M. V.; Barazzouk, S.; Hotchandani, S.; Kamat, P. V., Fullerene-functionalized gold nanoparticles.

A self-assembled photoactive antenna-metal nanocore assembly. *Nano Lett.* 2002, *2* (1), 29-35.

[135] Kamat, P. V.; Barazzouk, S.; Hotchandani, S.; Thomas, K. G., Nanostructured Thin Films of C60–Aniline Dyad Clusters: Electrodeposition, Charge Separation, and Photoelectrochemistry. *Chemistry–A European Journal* 2000, *6* (21), 3914-3921.

[136] Sakai, H.; Kamimura, T.; Tani, F.; Hasobe, T., Supramolecular photovoltaic cells utilizing inclusion complexes composed of Li+@C60 and cyclic porphyrin dimer. *J. Porphyrins Phthalocyanines*2015, *19* (01-03), 242-250.

[137] Hasobe, T.; Imahori, H.; Kamat, P. V.; Ahn, T. K.; Kim, S. K.; Kim, D.; Fujimoto, A.; Hirakawa, T.; Fukuzumi, S., Photovoltaic cells using composite nanoclusters of porphyrins and fullerenes with gold nanoparticles. *J. Am. Chem. Soc.* 2005, *127* (4), 1216-1228.

[138] Kawashima, Y.; Ohkubo, K.; Fukuzumi, S., Efficient Charge Separation in Li+@C60 Supramolecular Complexes with Electron Donors. *Chemistry – An Asian Journal* 2015, *10* (1), 44-54.

[139] Ooyama, Y.; Uenaka, K.; Kamimura, T.; Ozako, S.; Kanda, M.; Koide, T.; Tani, F., Dye-sensitized solar cell based on an inclusion complex of a cyclic porphyrin dimer bearing four 4-pyridyl groups and fullerene C60. *RSC Advances* 2016, *6* (20), 16150-16158.

[140] Dennler, G.; Bereznev, S.; Fichou, D.; Holl, K.; Ilic, D.; Koeppe, R.; Krebs, M.; Labouret, A.; Lungenschmied, C.; Marchenko, A.; Meissner, D.; Mellikov, E.; Méot, J.; Meyer, A.; Meyer, T.; Neugebauer, H.; Öpik, A.; Sariciftci, N. S.; Taillemite, S.; Wöhrle, T., A self-rechargeable and flexible polymer solar battery. *Solar Energy* 2007, *81* (8), 947-957.

[141] Brabec, C. J.; Hauch, J. A.; Schilinsky, P.; Waldauf, C., Production Aspects of Organic Photovoltaics and Their Impact on the Commercialization of Devices. *MRS Bull.* 2005, *30* (01), 50-52.

INDEX

C

D

E

F

G

H

I

J

K

L

M

N

O

P

Q

R

S

T

U

V

W

Y

Z